Nonlinear Evolution of Shear Instabilities of the Longshore Current

by

H. Tuba Özkan-Haller

and

James T. Kirby

RESEARCH REPORT NO. CACR-97-08

September, 1997

Center for Applied Coastal Research
Ocean Engineering Laboratory
University of Delaware
Newark, DE 19716
U.S.A.

ACKNOWLEDGMENTS

This research was sponsored by the Office of Naval Research, Coastal Sciences Program, Grant N00014-94-1-0214. The authors thank Dr. U. Putrevu for providing the software used to carry out linear instability calculations. Thanks are also due to Drs. J. Oltman-Shay and N. Dodd for providing the SUPERDUCK data as well as the software to obtain estimates for two-dimensional spectra of the data.

This work was originally submitted by H. Tuba Özkan-Haller in the Fall of 1997 as a dissertation to the Faculty of the University of Delaware in partial fulfillment of the requirements for the degree of Doctor of Philosophy in Civil Engineering. The color plots contained in the dissertation are reproduced in black-and-white for this report. Copies of the color plots can be obtained by directly contacting the first author.

TABLE OF CONTENTS

LIST OF FIGURES

LIST OF TABLES

ABSTRACT

Surface gravity waves breaking in the nearshore region force a longshore surf zone current. This current can be unstable to longshore periodic perturbations. The continuity and momentum conservation equations averaged over the short wave time scales and over depth present a suitable basis for the modeling of these motions. The governing equations are in the form of the well-known shallow water equations with additional terms accounting for short wave forcing and dissipational effects. The objective of this study is to analyze the finite amplitude behavior of instabilities of the surf zone longshore current utilizing numerical experiments.

For this purpose a solution method for the shallow water equations governing wave motions in the nearshore environment is developed. Spatial derivatives contained in these equations are computed using spectral collocation methods. A high-order time integration scheme is used to compute the time evolution of the velocities and water surface elevation given initial conditions. The model domain extends from the shoreline to a desired distance offshore and is periodic in the longshore direction. Properly posed boundary conditions for the governing equations are discussed. A curvilinear moving boundary condition is incorporated at the shoreline to account for wave runup. An absorbing-generating boundary is incorporated offshore. The boundary treatments are tested using analytical and numerical results. The model is applied to the prediction of neutral stability

boundaries and equilibrium amplitudes of subharmonic edge waves. Numerical results are compared to weakly nonlinear theory and are found to reproduce the theory well.

The solution method is utilized to simulate instabilities of an analytic longshore current profile over a plane beach. The instabilities are observed to grow and equilibrate at amplitudes up to 50% of the original peak mean longshore current. For long domains in the longshore direction the long time behavior is observed to be dominated by subharmonic transitions that result in a reduction of the number of waves in the domain. The resulting longshore periodic flow structures exhibit strong offshore directed velocities and propagate in the longshore direction at a fraction of the peak current speed. Details of the subharmonic transitions as well as the effect of nonlinearity on the flow structures are analyzed.

Next, the shear instability climate during the SUPERDUCK field experiment is simulated. Observations of undulations in the longshore current were first made during this field experiment by Oltman-Shay *et al.* (1989), who stated that the frequency range less than 0.01 Hz is dominated by these motions. Due to uncertainties in the friction and lateral mixing coefficients, numerical simulations are carried out for a realistic range of values for these coefficients. The resulting flow structures can be characterized as unsteady vortices propagating in the longshore direction. These vortices interact, occasionally merge and are shed offshore. During the shedding process, locally strong offshore directed currents are generated. Lateral mixing induced by the finite amplitude shear instabilities is analyzed and found to be of comparable magnitude to other mixing processes in the surf zone.

Results from simulations of shear instabilities on plane and barred beaches show the existence of localized, migrating, offshore directed currents. Since the

short wave field can be affected by these flow features, the modeling effort is extended to include the effects of time-varying short wave forcing and interactions between the short wave and current fields. The extension involves the solution of the time-dependent energy equation for the short wave motions and refraction equation due to variations in the bathymetry as well as current fields. The inclusion of a more realistic bottom friction treatment is also discussed.

Chapter 1

INTRODUCTION

As water waves approach the shore they shoal and break. The region between the breaker line and the shoreline is referred to as the surf zone. The surf zone is an energetic region of the ocean where motions at many time scales, generated and sustained by different processes, coexist and interact. It is also a very dynamic coastal region where sediment transport and bathymetry changes are driven by breaking waves as well as wave-driven currents.

Gravity waves approaching the shore at an oblique angle are most easily noticed by an observer since they break as they approach the shore. They typically display time scales of order 10 sec and consist of wind waves and swell. In this study these waves will be referred to as "short waves". The wave breaking process induces a decay in wave height towards the shore and can be violent, involving air entrapment and generation of turbulence. The wave-induced turbulence can serve as a mixing mechanism in the surf zone.

Gravity waves propagating parallel to the shoreline also exist and are referred to as "edge waves" since their amplitude is largest at the shoreline and decays in the offshore direction. Edge waves are often observed at time scales of order 100 sec and are, therefore, also referred to as "infragravity" waves. Forced long waves (such as surf beat), edge waves and leaky waves fall into this category.

Energy in the infragravity band of the frequency spectrum can be dominant in the region close to the shoreline where the short waves have been dissipated by the breaking process (Wright *et al.*, 1982).

Recently, motions with time scales up to order 1000 sec have been identified (Oltman-Shay *et al.*, 1989) during the SUPERDUCK field experiment. Observations showed that the length scales associated with these waves are too short to satisfy gravity wave dynamics. They are, therefore, not gravity waves. Since they occupy the lower region of the infragravity frequencies they have been termed "far-infragravity waves" (Bowen and Holman, 1989). They are also often referred to as "shear waves" since their dynamics was observed to be linked to the presence of a longshore current with a pronounced shear structure.

The steady circulation system in the surf zone consists of short wave-driven currents, tidal currents and wind-driven currents. Short wave-driven currents are generated when the short waves break, their wave height decays and their excess energy and momentum is released into the surf zone. The excess momentum of the short waves induces currents and a change in the mean water level, or setup, in the nearshore region (Longuet-Higgins and Stewart, 1964). In the absence of longshore variations in the bathymetry, a stationary long crested wave field approaching the shore at oblique incidence generates a longshore current and a steady setup. The longshore current is generally relatively constant over depth. Wave-driven currents are also generated when shoreward mass transport attributed to the incoming short waves is returned offshore in the form of a depth-varying cross-shore flow referred to as the "undertow". This return flow can also be established in the form of a localized offshore directed jet or "rip current". Spatial and temporal variations in the short wave field, in the form of wave groups, induce variations in this steady system causing motions such as forced infragravity waves (Schäffer,

1993, 1994) and possibly forced far-infragravity waves (Haller *et al.*, 1997).

Although breaking gravity waves are the most dramatic feature in the surf zone, the processes of wave-driven time-varying nearshore circulation display higher correlations with sediment and pollution transport in the nearshore region. Accurate prediction of sediment transport in the nearshore region is, therefore, directly linked to a good understanding of the wave induced nearshore circulation system consisting of steady currents as well as time dependent variations of the current velocities due to infragravity or far-infragravity motions.

Nearshore circulation is generally modeled using the mass and momentum conservation equations that have been integrated over the short wave time scale. Effects of processes at the short wave time scale enter the equations of motion through radiation stress gradient terms. This concept was first introduced by Longuet-Higgins and Stewart (1962, 1963, 1964) and was applied to the prediction of steady depth-uniform longshore currents and wave setup by several investigators including Bowen (1969), Longuet-Higgins (1970), Thornton and Guza (1986) and Larson and Krauss (1991). These equations can also be applied to a two-dimensional-horizontal (2DH) domain to study steady or time-dependent depth-uniform nearshore circulation. Examples of such studies are Noda (1974), Birkemeier and Dalrymple (1975), Keely and Bowen (1977), Ebersole and Dalrymple (1979) and Wind and Vreugdenhill (1986).

Although longshore currents are relatively uniform over depth, the undertow profiles exhibit strong variations in depth inside the surf zone. The quasi-three-dimensional (quasi-3D) approach has been used in recent studies to obtain information about the vertical variations of the currents without the complications of a full 3D model. The quasi-3D approach involves calculating the depth-averaged

current velocities using depth- and time-averaged mass and momentum conservation equations. The results for the depth-averaged velocities are then utilized to compute the local velocity profile from a separate profile model. Such studies have been carried out by De Vriend and Stive (1987), Svendsen and Lorenz (1989), Svendsen and Putrevu (1990), Sanchez-Arcilla *et al.* (1992), Van Dongeren *et al.* (1994) and Faria *et al.* (1995).

1.1 Linear Instability of Longshore Currents

Since the longshore current is only weakly dependent on depth, it can be approximated as a two-dimensional flow. Although two-dimensional flows in fluid mechanics have often been observed to be unstable (see Drazin and Reid, 1982), the need to analyze the stability characteristics of the longshore current did not arise until Oltman-Shay *et al.* (1989) observed a meandering of the longshore current during the SUPERDUCK field experiment. Observations showed that the undulations propagated in the direction of the longshore current and did not satisfy gravity wave dynamics. Therefore, alternate mechanisms were sought to explain the observations.

Bowen and Holman (1989) performed an analytic study of an idealized longshore current profile over constant depth using the "rigid lid" assumption and identified a mechanism well studied in larger-scale physical oceanography, but new to the nearshore: a shear instability of the mean longshore current. They showed that the shear instability can reproduce the nondispersive character and meandering nature of the motions observed by Oltman-Shay *et al.* (1989). The restoring mechanism for these alongshore propagating motions, termed shear waves, is potential vorticity where the background vorticity is supplied by the shear structure of the mean longshore current in analogy to the effect of the

Earth's rotation in larger scale applications.

Several other mechanisms have been proposed to explain the experimental observations by Oltman-Shay *et al.* (1989). Shemer *et al.* (1991) suggested that oscillations in the longshore current and radiation stresses may be due to the long time evolution of a three-wave system, composed of a carrier wave and the two most unstable Benjamin-Feir sidebands. Tang and Dalrymple (1989) and Fowler and Dalrymple (1990), in turn, showed that wave trains incident at slightly different angles to the beach can generate rip currents that migrate in the longshore direction at slow time scales. More recently, Haller *et al.* (1997) suggested that offshore wave groups can directly force low frequency vorticity motions. All of these approaches assume the observed oscillations to be forced phenomena whereas the linear instability theory proposes eigenmodes of resonance resulting in free oscillations. It should also be taken into account that the forced oscillation theories can provide the necessary perturbations for the eigenmodes associated with the linear instability theory.

The instability theory has, so far, been the most studied alternative for explaining the observations by Oltman-Shay *et al.* (1989). Since the pioneering work by Bowen and Holman (1989) and Oltman-Shay *et al.* (1989), several subsequent investigators applied the linear instability theory to more realistic current and bottom profiles. Dodd and Thornton (1990) performed an analytical study analyzing the energy transfer between the mean current and the shear instabilities and extended the theory by Bowen and Holman (1989) by applying the analysis to a simplified current profile over nonconstant depth. Putrevu and Svendsen (1992) carried out a numerical study applying the instability theory to realistic current and bottom profiles including plane and barred beaches. They observed that the instability is stronger on barred beaches.

In the same year, Dodd *et al.* (1992) lifted one more limitation of the original shear instability theory by introducing bottom friction. They simulated the linear shear wave climate for several days of the SUPERDUCK experiment where energetic meandering of the longshore current was originally observed. They found good agreement with the observed range of frequencies and propagation speeds of shear waves. Results from this study seemed to suggest that the observed fluctuations were weakly nonlinear equilibrated shear instabilities but no conclusive information about the final amplitudes of the shear instabilities could be deduced due to the linearity assumption.

Church *et al.* (1992) performed a linear instability study simulating the DELILAH experiment and inferred the amplitudes of the oscillations by scaling the computed energy density of the oscillations to reproduce the observed energy density. They found that velocity fluctuations with the inferred amplitudes can cause significant lateral mixing in the surf zone.

Later, Falqués and Iranzo (1994) analyzed the effects of bottom friction and turbulent momentum mixing, and also confirmed the applicability of the "rigid lid" assumption for longshore currents with small Froude numbers. Finally, Dodd (1994) analyzed in further detail the effect of bottom friction on the instability and showed that increasing the friction coefficient results in a weakening of the instability and a slight shift in the most unstable wavenumber.

1.2 Nonlinear Instability of Longshore Currents

In order to study the disturbances as they reach finite amplitude, a nonlinear analysis needed to be employed. Analytical studies utilizing weakly nonlinear theories were carried out by Dodd and Thornton (1992) and Feddersen (1996)

who examined weakly unstable longshore currents on a beach and found that the instabilities reach finite amplitude and have the potential to alter the mean longshore current profile.

Falqués *et al.* (1994) modeled the nonlinear shallow water equations utilizing a "rigid lid" assumption and performed numerical experiments for a plane beach geometry incorporating bottom friction and lateral mixing. They found that the instabilities equilibrate with constant or modulated amplitudes and observed that the period of the disturbances increased with increasing amplitude.

Allen *et al.* (1996) carried out a detailed numerical study of the effects of varying the bottom friction coefficient as well as the longshore width of the modeling domain. They neglected lateral mixing and generated an initial longshore current profile and observed the subsequent temporal growth of the shear instabilities. They found that finite amplitude disturbances with constant amplitudes result for high values of the friction factor corresponding to a weakly unstable longshore current. The computed final amplitudes and cross-shore distributions of the shear instabilities agree with analytical results by Feddersen (1996). As the friction factor is decreased the disturbances display modulated amplitudes, period doubling bifurcations and, eventually, chaotic behavior. When the width of the modeling domain is increased the behavior is dominated by the transition of the motions to larger scale nonlinear propagating disturbances. This behavior was also observed by Özkan and Kirby (1995). Allen *et al.* (1996) furthermore found that fully developed shear instabilities alter the mean longshore current profile significantly. In the presence of the finite amplitude disturbances the mean longshore current displays marginal stability even though the initial mean current was strongly unstable. This is an important finding since measured mean current

profiles in reality correspond to the final mean current in the presence of the fluctuations and could display much different stability characteristics than the often unknown, but relevant, fluctuation-free initial state.

More recently, Özkan-Haller and Kirby (1996a, 1996b) simulated shear instabilities for the SUPERDUCK experiment using the nonlinear shallow water equations including the effects of bottom friction and lateral mixing. They compared the predicted velocity spectra, the obtained propagation speeds of the disturbances as well as the final mean longshore current profiles to data. They found that the lateral mixing caused by the fully developed shear instabilities is of comparable magnitude to mixing due to more traditional mechanisms such as turbulence or the Taylor dispersion process outlined by Svendsen and Putrevu (1994).

Most recently, Slinn *et al.* (1997) examined the nonlinear instability of the longshore current over a barred topography including bottom friction and neglecting lateral mixing. They found equilibrated shear waves for high values of bottom friction and irregular fluctuations for lower values of the frictional coefficient and showed that these instabilities cause substantial lateral mixing of momentum in the surf zone and alter the initial current profile significantly. They carried out linear instability analyses of the initial fluctuation-free current profile as well as the final mean longshore current in the presence of the fluctuations. The results for the two current profiles show that the range of unstable wavenumbers as well as the most unstable wavenumber agree approximately for cases involving irregular fluctuations. The growth rates in the former current profile are an order of magnitude larger than in the latter. This observation provides an explanation to the fact that results of linear instability analyses of measured currents can produce good agreement for the range of unstable wavenumbers and propagation speeds. Slinn *et al.* (1997) also state that good reproduction of the propagation speeds

by linear theory does, therefore, not necessarily imply a weakly nonlinear flow regime.

In all the studies outlined above, the spirit of the linear instability analysis by Bowen and Holman (1989) is preserved since an initial current is generated and subsequently the temporal growth of the instabilities to finite amplitude is observed. In contrast, Deigaard *et al.* (1994) performed a study where the spatial growth of the instabilities was observed.

In addition to observations during field experiments, low frequency oscillations of the longshore current have also been observed in the laboratory by Reniers *et al.* (1994). In this study a longshore current was generated in a wave basin by obliquely incident waves, the apparent mean longshore current at the downstream end of the basin was recirculated and reintroduced at the upstream end. Spatial growth of instabilities was observed. Dodd and Falqués (1996) showed that the simpler temporal instability analysis, utilized in the linear instability studies outlined above, can be used in place of the more complicated spatial instability theory to obtain good indications of the instability properties in cases where a spatial growth of instabilities is observed. Therefore, Reniers *et al.* (1997) applied the temporal instability analysis to the measured current profile and obtained good predictions of the range of unstable wavenumbers and the propagation speeds of the instabilities but underpredicted the growth rates. Reniers and Battjes (1996) recently found that the measured motions have a potential to cause lateral mixing in the surf zone. However, the current recirculating system in the basin was designed to obtain a longshore uniform current, making it impossible to observe changes in the mean longshore current profile as the instabilities grew with longshore distance. The measured longshore current profile is likely to include the

effects of mixing due to shear instabilities. Therefore, it is likely that the measured current displays a weaker instability than the relevant fluctuation-free initial current. Analysis of this unknown initial state could produce the observed growth rates.

1.3 Scope of Present Study

In this study, we seek to assess the importance of shear instablities of the longshore current in the surf zone. Our approach is to carry out numerical simulations of shear instabilities for realistic situations. This dissertation contains work prepared for various conferences and journal publications.

In Chapter 2 the mechanisms causing a short wave-induced longshore current are reviewed, the conditions leading to the instability of wave-induced longshore currents are discussed. The linear instability theory of Bowen and Holman (1989) is derived.

The boundary value problem for the nonlinear instability calculations is stated is Chapter 3. The incorporation of a moving shoreline boundary, an absorbing-generating offshore boundary as well as periodic longshore boundaries is described. Chapter 3 also details the solution method to predict the time dependent behavior of the current velocities and the mean surface elevation.

Chapter 4 documents the testing of the model. The test cases include simulations of single wave runup on beaches with and without longshore variations as well as generation and absorption of long gravity waves at the offshore boundary. As a final test case edge waves resulting from an instability of a normally incident (and reflected) long wave are simulated. The results are compared to the weakly nonlinear theory by Guza and Bowen (1976).

Having verified the solution technique, we first choose to simulate shear instabilities of the longshore current in the simplest possible mathematical setting. These simulations are documented in Chapter 5. An analytical current profile on a plane slope is considered. The simplest possible mathematical representation of dissipation due to bottom friction is included and a finite domain width in the longshore direction is chosen. Simulations are carried out for a fixed bottom frictional coefficient with the objective of evaluating the appropriateness of the remaining simplifying assumptions.

Since several mechanisms have been proposed to explain the observations by Oltman-Shay *et al.* (1989) we further seek to find out if instabilities of the longshore current can account for the low frequency energy observed during the SUPERDUCK experiment and to assess the importance of lateral mixing caused by shear instabilities. For this purpose, in Chapter 6, we choose to simulate the rather distinct low frequency climate observed at SUPERDUCK during the period of October 15 through October 18, 1986 where the frequencies less than 0.01 Hz were dominated by shear waves. Linear instability calculations for these days were previously carried out by Dodd *et al.* (1992) assuming straight and parallel bottom contours and a stationary short wave field, resulting in good predictions of the observed range of wavenumbers and propagation speeds. Here, the analysis by Dodd *et al.* (1992) is taken one step further by carrying out a similar analysis using nonlinear computations. The assumptions of straight and parallel bottom contours and a stationary wave field are retained. The effects of bottom friction as well as lateral momentum mixing are included using simple parameterizations. A bottom friction coefficient (c_f) and a mixing coefficient (M) to be defined later are the free parameters of the model. Simulations are carried out for several values of the free parameters. The instabilities are observed to grow to a finite amplitude, the mean longshore current is also observed to change suggesting that the finite

amplitude shear instabilities induce additional lateral mixing in the surf zone.

In Chapter 7 we state the necessary extensions to the modeling effort in order to consider temporal and spatial variations in the short wave field as well as interactions between the time dependent short wave and current fields. By lifting the assumption of a stationary short wave field we can analyze the possibility of coherent variations in the short wave field to cause forced fluctuations at the time scales of far-infragravity waves. Furthermore, by including the effect of the current field on the short waves, the extent to which fully developed shear instabilities can alter the incident short wave field can be assessed. In Chapter 8, the results from the study are summarized and suggestions for future study are made.

Chapter 2

GENERATION AND STABILITY OF THE LONGSHORE CURRENT

2.1 Introduction

The transition of laminar flow to turbulent flow in a two-dimensional flow field is often attributed to an instability mechanism. If the two-dimensional flow is stable, small wavelike disturbances that are inevitably present in any natural system remain small and the flow is steady. However, if the flow is unstable the disturbances will grow and reach finite amplitude. The flow will exhibit a time varying character and the mean flow can be affected by the presence of the wavelike motions. Therefore, the mean flow in the presence of fluctuations can be drastically different from the initial flow (or basic state) that developed the instabilities.

Observations of laminar flows developing wavelike finite amplitude fluctuations were made as early as 1883 (Reynolds, 1883). Theories that predict whether or not small perturbations will grow for a given flow field date as far back as 1868 (Helmholtz, 1868). It was several years later that Rayleigh (1880) formulated the linear instability problem for the inviscid flow of an incompressible fluid of constant density and obtained an important result. He stated that a necessary condition for an instability to exist is the presence of an inflection point in the flow

profile. The wave-induced longshore current in the surf zone is often considered to be invariant over depth and therefore constitutes a two-dimensional flow. The linear instability theory of Rayleigh (1880) can be used with minor modifications to study the stability characteristics of the longshore current.

In order to carry out an instability analysis of the surf zone longshore current, the basic state consisting of a steady cross-shore variable current profile is considered. This basic state is created when obliquely incident, long crested short waves approach the shore and break a certain distance offshore, exerting a net force on the water column due to the decrease in the radiation stress (Longuet-Higgins and Stewart, 1963, 1964). The longshore component of this force causes a current in the longshore direction that is balanced by bottom friction. The longshore current is also diffused by mixing processes in the surf zone due to motions such as turbulence. The excess momentum due to the breaking waves in the cross-shore direction causes a setup of the mean surface elevation. If the wave field is stationary the setup and longshore current are expected to be steady and longshore-invariant. Whether or not wavelike disturbances in the current velocity become unstable and grow can be determined utilizing a linear instability analysis. If the basic state consisting of a steady longshore current is unstable to longshore periodic perturbations, the perturbations will grow and be observable as finite amplitude undulations in the current velocities. In order to analyze the behavior of the perturbations once they reach finite amplitude, a nonlinear analysis must be employed.

In this chapter, the momentum balance resulting in a steady longshore current is reviewed and the linear instability theory of a steady longshore current is derived following Bowen and Holman (1989). The derivation results in an instability equation similar to the equation by Rayleigh (1880) for the stability of

a two-dimensional flow. Necessary conditions for instability are stated.

2.2 Longshore Current Generation

The horizontal momentum balance equations and the continuity equation averaged over the short wave time scales and over depth form a two-dimensional model for the time varying behavior of surf zone currents. They are in the form of the shallow water equations with additional terms to account for the effects of motions at shorter time scales (short waves and turbulence) as well as dissipation effects in the form of bottom friction.

$$\begin{aligned}
&\frac{\partial \eta}{\partial t} + \frac{\partial}{\partial x}[ud] + \frac{\partial}{\partial y}[vd] = 0 \\
&\frac{\partial u}{\partial t} + u\frac{\partial u}{\partial x} + v\frac{\partial u}{\partial y} = -g\frac{\partial \eta}{\partial x} + \tilde{\tau}_x + \tau'_x - \tau_{bx} \\
&\frac{\partial v}{\partial t} + u\frac{\partial v}{\partial x} + v\frac{\partial v}{\partial y} = -g\frac{\partial \eta}{\partial y} + \tilde{\tau}_y + \tau'_y - \tau_{by}.
\end{aligned} \tag{2.1}$$

Here, η is the short wave-averaged water surface elevation above the still water level, h is the water depth with respect to the still water level, $d = (h + \eta)$ is the total water depth, u and v are the depth-averaged current velocities in the x and y directions, respectively, where x points offshore and y points in the longshore direction.

The parameters $\tilde{\tau}_x$ and $\tilde{\tau}_y$ represent short wave forcing effects, τ'_x and τ'_y represent the effects of lateral mixing due to turbulence or other mechanisms. Bottom friction effects are included through the terms τ_{bx} and τ_{by}. The subscripts denote the direction in which the stresses act. The specification of these terms is discussed in the next subsections.

2.2.1 Short Wave Forcing

As the short waves approach the shore they break, releasing their momentum into the surf zone as their wave height decays. This excess momentum, referred to as the radiation stress (Longuet-Higgins and Stewart, 1964), constitutes a mechanism that can force current motions. The short wave forcing terms $\tilde{\tau}_x$ and $\tilde{\tau}_y$ can be modeled utilizing the radiation stress formulation of Longuet-Higgins and Stewart (1964) as

$$\begin{aligned} \tilde{\tau}_x &= -\frac{1}{\rho d}\left(\frac{\partial S_{xx}}{\partial x}+\frac{\partial S_{xy}}{\partial y}\right), \\ \tilde{\tau}_y &= -\frac{1}{\rho d}\left(\frac{\partial S_{xy}}{\partial x}+\frac{\partial S_{yy}}{\partial y}\right). \end{aligned} \tag{2.2}$$

This expression can be written in index notation as

$$\tilde{\tau}_\alpha = -\frac{1}{\rho d}\frac{\partial S_{\alpha\beta}}{\partial x_\beta}, \tag{2.3}$$

where the indices α, β represent the x, y directions and repeated indices are assumed to be summed. The radiation stress components $S_{\alpha\beta}$ are defined in terms of the orbital wave velocities $(\tilde{u}, \tilde{v})$ and can be computed utilizing an appropriate water wave theory. In this study we use linear water wave theory. For monochromatic waves with wave height H, frequency $\tilde{f}$ and angle of incidence θ, the radiation stress components computed from linear theory can be written as

$$\begin{aligned} S_{xx} &= E\left[\frac{c_g}{\tilde{c}}\left(\cos^2\theta+1\right)-\frac{1}{2}\right], \\ S_{xy} &= E\frac{c_g}{\tilde{c}}\sin\theta\cos\theta, \\ S_{yy} &= E\left[\frac{c_g}{\tilde{c}}\left(\sin^2\theta+1\right)-\frac{1}{2}\right], \end{aligned} \tag{2.4}$$

where the wave energy density E is given by

$$E = \frac{1}{8}\rho g H^2 \tag{2.5}$$

and the short wave celerity $\tilde{c} = (2\pi\tilde{f})/\tilde{k}$, where the wavenumber $\tilde{k}$ can be computed from the linear dispersion relationship

$$(2\pi\tilde{f})^2 = g\tilde{k}\tanh\tilde{k}h. \tag{2.6}$$

The group velocity is defined as $c_g = n\tilde{c}$ where

$$n = \frac{1}{2}\left(1 + \frac{2\tilde{k}h}{\sinh 2\tilde{k}h}\right) \tag{2.7}$$

For random waves, the directional spectrum is considered to be made up of discrete components of height H_i, frequency $\tilde{f}_i$ and angle of incidence θ_i. The radiation stress can then be defined as the sum of the radiation stresses due to all wave components.

$$\begin{aligned} S_{xx} &= \sum_i E_i\left[n_i\left(\cos^2\theta_i + 1\right) - \frac{1}{2}\right], \\ S_{xy} &= \sum_i E_i n_i \sin\theta_i\cos\theta_i, \\ S_{yy} &= \sum_i E_i\left[n_i\left(\sin^2\theta_i + 1\right) - \frac{1}{2}\right], \end{aligned} \tag{2.8}$$

where $E_i = (1/8)\rho g H_i^2$ is the energy of each component and n_i is computed from (2.7) for the wavenumber $\tilde{k}_i$ of the component. The total energy in the spectrum is

$$E = \sum_i E_i = \frac{1}{8}\rho g H_{rms}^2, \tag{2.9}$$

where H_{rms} is the root-mean-square (rms) wave height.

Higgins *et al.* (1981) stated that the forcing due to a random sea with a narrow banded spectrum can be collapsed into forcing due to an equivalent plane wave. The equivalent wave train is chosen such that it has the energy of the entire spectrum and a direction $\overline{\theta}$ that yields the total radiation stress S_{xy}. Therefore,

the equivalent wave has wave height H_{rms}, its frequency is equal to the peak frequency $\tilde{f}_p$ of the spectrum and its direction is given by

$$\overline{\theta} = \frac{1}{2} \arcsin \left(\frac{16 S_{xy}}{\rho g H_{rms}^2 (c_g / \tilde{c})} \right), \tag{2.10}$$

where $\tilde{c}$ and c_g are evaluated for the frequency $\tilde{f}_p$. The radiation stress components for a narrow banded sea can be computed using this equivalent wave and utilizing methods for monochromatic waves.

In order to specify the radiation stress forcing using the above formulations for monochromatic or random waves, the wave height H, the wavenumber $\tilde{k}$ and the angle of incidence θ of the waves have to be known as a function of space and time. Given the offshore values of these parameters they can be obtained for the entire domain from the calculation of the short wave transformation due to depth-limited shoaling, refraction, diffraction and breaking. In general, the short wave field will be affected by the current field it generates. In the case of obliquely incident long crested waves forcing a surf zone longshore current, computations have shown that this effect is minimal (Thornton and Guza, 1986). However, localized cross-shore currents such as rip currents can cause significant changes in the short wave field due to processes such as current-limited refraction and breaking. In practice, however, the possible interaction between the short wave field and the wave-induced current field is often neglected. The radiation stress forcing can then be computed externally and the forcing terms $\tilde{\tau}_x$ and $\tilde{\tau}_y$ can be specified.

2.2.2 Lateral Momentum Mixing

The parameters τ_x' and τ_y' in (2.1) represent the effects of lateral momentum mixing in the surf zone. One source of mixing in the surf zone arises due to gradients of turbulence-induced momentum fluxes (depth-integrated Reynolds' stresses S'). The turbulence-induced stresses τ_x^t and τ_y^t in the momentum equations are given by

$$\tau_\alpha^t = -\frac{1}{\rho d}\frac{\partial S'_{\alpha\beta}}{\partial x_\beta} \tag{2.11}$$

The depth-integrated Reynolds' stresses $S'_{\alpha\beta}$ are defined as

$$S'_{\alpha\beta} = \overline{\int_{-h}^{\eta} \rho u_\alpha^t u_\beta^t dz} \tag{2.12}$$

where η is the instantaneous water surface elevation, and u_α^t is the velocity component due to turbulence. The overbar denotes time averaging over the time scale of the short waves. Since the turbulent velocities are in general not known, the depth-integrated Reynolds' stresses are often linked to the mean flow by parameterizing the stresses using an eddy viscosity. A popular eddy viscosity parameterization is given by

$$S'_{\alpha\beta} = -\rho\nu_t d\left(\frac{\partial u_\alpha}{\partial x_\beta} + \frac{\partial u_\beta}{\partial x_\alpha}\right). \tag{2.13}$$

where $(u_\alpha, u_\beta) = (u, v)$ are the current velocities. The parameter ν_t is the turbulent eddy viscosity.

Another important source of lateral mixing in the surf zone is analogous to the Taylor dispersion process of dissolved matter in pipe flow (Taylor, 1954). This process was identified by Svendsen and Putrevu (1994) who considered the case of a steady longshore current and parabolic undertow profile on a longshore uniform beach. They found that the depth nonuniformity of the nearshore currents leads to additional terms in the depth-averaged momentum equations. The extension of the theory to unsteady flow over arbitrary bathymetry was performed by Putrevu

and Svendsen (1997). The form of the momentum equations with the additional terms is stated in Putrevu and Svendsen (1997) as

$$\frac{\partial u_\alpha}{\partial t} + u_\beta \frac{\partial u_\alpha}{\partial x_\beta} = -g\frac{\partial \eta}{\partial x_\alpha} - \frac{1}{\rho d}\frac{\partial S_{\alpha\beta}}{\partial x_\beta} + \frac{1}{d}\frac{\partial}{\partial x_\beta}\left[\nu_t d\left(\frac{\partial u_\alpha}{\partial x_\beta} + \frac{\partial u_\beta}{\partial x_\alpha}\right)\right] - \tau_{b\alpha}$$
$$-\frac{1}{d}\frac{\partial}{\partial x_\beta}\left[M_{\alpha\beta} + A_{\alpha\beta\delta}u_\delta - d\left(D_{\alpha\beta}\frac{\partial u_\alpha}{\partial x_\delta} + D_{\delta\alpha}\frac{\partial u_\beta}{\partial x_\delta} + B_{\alpha\beta}\frac{\partial u_\delta}{\partial x_\delta}\right)\right], \qquad (2.14)$$

where the coefficients $M_{\alpha\beta}$, $A_{\alpha\beta\delta}$, $D_{\alpha\beta}$ and $B_{\alpha\beta}$ are functions of the depth variations of the current velocities. Their specification requires the prediction of the vertical structure of the longshore and cross-shore currents. Considering a depth-uniform return flow to compensate for the wave-induced volume flux $Q_{w\alpha}$, Putrevu and Svendsen (1997) argue that the dominant effects are due to the $D_{\alpha\beta}$ terms in the above equation. Therefore, in the remainder of the discussion, we only consider the effects due to the $D_{\alpha\beta}$ terms.

In the general case, $D_{\alpha\beta}$ is a function of the turbulent eddy viscosity and the depth variations of the currents. Since undertow profiles are strongly curved in the surf zone but not outside the surf zone, $D_{\alpha\beta}$ varies with cross-shore distance. The specification of $D_{\alpha\beta}$, therefore, requires knowledge about the local depth profiles of the velocities. The quasi-three-dimensional approach has been used in recent studies to obtain information about the vertical variations of the currents without the complications of a full 3D model (e.g. De Vriend and Stive, 1987; Svendsen and Lorenz, 1989; Svendsen and Putrevu, 1990; Sanchez-Arcilla *et al.*, 1992; Svendsen and Putrevu, 1994; Van Dongeren *et al.*, 1994). The quasi-3D approach involves calculating the depth-averaged current velocities using the depth-averaged momentum equations and utilizing the results to compute the local velocity profiles from a separate profile model. Since such computations are beyond the scope of this study, we seek to include the effects of the $D_{\alpha\beta}$ terms to leading order by estimating the order of magnitude of the coefficients $D_{\alpha\beta}$ along with a reasonable variation in the cross-shore direction.

Putrevu and Svendsen (1997) stated that for a depth-uniform return flow, the coefficient matrix $D_{\alpha\beta}$ is proportional to the wave-induced fluxes in the horizontal directions such that

$$D_{\alpha\beta} \sim \frac{Q_{w\alpha} Q_{w\beta}}{\nu_t}. \tag{2.15}$$

For short waves obliquely incident to the beach at small angles the volume flux due to the waves will occur mostly in the x direction so that

$$Q_{wx} \gg Q_{wy}. \tag{2.16}$$

Under this assumption, $D_{xx} > D_{xy} > D_{yy}$. Note that the subscripts do not denote differentiation but the plane and direction of action. As a first approximation, we retain terms with the coefficient D_{xx} only. The momentum equations then reduce to

$$\begin{aligned}
&\frac{\partial u}{\partial t} + u\frac{\partial u}{\partial x} + v\frac{\partial u}{\partial y} = -g\frac{\partial \eta}{\partial x} - \frac{1}{\rho d}\left(\frac{\partial S_{xx}}{\partial x} + \frac{\partial S_{xy}}{\partial y}\right) - \tau_{bx} \\
&+\frac{1}{d}\frac{\partial}{\partial y}\left(\nu_t d\frac{\partial u}{\partial y}\right) + \frac{2}{d}\frac{\partial}{\partial x}\left(d(\nu_t + D_{xx})\frac{\partial u}{\partial x}\right) + \frac{1}{d}\frac{\partial}{\partial y}\left(d(\nu_t + D_{xx})\frac{\partial v}{\partial x}\right), \\
&\frac{\partial v}{\partial t} + u\frac{\partial v}{\partial x} + v\frac{\partial v}{\partial y} = -g\frac{\partial \eta}{\partial y} - \frac{1}{\rho d}\left(\frac{\partial S_{xy}}{\partial x} + \frac{\partial S_{yy}}{\partial y}\right) - \tau_{by} \\
&+\frac{1}{d}\frac{\partial}{\partial x}\left(\nu_t d\frac{\partial u}{\partial y}\right) + \frac{2}{d}\frac{\partial}{\partial x}\left(\nu_t d\frac{\partial v}{\partial y}\right) + \frac{1}{d}\frac{\partial}{\partial x}\left(d(\nu_t + D_{xx})\frac{\partial v}{\partial x}\right).
\end{aligned} \tag{2.17}$$

It is evident from (2.17) that the D_{xx} terms act to reinforce the turbulent momentum mixing in certain directions. The coefficient of these combined terms is a composite eddy viscosity $\nu = \nu_t + D_{xx}$. Svendsen and Putrevu (1994) show that the value of the coefficient D_{xx} (termed D_c in Svendsen and Putrevu (1994)) can be orders of magnitude larger than ν_t. Therefore, we only retain the mixing terms that are premultiplied by $(\nu_t + D_{xx})$, effectively neglecting turbulent momentum mixing unless it is reinforced by the dispersion process.

As a result, the lateral mixing terms in the momentum equations can be expressed as

$$\tau_x' = \frac{2}{d}\frac{\partial}{\partial x}\left(\nu d\frac{\partial u}{\partial x}\right) + \frac{1}{d}\frac{\partial}{\partial y}\left(\nu d\frac{\partial v}{\partial x}\right), \qquad \tau_y' = \frac{1}{d}\frac{\partial}{\partial x}\left(\nu d\frac{\partial v}{\partial x}\right), \tag{2.18}$$

where $\nu = \nu_t + D_{xx}$.

Since both ν_t as well as D_{xx} are more pronounced in the surf zone, ν will also be more pronounced inside the surf zone. To obtain a reasonable cross-shore variation, it is convenient to parameterize the total horizontal eddy viscosity following Battjes (1975) as

$$\nu = Md\left(\frac{\epsilon_b}{\rho}\right)^{1/3}, \tag{2.19}$$

where M is an $O(1)$ coefficient and ϵ_b is the ensemble-averaged energy dissipation due to wave breaking. This relationship was originally formulated to account for the cross-shore variation of the turbulent eddy viscosity ν_t. Therefore, the order of magnitude of M needs to be reevaluated to account for mixing due to turbulence as well as the Taylor dispersion process.

In order to estimate the order of magnitude of M for field applications, we focus our attention to the inner surf zone and use linear shallow water theory to construct a simple expression for ϵ_b given by

$$\epsilon_b = \frac{d}{dx}\left(\frac{1}{8}\rho g H^2 c\right), \tag{2.20}$$

where H is the wave height and c is the short wave celerity. Assuming wave breaking in a saturated surf zone, we can use $(H/h) = \gamma$ and write

$$\left(\frac{\epsilon_b}{\rho}\right)^{1/3} = (\frac{5}{16}\gamma^2 h_x)^{1/3}\sqrt{gh}, \tag{2.21}$$

where h_x is the bottom slope. An average bottom slope of 0.05 applies to field experiments at Duck, NC. Furthermore, Thornton and Guza (1983) found good

agreement with measured wave height variations in field applications for a value for γ of 0.42. With these values the order of magnitude of ν can be estimated to be

$$\nu \approx 0.14Mh\sqrt{gh}. \tag{2.22}$$

On the other hand, ν is composed of the turbulent mixing coefficient ν_t and the Taylor dispersion coefficient D_{xx}. A typical value of the turbulent eddy viscosity coefficient ν_t derived from laboratory studies by Svendsen *et al.* (1987) is 0.01 $h\sqrt{gh}$. However, George *et al.* (1994) state that this estimate should be reduced by $\frac{1}{2}$ to $\frac{1}{4}$ for field applications. A reasonable range of values for ν_t in the field is then

$$0.0025h\sqrt{gh} < \nu_t < 0.005h\sqrt{gh}. \tag{2.23}$$

Svendsen and Putrevu (1994) state that a crude estimate of the magnitude of D_{xx} is given by

$$D_{xx} = \frac{1}{2}\frac{Q_{wx}^2}{\nu_t}, \tag{2.24}$$

where Q_{wx} is the wave volume flux in the cross-shore direction with typical values in the range (see e.g. Svendsen *et al.*, 1987)

$$0.03\left(\frac{H}{h}\right)^2 h\sqrt{gh} < Q_{wx} < 0.1\left(\frac{H}{h}\right)^2 h\sqrt{gh}. \tag{2.25}$$

Once again we can use $(H/h) = \gamma = 0.42$ and get

$$0.005h\sqrt{gh} < Q_{wx} < 0.018h\sqrt{gh}. \tag{2.26}$$

The effective eddy viscosity ν is given by the sum of ν_t and D_{xx}. For the range of values stated above, reasonable values for ν will be in the range

$$0.008h\sqrt{gh} < \nu < 0.067h\sqrt{gh}. \tag{2.27}$$

Comparing (2.22) and (2.27), the order of magnitude of the mixing coefficient M can be stated as

$$0.06 < M < 0.48, \tag{2.28}$$

when lateral mixing due to turbulence as well as the dispersion mechanism described by Svendsen and Putrevu (1994) are taken into account in a rudimentary fashion.

2.2.3 Bottom Friction

The bottom friction terms can in general be written as

$$\begin{aligned} \tau_{bx} &= \frac{1}{d} c_f \overline{|\vec{u} + \vec{\tilde{u}}|(u + \tilde{u})}, \\ \tau_{by} &= \frac{1}{d} c_f \overline{|\vec{u} + \vec{\tilde{u}}|(v + \tilde{v})}, \end{aligned} \tag{2.29}$$

where c_f is a friction coefficient. Furthermore, $\tilde{u}$ and $\tilde{v}$ denote the components in the x and y directions, respectively, of the short wave orbital velocity vector $\vec{\tilde{u}}$. Similarly, u and v denote the x and y components of the current velocity vector $\vec{u}$. The overbar denotes time averaging over the time scale of the short waves. The simplest formulation for the bottom friction can be obtained by assuming that short waves approach the shore at small angles of incidence and the maximum orbital velocity u_0 associated with the short waves is much larger than the mean current (Longuet-Higgins, 1970). Linearizing with respect to u_0 results in linear damping terms in the momentum equations. Linear damping terms in the x and y momentum equations are the mathematically simplest frictional resistance terms and can be expressed as

$$\tau_{bx} = \frac{\mu}{d} u, \qquad \tau_{by} = \frac{\mu}{d} v, \tag{2.30}$$

where

$$\mu = \frac{2}{\pi} c_f u_0. \tag{2.31}$$

The orbital velocity is a function of offshore distance and can be specified according to the wave theory used to compute the short wave climate. The simplest formulation can be obtained when linear shallow water waves are assumed in the surf zone. For monochromatic waves, this assumption gives

$$u_0 = \frac{cH}{2h}. \tag{2.32}$$

For random waves with Rayleigh distributed wave heights, the relationship is

$$u_0 = \frac{1}{4}\sqrt{\frac{g\pi}{h}}H_{rms}. \tag{2.33}$$

It is noted that the above formulation for bottom friction is rudimentary. The assumption regarding the strength of the current in relation to the wave orbital velocity as well as the incorporation of linear shallow water theory for the computation of u_0 is highly restrictive and often unrealistic. The size of the friction coefficient c_f is also a major source of uncertainty. However, the goal is to obtain an estimate of the order of magnitude of the dissipative terms so that the dynamics of shear instabilities can be analyzed in a mathematically simple setting. Furthermore, the formulation given by (2.30) has so far been used by a number of investigators for linear (Dodd *et al.*, 1992) and nonlinear (Allen *et al.*, 1996; Slinn *et al.*, 1997) shear instability computations. Therefore, retaining this simple formulation facilitates comparisons to other studies. For these reasons we continue to use (2.30) for simulations of shear instabilities over plane and barred beaches discussed herein. Extension of the model to incorporate the full formulation (2.29) is discussed in Chapter 7.

We substitute the expressions for the forcing and damping terms $\tilde{\tau}_\alpha$, τ'_α and $\tau_{b\alpha}$ into the governing equations (2.1) and obtain

$$\frac{\partial u}{\partial t} + u\frac{\partial u}{\partial x} + v\frac{\partial u}{\partial y} = -g\frac{\partial \eta}{\partial x} - \frac{1}{\rho d}\left(\frac{\partial S_{xx}}{\partial x} + \frac{\partial S_{xy}}{\partial y}\right) - \frac{\mu}{d}u$$

$$+\frac{2}{d}\frac{\partial}{\partial x}\left(\nu d\frac{\partial u}{\partial x}\right)+\frac{1}{d}\frac{\partial}{\partial y}\left(\nu d\frac{\partial v}{\partial x}\right),$$

$$\begin{aligned}\frac{\partial v}{\partial t}+u\frac{\partial v}{\partial x}+v\frac{\partial v}{\partial y} &= -g\frac{\partial \eta}{\partial y}-\frac{1}{\rho d}\left(\frac{\partial S_{xy}}{\partial x}+\frac{\partial S_{yy}}{\partial y}\right)-\frac{\mu}{d}v \\ &\quad +\frac{1}{d}\frac{\partial}{\partial x}\left(\nu d\frac{\partial v}{\partial x}\right). \end{aligned} \tag{2.34}$$

We first seek the steady momentum balance. For the case of a stationary short wave field and straight-and-parallel bottom contours this balance reduces to

$$\begin{aligned} g\frac{\partial \overline{\eta}}{\partial x} &= -\frac{1}{\rho d}\frac{\partial S_{xx}}{\partial x} \\ -\frac{\partial}{\partial x}\left(\nu d\left(\frac{\partial V}{\partial x}\right)\right)+\mu V &= -\frac{1}{\rho}\frac{\partial S_{xy}}{\partial x}. \end{aligned} \tag{2.35}$$

These equations describe a steady short wave-induced longshore current V and a steady short wave-induced setup $\overline{\eta}$. The longshore current described by the longshore momentum balance constitutes the fluctuation-free basic state. The stability of this basic state will be analyzed next.

2.3 Linear Instability Theory

Following the development by Bowen and Holman (1989), we perturb the basic flow consisting of a steady longshore current $V(x)$ and steady setup $\overline{\eta}(x)$ such that

$$\begin{aligned} \eta(x,y,t) &= \overline{\eta}(x)+\eta'(x,y,t) \\ u(x,y,t) &= 0+u'(x,y,t) \\ v(x,y,t) &= V(x)+v'(x,y,t), \end{aligned} \tag{2.36}$$

The perturbations u', v' and η' are assumed to be small. Therefore, the relationships

$$\frac{u'}{V}\ll 1, \quad \frac{v'}{V}\ll 1 \quad \text{and} \quad \frac{\eta'}{\overline{\eta}}\ll 1 \tag{2.37}$$

hold.

Subtracting the momentum balance given by (2.35) from the governing equations (2.34) and linearizing in the perturbation variables η', u' and v' results in a system of equations for the perturbations consisting of the continuity equation

$$\frac{\partial \eta'}{\partial t} + \frac{\partial}{\partial x}(hu') + \frac{\partial}{\partial y}(hv') = 0, \tag{2.38}$$

and the x and y momentum equations

$$\begin{aligned} \frac{\partial u'}{\partial t} + V\frac{\partial u'}{\partial y} &= -g\frac{\partial \eta'}{\partial x} - \frac{\mu}{h}u' + \frac{2}{h}\frac{\partial}{\partial x}\left(\nu h \frac{\partial u'}{\partial x}\right) + \frac{1}{h}\frac{\partial}{\partial y}\left(\nu h \frac{\partial v'}{\partial x}\right), \\ \frac{\partial v'}{\partial t} + u'\frac{\partial V}{\partial x} + V\frac{\partial v'}{\partial y} &= -g\frac{\partial \eta'}{\partial y} - \frac{\mu}{h}v' + \frac{1}{h}\frac{\partial}{\partial x}\left(\nu h \frac{\partial v'}{\partial x}\right). \end{aligned} \tag{2.39}$$

Since the waves observed by Oltman-Shay *et al.* (1989) are too short to satisfy gravity wave dynamics, Bowen and Holman (1989) searched for alternate solutions to the equations of motions. In particular, they searched for motions under the nondivergent, or "rigid lid", assumption. In this case, accelerations of the flow are driven by inertial terms involving the mean longshore current. The "rigid lid" assumption involves assuming that the term $\frac{\partial \eta'}{\partial t}$ in the continuity equation (2.38) is negligible in comparison to the horizontal fluxes. The continuity equation then reads

$$\frac{\partial}{\partial x}(hu') + \frac{\partial}{\partial y}(hv') = 0 \tag{2.40}$$

and a streamfunction Ψ can be defined to satisfy this equation exactly.

$$(hu') = -\frac{\partial \Psi}{\partial y}, \qquad (hv') = \frac{\partial \Psi}{\partial x} \tag{2.41}$$

In their discussion, Bowen and Holman (1989) neglected the dissipational terms in the perturbation equations and cross-differentiated (2.39) to eliminate η'. Substituting the definition of the streamfunction results in

$$\left(\frac{\partial}{\partial t} + V\frac{\partial}{\partial y}\right)\left(\frac{\Psi_{yy}}{h} + \left(\frac{\Psi_x}{h}\right)_x\right) = \Psi_y\left(\frac{V_x}{h}\right)_x \tag{2.42}$$

where subscripts in this equation denote differentiation. Bowen and Holman (1989) pointed out that this equation is the linearized version of the equation for the conservation of potential vorticity Π,

$$\frac{\partial \Pi}{\partial t} + u\frac{\partial \Pi}{\partial x} + v\frac{\partial \Pi}{\partial y} = 0 \tag{2.43}$$

where $u = u'$ and $v = V + v'$ are the total current velocities and Π is defined as

$$\Pi = \frac{1}{h}\left(\frac{\partial v}{\partial x} - \frac{\partial u}{\partial y}\right) = \frac{1}{h}\left(\frac{\partial V}{\partial x} + \left(\frac{\partial v'}{\partial x} - \frac{\partial u'}{\partial y}\right)\right). \tag{2.44}$$

In analogy to the Coriolis parameter in larger scale geophysical flows, the background vorticity in this flow is provided by the shear of the longshore current $(\partial V/\partial x)$.

Bowen and Holman (1989) proceeded with the linear instability analysis by assuming a solution of the form

$$\Psi = \Re e\left\{\psi e^{i(\lambda y - \sigma t)}\right\} \tag{2.45}$$

where the longshore wavenumber λ is assumed to be real, but σ may be complex such that $\sigma = \sigma_{re} + i\sigma_{im}$. In this case the resulting solutions are in the form of progressive waves with speed $c = \sigma_{re}/\lambda$ and an exponentially growing amplitude with growth rate σ_{im}.

Substituting this form into (2.42) results in

$$(V - c)\left(\psi_{xx} - \left(\frac{h_x}{h}\right)\psi_x - k^2\psi\right) = h\left(\frac{V_x}{h}\right)_x \psi. \tag{2.46}$$

It should be noted that in the absence of bottom variation (2.46) reduces to the well-known Rayleigh equation (Rayleigh, 1880) for two-dimensional flow,

$$(V - c)\left(\psi_{xx} - k^2\psi\right) - V_{xx}\psi = 0 \tag{2.47}$$

For Rayleigh's equation Fjørtoft's theorem states that a necessary (but not sufficient) condition for instability is that an inflection point exists in the basic flow so

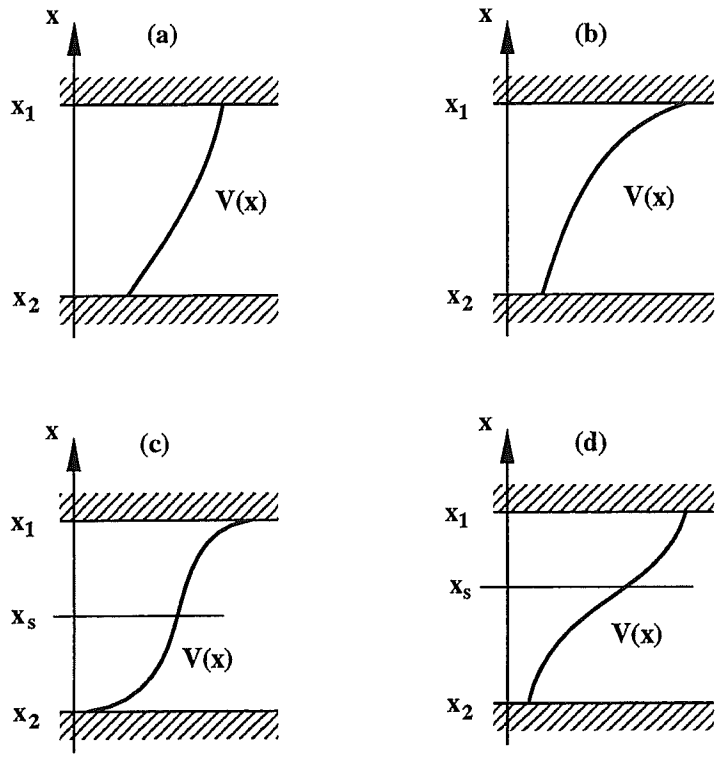

Figure 2.1: (a) Stable: $V_{xx} < 0$; (b) stable:$V_{xx} > 0$; (c) stable: $V_{xx} = 0$ at x_s but $V_{xx}(V - V_s) \geq 0$; (d) possibly unstable: $V_{xx} = 0$ at x_s but $V_{xx}(V - V_s) \leq 0$ (reproduced from Drazin and Howard, 1966).

that $V_{xx} = 0$ at a point x_s. Furthermore, $V_{xx}(V - V_s) < 0$ somewhere in the field of flow, where $V_s = V(x_s)$. Examples of two-dimensional flows that are stable or possibly unstable are given in Drazin and Howard (1966) and reproduced in Figure 2.1.

The equivalent condition for the stability of the longshore current (2.46) was derived by Putrevu and Svendsen (1992) and states that for instability (V_x/h) must have an extremum so that $(V_x/h)_x = 0$ at a point x_s with the condition $V_{xx}(V - V_s) < 0$, where $V_s = V(x_s)$. A typical longshore current profile often observed on natural beaches is shown in Figure 2.2, the shoreline is located at

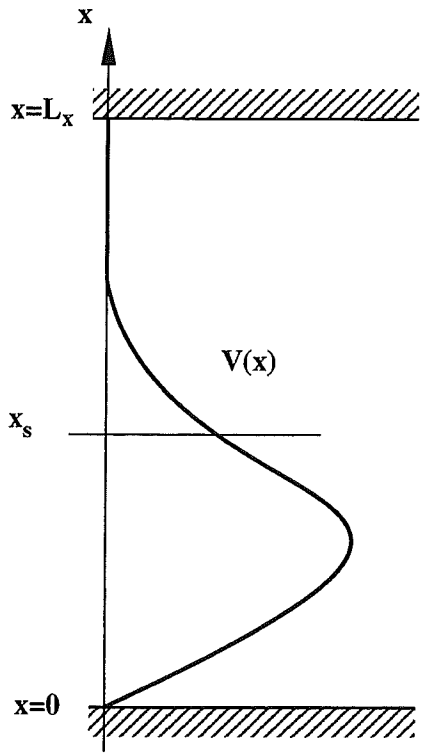

Figure 2.2: Generic longshore current profile.

$x = 0$. An inflection point is often present at the point of maximum shear; therefore, the longshore current is possibly unstable.

Bowen and Holman (1989) solved (2.46) analytically for the simple geometry of a constant depth bottom and a piecewise smooth longshore current profile. They obtained solutions for the eigenvectors ψ with complex eigenvalues σ for a range of values of λ and thereby showed that instabilities of the longshore current exist. However, (2.46) is difficult to solve analytically for a general velocity distribution and bathymetry. Therefore, several investigators (e.g. Putrevu and Svendsen, 1992; Dodd *et al.*, 1992; Falqués and Iranzo, 1994) used various numerical solution methods to solve (2.46) as well as its counterpart including the

effects of dissipation due to bottom friction or lateral mixing.

Putrevu and Svendsen (1992) solved the instability equation including the effects of linear bottom friction given by

$$\left(V - c - i\frac{\mu}{kh}\right)\left(\psi_{xx} - \left(\frac{h_x}{h}\right)\psi_x - k^2\psi\right) = h\left(\frac{V_x}{h}\right)_x \psi - i\frac{\mu}{kh}\left(\frac{h_x}{h}\right)\psi_x, \quad (2.48)$$

where μ is a constant linear friction coefficient and $i = \sqrt{-1}$ is the unit imaginary number. The solution method by Putrevu and Svendsen (1992) utilized finite difference approximations of the spatial derivatives. The resulting matrix equation was solved for the eigenvalues and eigenvectors for a given wavenumber λ. Their solution method will be used in this study to compute linear instability characteristics of current profiles whenever necessary. The reader is referred to Putrevu and Svendsen (1992) for further information about the numerical methods implemented.

A generic case of a longshore current profile over a beach profile with straight-and-parallel contours is shown in Figure 2.3. A numerical solution of the linear instability equations for such a basic state results in predictions of the complex frequency σ for each value of the wavenumber λ. Often a range of unstable wavenumbers exists, perturbations at these wavenumbers are expected to display temporal growth. The imaginary part of the frequency σ_{im} then provides an estimate of the strength of the instability at a wavenumber, the real part σ_{re} can be used to compute the speed at which the instabilities propagate alongshore as they grow. Typical graphs of the real and imaginary frequency as a function of wavenumber are shown in Figure 2.3. The wavenumber at which the maximum growth rate occurs is referred to as λ_{max} and is considered to be representative of the length scale of the motions.

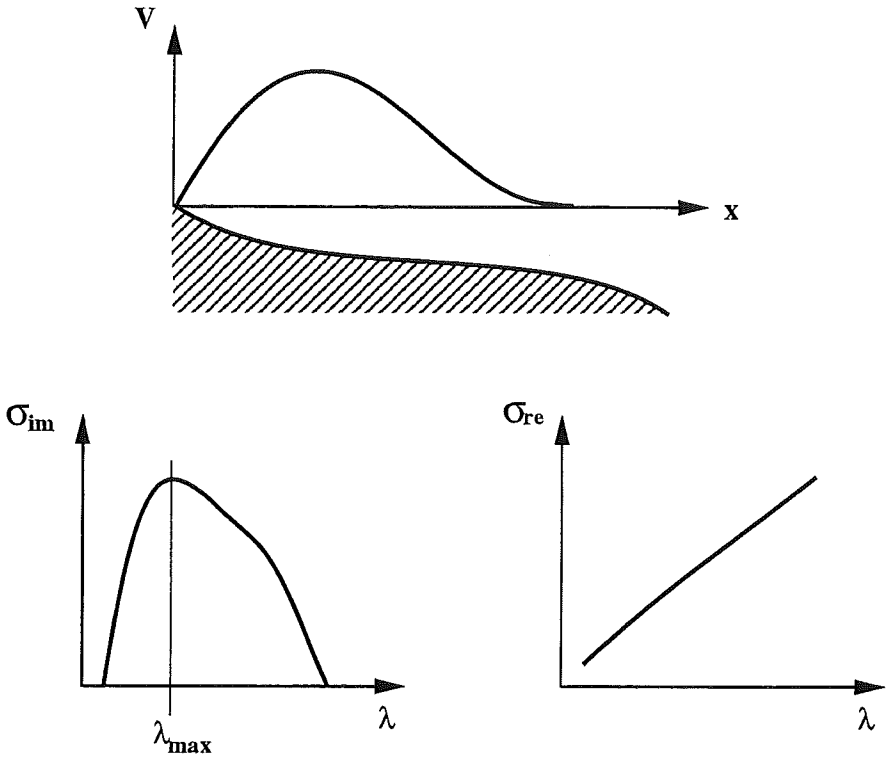

Figure 2.3: Typical results from an instability analysis.

Studies carried out by Dodd (1994) and Falqués and Iranzo (1994) analyzing the effects of linear bottom friction and lateral diffusion suggested that the dissipational terms affect the instability characteristics of a basic state by reducing the growth rates. The location of the most unstable wavenumber, however, is altered only slightly. Therefore, for the purposes of identifying the most unstable wavenumber, linear instability calculations for the inviscid case are useful. However, when estimates of the linear growth rates are needed, the viscous problem has to be considered.

2.4 Nonlinear Instability

An important assumption that was made during the derivation of the stability equation states that the perturbations to the basic velocity profile are small. However, once the instability is initiated, the growth rates are often large enough (Bowen and Holman, 1989; Dodd *et al.*, 1994) for the perturbations to reach finite amplitude relatively quickly. The perturbations are then no longer small in relation to the basic current and a nonlinear analysis is necessary to investigate the behavior of the resulting undulating currents. Such an analysis involves the solution of the full problem given by (2.34).

To date, studies solving the nonlinear equations often retained the "rigid lid" assumption (e.g. Allen *et al.*, 1996; Falqués and Iranzo, 1994). Various studies reviewed in Chapter 1 include the effects of bottom friction, lateral mixing or both. All have chosen rudimentary representations for the dissipational terms as well as the short wave forcing terms and have assumed a stationary short wave field neglecting any effects of wave-current interactions. In spite of these simplifying assumptions the resulting finite amplitude instabilities were seen to exhibit complicated behavior.

In this study we construct a time domain model of the governing equations (2.1). The "rigid lid" assumption will not be invoked, instead the time dependent behavior of the surface is computed along with the velocity components. The linear bottom friction formulation (2.30) is used along with an eddy viscosity parameterization of lateral mixing. The short wave field is considered to be stationary and all interactions between the short wave and current fields are neglected. These simple representations of the forcing and damping effects are purposefully chosen to study the resulting motions in the simplest possible mathematical setting. Future studies can then identify the features caused by more

complicated and complete representations of dissipational effects. The detailed description of the specification of the forcing and dissipational terms is given in Chapters 5 and 6 where simulations of shear instabilities on a plane and barred beach are simulated, respectively.

The instability theory considers a steady longshore current created by a stationary wave field and analyzes the stability of this basic state. In reality, however, the incident wave field is rarely stationary. Observations from the SUPERDUCK experiment (Oltman-Shay *et al.*, 1989) show that when a wave field becomes more energetic due to a local storm, amplitudes of the longshore current velocities as well as undulation velocities are seen to increase simultaneously. The response of the instabilities to time varying short wave forcing is, therefore, relevant. Furthermore, spatially and temporally coherent variations in the short wave climate, for example in the form of wave groups, are known to force infragravity motions (Schäffer, 1993, 1994). Such variations in the short wave climate also have the potential to cause lower frequency vorticity motions (Haller *et al.*, 1997). The investigation of these issues involves considering the effects of a time varying short wave field on the currents by lifting the assumption of a stationary short wave field.

In turn, the effect of the surf zone currents on the short wave field is of equal importance. The short wave field can be altered by the underlying current field due to current limited diffraction and breaking. If the currents are time-dependent the short wave field will lose its stationary character and the problems of short wave transformation and current generation can no longer be decoupled. The inclusion of a time dependent calculation of the short wave field is, therefore, of interest and will be described in Chapter 7.

Chapter 3

BOUNDARY VALUE PROBLEM AND SOLUTION METHOD

A solution method for the shallow water equations governing wave motions in the nearshore environment is presented. The model domain extends from the shoreline to a desired distance offshore and is periodic in the longshore direction. Properly posed boundary conditions for the governing equations are discussed. A curvilinear moving boundary condition is incorporated at the shoreline to account for wave runup. An absorbing-generating boundary based on a method by Van Dongeren and Svendsen (1997) is constructed offshore. Spatial derivatives contained in the governing equations are computed using spectral collocation methods. A high-order time integration scheme is used to compute the time evolution of the velocities and water surface elevation given initial conditions.

3.1 Introduction

The nonlinear shallow water equations are a set of coupled hyperbolic equations governing many types of processes in the nearshore region. They have been widely employed to model long wave propagation in a variety of cases including tsunami propagation or tidal oscillations. They may also be utilized to model short surface wave propagation, if provision is made to account for dissipation due

to wave breaking. Finally, they provide a theoretical basis for modeling currents and other quasi-steady flows.

Recently, it has been demonstrated that longshore currents induced by obliquely-incident waves breaking on a beach may be unstable to perturbations that induce undulating flow patterns in the longshore direction and time (Oltman-Shay *et al.*, 1989; Bowen and Holman, 1989). The nonlinear shallow water equations provide a good basis for modeling the long-time evolution of these instabilities. Viewed in isolation, these instabilities induce flow perturbations which are primarily horizontal in nature (with vorticity as the primary restoring force), and thus can be studied using rigid-lid models (Allen *et al.*, 1996). However, these motions occur in a complex surf zone environment characterized by a number of additional low frequency motions, including edge waves and surf beat, which are primarily gravity dominated. The nonlinear shallow water equations provide the leading order approximation of the free surface effects needed to study vorticity and gravity-dominated motions in tandem.

In this chapter, we present a numerical treatment of the nonlinear shallow water equations which is specialized to motions which can be assumed to be periodic in the longshore direction. Our aim in this and the following chapter is to describe the numerical approach and verify it in comparison to analytical results for the case of gravity wave motion. Tests involving vorticity waves are not described here, as there are no documented "correct" answers that would serve as a basis for model verification. Instead, results on the evolution of shear instabilities of longshore currents in the surf zone will be described in later chapters.

First, a solution method for the nonlinear shallow water equations using Chebyshev collocation in the shore-normal direction in conjunction with Fourier

collocation in the shore-parallel direction is presented. The properly posed boundary treatments for these equations are discussed. A curvilinear moving boundary condition at the shoreline is constructed using an Eulerian model in conjunction with a moving grid. This boundary condition is tested for both one and two-dimensional shoreline runup.

An absorbing-generating boundary condition at the offshore boundary is derived based on the method of characteristics following Van Dongeren and Svendsen (1997). It is tested for waves leaving the domain at normal or oblique incidence to the artificial offshore boundary.

As we are primarily interested in using the solution method developed here to study the onset and evolution of instabilities of the surf zone longshore current, the question of whether the method is capable of reproducing unstable behavior in a well understood case is of extreme importance. We thus conclude the chapter with an analysis of the growth of subharmonic standing edge waves, which evolve on a long straight beach as a result of an instability of a normally incident (and reflected) long-crested wave. This instability has been studied extensively, and predictions for equilibrium edge wave amplitudes as a function of incident wave conditions and frictional damping rates are available. We show that the present method is capable of reproducing the neutral stability boundaries and equilibrium amplitude predictions for this particular class of motions.

3.2 Governing Equations

In this study, a two-dimensional horizontal model of the non-dispersive continuity and momentum equations is used. The governing equations, given

below, are the nonlinear shallow water equations.

$$d_t + (ud)_x + (vd)_y = 0 \tag{3.1}$$

$$u_t + uu_x + vu_y = -g\eta_x + F(x,y,t) \tag{3.2}$$

$$v_t + uv_x + vv_y = -g\eta_y + G(x,y,t). \tag{3.3}$$

Here, η is the water surface elevation above the still water level, h is the still water depth, $d = h + \eta$ is the total water depth, u and v are the velocity components in the x and y directions, respectively, where x points offshore and y points in the longshore direction. The functions F and G represent external forcing effects as well as dissipational effects.

The domain in which these equations are solved is shown in Figure 3.1. It is bounded by a curvilinear moving shoreline at $x = \zeta(y,t)$. This representation of the shoreline boundary imposes the restriction that the shoreline position be single valued. The kinematic condition for the shoreline dictates that

$$\zeta_t = u^s - v^s\zeta_y, \tag{3.4}$$

where the superscript s denotes that the variables are evaluated at the shoreline. The physical requirement for a shoreline to exist is

$$d = h + \eta = 0 \quad \text{on } x = \zeta(y,t). \tag{3.5}$$

Furthermore, the domain is bounded by an open boundary at $x = L_x$. The characteristic horizontal length scale is denoted by L. Periodicity is assumed in the y direction.

Using spectral collocation schemes to determine the spatial derivatives and an explicit time stepping scheme, the most straightforward boundary treatment at, say, $x = L_x$ would be to specify one of the unknowns at the boundary (e.g.

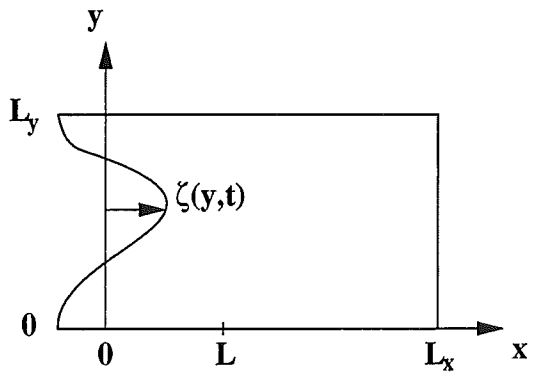

Figure 3.1: Physical Domain

u) and update the other two unknowns (v and d) at the boundary using (3.1), (3.2) and (3.3). Although this type of approach may not lead to problems when using finite difference methods, it is strongly unstable when spectral collocation methods are used (Gottlieb *et al.*, 1982). The reason is that the use of (3.1) and (3.3) for the evolution of d and v is an incorrect extrapolation of the equations to the boundary.

In order to impose the onshore and offshore boundary conditions properly, we use the method of characteristics and rewrite the governing equations in the unknowns u, v and d in terms of variables that carry information across the onshore and offshore boundaries (herein called the β-characteristic variables) as well as along those boundaries (herein called the γ-characteristic variable). This manipulation is similar to the derivation of Abbott (1979) and is carried out following Van Dongeren *et al.* (1994).

The governing equations can be written in matrix form as

$$\mathbf{q}_t + \mathbf{A}\mathbf{q}_x + \mathbf{B}\mathbf{q}_y = \mathbf{C}. \tag{3.6}$$

where

$$\mathbf{q} = \begin{bmatrix} d \\ u \\ v \end{bmatrix}, \quad \mathbf{A} = \begin{bmatrix} u & d & 0 \\ g & u & 0 \\ 0 & 0 & u \end{bmatrix}, \quad \mathbf{B} = \begin{bmatrix} v & 0 & d \\ 0 & v & 0 \\ g & 0 & v \end{bmatrix}, \tag{3.7}$$

$$\text{and } \mathbf{C} = \begin{bmatrix} 0 \\ gh_x + F \\ gh_y + G \end{bmatrix}. \tag{3.8}$$

The eigenvector matrix $\mathbf{P}$ of the matrix $\mathbf{A}$ is given by

$$\mathbf{P} = \begin{bmatrix} -\frac{1}{2}\sqrt{d/g} & \frac{1}{2}\sqrt{d/g} & 0 \\ \frac{1}{2} & \frac{1}{2} & 0 \\ 0 & 0 & 1 \end{bmatrix}. \tag{3.9}$$

Premultiplying (3.6) by the inverse matrix $\mathbf{P^{-1}}$ gives

$$\mathbf{P^{-1}q}_t + \left(\mathbf{P^{-1}AP}\right)\mathbf{P^{-1}q}_x + \left(\mathbf{P^{-1}BP}\right)\mathbf{P^{-1}q}_y = \mathbf{P^{-1}C}. \tag{3.10}$$

Algebraic manipulation of this equation results in

$$\mathbf{w}_t + \mathbf{A'w}_x + \mathbf{B'w}_y = \mathbf{C'}. \tag{3.11}$$

where

$$\mathbf{A'} = \begin{bmatrix} u - \sqrt{gd} & 0 & 0 \\ 0 & u + \sqrt{gd} & 0 \\ 0 & 0 & u \end{bmatrix}, \quad \mathbf{B'} = \begin{bmatrix} v & 0 & -\sqrt{gd} \\ 0 & v & \sqrt{gd} \\ -\frac{1}{2}\sqrt{gd} & \frac{1}{2}\sqrt{gd} & v \end{bmatrix},$$

$$\text{and } \mathbf{C'} = \begin{bmatrix} gh_x + F \\ gh_x + F \\ gh_y + G \end{bmatrix}. \tag{3.12}$$

The unknown vector $\mathbf{w}$ is defined by

$$\mathbf{w} \equiv \begin{bmatrix} u - 2\sqrt{gd} \\ u + 2\sqrt{gd} \\ v \end{bmatrix} \equiv \begin{bmatrix} \beta^- \\ \beta^+ \\ \gamma \end{bmatrix}. \tag{3.13}$$

The three equations can now be written as

$$\beta_t^- + (u - c)\beta_x^- + v\beta_y^- - c\gamma_y = 2c_0 c_{0x} + F \tag{3.14}$$

$$\beta_t^+ + (u + c)\beta_x^+ + v\beta_y^+ + c\gamma_y = 2c_0 c_{0x} + F \tag{3.15}$$

$$\gamma_t + u\gamma_x + v\gamma_y = -g\eta_y + G. \tag{3.16}$$

Here, c is the nonlinear shallow water wave speed $\sqrt{gd} = \sqrt{g(h+\eta)}$ and c_0 is the linear shallow water wave speed $\sqrt{gh}$. Note that, in the absence of longshore variability, the above equations reduce to uncoupled one-way wave equations. As desired, the variables β^- and β^+ carry information across the onshore and offshore boundaries whereas the variable γ carries information along those boundaries.

Note that the equation governing $\beta^+ = u + 2c$ ($\beta^- = u - 2c$) carries information in the $+x$ ($-x$) direction and is therefore valid everywhere inside the domain and on the right (left) boundary point but not on the left (right) boundary point. The equation governing the evolution of the glancing variable $\gamma = v$ is valid everywhere in the domain including the boundary points.

In order to impose the boundary condition at $x = L_x$ properly, the incoming β-variable β^- has to be specified, while the outgoing β-variable β^+ and the glancing variable γ can be computed using (3.15) and (3.16), respectively. The simplest boundary that can be constructed in this manner at, say, $x = L_x$ is a fully reflective wall boundary, where β^+ and γ are calculated using (3.15) and (3.16) and β^- is specified as $\beta^- = -\beta^+$. Numerical calculations using this condition lead to stable solutions.

3.3 Treatment of Moving Shoreline

Gravity driven motions in the nearshore region have significant shoreline runup associated with them. The most commonly used techniques to model shoreline runup are Eulerian models with fixed numerical grids or meshes. Examples of the implementation of such methods can be found in studies of solitary wave and tsunami runup such as Liu *et al.* (1995). In these methods the shoreline is defined as the interface between wet and dry cells; therefore, it is usually defined within the accuracy of the grid size. The shoreline is advanced or retreated in discrete steps. The amount of movement is dictated by the volume flux at the last wet point. These methods are fairly straightforward to implement. However, the impulsive filling of a cell with fluid can lead to numerical problems or time step constraints unless treated carefully. Also, an *a priori* estimate of the maximum runup needs to be available in order to keep the domain large enough to accommodate it.

Lagrangian methods are very well suited for the treatment of moving boundaries. In these methods, the fluid is represented as a large number of fluid particles. Tracking the position of a particle at the shoreline is in general no more difficult than tracking a particle in the interior of the fluid. Examples of computations for solitary wave runup using Lagrangian methods are presented by Pedersen and Gjevik (1983) and Zelt and Raichlen (1990). However, Lagrangian methods employed in regions with a net streaming velocity (such as the longshore current in the surf zone) may require frequent regridding, since the computational grid would tend to be advected and sheared by the steady flow.

Eulerian models with deforming grids are less frequently used in association with long wave runup. Lynch and Gray (1980) and Gopalakrishnan and Tung (1983) reported techniques whereby moving boundaries can be treated by finite

element Eulerian models. They involve moving grids where one boundary of the grid tracks the position of the shoreline, and are more difficult to implement than methods involving a fixed grid. However, they do not exhibit the problems associated with grid draining and filling in fixed grid models, and would not experience the difficulties associated with steady flows in a purely Lagrangian model. Therefore, we have chosen to develop an Eulerian model with a moving grid for application to the surf zone in the present study.

The problem at hand consists of solving a set of well-known governing equations (3.14), (3.15) and (3.16) in a complicated physical domain bounded by one curvilinear moving boundary defined by (3.4) and (3.5) and three stationary boundaries. The challenge of modeling the moving boundary can be overcome by mapping the variable size domain onto a fixed domain. Such a transformation will lead to a grid that follows the shoreline with one grid boundary and will introduce additional terms into the governing equation.

The coordinate transformation from the physical variables $x \in [\zeta(y,t), L_x]$ and $y \in [0, L_y]$ to the intermediate variables $\phi \in [0, L_x]$ and $\psi \in [0, L_y]$ used here is given by

$$x = \phi + \zeta(y,t)e^{-\alpha\phi^2}, \qquad y = \psi. \tag{3.17}$$

A stationary orthogonal grid in the (ϕ, ψ) domain corresponds to a physical grid that is following the shoreline (see Figure 3.2). The movement of the grid lines is damped out exponentially with offshore distance so that the grid is almost stationary at a certain distance offshore. This distance is dictated by the value of the parameter α. As a result of the transformation, the derivatives in the governing equations are altered, resulting in a few additional terms. The derivatives in the

governing equations now become

$$\begin{aligned} (\ )_t|_x &= (\ )_t|_\phi + (\ )_\phi \phi_t \\ (\ )_x &= (\ )_\phi \phi_x \\ (\ )_y &= (\ )_\psi + (\ )_\phi \phi_y, \end{aligned} \tag{3.18}$$

where $\phi(x, y, t)$ is given by (3.17) and $(\ )_t|_x$ and $(\ )_t|_\phi$ denote time derivatives in a reference frame where x and ϕ are fixed, respectively.

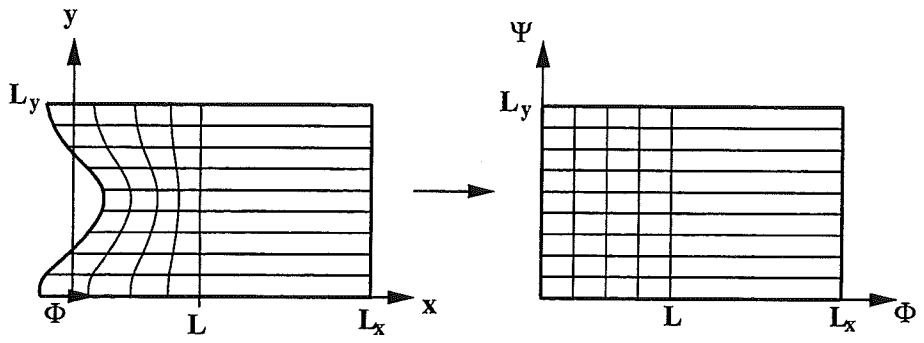

Figure 3.2: Shoreline Boundary Condition: Transformation from the physical to the intermediate domain

The intermediate grid in the variables $\phi \in [0, L_x]$ and $\psi \in [0, L_y]$ obtained above is next mapped onto a computational grid in the variables $s \in [-1, 1]$ and $r \in [0, L_y]$ (see Figure 3.3). Given the positions of the computational points in the (s, r) domain, a variety of coordinate transformations can be used depending on the desired distribution of the interior points in the (ϕ, ψ) domain. Examples of frequently used transformations are given in Boyd (1988). One of the simplest transformations is

$$\phi = L(1 + s), \qquad \psi = r. \tag{3.19}$$

Since a linear relationship between the intermediate variables (ϕ, ψ) and the computational variables (s, r) is dictated by this transformation, the grid point distributions chosen for s and r are preserved in the physical grid.

The coordinate transformation

$$\phi = L\frac{1+s}{s_0 - s}, \qquad \psi = r \tag{3.20}$$

has the effect of concentrating grid points in the physical domain in the vicinity of the shoreline and is used for the runup simulations in Section 4.1. This transformation also presents the opportunity of modeling a domain where the offshore boundary is located at infinity since the location of the offshore boundary is dictated by the value of the parameter s_0. If the offshore boundary is located at infinity s_0 equals unity. In this case a physical domain in the shape of a semi-infinite strip is modeled while the computations are carried out in a box-shaped domain. For a finite offshore width $s_0 > 1$. Shear instability computations for a plane beach documented in Chapter 5 were carried out using a value of 2 for s_0 in (3.20).

A grid of nearly uniformly spaced collocation points in the cross-shore direction along with a uniform grid in the longshore direction is used in Chapter 6. The transformation

$$\phi = L\frac{\arccos(-ps) - \arccos(p)}{\arccos(-p) - \arccos(p)}, \qquad \psi = r \tag{3.21}$$

is utilized with $p = 0.999$. Many other transformations are possible and their incorporation into the solution scheme is trivial, so that the grid point distributions can be tailored to the case at hand.

As a result of this second transformation the derivatives in the governing equation are further modified and become,

$$\begin{aligned} (\,)_t|_x &= (\,)_t|_s + (\,)_s s_\phi \phi_t \\ (\,)_x &= (\,)_s s_\phi \phi_x \\ (\,)_y &= (\,)_r + (\,)_s s_\phi \phi_y, \end{aligned} \tag{3.22}$$

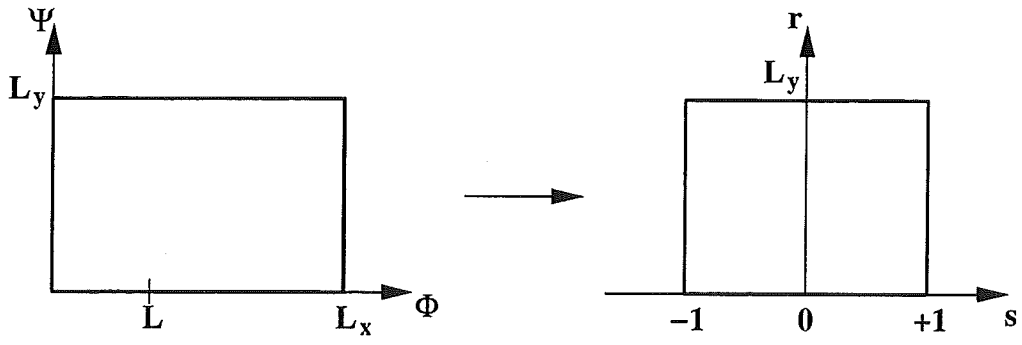

Figure 3.3: Transformation from the intermediate to the computational domain

where $(\,)_t|_s$ denotes time derivatives at fixed values of s.

As a result of the two coordinate transformations the governing equations now read

$$\beta_t^- + [s_t + s_x(u-c) + s_y v]\,\beta_s^- + v\beta_r^- - c\gamma_r - s_y c\gamma_s = 2s_x c_0 c_{0_s} + F \quad (3.23)$$

$$\beta_t^+ + [s_t + s_x(u+c) + s_y v]\,\beta_s^+ + v\beta_r^+ + c\gamma_r + s_y c\gamma_s = 2s_x c_0 c_{0_s} + F \quad (3.24)$$

$$\gamma_t + [s_t + s_x u + s_y v]\,\gamma_s + v\gamma_r = -g\eta_r - g s_y \eta_s + G. \quad (3.25)$$

At the shoreline $c = \sqrt{gd} = 0$, and the equations in the β-variables collapse into one redundant equation and no information about the values of the β-variables can be deduced. However, the velocity at the shoreline can be determined using the x-momentum equation

$$u_t^s + [s_t + s_x u^s + s_y v^s]\,u_s^s + v u_r^s = -g s_x \eta_s^s + F^s, \quad (3.26)$$

where the superscript s denotes that the variables are evaluated at the shoreline. After applying the two coordinate transformations the kinematic condition (3.4) reads

$$\zeta_t = u^s - v^s \zeta_r. \quad (3.27)$$

The physical requirement (3.5) for a shoreline to exist becomes

$$d = h + \eta = 0 \quad \text{on } s = -1. \tag{3.28}$$

The evolution of the wave field is calculated by time stepping (3.23), (3.24) and (3.25) along with (3.26) and (3.27) while imposing the condition stated in (3.28) and an offshore boundary condition to be discussed next.

In the following sections, it will be shown that this boundary treatment compares favorably to analytical and other numerical results. However, in some situations, especially when steep waves are involved, it causes grid points to run up the shore to form a very thin film of water on the beach. As a result grid points are lost to the beach and the resolution of the solution is decreased. Therefore, it is necessary to prevent the occurrence of a thin film which is evidenced by more than one grid point with $d < d_{\text{thresh}}$ associated with them. The parameter d_{thresh} is a threshold value appropriate for the application and should be chosen in relation to the runup amplitude and beach slope associated with the application as well as the grid point distribution. Care should be taken to choose d_{thresh} to be significantly smaller than the depth value at the first grid point seaward of the shoreline at the initial time level.

If the occurrence of a thin film is detected during a simulation, the shoreline position is redefined as the average of the positions of the most seaward point with $d < d_{\text{thresh}}$ and the next offshore point with $d > d_{\text{thresh}}$. The row at the longshore positions where the thin film was detected is then regridded. In order to minimize computational time, in this study a nonzero value for d_{thresh} is only used if visual inspection of preliminary results for a case shows the occurrence of a thin film.

3.4 Offshore Absorbing-Generating Boundary

An absorbing-generating boundary condition needs to be specified at the offshore boundary to simultaneously allow waves to exit the domain of interest with minimum reflection as well as specify incoming waves at the offshore boundary. The logic of the absorbing-generating boundary condition can be best understood when the problem is reduced to a one-dimensional case. The extension to the two-dimensional problem follows in a straightforward manner.

3.4.1 One-Dimensional Problem

In one dimension and in the absence of any forcing terms F and G, the governing equations at the offshore boundary $x = L_x$ reduce to

$$\beta_t^- + (u - c)\beta_x^- = 2c_0 c_{0x} \tag{3.29}$$

$$\beta_t^+ + (u + c)\beta_x^+ = 2c_0 c_{0x}, \tag{3.30}$$

which are uncoupled one-way wave equations. The characteristic variables are given by $\beta^- = u - 2c$ traveling in the $-x$ direction and $\beta^+ = u + 2c$ traveling in the $+x$ direction.

If an outgoing wave exists in the absence of an incoming wave, the incoming characteristic will carry no information and will reduce to $\beta^- = u - 2c = -2c_0$. Therefore, the particle velocity associated with the outgoing wave is $U_{\text{out}} = 2c_{\text{out}} - 2c_0$, where $c_{\text{out}} = \sqrt{g(h + \eta_{\text{out}})}$. In this case the boundary condition at the offshore boundary $x = L_x$ would be constructed by computing the outgoing characteristic β^+ using (3.30) and specifying the incoming characteristic β^- as $-2c_0$.

In turn, if an incoming wave exists in the absence of an outgoing wave, the outgoing characteristic will carry no information and will reduce to $\beta^+ =$

$u+2c = 2c_0$. The particle velocity associated with the incoming wave is then $U_{\text{in}} = -2c_{\text{in}} + 2c_0$, where $c_{\text{in}} = \sqrt{g(h+\eta_{\text{in}})}$. The specification of the boundary condition is again straightforward; β^+ can be computed using the governing equation and β^- has to be specified as the incoming wave.

Assuming that the incoming and outgoing waves exist simultaneously but that their particle velocities are independent of each other the observed velocity at the boundary is $u = U_{\text{in}} + U_{\text{out}} = 2(c_{\text{out}} - c_{\text{in}})$ and the total water surface elevation is $\eta = \eta_{\text{in}} + \eta_{\text{out}}$. This assumption is equivalent to superimposing the incoming and outgoing waves at the boundary. However, this superposition does not imply a linearization of the problem at the boundary since the velocities associated with the waves are calculated using the nonlinear equations. As a result, the interactions between the incoming and outgoing waves are neglected while the self-interactions of these waves are included.

3.4.2 Two-Dimensional Problem

The extension of the above ideas to the two-dimensional case has previously been presented by Verboom and Slob (1984) for the case of wave absorption for a viscous fluid. The following technique has been developed by Van Dongeren and Svendsen (1997) for simultaneous absorption-generation in the context of long wave propagation and is used here with minor modifications.

The technique involves defining the particle velocities of the incoming and outgoing waves as U_{in} and U_{out}, respectively, along with their components in the x direction u_{in} and u_{out} and their components in the y direction v_{in} and v_{out} (see Figure 3.4). Known quantities at the offshore boundary $x = L_x$ are variables associated with the known incoming wave u_{in}, v_{in} and η_{in} as well variables

determined from the governing equations $v = v_{\text{in}} + v_{\text{out}}$ and $\beta^+ = u + 2c$ where $u = (u_{\text{in}} + u_{\text{out}})$ and $c = \sqrt{g(h + \eta_{\text{in}} + \eta_{\text{out}})}$. The unknowns are the x-component of the outgoing wave particle velocity u_{out} and its propagation speed c_{out}, which is defined above.

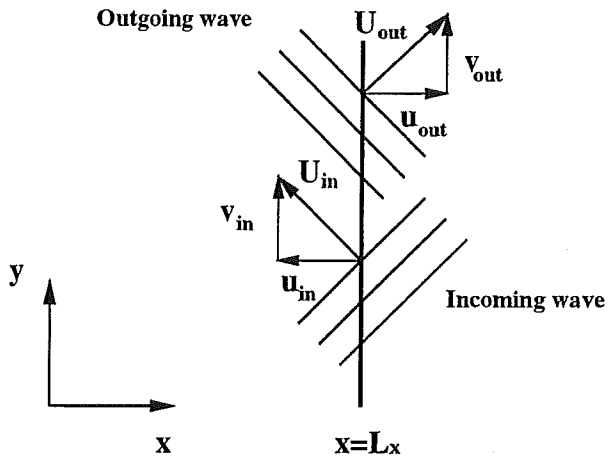

Figure 3.4: Sketch of the offshore boundary

The total celerity c can be rewritten as

$$c^2 = c_{\text{in}}^2 + c_{\text{out}}^2 - c_0^2. \tag{3.31}$$

Since $\beta^+ = u + 2c$ is known, we can write,

$$4c_{\text{out}}^2 = \left(\beta^+ - u\right)^2 - 4c_{\text{in}}^2 + 4c_0^2. \tag{3.32}$$

From the discussion about the one-dimensional problem, we can deduce that in the absence of any interaction with the incoming wave, the particle velocity of the outgoing wave in the propagation direction is given by,

$$U_{\text{out}} = 2c_{\text{out}} - 2c_0 \tag{3.33}$$

or,

$$4c_{\text{out}}^2 = \left(U_{\text{out}} + 2c_0\right)^2. \tag{3.34}$$

Equating the right hand sides of (3.32) and (3.34), rearranging and using $u = (u_{\text{in}} + u_{\text{out}})$ gives,

$$u_{\text{out}} = (\beta^+ - u_{\text{in}}) - \left[U_{\text{out}}^2 + 4U_{\text{out}}c_0 + 4c_{\text{in}}^2\right]^{1/2}. \tag{3.35}$$

Using geometrical arguments (see Figure 3.4), it can be stated that $U_{\text{out}}^2 = u_{\text{out}}^2 + v_{\text{out}}^2$. Substituting the expression for u_{out} given in (3.35) and rearranging gives

$$dU_{\text{out}}^2 + eU_{\text{out}} + f = 0, \tag{3.36}$$

where,

$$\begin{aligned} d &= (\beta^+ - u_{\text{in}} - 2c_0)(\beta^+ - u_{\text{in}} + 2c_0) \\ e &= 2c_0\left[(\beta^+ - u_{\text{in}})^2 - v_{\text{out}}^2 - 4c_{\text{in}}^2\right] \\ f &= -\frac{1}{4}\left[(\beta^+ - u_{\text{in}} - 2c_{\text{in}})^2 + v_{\text{out}}^2\right]\left[(\beta^+ - u_{\text{in}} + 2c_{\text{in}})^2 + v_{\text{out}}^2\right]. \end{aligned} \tag{3.37}$$

Now, the unknown particle velocity U_{out} can be found to be

$$U_{\text{out}} = \begin{cases} \left(-e \pm \sqrt{e^2 - 4df}\right)/(2d) & \text{for } d \neq 0 \\ -f/e & \text{for } d = 0 \end{cases} \tag{3.38}$$

Therefore,

$$\begin{aligned} u_{\text{out}} &= \text{sgn}(U_{\text{out}})\sqrt{U_{\text{out}}^2 - v_{\text{out}}^2} \\ c_{\text{out}} &= c_0 + \frac{1}{2}U_{\text{out}}. \end{aligned} \tag{3.39}$$

The incoming β-variable can be specified as

$$\beta^- = (u_{\text{in}} + u_{\text{out}}) - 2c, \tag{3.40}$$

where c is given by (3.31).

3.5 Numerical Solution Method

Traditionally, the most straightforward method to solve the shallow water equations has involved making finite difference approximations of spatial derivatives in conjunction with an explicit or implicit time stepping scheme. The accuracy of such methods is limited due to truncation errors associated with the difference approximations. These errors usually arise in the form of dispersion or dissipation errors. More recently, spectral and pseudospectral methods have become more popular. A wide variety of spectral schemes exist and are reviewed in Canuto *et al.* (1987) and Boyd (1988). A recent application of spectral schemes to water wave propagation problems has been performed by Panchang and Kopriva (1989) who used a Chebyshev collocation method to analyze short wave propagation over complicated bathymetry. In addition, Falqués and Iranzo (1992) applied spectral collocation methods to the linear shallow water equations for the purpose of simulating edge waves. Dalrymple *et al.* (1994) compared several spectral methods in the context of forward propagating water waves.

When compared to finite difference methods, spectral methods give more accurate approximations for spatial derivatives, as they have no truncation errors and therefore lead to more accurate solutions with less dispersion and dissipation errors. For smooth solutions, the error in the derivatives asymptotically decays faster than any order polynomial (see Canuto *et al.*, 1987) compared to a low fixed order polynomial for finite difference derivatives. Furthermore, spectral methods can be tailored to suit the motions of interest since basis functions for the spectral derivatives can be chosen to naturally satisfy the boundary conditions, and variable grid spacing can easily be incorporated to achieve high resolution where steep solutions are expected. In this manner a solution of the desired accuracy can be achieved with far less spatial points and therefore, less computational time

than with finite difference schemes. Since these are desired features of the solution method developed here, spectral collocation schemes are employed herein for the computation of the spatial derivatives.

Given initial conditions for the water surface elevation η and the velocities u and v, the governing equations given in (3.23), (3.24) and (3.25) are integrated in time using an explicit third order Adams-Bashforth scheme. The governing equations can be written in the form

$$\beta_t^- = F_1(\eta, u, v) \tag{3.41}$$

$$\beta_t^+ = F_2(\eta, u, v) \tag{3.42}$$

$$\gamma_t = F_3(\eta, u, v). \tag{3.43}$$

The definitions for $F_1(\eta, u, v)$, $F_2(\eta, u, v)$ and $F_3(\eta, u, v)$ contain spatial derivatives of their arguments and can be obtained by comparing (3.41) through (3.43) to (3.23) through (3.25).

The spatial derivatives contained in the functions F_1, F_2 and F_3 will be evaluated using spectral collocation. Since the resulting differentiation matrix for a system of ordinary differential equations such as (3.41) through (3.43) is full, the system is typically integrated using explicit methods. An appropriate time integration scheme often used in advection problems in conjunction with Fourier or Chebyshev collocation is the Adams-Bashforth method (see Canuto *et al.*, 1987). Since the second order Adams-Bashforth scheme displays a slow growth rate when used with Fourier collocation methods, the third order Adams-Bashforth scheme is chosen. This scheme is given by

$$\left(\beta^-\right)^{n+1} = \left(\beta^-\right)^n + \frac{\Delta t}{12}\left[23F_1^n - 16F_1^{n-1} + 5F_1^{n-2}\right] \tag{3.44}$$

$$\left(\beta^+\right)^{n+1} = \left(\beta^+\right)^n + \frac{\Delta t}{12}\left[23F_2^n - 16F_2^{n-1} + 5F_2^{n-2}\right] \tag{3.45}$$

$$\gamma^{n+1} = \gamma^n + \frac{\Delta t}{12}\left[23F_3^n - 16F_3^{n-1} + 5F_3^{n-2}\right]. \tag{3.46}$$

The superscripts denote the time level at which the terms are evaluated with n being the present, known time level.

In order to apply spectral methods to the problem at hand, the domain of interest is discretized into an $(NX+1) \times (NY+1)$ point mesh. The collocation points in the offshore direction s are chosen as the reversed Gauss-Lobatto points given by $s_i = -\cos(\pi i/NX)$ $(i = 0, \ldots, NX)$. This choice ensures that the grid points in the physical domain are concentrated close to the shoreline. Using these collocation points, the Chebyshev collocation calculations can also be carried out using efficient Fast Fourier Transform (FFT) routines.

The collocation points in the longshore direction r are chosen to be equally spaced so that $r_j = j\Delta y$ $(j = 0, \ldots, NY)$. Fourier collocation is applied in this direction since the Fourier basis functions naturally satisfy the periodicity boundary condition imposed in the longshore direction. Note that any desired grid point distribution in the physical domain (x, y) can be obtained by choosing appropriate transformation functions from the physical to the computational domain as described in Section 3.3.

Let Q represent one of the variables β^-, β^+ or γ at a certain time level. Using Fourier collocation for the r direction derivatives in the governing equations and a Chebyshev collocation method for the s direction derivatives, Q will be approximated by

$$Q(s,r) \approx Q_p(s,r) = \sum_{m=-\mathrm{NY}/2}^{\mathrm{NY}/2-1} \sum_{n=0}^{NX} a_{nm} T_n(s) e^{imkr} \tag{3.47}$$

where $T_n(s), n = 0, 1, \ldots$ are Chebyshev polynomials of the first kind and are given by

$$T_n(s) = \cos n\theta, \qquad \theta = \arccos(-s). \tag{3.48}$$

Approximations to the derivatives in the longshore direction r are computed by differentiating (3.47) with respect to r. Rewriting the equation gives

$$Q_p(s,r) = \sum_{m=-\mathrm{NY}/2}^{\mathrm{NY}/2-1} A_m(s) e^{imkr}, \text{ where } A_m(s) = \sum_{n=0}^{NX} a_{nm} T_n(s). \tag{3.49}$$

The function $A_m(s)$ is known since it is the Fourier transform of Q_p in r at a fixed s location. Differentiating the above equation yields

$$\frac{\partial}{\partial r}\left(Q_p(s,r)\right) = \sum_{m=-\mathrm{NY}/2}^{\mathrm{NY}/2-1} A'_m(s) e^{imkr}, \text{ where } A'_m(s) = imkA_m(s) \tag{3.50}$$

Thus, inverse Fourier transforming $A'_m(s)$ gives the desired spatial derivative. Note that the r derivative of Q_p at an s location is a function of the values of Q_p at all the r locations, and hence the derivative has a global character. Furthermore, the procedure defines the values of the derivatives at all mesh points, so no special procedure is required to evaluate derivatives at the boundaries.

The derivatives in the s direction are computed using Chebyshev collocation. The procedure is much like that described above for Fourier collocation. Rewriting (3.47) yields

$$Q_p(s,r) = \sum_{n=0}^{NX} B_n(r) T_n(s), \text{ where } B_n(r) = \sum_{m=-\mathrm{NY}/2}^{\mathrm{NY}/2-1} a_{nm} e^{imkr}. \tag{3.51}$$

The function $B_n(r)$ is known as the Chebyshev transform of Q_p in s at a fixed r location. Differentiating with respect to s gives

$$\frac{\partial}{\partial s}\left(Q_p(s,r)\right) = \sum_{n=0}^{NX} B'_n(r) T_n(s). \tag{3.52}$$

Using the definition for the Chebyshev polynomials given in (3.48) and the trigonometric identity $2\sin\theta\cos n\theta = \sin(n+1)\theta - \sin(n-1)\theta$, the coefficients $B'_n(r)$ can be computed in decreasing order by the recurrence relation

$$c_n B'_n(r) = B'_{n+2}(r) - 2(n+1)B_{n+1}(r), \tag{3.53}$$

where

$$c_n = \begin{cases} 2 & \text{if } n = 0 \\ 1 & \text{if } n \geq 1 \end{cases} \qquad \text{and} \qquad B'_n(r) = 0 \quad \text{for } n \geq NX \tag{3.54}$$

Once again, no special boundary treatment is needed. Both methods of differentiation are described in detail by Canuto *et al.* (1987).

A type of instability in the time integration of nonlinear systems is caused by the process known as aliasing. The onset of the aliasing instability is characterized by the excitement of waves at the limit of the resolution. These waves have wavelengths L of $2\Delta x$ where Δx represents the grid spacing in the computational grid. In the simulations shown here, a solution smoothing technique involving a high order filter developed by Shapiro (1970) is used to prevent the spurious growth of these shortest waves that can be resolved. The one-dimensional form of the filtering technique involves replacing a variable Q at a grid point by a weighted average of its $(2N + 1)$ neighbors centered around the grid point. The new value of the variable at the grid point is referred to as Q^* and the response of the filter is quantified using an amplification factor (or response function) defined as the quotient of the filtered value Q^* to the original value Q ,

$$R = \frac{Q^*}{Q}. \tag{3.55}$$

Shapiro (1970) devised a method of evaluating the weighting coefficients such that the response function R is given by

$$R = 1 - \sin^{2N}\left(\frac{\pi}{M}\right), \tag{3.56}$$

where $M = L/\Delta x$ is the number of grid points per wavelength. The value $2N$ is referred to as the order of the filtering method and only assumes the values

$$(2N) = 2^j, \qquad j = 1, 2, 3, \ldots \tag{3.57}$$

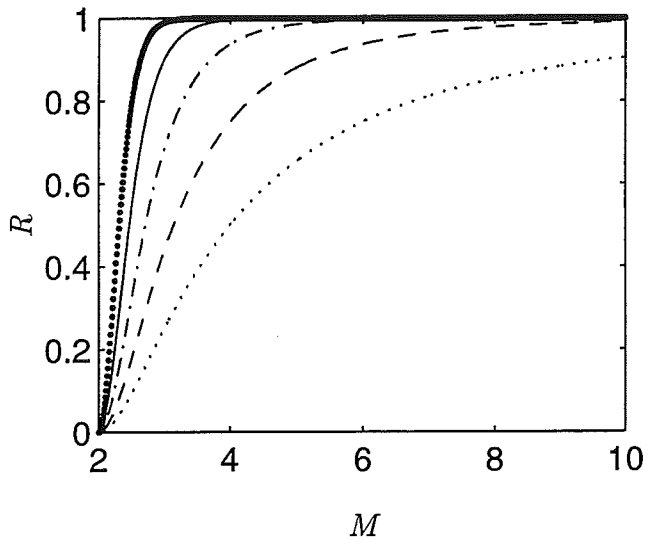

Figure 3.5: Response function for Shapiro filters of order $2N$=2 (· · ·), 4 (– –), 8 (– · –), 16 (——), 32 (• • •).

The response function R is depicted in Figure 3.5 as a function of the resolution M for different orders $2N$. Waves at the limit of resolution have $M = 2$ and are eliminated completely since the response function is equal to zero for $M = 2$ for all N. For waves with longer wavelengths (higher M values) the value of the response function R approaches one. Therefore, longer waves are filtered less. The transition from $R = 0$ to $R = 1$ occurs faster for higher order filters. As suggested by Shapiro (1970), the filtering technique is extended to two dimensions by sequentially applying a one-dimensional filter in the x and y directions.

3.6 Summary

In this chapter, a solution method for the nonlinear shallow water equations has been developed with the objective of studying low frequency motions in the surf and swash zones. The solution method involves a high order time

integration scheme in conjunction with spectral collocation for the calculation of spatial derivatives. Two-dimensional shoreline runup is modeled using an Eulerian shoreline model in conjunction with a moving grid. An absorbing-generating boundary condition originally developed by Van Dongeren and Svendsen (1997) is used at the offshore boundary.

In the Chapter 4, the solution method is tested for gravity wave motions. Additional terms accounting for dissipational and external forcing effects are added in Chapter 5 and the method is used to simulate vorticity motions as documented in Chapters 5 and 6. The model is extended further in Chapter 7 to include the effects of time varying external forcing by short waves as well as interactions between the short wave climate and the currents.

Chapter 4

TEST CASES

In this section, the accuracy of the boundary treatments is verified using analytical and numerical results. First the shoreline boundary condition is tested for one-dimensional as well as two-dimensional runup. The offshore boundary is tested for waves leaving the domain of interest at normal incidence or at an angle to the offshore direction. The developed method is then applied to the prediction of neutral stability boundaries and equilibrium amplitudes of subharmonic edge waves. Numerical results are compared to weakly nonlinear theory and are found to reproduce the theory very well.

4.1 Shoreline Boundary

4.1.1 1D Runup

An analytical solution for single wave runup on a sloping beach by Carrier and Greenspan (1958) is used to verify the accuracy of the shoreline treatment. This example corresponds to the physical problem in which the water level at the shoreline is depressed, the fluid is held motionless and then released. The shoreline water level climbs to a position higher than the still water level, and then slowly settles back to it.

The initial water surface elevation η as a function of offshore distance x can be expressed in parametric form as

$$\begin{aligned} \eta &= \epsilon m L \left[1 - \frac{5}{2} \frac{a^3}{(a^2+\xi^2)^{3/2}} + \frac{3}{2} \frac{a^5}{(a^2+\xi^2)^{5/2}} \right] \\ x &= -\frac{L}{16}\xi^2 + \epsilon m L \left[1 - \frac{5}{2} \frac{a^3}{(a^2+\xi^2)^{3/2}} + \frac{3}{2} \frac{a^5}{(a^2+\xi^2)^{5/2}} \right] \end{aligned} \tag{4.1}$$

for $\xi > 0$, where $a = 1.5(1 + 0.9\epsilon)^{1/2}$. The parameter ϵ is the maximum nondimensional water surface elevation, m is the beach slope, L is a cross-shore length scale. The water surface elevation approaches the still water level far from the shoreline.

In order to simulate this situation in dimensional space a beach slope m of 0.02 and a length scale L of 20 m is chosen. The parameter ϵ is given by 0.2 in the simulation shown. The theory by Carrier and Greenspan (1958) predicts that a surging breaker results if the initial nondimensional depression is 0.23.

In this simulation the parameter s_0 in (3.20) is chosen to be unity so that the domain extends to infinity in the offshore direction. The parameter α in (3.17) is specified as 2.76×10^{-3} so that the movement of the grid 50 m offshore is damped to only 0.1% of the runup amplitude. The depth threshold value at the shoreline d_{thresh} discussed in Section 3.3 is chosen as zero for this application. The simulation is carried out using 128 collocation points in the x direction with a time step of 0.01 s. A 16th order Shapiro filter is applied. Figure 4.1 (a) shows snapshots of the water surface elevation η as a function of offshore distance every 1.6 seconds, with $t = 0$ s corresponding to the initial depression of the water surface and the maximum rundown position, and $t = 19.2$ s corresponding to the maximum runup position. Figure 4.1 (b) shows the time series of the shoreline position. The numerical and analytical solutions are seen to agree to within visual resolution.

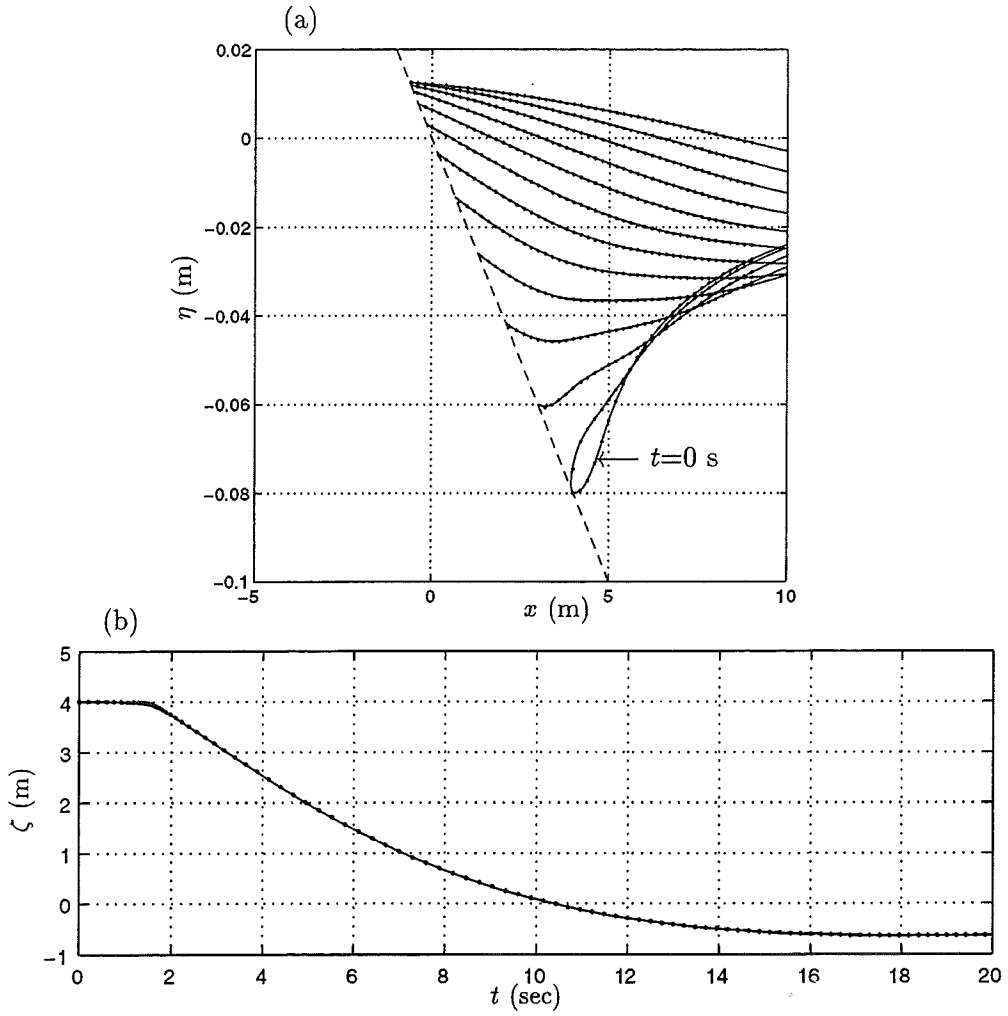

Figure 4.1: Runup in 1D: (a) Snapshots with $\Delta t = 1.6$ sec of η versus x. (b) Time series of shoreline position. Exact solution (· · ·), present method (——).

4.1.2 2D Runup

The second test case for the shoreline boundary condition involves solitary wave runup on a bay with a sloping bottom. The test case geometry combines a curved still water shoreline with a sloping nearshore bathymetry that merges with a constant depth region offshore. This geometry was used by Zelt (1986) in the context of the response of harbors with sloping boundaries to long wave excitation. The geometry is depicted in Figure 4.2. The still water surface is outlined with a single closed thick line above the bottom. The curved portion of the shoreline traces a period of a cosine curve. It is given by

$$\zeta(y, t = 0) = \zeta_0(y) = -\frac{L}{\pi} \cos \frac{\pi y}{L} \tag{4.2}$$

where L is the half-width of the bay and is chosen to be 20 m. The depth grid is given by

$$h = \begin{cases} h_0 - h_0 \frac{x - \frac{3L}{\pi}}{\zeta_0(y) - \frac{3L}{\pi}} & \text{for} \quad x \leq \frac{3L}{\pi} \\ h_0 & \text{for} \quad x > \frac{3L}{\pi} \end{cases} \tag{4.3}$$

where $h_0 = 0.4L/\pi$. A resulting maximum bottom slope of 1:5 occurs at $y = \pm L$, a minimum bottom slope of 1:10 occurs at $y = 0$.

The incoming wave is specified as a solitary wave. The dispersive parameter β given by $(h_0/L)^2$ is fixed at $(0.4/\pi)^2$ following the choice for h_0 and the wave height to offshore water depth ratio $\alpha' = (H/h_0)$ of 0.02 is used. The incident wave on the constant depth region is then given by

$$\eta = \alpha' h_0 \ \text{sech}^2 \left\{ \frac{\sqrt{g h_0}}{L} \chi \left(t + \frac{x}{\sqrt{g h_0 (1 + \alpha')}} \right) \right\}, \tag{4.4}$$

where

$$\chi = \sqrt{\frac{3\alpha'}{4\beta}(1 + \alpha')}. \tag{4.5}$$

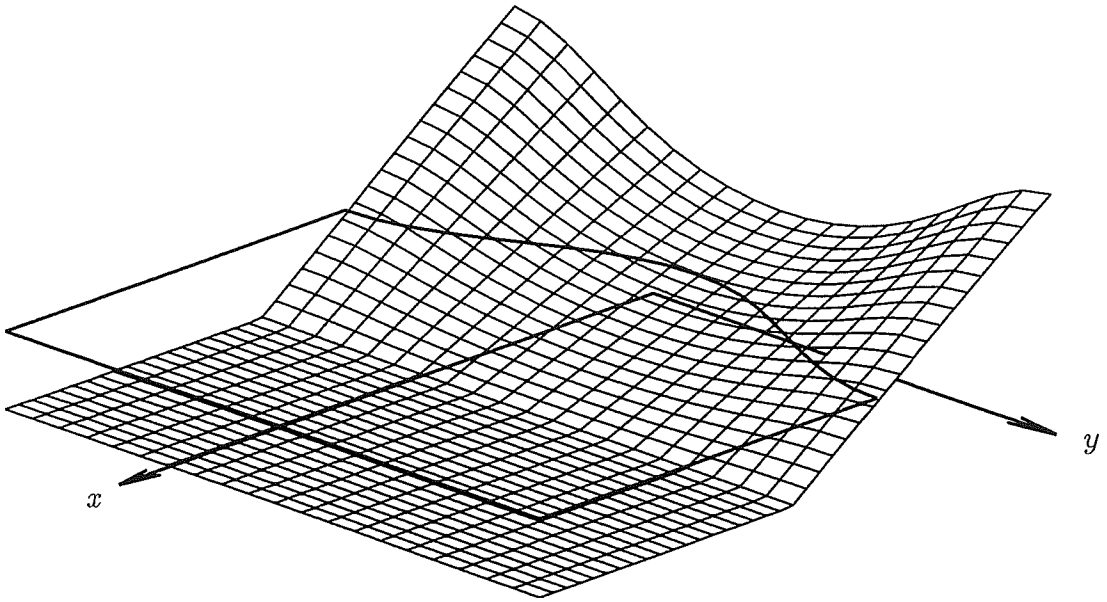

Figure 4.2: Bathymetry of the 2D runup test case.

Computations previously carried out by Zelt (1986) for this case show that breaking waves result if the wave height to water depth ratio is increased to 0.03. Zelt's calculations were carried out using a fully Lagrangian finite element model, and the results show pronounced two-dimensional runup.

In this simulation the parameter s_0 in (3.20) is chosen to be unity. Therefore, the domain extends to infinity in the offshore direction. The parameter α in (3.17) is specified as 2.76×10^{-3}. The shoreline threshold depth d_{thresh} is chosen to be zero. The computations are carried out using 128×64 collocation points with a time step of 0.01 s, and a 16th order filter is applied in both horizontal directions.

Figure 4.3a shows normalized runup in the cross-shore direction as a function of the nondimensional time scale $t' = t\sqrt{gh_0}/L$ at different locations along

the bay, where $y = 0$ denotes the midpoint of the bay and $y = \pm L$ denote the boundaries in the longshore direction. Figure 4.3b shows the normalized maximum runup and rundown in the cross-shore direction as a function of longshore location. The present method is seen to compare well with results by Zelt (1986).

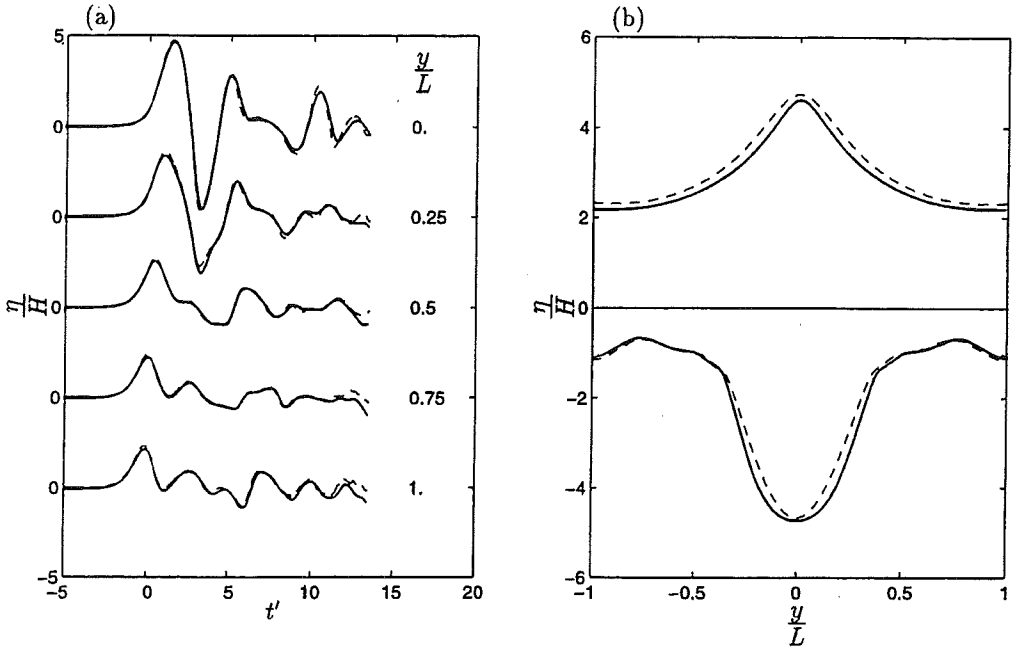

Figure 4.3: (a) Runup in 2D: Time series of runup along y. (b) Maximum runup and rundown. Zelt (——), present method (– –).

4.2 Absorbing-Generating Boundary

4.2.1 1D Absorption-Generation: A Group of Waves

The first test case for the offshore boundary condition involves the specification of a group of 12 waves at the offshore boundary of a constant depth (h =1 m) domain that is bounded onshore by a wall. The wave packet is expected to undergo a full reflection at the wall and travel back out of the domain at the offshore

boundary. The packet is made up of sufficiently many waves so that a standing wave pattern will be formed. Eventually, no more incoming waves are present and the last waves reflect off the wall and leave the domain through the offshore boundary. Using this test, the error at the offshore boundary can be quantified since the wave height of the individual incident (H_{in}) and reflected (H_{out}) waves are expected to be the same although the shape of the waves is expected to change as they travel through the domain. The error can be quantified in the form of a reflection coefficient for simultaneous absorption-generation defined as

$$R_{\text{ag}} = \frac{|H_{\text{in}} - H_{\text{out}}|}{H_{\text{in}}}. \tag{4.6}$$

Once the theoretical amount of time for the wave packet to leave the domain has elapsed, any disturbances left in the domain are errors in the absorption process only as no generation is present at that time. Therefore, the reflection due to only absorption can be quantified as

$$R_{\text{a}} = \frac{H_l}{H_{\text{in}}} \tag{4.7}$$

where H_l is the height of any leftover disturbance in the domain.

Figure 4.4 shows time series at the offshore boundary of the incident prescribed wave and the outgoing wave. The associated reflection coefficients, R_{ag} and R_{a}, are given in the caption of the figure and are about 0.06% and 0.02%, respectively. The reflection due to only absorption R_{a} is seen to be significantly lower than the reflection due to simultaneous absorption-generation R_{ag}. Since this is a consistent result of this and other similar test cases not shown here, results for only R_{ag} will be shown in the following test cases that focus on the effect of oblique incidence.

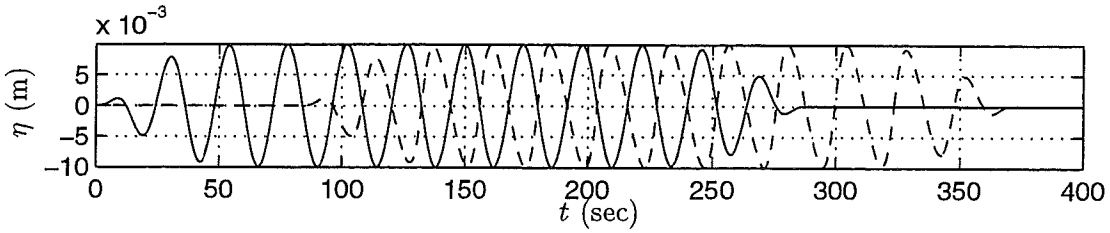

Figure 4.4: Simultaneous absorption-generation: Incoming wave (——) and outgoing wave (– –). $R_{ag} = 6.3 \times 10^{-4}$, $R_a = 1.9 \times 10^{-4}$

4.2.2 2D Absorption-Generation: Obliquely Incident Waves

Keeping the same domain as in the previous test case, incoming waves are now specified at the offshore boundary at an angle to the offshore direction. Furthermore, the standing wave system that results from the reflection of such a wave from the wall is specified as an initial condition. The propagation and evolution of this system is then observed by continuing to specify the incoming wave and allowing the reflected wave to leave the domain. Several test cases involving different angles of incidence ranging from 0° to 67.5° are carried out. The reflection coefficient at the boundary R_{ag} is computed as before and is shown as a function of angle of incidence in Figure 4.5. It is seen to increase with angle of incidence but to remain below 1% for a wide range of angles.

4.3 Application: Subharmonic Edge Waves

We now consider whether the present method is intrinsically stable and non-dissipative enough to reproduce the analytically known properties of a certain nonlinear instability mechanism, in which subharmonic edge waves are excited by normally-incident, cleanly-reflected surface waves.

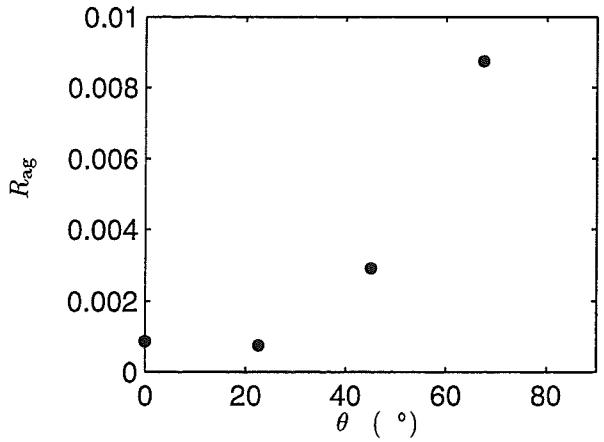

Figure 4.5: Simultaneous absorption-generation: Reflection as a function of incident angle θ.

Guza and Davis (1974) showed that a monochromatic wave train, normally incident on a beach and strongly reflected, is unstable to edge wave perturbations, identifying a mechanism of edge wave generation through resonant interactions between the incident wave and the resulting edge waves. They also derived growth rates of the initially small edge wave perturbations and showed that the strongest resonance arises between the incident wave of period T_i and two mode zero edge waves of period $T_e = 2T_i$ traveling in opposite directions along the beach, forming a standing edge wave. This standing edge wave is hence a subharmonic of the incident wave. Guza and Bowen (1976) further analyzed this mechanism and identified three processes that may limit edge wave growth: further nonlinear edge wave-edge wave interactions leading to the radiation of edge wave energy into the far field, finite amplitude demodulation due to the fact that the natural frequency of the edge wave σ_f increases with amplitude and eventually detunes such that the forcing frequency ceases to lie within the resonant bandwidth, and viscosity.

Using nonlinear perturbation analysis, Guza and Bowen (1976) showed that radiation and detuning are of comparable importance in limiting edge wave growth and that viscosity is relatively unimportant, once edge wave growth is initiated. In their analysis, the lowest order potential is described as the sum of the normally incident wave at frequency 2σ and the standing edge wave at the subharmonic frequency σ such that

$$\phi_0 = \phi_i + \phi_e \tag{4.8}$$

where

$$\begin{aligned} \phi_i &= \frac{a_i g}{2\sigma} J_0(\chi) \sin 2\sigma t, \qquad \chi^2 = \frac{4(2\sigma)^2 x}{gm} \\ \phi_e &= \frac{a_e g}{\sigma} e^{-\lambda x} \cos \lambda y \ \cos(\sigma t + \theta), \end{aligned} \tag{4.9}$$

where m is the beach slope and λ is the edge wave wavenumber. The variable θ is the phase difference between the incident and edge waves and a_i and a_e are the amplitudes of the water surface elevations of the lowest order incident and edge wave, respectively, at the still water shoreline.

The theory by Guza and Bowen (1976) predicts that the frequency band within which edge waves will grow for a given wavelength in the absence of viscosity is centered on $\sigma_0 = gm\lambda$, where the initial growth rate is maximum, and has the bandwidth

$$(1 - 0.0338\epsilon_i)\sigma_f \leq \sigma \leq (1 + 0.0338\epsilon_i)\sigma_f. \tag{4.10}$$

The parameter ϵ_i is a measure of the nonlinearity of the incident wave and is given by

$$\epsilon_i = \frac{a_i(2\sigma)^2}{gm^2}. \tag{4.11}$$

Perturbation analysis predicts the natural edge wave frequency σ_f as

$$\sigma_f = (1 + 0.055\epsilon_e^2)\sigma_0. \tag{4.12}$$

where

$$\epsilon_e = \frac{a_e \sigma^2}{gm^2}, \tag{4.13}$$

is a measure of the nonlinearity of the edge wave.

Their results further indicate an upper limit on the possible maximum edge wave amplitude for a given frequency σ due to the effects of radiation and detuning in the absence of viscosity. This upper limit is given by

$$\epsilon_e = 0.767\sqrt{\epsilon_i} \tag{4.14}$$

This edge wave amplitude occurs when the forced edge wave has frequency σ_f given by (4.12) as $(1 + 0.0324\epsilon_i)\sigma_0$, as stated by Rockliff (1978). The phase of the edge wave in relation to the incoming wave can also be determined. The maximum nondimensional edge wave amplitudes and the phase differences are given in Figure 4.6 as a function of a nondimensional detuning parameter Δ. The actual edge wave frequency is given by

$$\sigma = (1 + 0.0338\Delta\epsilon_i)\sigma_0. \tag{4.15}$$

The maximum response occurs at $\Delta = 0.96$.

Existing laboratory experiments (Bowen and Inman, 1971; Guza and Inman, 1975) confirm that edge wave amplitudes substantially larger than the incoming wave amplitude at the shoreline occur when the incoming wave is strongly reflected by the beach. However, the subharmonic resonance ceases when the wave breaks, which occurs at $\epsilon_i \cong 2$ (Guza and Inman, 1975).

The numerical solution method of the nonlinear shallow water equations described in Chapter 3 is expected to reproduce the theoretically predicted and experimentally observed phenomenon of the generation of subharmonic edge waves and their growth to finite amplitude. For a simulation, a beach slope of 0.1 is

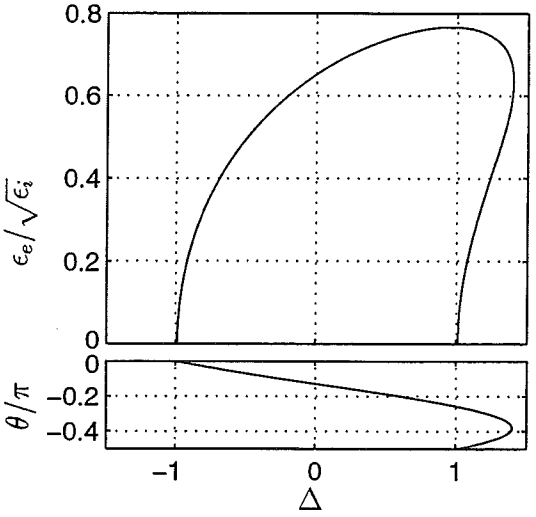

Figure 4.6: Equilibrium nondimensional amplitude of a subharmonic edge wave and its phase θ in relation to the incoming wave as a function of edge wave frequency detuning.

chosen, the longshore width L_y of the domain is chosen to be $(2\pi/\lambda)$, where λ is determined such that the natural frequency of a small amplitude edge wave is $\sigma_0 = 2\pi/20$ rad/sec. The amplitude of the incident wave is specified as $A = 0.01$ m at the offshore boundary located at $x = 100$ m. Since the lowest order water surface elevation of the incident wave is given by

$$\eta_i = a_i J_0(\chi) \cos 2\sigma t, \tag{4.16}$$

a_i can be determined to be 0.091 m. Furthermore, an initial perturbation at the subharmonic edge wave wavenumber is introduced by specifying the initial water surface elevation to be

$$\eta_e(x, y, 0) = a_e e^{-\lambda x} \cos \lambda y. \tag{4.17}$$

The initial amplitude $a_e = O(10^{-3})$ and $u = v = 0$ are also specified and the growth of the edge wave amplitude a_e is observed. Edge waves of different periods can be forced by varying the period of the incoming wave. The physical domain

is modeled using 64×32 collocation points with a time step of 0.003 s. An 8th order Shapiro filter is applied in both horizontal directions, the parameter α in (3.17) is specified as 0.001 and the depth threshold value at the shoreline d_{thresh} discussed in Section 3.3 is chosen as 1 mm. This value is found to be large enough to prevent the occurrence of a thin film that can be detected by visual inspection of the results.

Since a complete time series is not available at the still water shoreline as it becomes dry during the rundown period, time series at $x = 6$ m are used to determine the equilibrium amplitude of the edge wave. Figure 4.7 shows the theoretical maximum edge wave amplitude at $x = 6$ m as a function of the nondimensional detuning parameter Δ.

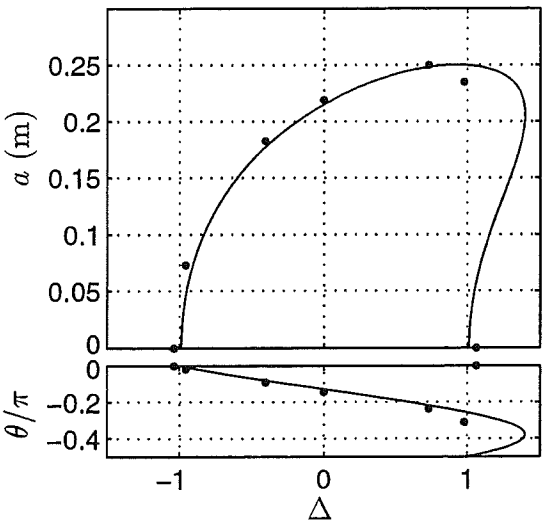

Figure 4.7: Equilibrium amplitude of a subharmonic edge wave at $x = 6$ m and its phase θ in relation to the incoming wave as a function of edge wave frequency detuning. Perturbation theory (——), present method (•).

Time series for edge waves corresponding to a number of Δ values ranging

from -1.06 to 1.04 have been simulated. Figure 4.8 shows time series for several Δ values recorded at $y = 0$ where maximum runup of the standing edge wave occurs. It can be observed that the equilibrium amplitude is reached most rapidly for $\Delta = 0$, corresponding to an edge wave at the linear natural period of $T_e = 20$ sec, where the initial growth rate of the instability is highest. It can be noted that the maximum amplitude is reached later for cases corresponding to higher $|\Delta|$ values. This is consistent with theory since the initial growth rates decrease with increasing $|\Delta|$. The instability ceases to exist altogether for $|\Delta| > 1$.

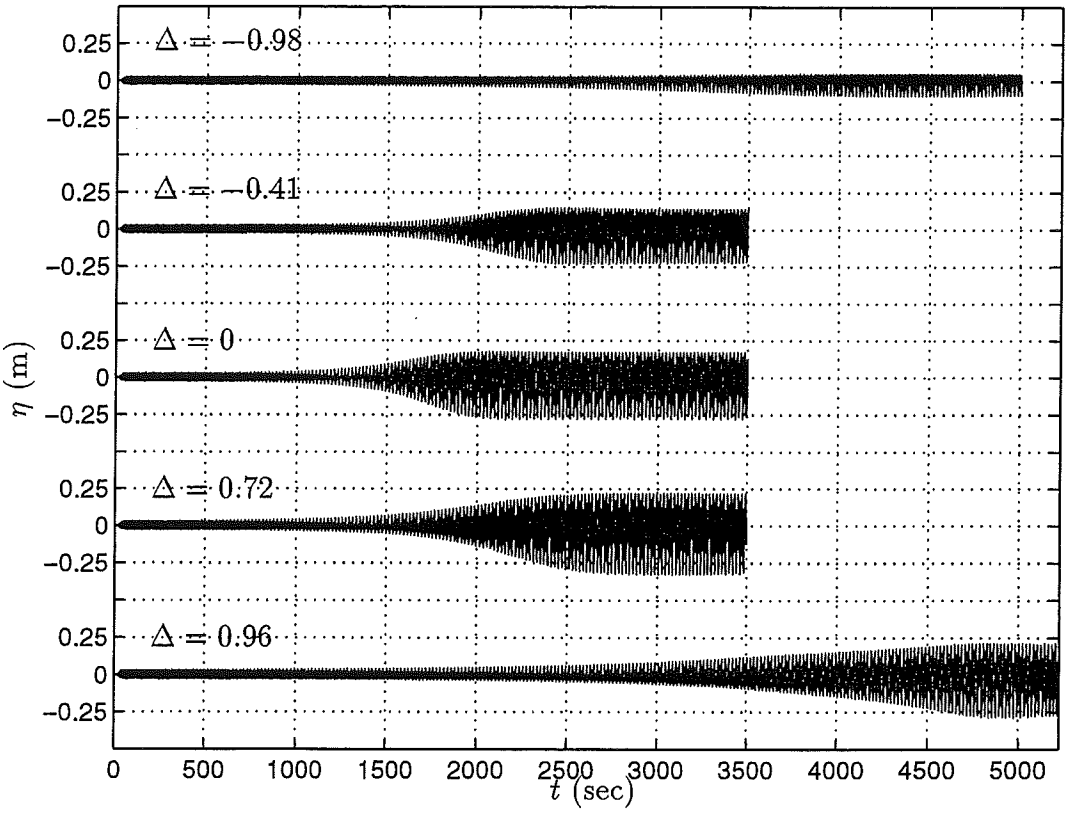

Figure 4.8: Water surface elevation η at $(x, y) = (6, 0)$ m for various Δ values

The computed maximum edge wave amplitude is found for comparison with theory by isolating the linear edge wave component at the frequency $f =$

$\sigma/2\pi$ by bandpassing the computed time series of the water surface elevation at $(x, y) = (6\text{m}, 0\text{m})$ using a bandwidth of 0.02 Hz. Furthermore, the phase relation between the bandpassed edge wave and the lowest order incident wave given in (4.16) can also be determined by observing the time lag between zero-upcrossings of the incident and edge wave.

Figure 4.7 also shows the nondimensional maximum edge wave amplitude for results from the present solution method for the cases seen in Figure 4.8 as well as two additional cases. It can be observed that the low and high frequency cut-offs of the unstable motion below and above which edge wave perturbations are stable are predicted. Also shown are the phase differences between the edge wave and the incoming wave predicted by theory and numerical computations. It is seen that the phase lag increases with increasing Δ.

4.4 Summary

In this chapter, the solution method for the shallow water equations is applied to several test cases concerning gravity wave motions. Two-dimensional shoreline runup is modeled using an Eulerian shoreline model in conjunction with a moving grid. This method compares favorably to analytical and numerical results for both one-dimensional and two-dimensional shoreline runup. An absorbing-generating boundary condition originally developed by Van Dongeren and Svendsen (1997) is used at the offshore boundary. It is shown that errors (in the form of partially reflected waves) remain small for a wide range of incident angles.

The developed method is used to predict the growth of subharmonic edge waves to finite amplitude. This application is physically representative of the complexity of motions in the surf and swash zones since onshore and longshore directed

motions coexist and interact to create a wave field with significant two-dimensional shoreline runup. It also constitutes a severe and physically relevant test of the method. Since high amplitude edge waves cause significant two-dimensional shoreline runup, an accurate shoreline treatment is important. Since the edge wave amplitudes are limited by the loss of energy to waves radiating offshore, the absorbing boundary condition is essential. Furthermore, since the maximum edge wave amplitude is reached at large time scales with respect to the periods involved, low dispersion and dissipation errors are desired.

The growth of subharmonic edge waves to finite amplitude is successfully simulated. The equilibrium edge wave amplitudes and phases are predicted with satisfactory agreement to weakly nonlinear theory. Neutral stability characteristics of the motion are also reproduced since a high frequency and low frequency cut-off are predicted and edge waves with frequencies beyond the unstable frequency band are observed to be stable. Since the predicted motion results from a physical instability of the basic state, the predicted low and high frequency cut-off points demonstrate that the method reproduces physical instabilities while remaining numerically stable.

It can be concluded that the developed numerical method is suitable for the further study of complex low frequency surf zone phenomena such as longshore and cross-shore directed currents, edge waves and shear instabilities of longshore currents and the nonlinear interactions between them. The next chapters will document the application of the solution method to vorticity motions.

Chapter 5

SHEAR INSTABILITIES OF THE LONGSHORE CURRENT ON A PLANE BEACH

In this chapter the solution method of the shallow water equations described in Chapter 3 and tested in Chapter 4 is utilized to study the nonlinear evolution of shear instabilities of the longshore current on a plane beach. The external forcing terms discussed in Chapter 2 are introduced into the shallow water equations to account for the effects of short wave forcing as well as damping due to bottom friction. Lateral momentum mixing due to turbulence or other mechanisms is neglected. We are purposefully choosing simple formulations for the bottom friction and forcing terms as well as the geometry of the case so that we can identify the resulting motions in the simplest possible mathematical setting.

The domain is chosen to be of finite length in the offshore direction and periodic in the longshore direction. The domain length in the longshore direction is chosen to be an integer multiple of the wavelength associated with the most unstable wavenumber. For a domain length equal to the most unstable wavelength, it is seen that for the chosen friction coefficient equilibrated finite amplitude longshore propagating disturbances with modulated amplitudes result. As the length of the domain in the longshore direction is increased the long term evolution of the disturbances is strongly dominated by subharmonic transitions that give flow structures that could be characterized as migrating rip currents. The nature of

the transitions is analyzed and conclusions about the natural longshore length scales of the motions are made.

5.1 Introduction

Observations by Oltman-Shay *et al.* (1989) were obtained for conditions where a shore-parallel bar formation was present in the surf zone. However, the instability theory by Bowen and Holman (1989) does not require the presence of such complicating bottom features. One of the simplest yet realistic beach geometries to which the instability mechanism applies is a plane beach. As a first step it seems appropriate to study the simpler case of a plane beach so that the characteristics of the resulting motions can be identified for simple geometry. Subsequent simulations for bottom bathymetries including complicating features such as bars can then be interpreted in light of the results for the simpler case. In this chapter we do not seek to simulate actual events as they occurred at SUPERDUCK or other experiments but deal with fictional, yet realistic, bottom and current profiles. The long time evolution of fully developed shear instabilities is studied in some detail. Comparisons are made to other studies incorporating the same or similar current and bottom profiles (e.g. Falqués and Iranzo, 1994; Allen *et al.*, 1996) to identify the effects of the different assumptions made in the various studies. The following issues will be addressed in this chapter.

In most finite amplitude shear instability studies carried out to date (see the review in Chapter 1), the steady setup resulting from short wave forcing in the cross-shore direction is neglected on the grounds that it only changes the mean water depth by less than 20% and has a minor effect on the linear instability properties of a given current profile. Once the steady setup is neglected by absorbing its effects into the water depth, the "rigid lid" assumption suggested by

Bowen and Holman (1989) and further justified by Falqués and Iranzo (1994) is invoked. One of the aims of this chapter is to identify the validity of both of these assumptions by comparing results from simulations that do or do not invoke the assumptions.

Most nonlinear instability studies (except Deigaard *et al.*, 1994, as discussed in the review in Chapter 1) preserve the spirit of a temporal stability analysis since an initial longshore current is generated and the temporal growth of instabilities that are harmonic in the longshore direction is observed. Therefore, periodicity is implied in the longshore direction. The length of the domain in the longshore direction is, therefore, a factor in the outcome of the simulations. A concern that needs to be addressed is then: How long does the domain have to be in the longshore direction so that sufficient number of waves are included in the domain yielding reliable estimates of the natural length scales of the motions?

Once the role of the above simplifying assumptions is identified the nature of the resulting motions can be analyzed in more detail. We will identify the effects of nonlinearity on the propagation speeds of the disturbances and the nonlinear interactions of individual alongshore propagating features. The analysis methods that we find useful in the interpretation of the results will be applied to the simulation of the SUPERDUCK experiment in the next chapter.

5.2 Model Formulation

The continuity and momentum equations governing the evolution of the short wave-averaged motions in the surf zone were shown earlier. They are in the form of the shallow water equations. In this chapter additional terms are introduced to include the effects of forcing due to incident short waves and damping

in the form of bottom friction. The governing equations are given by

$$\begin{aligned}
&\frac{\partial \eta}{\partial t} + \frac{\partial}{\partial x}[ud] + \frac{\partial}{\partial y}[vd] = 0, \\
&\frac{\partial u}{\partial t} + u\frac{\partial u}{\partial x} + v\frac{\partial u}{\partial y} = -g\frac{\partial \eta}{\partial x} + \tilde{\tau}_x - \tau_{bx}, \\
&\frac{\partial v}{\partial t} + u\frac{\partial v}{\partial x} + v\frac{\partial v}{\partial y} = -g\frac{\partial \eta}{\partial y} + \tilde{\tau}_y - \tau_{by}.
\end{aligned} \tag{5.1}$$

Here, η is the water surface elevation above the still water level, h is the water depth, u and v are the velocity components in the x and y directions, respectively, where x points offshore and y points in the longshore direction. The parameters τ_{bx} and τ_{by} represent the effects of bottom friction in the x and y directions, respectively. Furthermore, $\tilde{\tau}_x$ and $\tilde{\tau}_y$ represent the effect of short wave forcing in both horizontal directions.

In order to simulate growth of shear instabilities to finite amplitude, a plane beach geometry with a slope of $m = 0.05$ is chosen. This bottom slope is similar to an average slope of the bathymetry at SUPERDUCK.

The bottom friction is modeled using a linear representation (see Chapter 2), such that τ_{bx} and τ_{by} are given by

$$\tau_{bx} = \frac{\mu}{d}u, \qquad \tau_{by} = \frac{\mu}{d}v, \tag{5.2}$$

where

$$\mu = \frac{2}{\pi}c_f u_0. \tag{5.3}$$

Here, c_f is a friction coefficient and u_0 is the horizontal orbital velocity of the short waves. For the simulations shown in this chapter, a fixed friction coefficient μ of 0.006 m/s is used. This value was chosen in light of results by Dodd *et al.* (1992) and Allen *et al.* (1996) and represents the correct order of magnitude of friction present on natural beaches.

5.2.1 Short Wave Forcing

As reviewed in Chapter 2, the short wave forcing terms $\tilde{\tau}_x$ and $\tilde{\tau}_y$ can be modeled utilizing the radiation stress formulation by Longuet-Higgins and Stewart (1964) as

$$\begin{aligned} \tilde{\tau}_x &= -\frac{1}{\rho d}\left(\frac{\partial S_{xx}}{\partial x}+\frac{\partial S_{xy}}{\partial y}\right), \\ \tilde{\tau}_y &= -\frac{1}{\rho d}\left(\frac{\partial S_{xy}}{\partial x}+\frac{\partial S_{yy}}{\partial y}\right), \end{aligned} \tag{5.4}$$

where the radiation stress components S_{xx}, S_{xy} and S_{yy} can be computed from linear water wave theory.

Since a plane beach geometry is chosen, a stationary offshore wave field will exhibit no longshore variations and the y derivatives in the definitions of the radiation stresses will vanish. The forcing terms can then be written as

$$\begin{aligned} \tilde{\tau}_x &= -\frac{1}{\rho d}\left(\frac{\partial S_{xx}}{\partial x}\right), \\ \tilde{\tau}_y &= -\frac{1}{\rho d}\left(\frac{\partial S_{xy}}{\partial x}\right). \end{aligned} \tag{5.5}$$

The transformation of a stationary long crested short wave field over straight-and-parallel contours can be modeled using the energy equation for the short wave motions, which, in the absence of any interaction of the short waves with the current field, reduces to

$$\frac{\partial E c_g \cos\theta}{\partial x} = \epsilon_b, \tag{5.6}$$

where ϵ_b represents the energy dissipation due to breaking. Furthermore, the refraction of the short wave field over straight-and-parallel contours is described by Snell's law

$$\frac{\sin\theta}{\tilde{c}} = \text{const} = \frac{\sin\theta_0}{\tilde{c}_0} \tag{5.7}$$

where the subscripts 0 denote offshore values.

Using (5.6) and (5.7) in the definition of the forcing terms (5.5) simplifies the longshore forcing term to

$$\tilde{\tau}_y = -\frac{1}{\rho d}\frac{\sin\theta_0}{\tilde{c}_0}\epsilon_b. \tag{5.8}$$

The procedure to compute the steady longshore current and setup resulting from the short wave forcing generally involves choosing a model for the energy dissipation rate due to breaking ϵ_b and computing the wave height decay using (5.6). Given the variation of the wave height, the forcing terms $\tilde{\tau}_x$ and $\tilde{\tau}_y$ can be computed from (5.5). The steady momentum balance leading to the generation of a steady longshore current V and setup $\overline{\eta}$ was derived in Chapter 2. In the absence of any lateral mixing mechanisms in the surf zone, this balance is given by

$$g\frac{\partial\overline{\eta}}{\partial x} = \tilde{\tau}_x, \tag{5.9}$$

$$\frac{\mu}{d}V = \tilde{\tau}_y. \tag{5.10}$$

However, in this study we take an alternate approach by assuming that the short waves force a longshore current of the form

$$V(x) = Cx^2\exp\{-\left(\frac{x}{\alpha}\right)^3\}, \tag{5.11}$$

with the parameters C and α chosen such that a maximum current velocity of 1 m/s occurs at $x = 90$ m. This current profile along with a plane beach geometry has also been used by Allen *et al.* (1996); therefore, direct comparison of the two studies can be made. Such comparisons will aid in the evaluation of the importance of the rigid lid assumption, which is used in Allen *et al.*'s (1996) study but not in the present study.

The wave height decay that can result in the current profile given by (5.11) can be back-calculated if the peak frequency and offshore angle of incidence of the short waves are assumed. Using (5.8) in (5.10) the necessary dissipation rate of the short waves can be determined. Solving the energy equation for the short waves (5.6) results in the specification of the wave height decay. Given the spatial variation of the wave height, the short wave forcing in the x direction can be computed from (5.5). The steady setup associated with the current profile described by (5.11) can then be determined from (5.9).

The water depth h, the current profile given by (5.11) as well as the wave height decay and setup for an assumed peak frequency of 0.13 Hz and a mean direction of 20° at 18 m water depth are shown in Figure 5.1. The linear instability of the chosen current profile for the given bathymetry is computed using the solution by Putrevu and Svendsen (1992) for the friction coefficient of $\mu = 0.006$ m/s. The results for the growth rate σ_{im} and frequency σ_{re} are shown in Figure 5.2. The system is seen to be unstable for a range of wavenumbers. The largest growth rate occurs at $\lambda_{max} \approx 0.014$ rad/m and corresponds to a length scale of 450 m.

5.2.2 Modeling domain and solution method

The domain in which the governing equations (5.1) are solved is bounded by a curvilinear moving shoreline at $x = \zeta(y,t)$ and by an open boundary at $x = L_x$. Periodicity is assumed in the y direction. The offshore boundary is placed at $L_x = 360$ m. The width of the domain in the longshore direction is set such that

$$L_y = \mathrm{ND} \times \left(\frac{2\pi}{\lambda_{max}}\right), \tag{5.12}$$

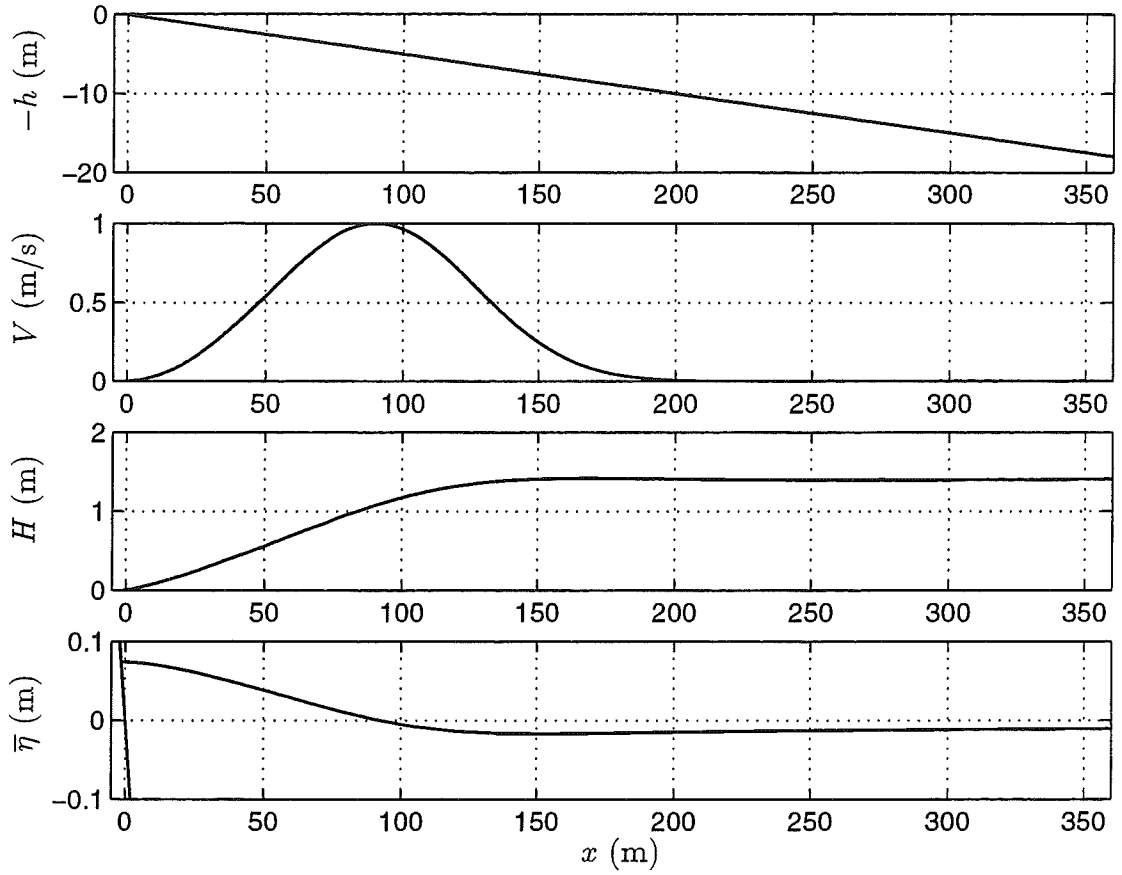

Figure 5.1: (a) Bathymetry for $m = 0.05$, (b) longshore current profile, (c) wave height decay and (d) setup for $\tilde{f}_p = 0.13$ Hz and $\theta_0 = 20$ °.

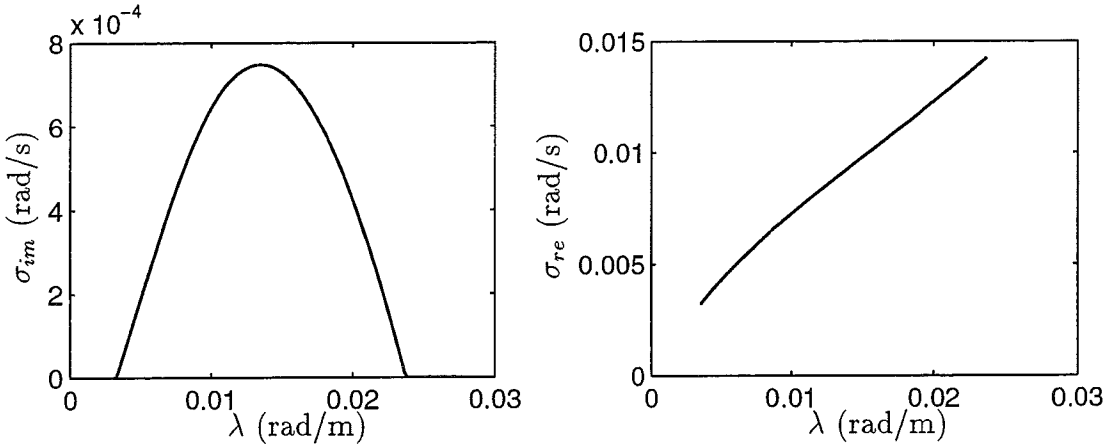

Figure 5.2: Linear instability results for the bottom and current profile shown in Figure 5.1.

where λ_{max} is the linearly most unstable wavenumber and ND is an integer. The wavelength associated with the most unstable wave is termed $L_{max} = (2\pi)/\lambda_{max}$. Due to the periodicity condition in the y direction, the choice of ND dictates the wavenumbers that can exist in the domain. For ND=1 only the most unstable wavenumber λ_{max} and its harmonics can exist in the domain. If ND=2 is used, waves with wavenumbers $\lambda_{max}/2$, $3\lambda_{max}/2$, $5\lambda_{max}/2, \ldots$ are also allowed to exist. Therefore, as ND is increased, the wavenumber spectrum is more densely populated with $\Delta\lambda = \lambda_{max}/\mathrm{ND}$, effectively simulating a continuous spectrum.

The initial condition for the model is obtained using the linear solution by Putrevu and Svendsen (1992) for the most unstable wavenumber λ_{max}, yielding the spatial variation of the perturbation velocities u_l and v_l. The initial velocities and water surface elevation are then prescribed as follows.

$$\begin{aligned} u(x,y,0) &= \epsilon u_l(x,y) \\ v(x,y,0) &= V(x) + \epsilon v_l(x,y) \end{aligned}$$

$$\eta(x,y,0) \;=\; \overline{\eta}(x), \tag{5.13}$$

where ϵ is of $O(10^{-3})$, and u_l and v_l are given by the linear instability solution of Putrevu and Svendsen (1992). The convective acceleration terms in the governing equations can transfer energy to higher harmonics. To facilitate the possible energy transfer to lower harmonics in cases where ND>1, the longshore velocity is further perturbed at all lower harmonics so that

$$v(x,y,t=0) = V(x) + \epsilon v_l(x,y) + \epsilon' \sum_{j=1}^{\mathrm{ND}-1} \cos\left(\frac{2\pi j y}{L_y}\right) \tag{5.14}$$

where $\epsilon' = 1\times10^{-3}$. Here, ND is the number of times the most unstable wavelength fits into the modeling domain. It should be noted that this initial condition can preferentially excite motions at the most unstable wavenumber since the spatial distribution of linear solution is specified only at that wavenumber. The subharmonic wavenumbers are excited with a cosine variation in y and no variation in x. Effects of using different initial conditions will be analyzed in Sections 5.3 and 5.4.

The solution is performed utilizing 32×ND equally spaced collocation points in the y direction ensuring a resolution of 32 collocation points per most unstable wavelength. In the x direction 32 unequally spaced collocation points are used. The distribution of the collocation points in the x direction was stated in Section 3.1. Computations were carried out with a time step of 0.1 sec. A 16th order Shapiro (1970) filter is used to avoid the excitation of waves at the limit of resolution. The filtering technique was discussed in Chapter 3.

Information about the longshore scale of the motion can be obtained by investigating the effect of the chosen domain width. This is achieved by successively increasing ND. In the following, time series at $(x,y) = (90\text{ m}, 0.5L_y)$, contour plots

of the vorticity

$$q = \frac{\partial v}{\partial x} - \frac{\partial u}{\partial y} \tag{5.15}$$

and plots of circulation patterns will be shown for ND=1, 2, 4, 8 and 16.

5.3 Results for $L_y = 1 \times (2\pi/\lambda_{max})$: Effects of Shoreline Runup

Time series of u, v and η at $x = 90$ m and $y = 0.5L_y$ given in Figure 5.3 show that the initial perturbations in the most unstable mode grow to finite amplitude and form a final steady wave of modulated amplitude. It can be seen that the initial perturbations in u grow to a maximum amplitude of about 20% of the maximum longshore current. This is in agreement with observations in the field and in the laboratory. The perturbations in v grow to an amplitude of about 50% of the maximum longshore current. We can also see a shift in the mean longshore current at this location. The water surface elevation η also grows to a finite amplitude, however this amplitude is very small ($O(1$ cm$)$). The horizontal runup associated with the fluctuations is of order 10 cm. All three time series show that the waves with the highest amplitudes have larger periods, suggesting that the larger waves travel slower.

The rigid lid approximation involves neglecting the steady setup as well as the temporal variations of the surface elevation due to the shear instabilities. Neglecting the steady setup involves subtracting the equation for the steady balance (5.9) from the full equations (5.1) resulting in

$$\begin{aligned}
&\frac{\partial \eta}{\partial t} + \frac{\partial}{\partial x}[ud] + \frac{\partial}{\partial y}[vd] = 0 \\
&\frac{\partial u}{\partial t} + u\frac{\partial u}{\partial x} + v\frac{\partial u}{\partial y} = -g\frac{\partial \eta}{\partial x} - \frac{\mu}{d}u \\
&\frac{\partial v}{\partial t} + u\frac{\partial v}{\partial x} + v\frac{\partial v}{\partial y} = -g\frac{\partial \eta}{\partial y} + \tilde{\tau}_y - \frac{\mu}{d}v,
\end{aligned} \tag{5.16}$$

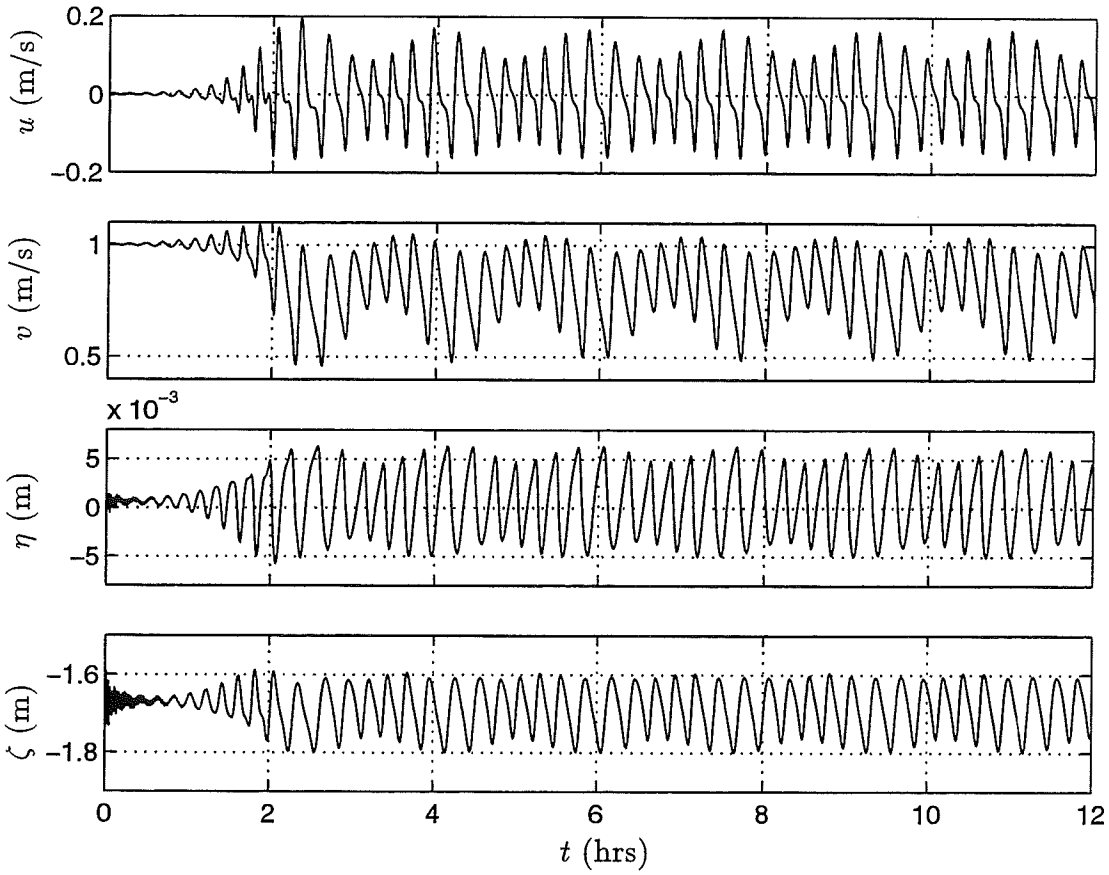

Figure 5.3: ND=1: Time series of u, v, η at $(x, y) = (90 \text{ m}, 0.5L_y)$ and ζ at $y = 0.5L_y$.

where η is now the water surface elevation with respect to the mean water level and $\tilde{\tau}_y = (\mu/d)V$ from (5.10). The contribution of the setup to the mean water level is also neglected so that h still describes a plane beach and $d = h + \eta$ is the total water depth excluding the steady setup.

Results from simulations carried out neglecting the steady setup but retaining the effects of shoreline runup due to the surface fluctuations associated with the shear instabilities are shown in Figure 5.4 in comparison to results from the full problem. Time series for the velocities show relatively minor differences, time series of η confirm that the total water surface elevation has decreased by the amount of the steady setup at this location. Shoreline runup due to the steady setup is not included anymore, however the fluctuations due to shear instabilities are of the same magnitude. Differences in the velocities and surface elevation are expected to be more pronounced near the shoreline. However, we can state that the general pattern of the flow is not altered by the exclusion of the steady setup.

Encouraged by the relatively minor effect of neglecting the steady setup, shoreline runup due to the fluctuations is also neglected by placing a wall boundary at a water depth of 0.01 m. A consequence of this assumption is that less computational time is required for the simulations. Comparison of time series of the velocities and water surface elevation from this simulation to simulations including shoreline runup due to the fluctuations agree within visual resolution (see Figure 5.5) at $x = 90$ m.

The effect of neglecting the steady setup is seen to be minor for this case. A more conclusive statement about the effect of the setup on the instability mechanisms can, however, not be made. Dalrymple and Lozano (1978) previously showed that, in addition to the solution consisting of a steady setup, neutrally stable solutions in the form of steady rip current circulation cells exist for normally

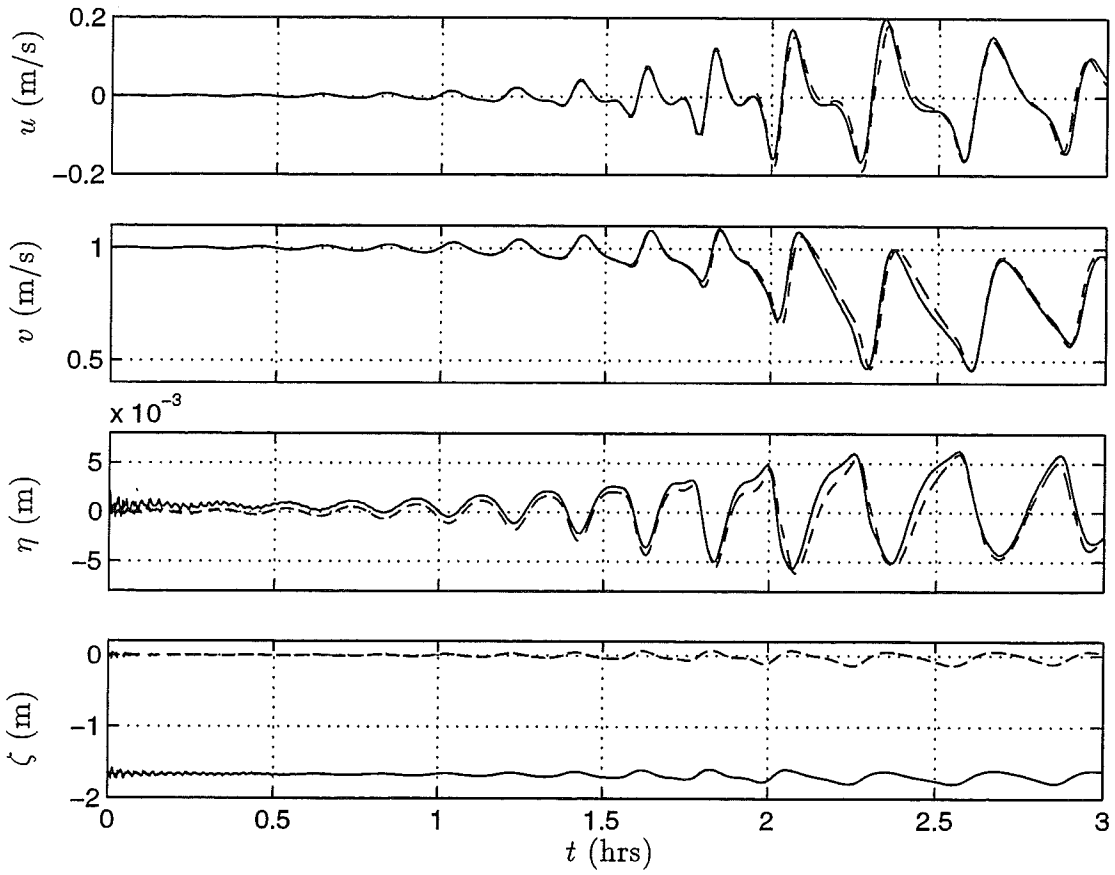

Figure 5.4: ND=1: Time series of u, v, η at $(x, y) = (90\text{ m}, 0.5L_y)$ and ζ at $y = 0.5L_y$. Steady setup included (——) and excluded (– –).

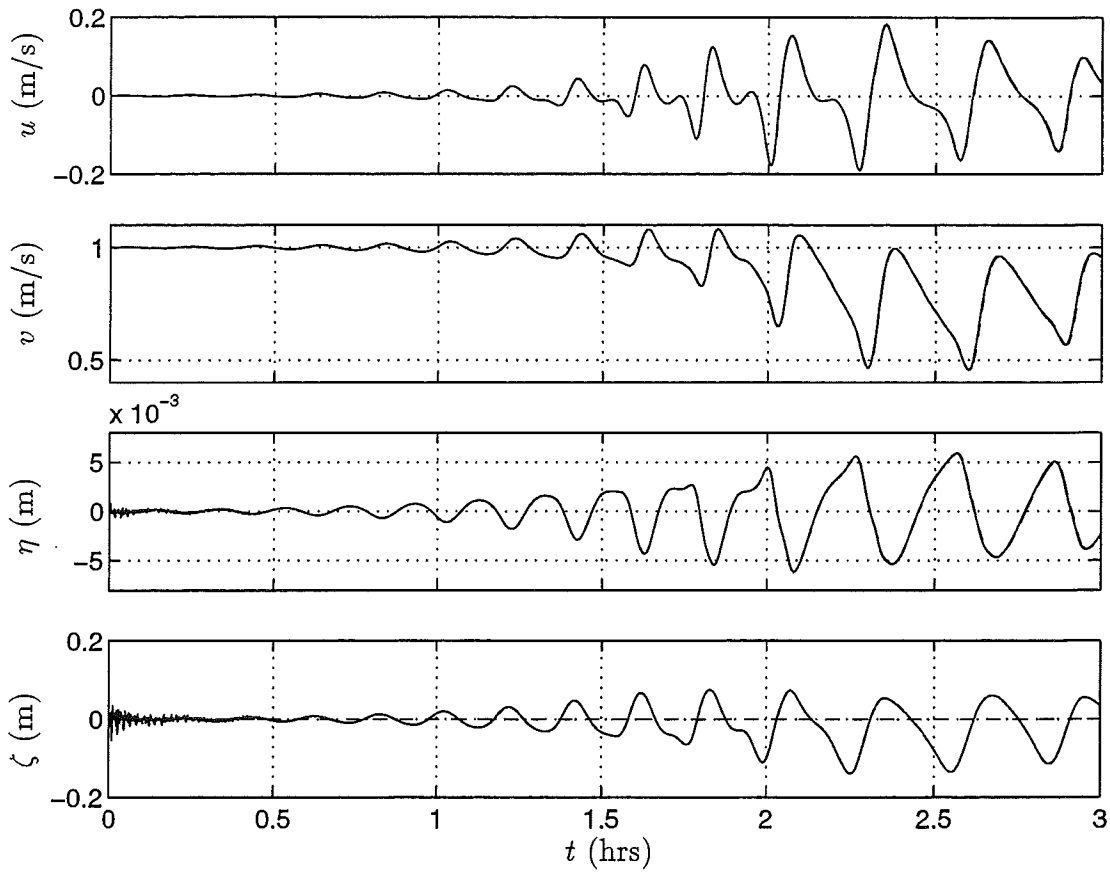

Figure 5.5: ND=1: Time series of u, v, η at $(x, y) = (90 \text{ m}, 0.5L_y)$ and ζ at $y = 0.5L_y$. Steady setup excluded but shoreline runup included (——) and excluded (– –).

incident waves over straight-and-parallel contours. Neutral or unstable solutions of this kind can exist on a plane beach. A detailed analysis of the stability characteristics of the wave induced setup or the interaction between the shear instabilities and the setup has to be conducted in order to draw more robust conclusions about the importance of setup in the problem at hand.

Based on the observation that the effect of shoreline runup due to the shear instabilities is small, simulations in the remainder of this dissertation will be carried out with a wall boundary at the shoreline. The steady setup will be neglected but the time dependent behavior of the surface fluctuations due to the shear instabilities will be included. The governing equations are given by (5.16).

Results for the velocity components can be compared to computations by Allen *et al.* (1996) who carried out simulations for the same velocity and current profiles for a range of values of the linear friction coefficient μ incorporating the rigid lid assumption. Results from Allen *et al.*'s (1996) study for the cross-shore velocities are shown in Figure 5.6. For μ=0.006, Allen *et al.* (1996) obtain finite amplitude shear instabilities with modulated amplitudes. The cross-shore velocities reach values up to 0.2 m/s. The modulation cycle is about 3 hrs long. The results from the present study display the same character but have a shorter modulational time scale.

To investigate this difference, simulations were carried out with an initial condition given by

$$\begin{aligned} u(x,y,0) &= 0, \\ v(x,y,0) &= V(x) + 0.001 \cos\left(\frac{2\pi y}{L_y}\right), \\ \eta(x,y,0) &= 0, \end{aligned} \tag{5.17}$$

and several different resolutions in the y direction. The results for the cross-shore

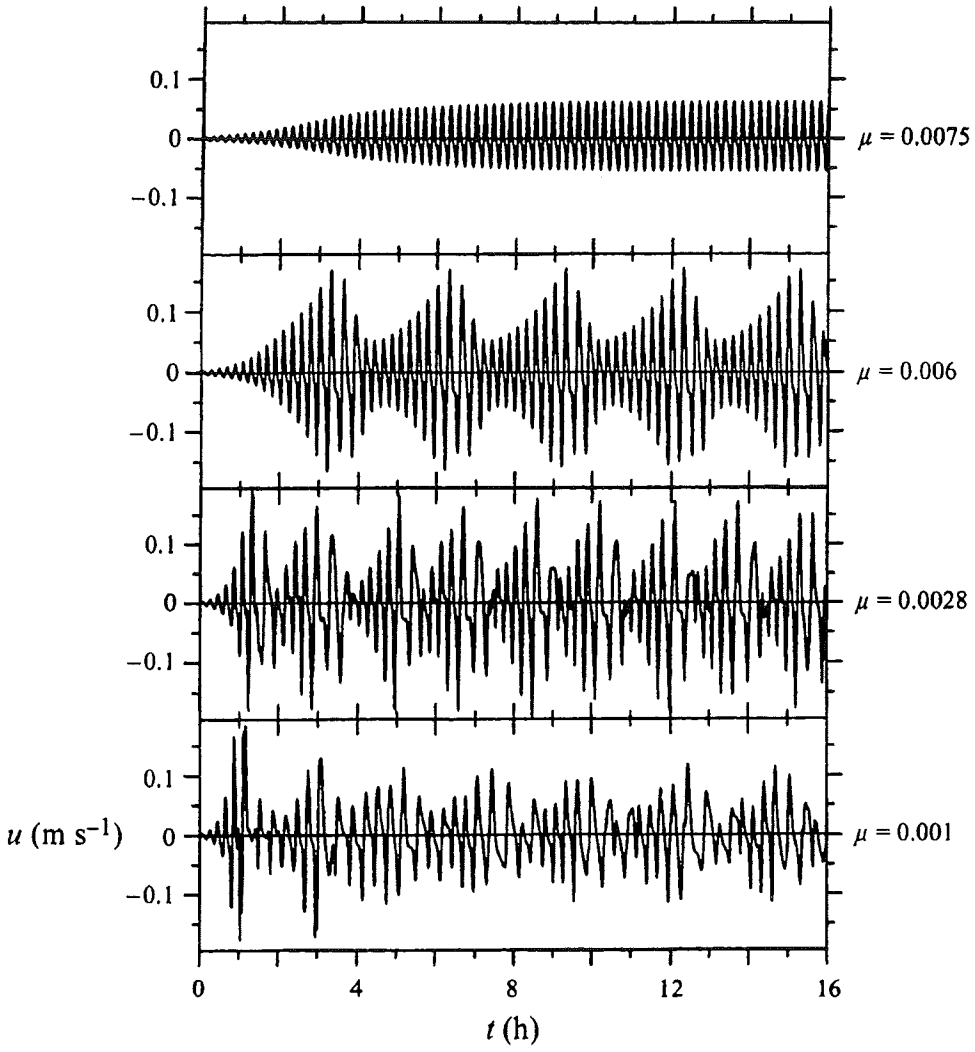

Figure 5.6: Time series of u at x=90 m from simulations by Allen *et al.* (1996) for several values of μ (from Allen *et al.*, 1996).

velocities are shown in Figure 5.7. Resolutions of 8, 16, 32 and 64 collocation points were used. Since a Fourier collocation method is used in the longshore direction, the number of collocation points in the domain corresponds to the number of harmonics of the most unstable wavenumber that are included in the computations. Figure 5.7 shows that the modulation cycles are about 3 hrs for NY=8 but are shorter when higher resolutions are used. Since the time scale of modulation is not altered for NY>32, 32 collocation points per most unstable wavelength is considered an appropriate resolution.

Comparison of Figure 5.7(c) and Figure 5.3 also gives insight into the effect of different initial conditions. It can be seen that the shear instabilities reach finite amplitude faster if the spatial distribution predicted by linear instability calculations is initially specified. However, once the instabilities reach finite amplitude they display the same behavior. The effect of specifying different initial conditions in computations with longer longshore domain widths is investigated in the next section.

We note that the behavior of the results obtained in this study corresponds closely to Allen *et al.*'s (1996) results for μ=0.006, obtained using the rigid lid assumption. In both studies, equilibrated motions with modulated amplitudes are predicted. The periods of the motions are observed to be larger during the large amplitude portion of the modulational cycle, suggesting that larger disturbances have lower propagation speeds. These results also qualitatively correspond to computations carried out by Falqués *et al.* (1994) for a similar current profile using the rigid lid assumption. In addition, computations in this study show that the surface elevation due to the instabilities η only reaches values of O(1 cm). It can be concluded that the rigid lid assumption is reasonable for this case.

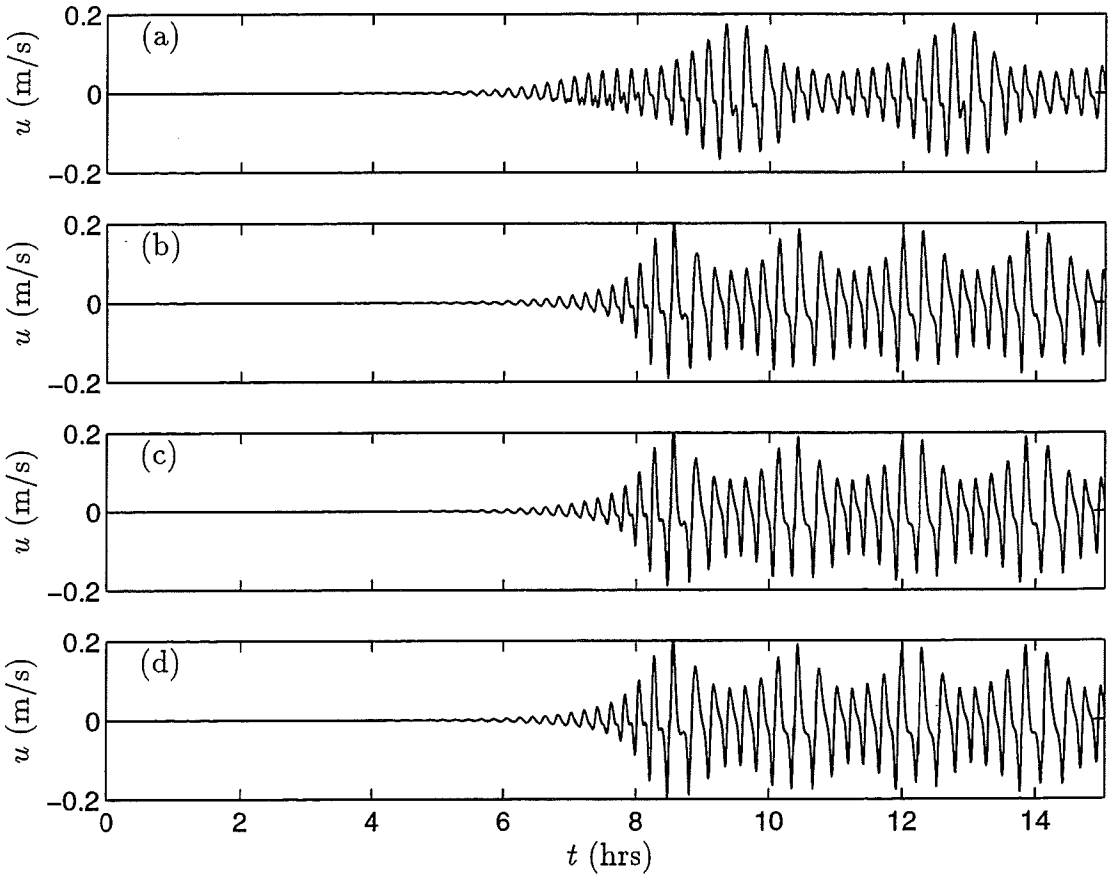

Figure 5.7: Time series of u at x=90 m for different resolution in the y direction (a) NY=8 (b) NY=16 (c) NY=32 (d) NY=64

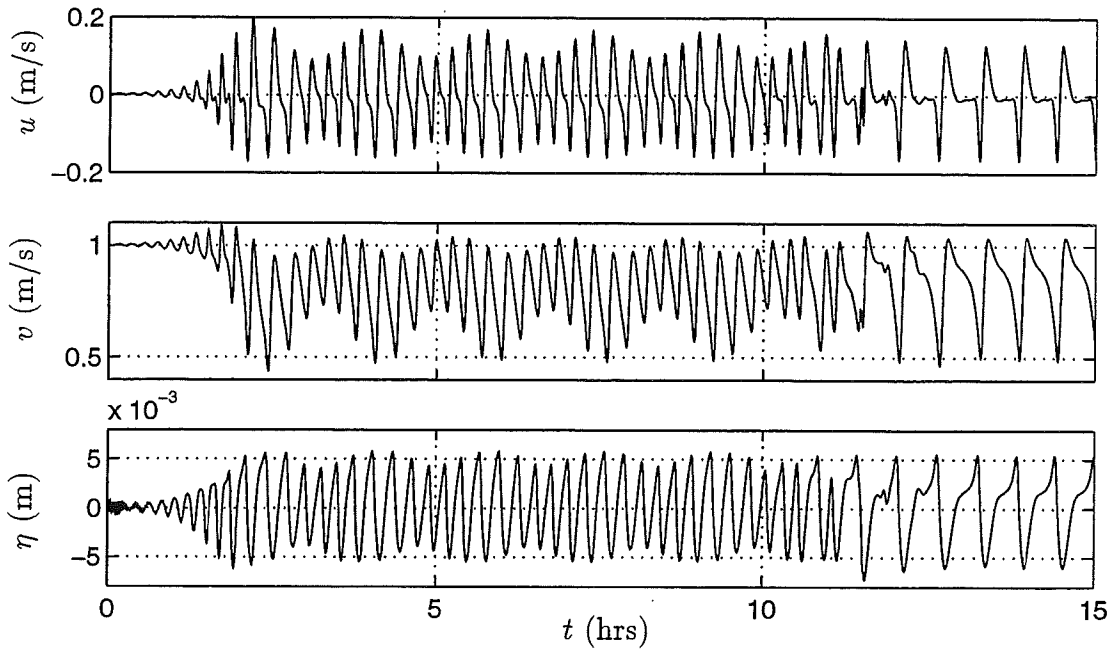

Figure 5.8: ND=2: Time series of u, v and η at $(x, y) = (90 \text{ m}, 0.5L_y)$.

5.4 Results for $L_y = 2 \times (2\pi/\lambda_{max})$: Effects of the Initial Condition and Variations in the Mean Current

In this case the domain is twice as wide as the length of the initially most unstable wave. Therefore, waves with wavenumbers $\lambda_{max}/2, \lambda_{max}, 3\lambda_{max}/2, 2\lambda_{max}, \ldots$ can exist in the domain. Time series of u, v and η given in Figure 5.8 show that the behavior is initially very similar to that of the previous case with ND=1. The amplitudes equilibrate and form a final steady wave of modulated amplitude.

The spatial structure of the flow can be observed utilizing snapshots of the flow pattern. Pseudocolor contour plots of the vorticity q before the instabilities are initiated and after they have reached finite amplitude are shown in Figure 5.9. Vector plots of the circulation pattern and streamlines for the same time levels

are depicted in Figures 5.10 and 5.11, respectively. Since the initial current profile has a region of positive gradient for $0 < x < 90$ m, the vorticity at $t = 0$ hrs is observed to be positive in that region. The initial velocity profile has a negative gradient for $90 < x < 200$ m where negative vorticity is observed. Further offshore the vorticity is zero. Therefore, the vorticity pattern at $t = 0$ hrs depicts a uniform flow in the y direction with the maximum flow occurring on the blue line between the regions of positive (pink) and negative (yellow and orange) vorticity. These observations are confirmed with the circulation plots and streamlines in Figures 5.10 and 5.11, respectively. At $t = 5.14$ hrs, the vorticity pattern has developed two regions of stronger negative vorticity, indicating clockwise rotation. The vorticity field is strongest at the locations where maximum curvature in the streamlines can be observed. The vorticity contours, the circulation patterns as well as the streamlines show that the flow has slowed down away from the regions of concentrated negative vorticity with a somewhat broader peak around $x = 100$ m. The offshore extend of the current has increased. The peak of the current profile (indicated by the blue line in Figure 5.9) undulates in the longshore direction. The current speeds up around the region of the strong negative vorticity. This is especially evident in Figure 5.11 since the streamlines are closer together at this location. The flow pattern has the nature of a meandering longshore current.

Contour plots of vorticity convey all the necessary information about the flow pattern with the most amount of detail. Therefore, vorticity plots will be shown in the remainder of the dissertation when snapshots of the flow field are analyzed. Circulation patterns or streamlines will be shown to clarify the nature of certain features in the flow.

Returning to the time series in Figure 5.8, it can be observed that the waves undergo a subharmonic transition after about five modulation cycles at $t \approx 11$

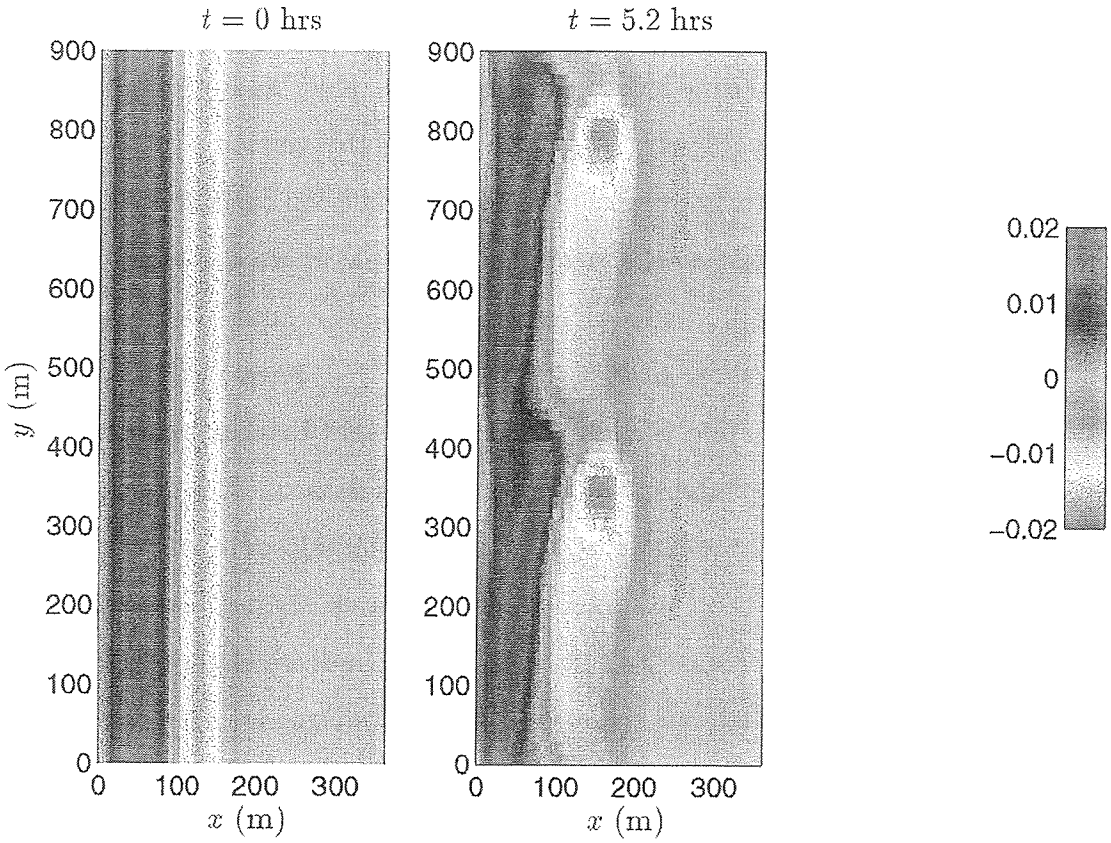

Figure 5.9: ND=2: Snapshots of contour plots of vorticity q (1/s)

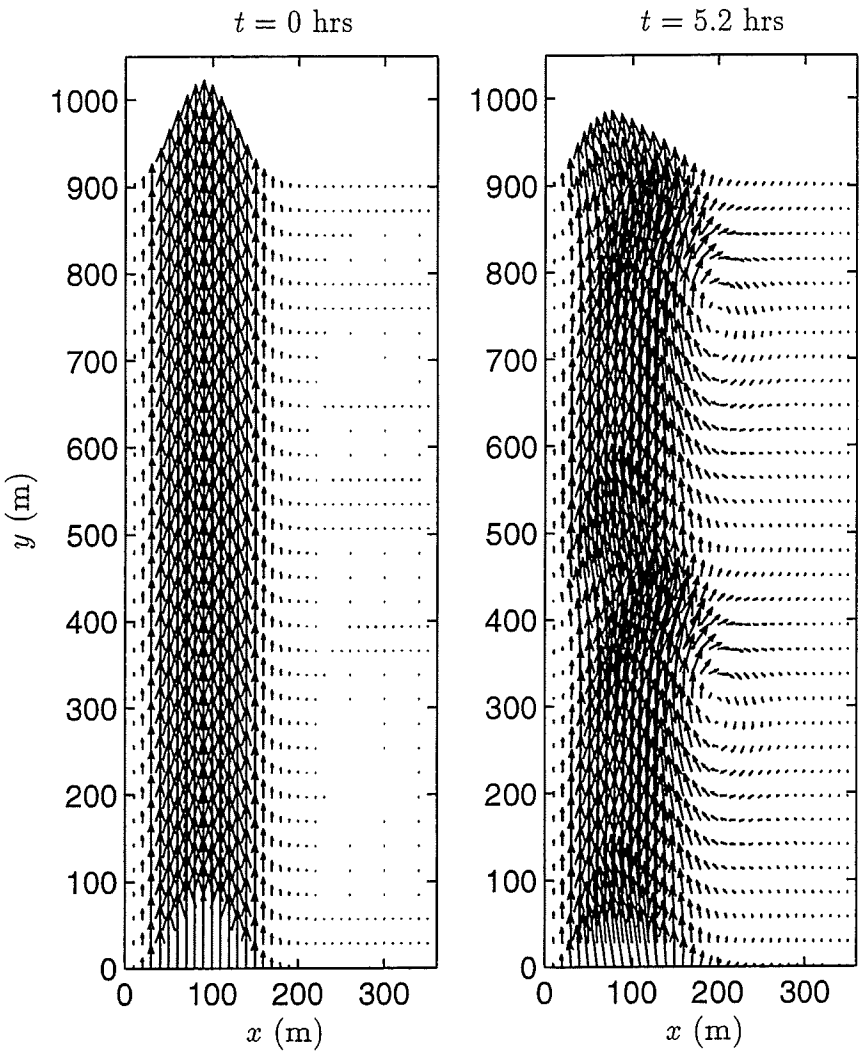

Figure 5.10: ND=2: Snapshots of vector plots of circulation

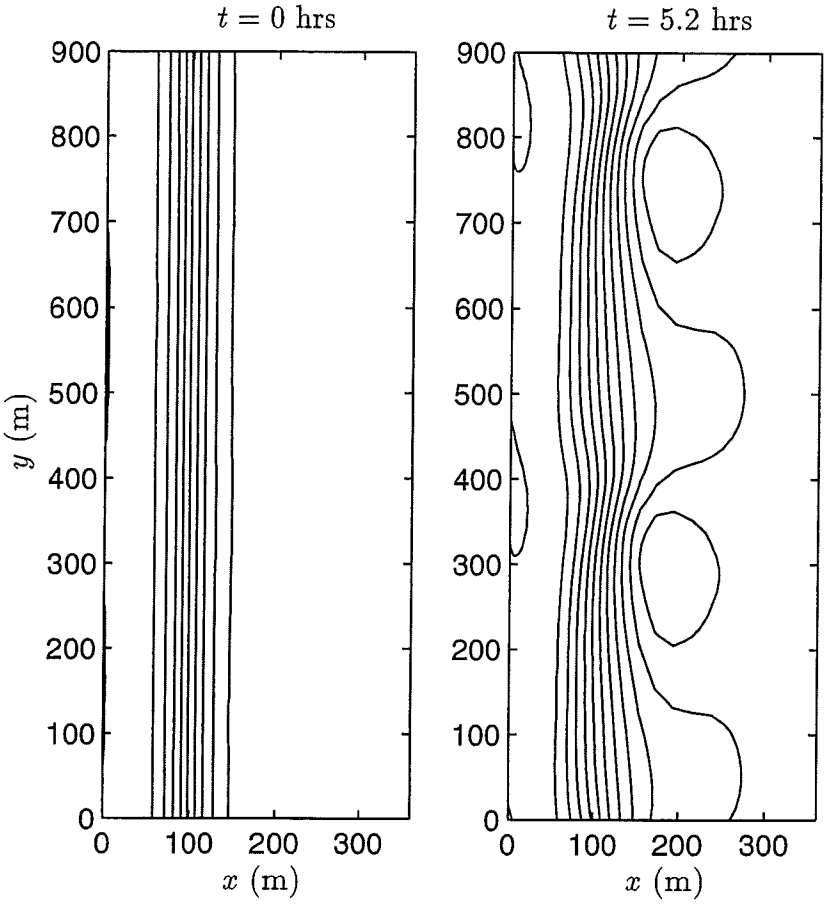

Figure 5.11: ND=2: Snapshots of streamlines

hrs and evolve into propagating disturbances with the wavenumber $\lambda_{max}/2$. The water surface elevation is again observed to be small and will not be shown for the simulations in the remainder of this chapter.

The subharmonic transition can be observed in the sequence of snapshots given in Figures 5.12 and 5.13. Figure 5.12 depicts pseudocolor contour plots of the vorticity, while streamlines are constructed and plotted in Figure 5.13. The disturbances in these plots are traveling in the $+y$ direction. It can be seen that once the disturbances reach finite amplitude one of the two disturbances develops a larger amplitude and consequently slows down. The smaller amplitude disturbance behind it catches up with the larger amplitude disturbance and merges with it, forming a circulation pattern with stronger offshore directed flow. We investigate this pairing process further in the next sections.

To investigate the effect of the chosen initial condition on the final flow pattern, a simulation with ND=2 is carried out with a different initial condition. The initial condition used is given by

$$v(x, y, t = 0) = V(x) + \frac{\epsilon}{\max\{f\}} f \tag{5.18}$$

where $\epsilon = 1 \times 10^{-4}$ and the function f is given by

$$f = \sum_{j=1}^{\mathrm{ND}} \cos\left(\frac{2\pi j y}{L_y} + 2\pi\phi_j\right). \tag{5.19}$$

where ϕ_j represents a random phase function between -1 and 1. The horizontal velocity u and the surface elevation η are specified to be zero initially. This initial condition ensures that the resulting longshore current is perturbed equally at the most unstable wavelength as well as all longer wavelengths that can exist in the modeling domain.

The time series of the velocities for this simulation (Figure 5.14) shows that, as before, the most unstable wavenumber grows first. However, the time needed

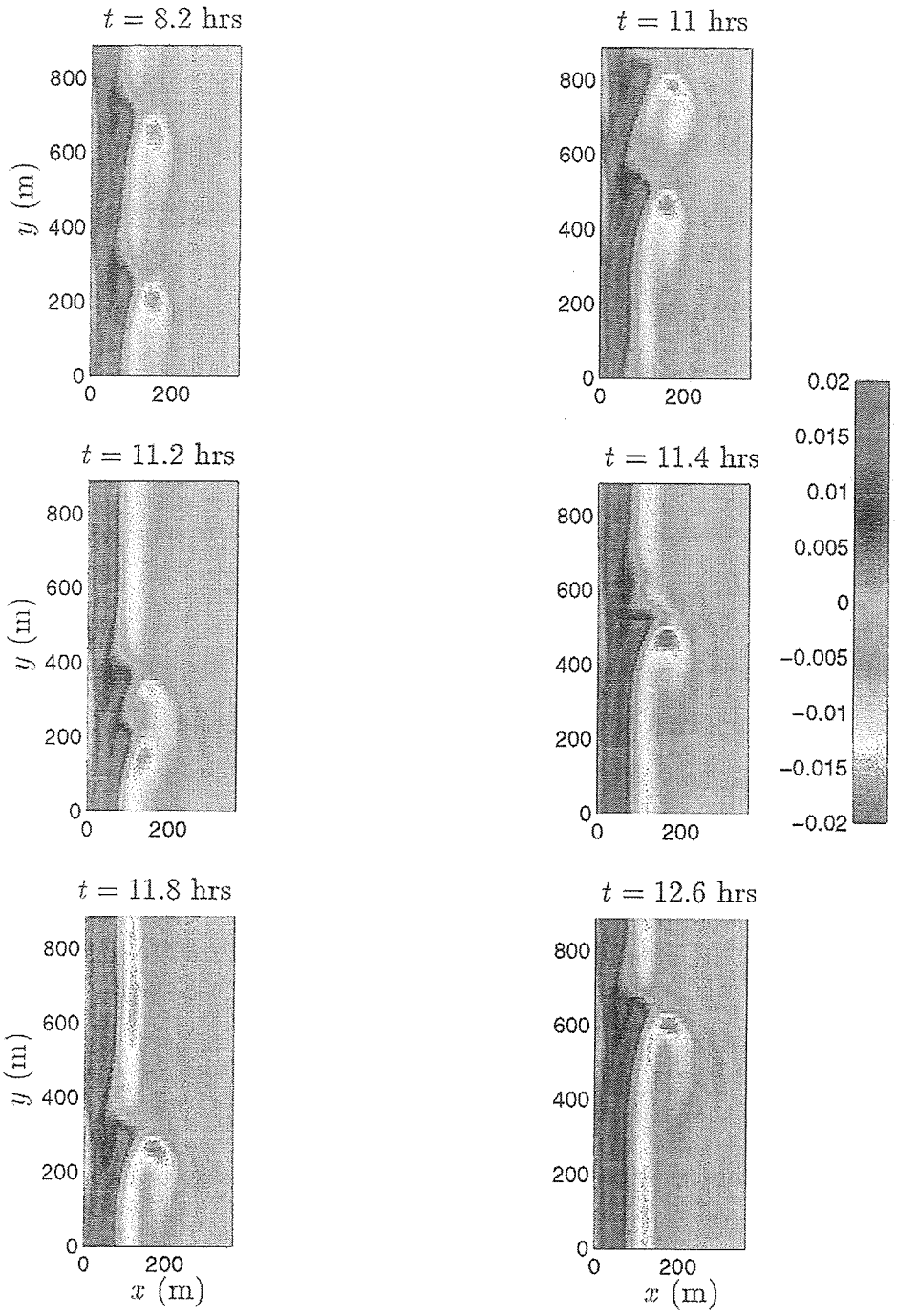

Figure 5.12: ND=2: Snapshots of contour plots of vorticity q (1/s)

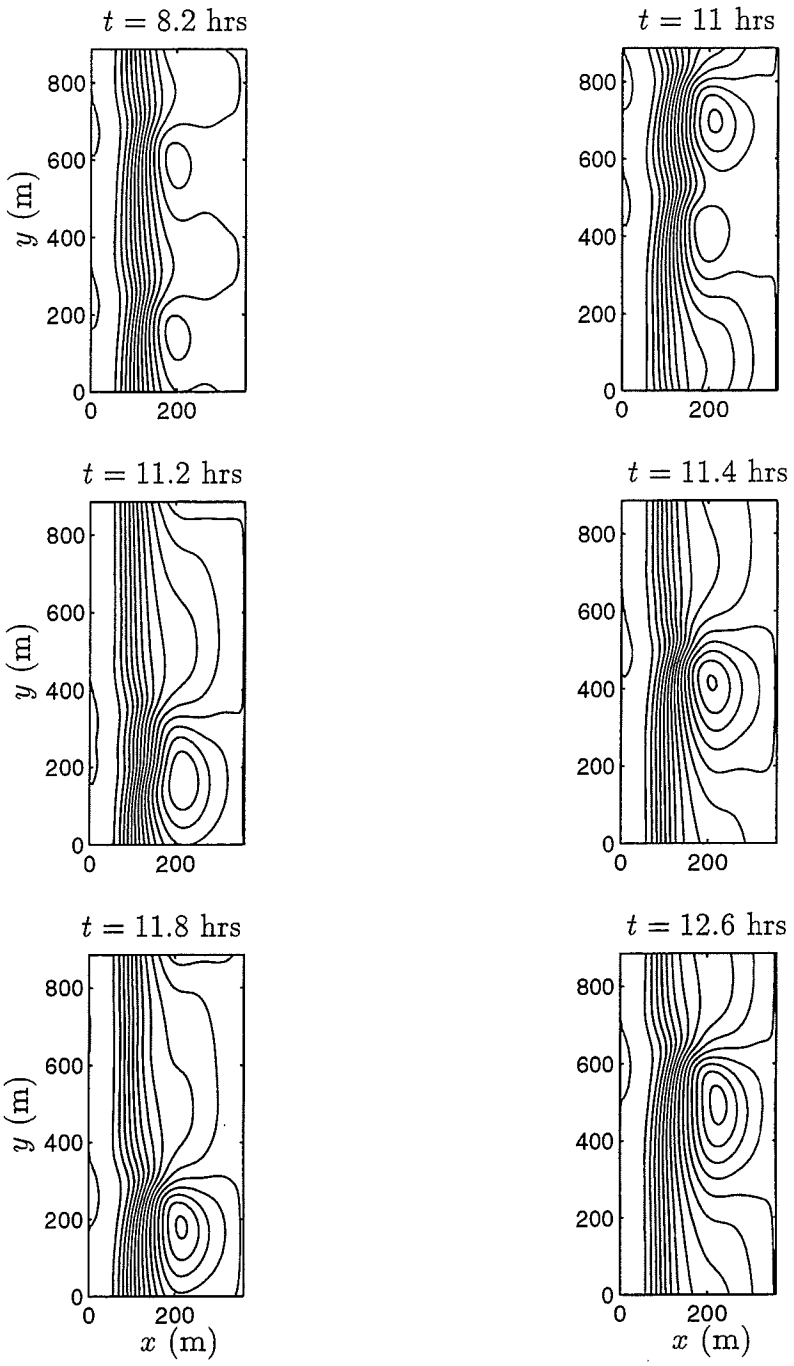

Figure 5.13: ND=2: Snapshots of streamlines

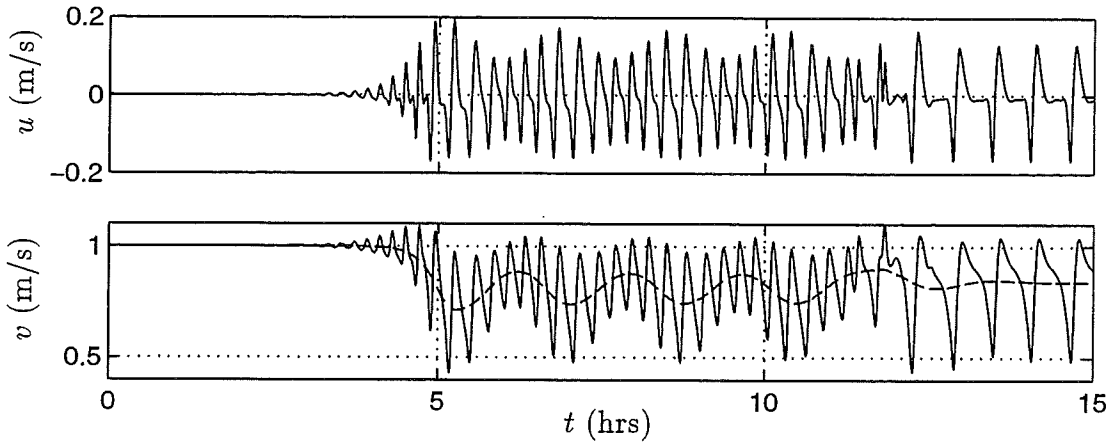

Figure 5.14: ND=2: Time series of u, v and $\langle v \rangle$ (– –) at $(x, y) = (90 \text{ m}, 0.5L_y)$. Alternate initial condition used.

for the instability to reach finite amplitude is longer. The subharmonic transition occurs after about 4 modulation cycles and, as before, at about $t = 11$ hrs. As before, the final flow pattern consists of one propagating disturbance. Results for this as well as other simulations with different initial conditions suggest that the initial condition only affects the initial growth of the instabilities but not the final flow pattern.

Figure 5.14 also depicts the longshore mean of the longshore velocity $\langle v \rangle$ defined as

$$\langle v \rangle(x,t) = \frac{1}{L_y} \int_0^{L_y} v(x,y,t)dy. \tag{5.20}$$

Due to the periodicity condition this quantity is a well-defined mean. Time series of $\langle v \rangle$ at $x = 90$ m are overlayed over the v time series at that location and confirm that the maximum mean longshore current is oscillating over the time scale of the modulational cycles and equilibrates at about 0.85 m/s. This indicates that the mean longshore current in the presence of the fluctuations has a lower maximum than the initial current V.

A plot of the initial as well as the final mean longshore current given in Figure 5.15(a) confirms that the final current has a lower maximum and a milder back shear suggesting that the velocities associated with the instabilities induce mixing to alter the current profile towards a more stable state. The lateral mixing caused by the shear instabilities can be quantified by examining the longshore-averaged longshore momentum equation given by

$$\langle\frac{\partial v}{\partial t}\rangle + \langle u\frac{\partial v}{\partial x}\rangle + \langle v\frac{\partial v}{\partial y}\rangle = -\langle g\frac{\partial \eta}{\partial y}\rangle - \langle\frac{\mu}{d}(v-V)\rangle. \tag{5.21}$$

The longshore average is defined as in (5.20). The resulting balance states that any change in the mean longshore current profile (last term) is balanced by a time variation of the mean current and a mixing term due to the fluctuating velocities (first and second terms, respectively). Note that the remaining terms involve y derivatives and, therefore, drop out of the mean balance. This balance is displayed in Figure 5.15(b). It can be seen that the changes in the mean current are mostly balanced by mixing induced by the instabilities.

Since the final profile shown in Figure 5.15(a) displays a lower peak and a milder shear, it is expected to be more stable. Results from linear instability calculations given in Figure 5.16 show that the final current profile displays a much weaker instability than the initial profile.

5.5 Results for $L_y = 4 \times (2\pi/\lambda_{max})$: Evolution of "Rips"

We continue to carry out simulations with successively longer longshore length scales. The initial condition given by (5.13) and (5.14) is once again adopted and the domain length is chosen to be four times as wide as the length of the initially most unstable wave. Figure 5.17 shows the growth of the initially most unstable wavenumber. The instabilities remain at a relatively low amplitude

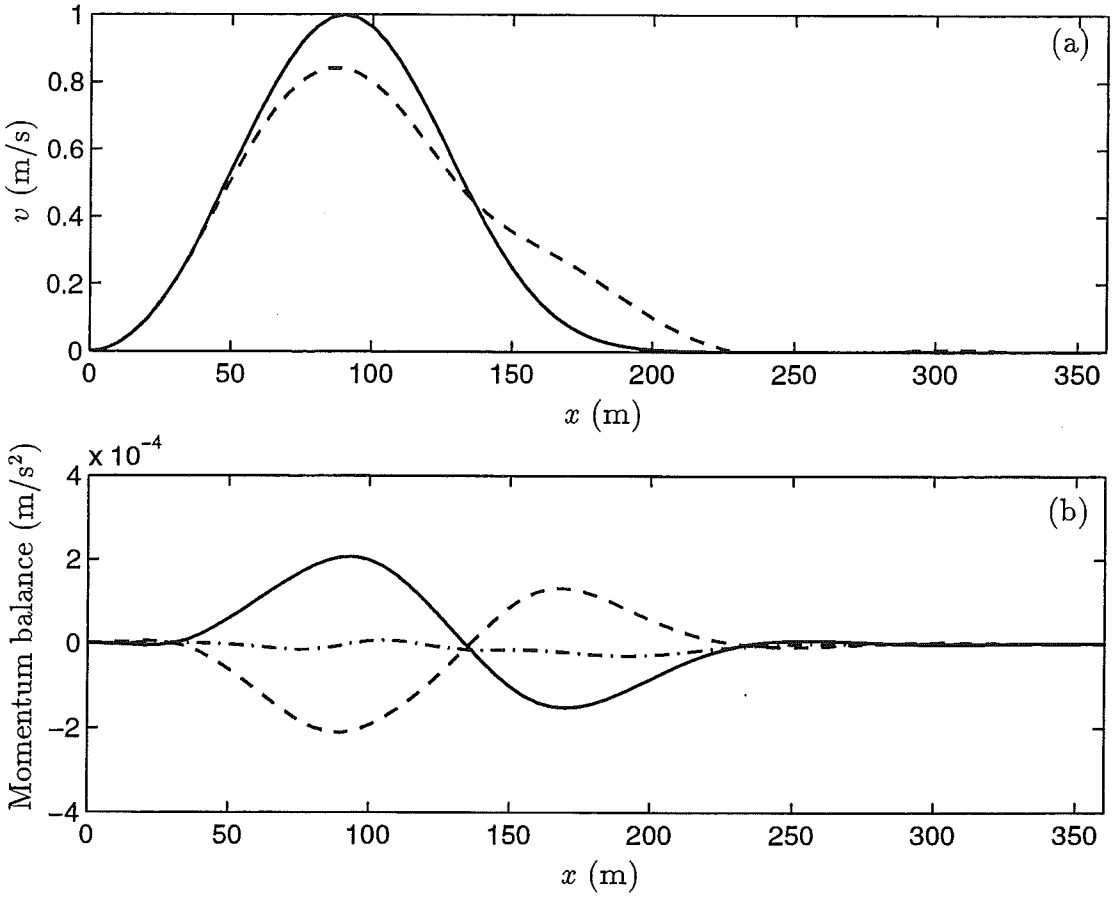

Figure 5.15: ND=2: (a) Initial (——) and final (– –) mean current profiles. (b) Longshore-averaged momentum balance. $\langle \partial v/\partial t \rangle$ (– · –), $\langle u(\partial v/\partial x) \rangle$ (– –), $\langle (\mu/d)(v - V) \rangle$ (——).

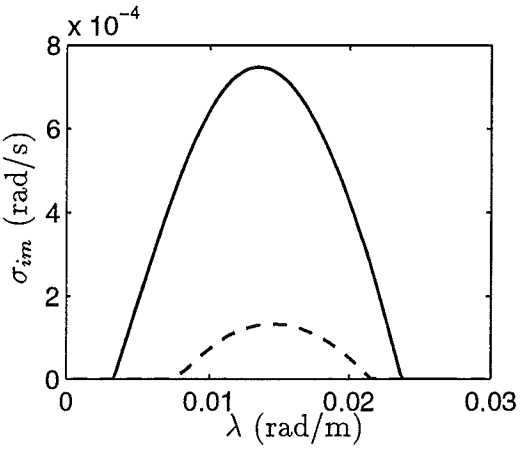

Figure 5.16: Linear instability results for the initial (——) and final (– –) current profiles shown in Figure 5.15(a).

for about 3 hrs. Then the amplitudes increase and we observe once again that waves with higher amplitudes have longer periods. In this case the subharmonic transition takes place earlier ($t \approx 5$ hrs). The resulting disturbance displays a wavenumber of $\lambda_{max}/4$.

The vorticity field at an early time in the simulation ($t = 3.3$ hrs) depicted in the left panel of Figure 5.18 displays a meandering nature. At $t = 7.4$ hrs we observe that one disturbance has gained strength and several weaker disturbances are trailing. The smaller disturbances have either dissipated or caught and merged with the larger disturbance by $t = 15$ hrs. In the next section, we find that the latter is true. The final disturbance propagates in the $+y$ direction and exhibits strong offshore directed velocities as is also confirmed by Figure 5.19. The flow structure is reminiscent of a migrating rip current since it extends offshore approximately 2-3 surf zone widths.

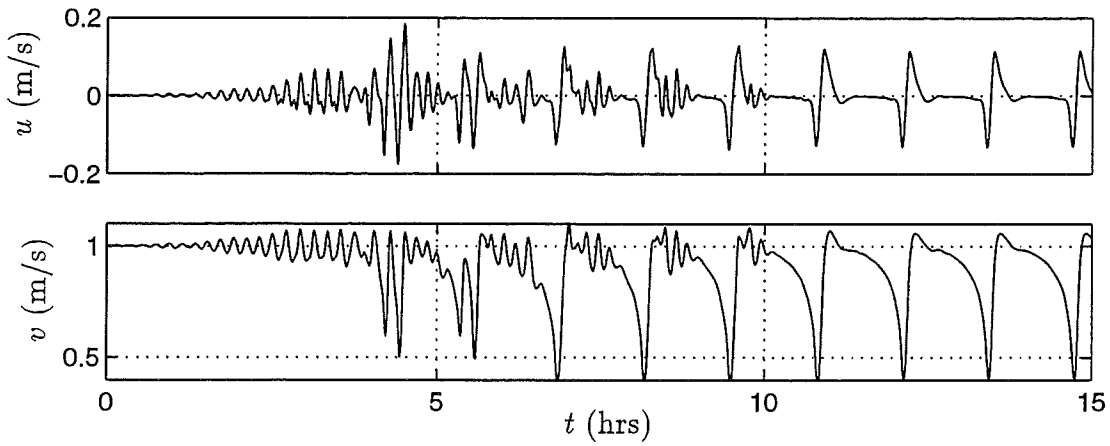

Figure 5.17: ND=4: Time series of u and v at $(x, y) = (90 \text{ m}, 0.5L_y)$.

5.6 Results for $L_y = 8 \times (2\pi/\lambda_{max})$: Vortex Pairing Mechanism

The pairing process is studied in more detail in simulations with a domain length of eight times the length of the initially most unstable wave. The time series of the velocity components (Figure 5.20) show evidence of subharmonic transitions at about 9 hrs.

Snapshots of the vorticity pattern shown in Figure 5.21 detail one pairing event. We follow two disturbances which are located at about $y = 1800$ m and $y = 2250$ m at $t = 7.8$ hrs. In 6 minutes ($t = 7.9$ hrs) the disturbances propagate in the y direction so that they are now located at $y = 2000$ m and $y = 2400$ m. The distance between them has decreased suggesting that the weaker second disturbance travels faster than the stronger first disturbance. Another 12 minutes ($t = 8.1$ hrs) bring the two fronts closer together, they are now located at $y = 2400$ m and $y = 2700$ m. In another 24 minutes they are observed to have merged and one strong disturbance is visible at $y = 3400$ m. At $t = 8.1$ hrs another pairing process is initiated since the distance between two fronts at $y = 900$ m and $y =$

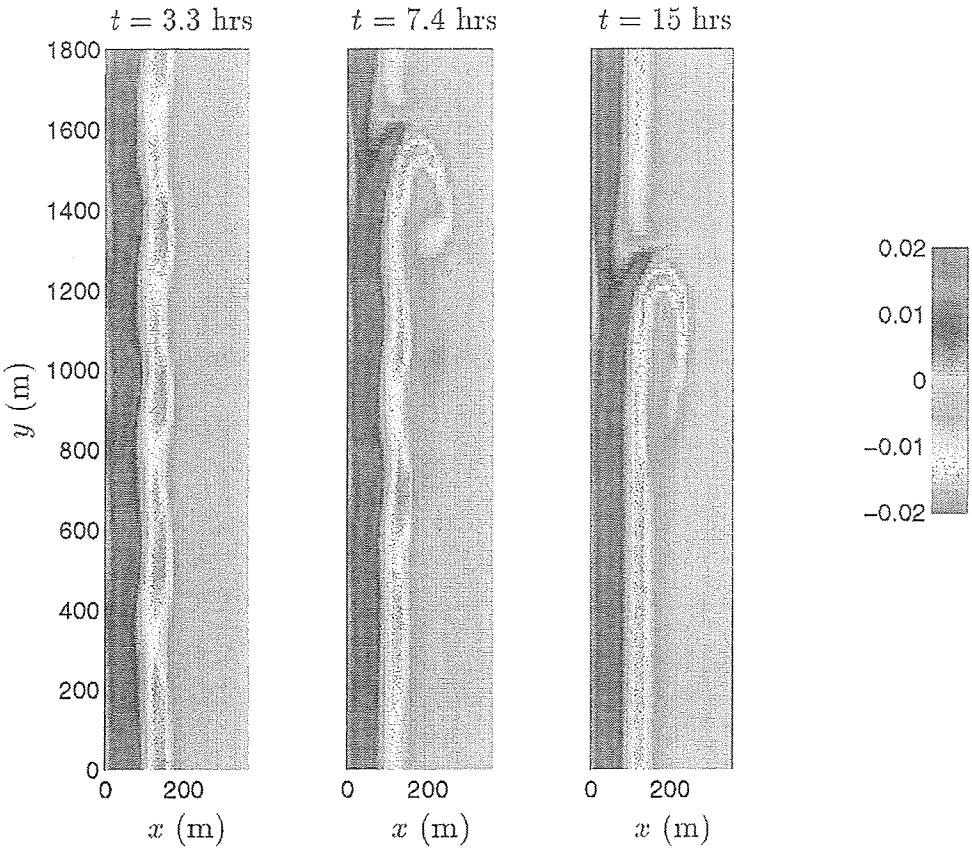

Figure 5.18: ND=4: Snapshots of contour plots of vorticity q (1/s)

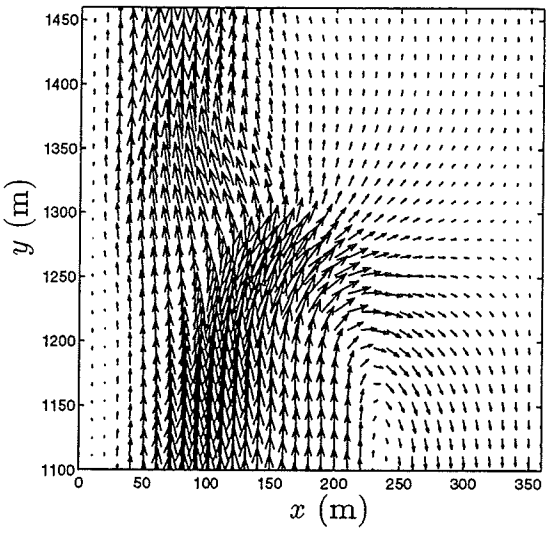

Figure 5.19: ND=4: Circulation pattern at $t = 15$ hrs.

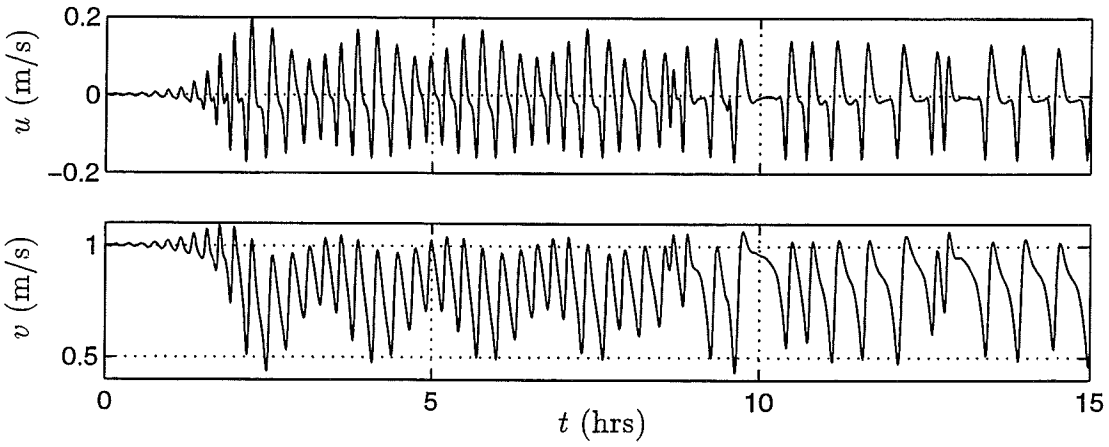

Figure 5.20: ND=8: Time series of u and v at $(x, y) = (90 \text{ m}, 0.5L_y)$.

1350 m decreases so that at $t = 8.5$ hrs they are located at $y = 1700$ m and $y = 2000$ m. The trailing disturbance can again be observed to be the weaker one.

The details of the vortex pairing process can best be observed when examining the time evolution of the vorticity q as a function of longshore distance and time at a chosen cross-shore location. In Figure 5.22 we show a contour plot of $q(x_0, y, t)$ where $x_0 = 90$ m. The blue and pink regions represent positive vorticity, the orange regions represent negative vorticity. The left panel of the figure shows the time series of $q(x_0, y_0, t)$ where $y_0 = 1940.6$ m. This y location is also marked on the contour plot with a thick line. The crests of the vorticity are observed to propagate in the $+y$ direction, the milder the slope of the resulting blue line the faster the propagation speed given by dy/dt.

At $t = 7.5$ hrs all 8 disturbances are observed to travel at the same speed of about 0.4 m/s. Around $t = 8$ hrs one of the disturbances is seen to speed up. The time series on the left panel confirms that the amplitude of the faster trailing wave is lower than the amplitude of the wave in front of it. The smaller disturbance eventually catches up with the disturbance in front of it and collides with it at about $y = 3000$ m. The resulting disturbance continues to propagate at the speed of the slower first wave. This pairing event was also observed in the snapshots of vorticity in Figure 5.21.

This type of pairing occurs again around $t = 8.75$ hrs and $y = 2500$ m. The time series in the left panel shows that the height difference between the two disturbances is larger than in the first merger since these two waves are at a later stage in the pairing process. The initial stages of this pairing process were observed in Figure 5.21.

The third pairing evident in Figure 5.22 occurs around $t = 9.25$ hrs. The

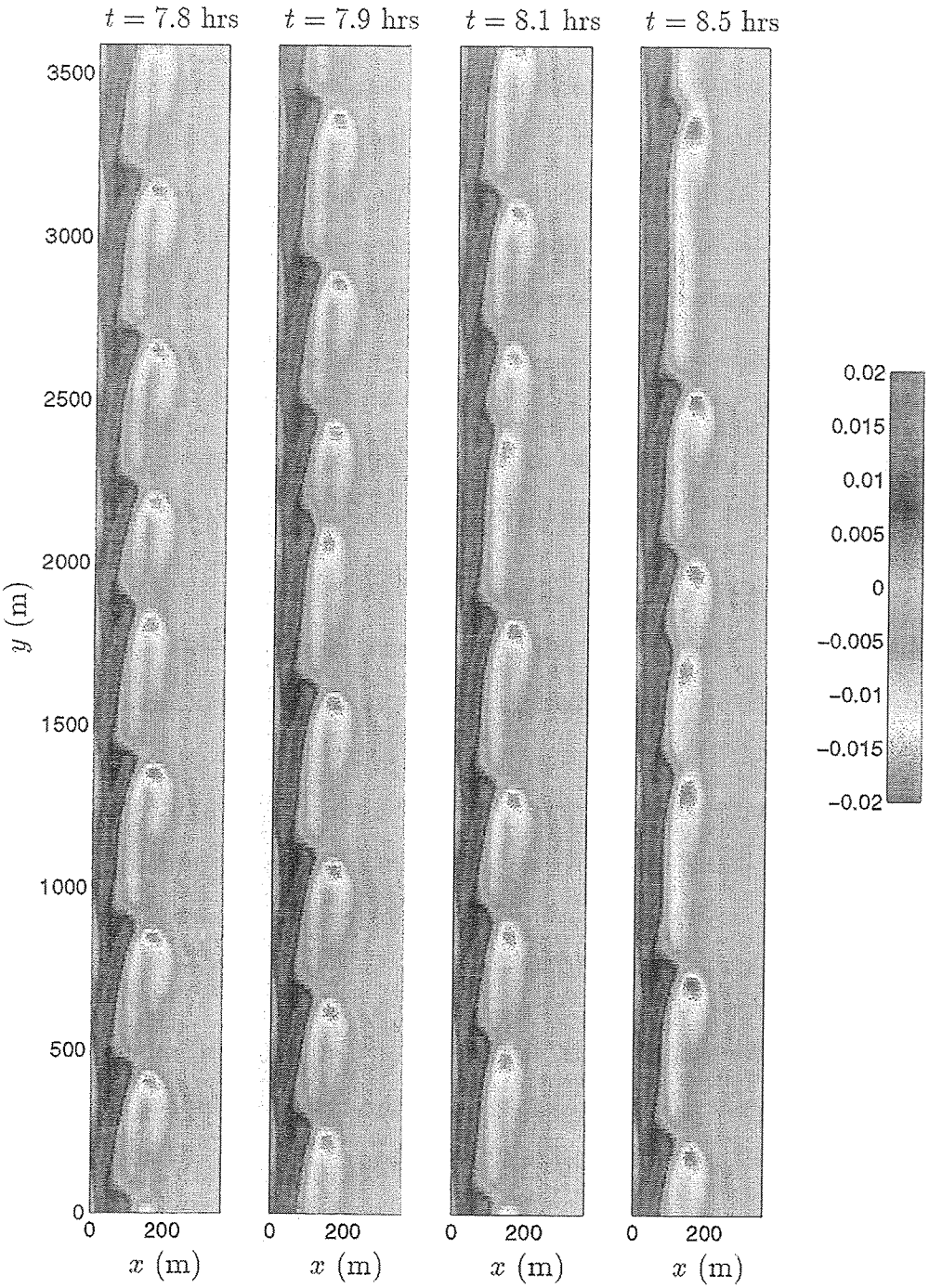

Figure 5.21: ND=8: Snapshots of vorticity q (1/s)

details of the process can best be observed in this case even though they are also evident in the previous events. It can be seen that as the faster trailing wave collides with the slower wave in front of it, it gains energy and slows down to the speed of the wave in front and propagates as the resulting front. The wave in the front, in turn, looses almost all of its amplitude but remains intact, continues to propagate at the higher speed of the initially trailing wave and propagates into a region of negative vorticity. This weakened wave can be seen in the time series on the left panel at $t = 9.5$ hrs as a small "blip" in the negative vorticity region. It dissipates before it reaches the next front of positive vorticity. We can conclude that the pairing occurs in the form of a collision where most of the energy is transferred to the trailing wave which subsequently travels at a slower speed. A small phase shift is also introduced at the time of the collision so that the lines representing the lower and higher speeds are slightly shifted. One final collision is initiated at the end of the time series reducing the number of propagating disturbances to four.

The vorticity field before and after the collisions is shown in Figure 5.23. More localized and stronger offshore flow structures result after the collisions. The resulting wavenumber is $\lambda_{max}/2$.

5.7 Results for $L_y = 16 \times (2\pi/\lambda_{max})$: Natural Length Scales

Simulations for a domain length that corresponds to 16 times the most unstable wavelength shows the same type of behavior as for ND=8 (see time series in Figure 5.24). Subharmonic transitions once again occur, the number of waves is reduced from the initial 16 to 8.

Contour plots of vorticity before and after the transitions (Figure 5.25)

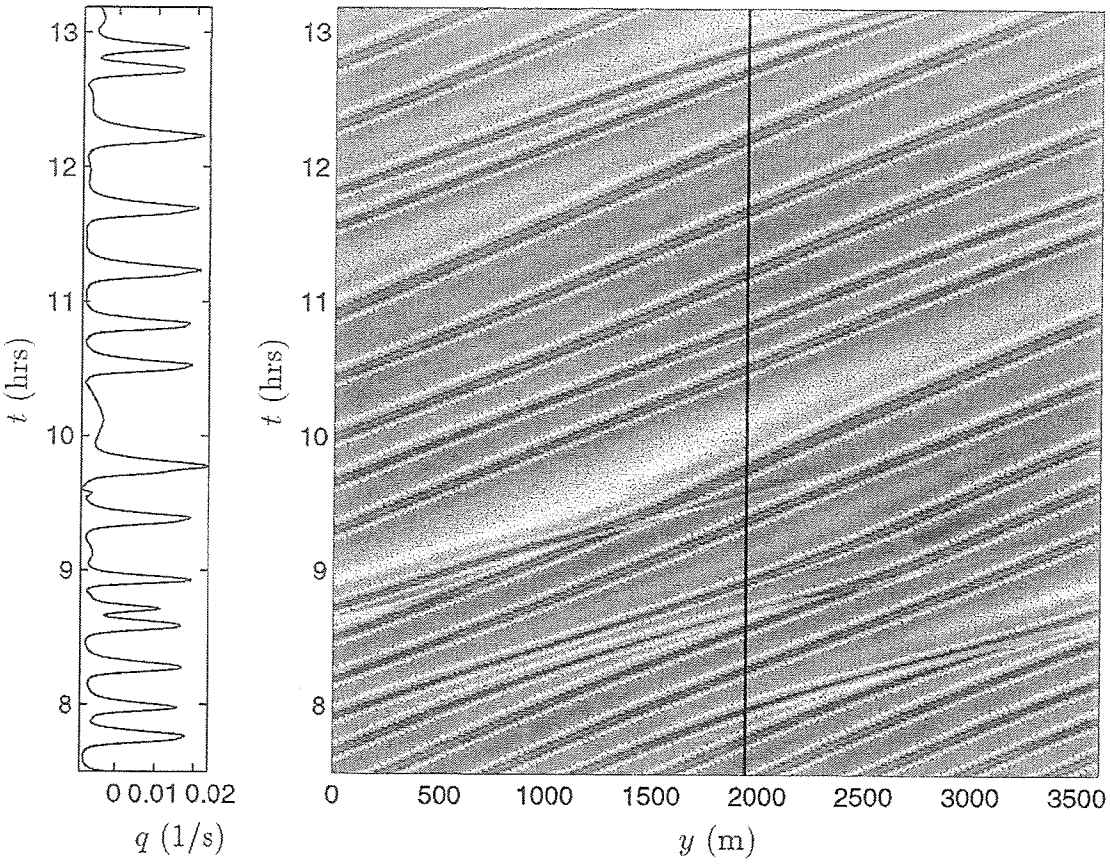

Figure 5.22: ND=8: Contour plot of vorticity q (1/s) as a function of y and t at $x = 90$ m.

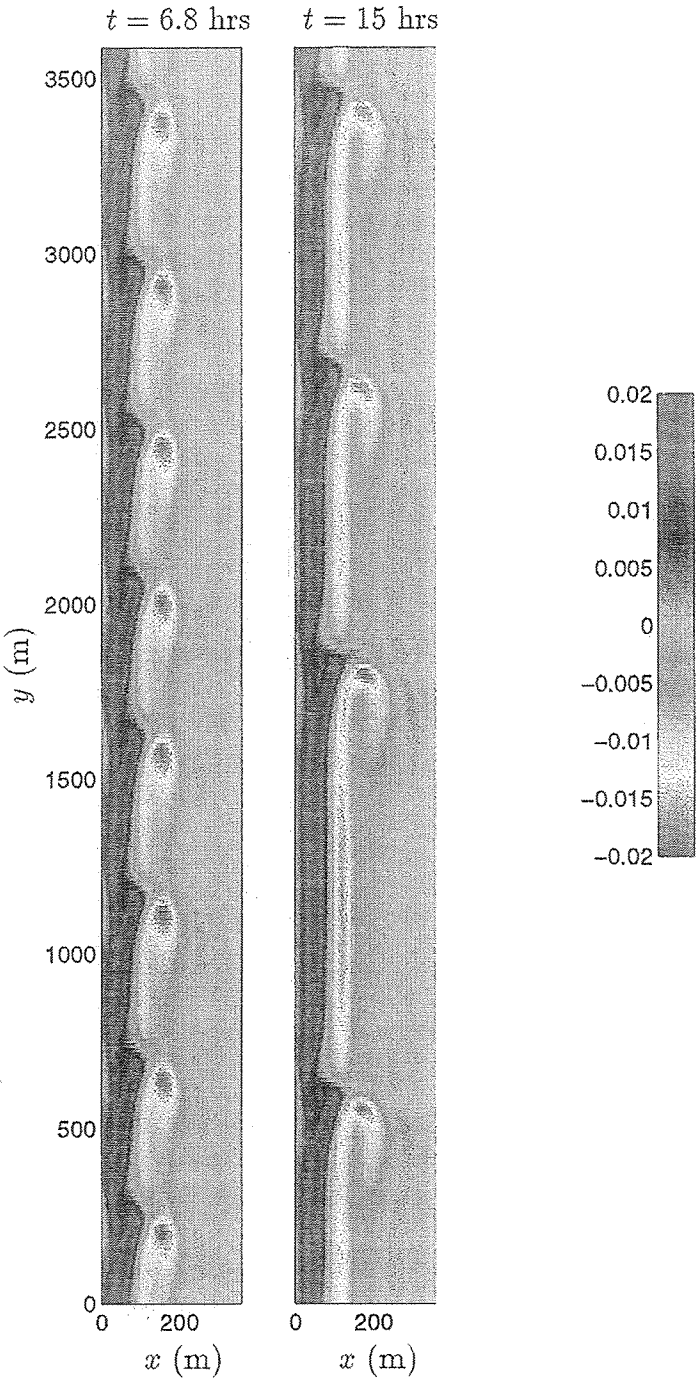

Figure 5.23: ND=8: Snapshots of vorticity q (1/s)

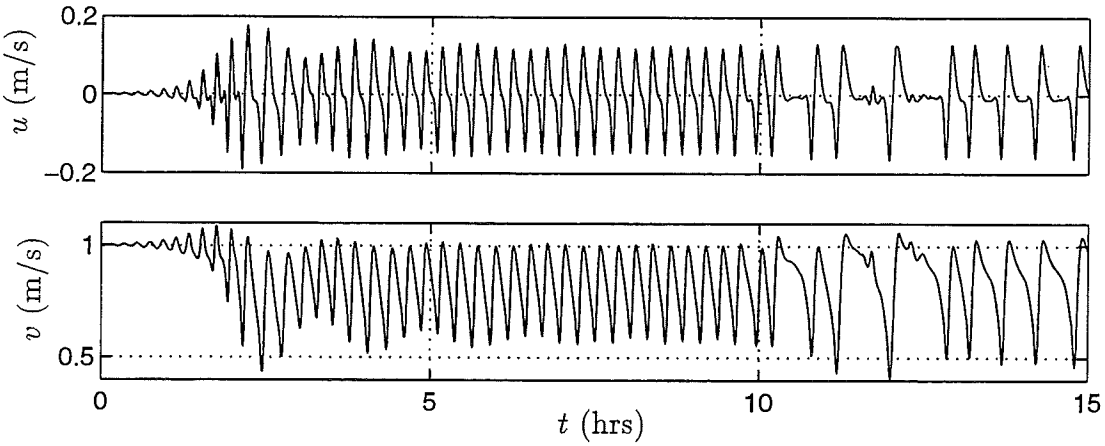

Figure 5.24: ND=16: Time series of u and v at $(x, y) = (90 \text{ m}, 0.5L_y)$.

show that 16 waves are initially present in the domain. The resulting flow field displays eight disturbances. The distances between the fronts are somewhat uneven. Simulations for another 15 hours were carried out and showed that the distances between the fronts evened out in time and no change in the flow pattern was observed.

A circulation plot of the resulting migrating current system is shown in Figure 5.26. The final flow structure exhibits a wavenumber of $\lambda_{max}/2$. Since the range of possible wavenumbers is densely populated with

$$\Delta\lambda = 2\pi/L_y \approx 8.7 \times 10^{-4}\text{rad/m} \tag{5.22}$$

the simulations show that the resulting wavenumber of the motions in this simulations is $(\lambda_{max}/2) \pm \Delta\lambda$. This corresponds to a natural longshore length scale L in the range 800 m $< L <$ 1028 m.

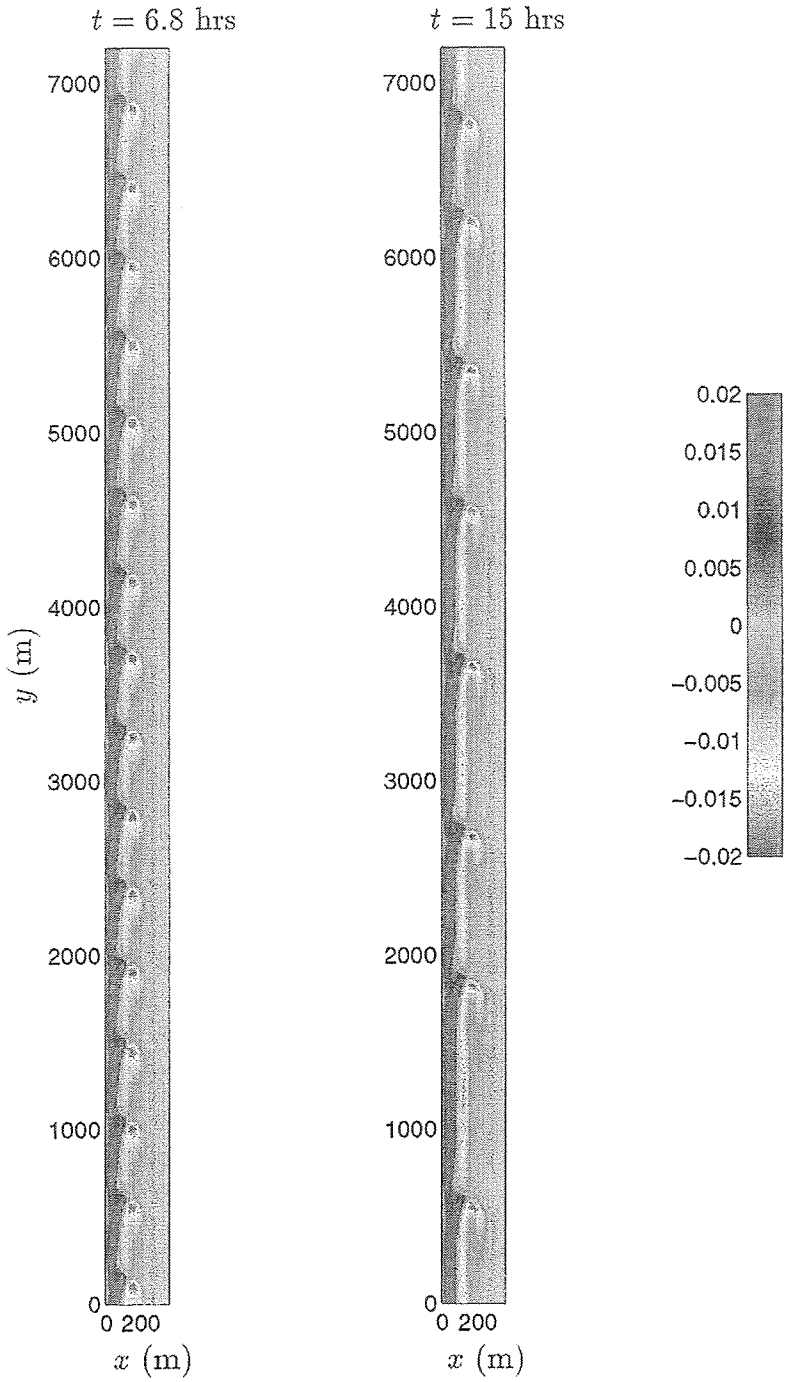

Figure 5.25: ND=16: Snapshots of contour plots of vorticity q (1/s)

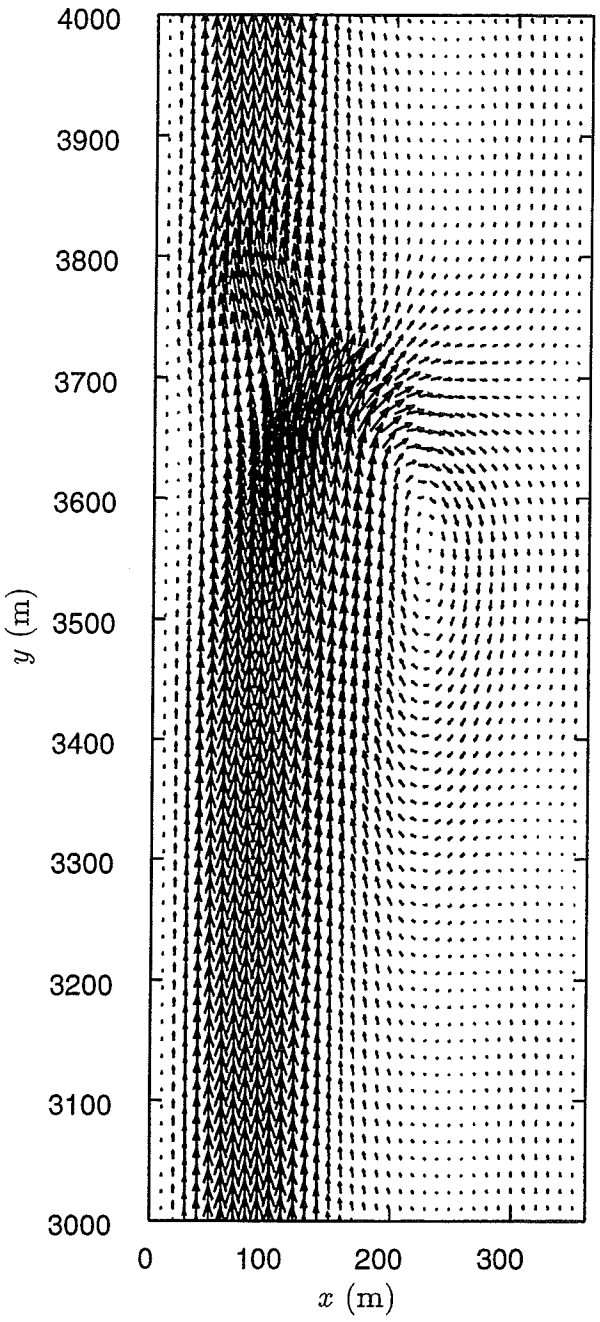

Figure 5.26: ND=16: Circulation pattern at $t = 15$ hrs.

5.8 Summary

In this chapter, the developed solution technique has been used to study instabilities of the longshore current over a plane beach. The errors from neglecting the wave induced setup as well as the shoreline runup due to surface fluctuations associated with the instabilities are found to be minor for this case. In addition, the resulting water surface elevations are found to be small. Therefore, the rigid lid assumption utilized in other studies is justified.

It can be seen that the long term evolution of instabilities in the longshore current in the considered domain is strongly dominated by subharmonic transitions. These transitions are initiated when the speed of one of the initial waves increases as its amplitude is selectively reduced. The smaller disturbance travels at a higher speed than the larger ones suggesting that nonlinearity acts to slow the waves down. The subharmonic transitions occur in the form of vortex collision and pairing, subsequent reduction in the number of waves is evident. The resulting flow structures are longshore progressive and exhibit strong offshore directed velocities. These results are intriguing and possibly suggestive of a mechanism for the formation of migrating rip currents. However, it is evident that the use of more realistic bottom topographies including bars and longshore non-uniformities is necessary to compare the trends in the results to observations.

The resulting flow features are periodic, their effects extend offshore about 300 m. Simulations by Allen *et al.* (1996) resulted in the same features. Allen *et al.* (1996) also found that if the value of the friction coefficient is decreased the flow exhibits more random behavior. At low friction coefficients the areas of concentrated vorticity strengthen further and possibly detach from the surf zone and are advected offshore as vortex pairs. This type of behavior will be observed and analyzed in the next chapter.

Chapter 6

SHEAR INSTABILITIES OF THE LONGSHORE CURRENT ON A BARRED BEACH

In this chapter we simulate shear instabilities of the longshore current on a barred beach. The effects of bottom friction, lateral momentum mixing and short wave forcing are included. Bathymetry and offshore wave data from four days of the SUPERDUCK field experiment are utilized. The shear instability climate for the four days is simulated for a realistic range of friction and mixing coefficients. We identify the effects of varying the coefficients by examining time series and frequency-longshore wavenumber spectra for the simulations as well as for the data. We also analyze the mean momentum balance in the longshore direction to quantify lateral mixing effects due to the instabilities. The details of the resulting flow features are also described.

6.1 Introduction

Surf zone current measurements from experiments such as SUPERDUCK, DELILAH, NSTS at Leadbetter Beach and others show that a variety of low frequency motions coexist in the surf zone. The existence of infragravity motions such as edge waves, leaky waves and surf beat has been known for some time.

These motions span the range of frequencies less than 0.05 Hz and are characterized as surface gravity waves since the restoring force is due to the gravitational acceleration. More recently, Oltman-Shay *et al.* (1989) observed a meandering of the longshore current during the SUPERDUCK experiment over time scales up to O(1000 sec). These motions are, therefore, at the lower end of the traditional low frequency limit for gravity waves but were shown to be much shorter than gravity waves at those frequencies (Oltman-Shay *et al.*, 1989). They display a nondispersive character and dominate the frequencies less than 0.01 Hz.

Bowen and Holman (1989) in a companion paper performed an analytic study and showed that a shear instability of the longshore current can reproduce the nondispersive character and meandering nature of the motions observed by Oltman-Shay *et al.* (1989). The restoring mechanism for these alongshore propagating motions, termed shear waves, is potential vorticity where the background vorticity is supplied by the shear structure of the mean longshore current in analogy to the effect of the Earth's rotation in larger scale applications.

Although several other mechanisms have been proposed to explain the experimental observations by Oltman-Shay *et al.* (1989) (see the review in Chapter 1), the instability theory has, so far, been the most studied alternative. Several investigators, whose work is reviewed briefly in Chapter 1, have applied the instability theory of Bowen and Holman (1989) to realistic current and bottom profiles and identified the effects of bottom friction. Much has been learned about the instability properties of longshore currents as well as the nature of the fully developed fluctuations, but an important question remains unanswered: Can fluctuations in the current velocities resulting from fully developed shear instabilities alone account for the energy in the shear wave band observed during SUPERDUCK? One of the objectives of this chapter is to attempt to answer this question

a shore parallel bar formation further offshore and a gentler beach beyond (Crowson *et al.*, 1988). The experiments incorporated an alongshore array of Marsh-McBirney bidirectional current meters located in the trough shoreward of the bar formation. The array was designed to observe primarily low mode progressive edge waves (Oltman-Shay *et al.*, 1989). The incident wave climate was monitored from bottom mounted pressure gages at 8 m water depth. Bathymetry data were also collected over the region where the surf zone instruments were deployed.

A cold front passed the experimental site on October 15 resulting in locally generated waves from the north quadrant. On this and subsequent days waves at about 15° to the beach with a root-mean-square (rms) wave height of about 1 m and a peak period of about 5 sec were measured at the 8 m array. These waves generated a southward longshore current with a peak of 1 m/s. On the following days the waves and currents diminished (Dodd *et al.*, 1992). The nearshore bathymetry in the region where the instruments were deployed is depicted in Figure 6.1 for October 16 and is typical of all four days. The coordinate system in Figure 6.1 is that used in the experiment. The dots show the positions of the alongshore array of seven current meters. Dodd *et al.* (1992) state that based on both observation and dynamical modeling, longshore variations in the bar regime are not significant enough to induce rip currents. Therefore, Dodd *et al.* (1992) carry out linear instability calculations using measured SUPERDUCK bathymetry from one transect assuming that the bottom contours are straight-and-parallel. We also adopt this assumption in our nonlinear modeling effort.

During a period of four days starting on October 15, current measurements were obtained using the surf zone current meter array with a sampling frequency of 2 Hz for 4 hours centered about low tide. The current meter array was located approximately 45 m from the shoreline for October 15, and 35 m from the

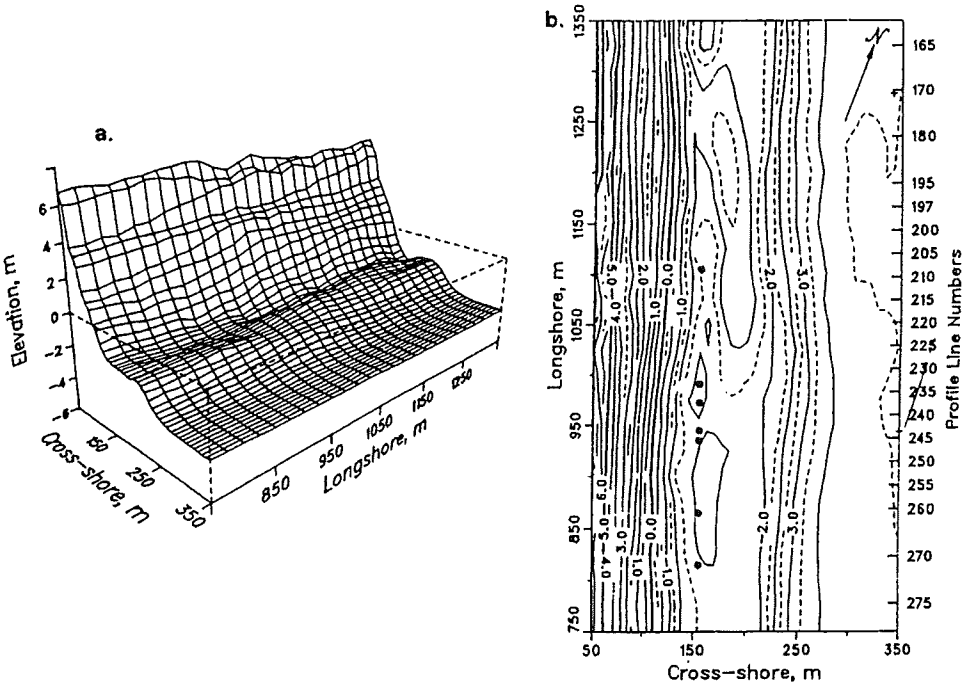

Figure 6.1: (a) Perspective and (b) Plan view of nearshore bathymetry at SUPERDUCK on October 16 (from Dodd *et al.*, 1992). The dots show the positions of the alongshore array of seven current meters.

shoreline for October 16 through October 18. Current and wave measurements were also obtained using wave gages and three Marsh-McBirney current meters mounted on a sled. The sled was initially deployed offshore of the breaker line in a geographic area with the highest degree of straight-and-parallel contours (Whitford and Thornton, 1996). The sled was then gradually pulled onshore collecting 34 minute time series of current measurements at several cross-shore locations including the point of maximum breaking, on top of the nearshore bar, and in the nearshore trough. The transects at which data were collected were located at 900 m on October 15, 1160 m on October 16 and 1170 m on October 17 and 18 according to the coordinate system used during the experiment (see Figure 6.1). Bathymetry measurements were available at those transects. These depth measurements are used in our numerical simulations with the assumption that the bottom contours are straight-and-parallel. Whitford and Thornton (1996) used the current measurements along with wind and wave measurements to determine an appropriate friction coefficient by examining the longshore momentum balance for the period of October 15 through October 18. They obtained values for the friction coefficient c_f in the range

$$0.001 < c_f < 0.004. \tag{6.1}$$

It should be noted that the current measurements obtained from the sled were acquired sequentially. Therefore, as Dodd *et al.* (1992) also point out, the values are representative of a distinct space *and* time location.

Oltman-Shay *et al.* (1989) and later Dodd *et al.* (1992) used measurements from five sensors from the surf zone array to construct frequency-wavenumber spectra of longshore and cross-shore currents for October 15 through October 18 using the high resolution Iterative Maximum Likelihood Estimator (IMLE) (Pawka, 1983). The procedure consisted of quadratically detrending the time

series to remove any effects of tidal variations and constructing spatially lagged cross-spectral matrix values. Contour plots of the frequency-longshore wavenumber spectra $S(f,k)$ for October 15 through October 18 are reproduced in Figures 6.2 through 6.5. Note that, following Oltman-Shay *et al.* (1989), the cyclic wavenumber k is defined as $(1/L)$, where L is the longshore wavelength of the motions.

The edge wave dispersion lines for a 0-mode edge wave for an effective plane beach slope of 0.05 are also shown on the frequency-wavenumber plots. Shear waves are readily distinguished from edge waves since they lie well outside the region bordered by the 0-mode edge wave dispersion curves. The results for the longshore velocities on October 17 do not convey conclusive information about the nature of the motions. However, cross-shore velocity spectra for this day show the presence of an energetic region outside the edge wave dispersion curves. On all four days, we observe that the range of frequencies $f < 0.007$ Hz is dominated by shear wave energy. In contrast to edge waves, shear waves exhibit a nearly linear dispersion curve. Taking advantage of the nearly nondispersive character of the observed motions, we seek to identify a representative propagation speed of the shear waves.

6.2.1 Estimation of the Propagation Speeds

For the purpose of identifying the dispersion line, the energy in the shear wave band needs to be identified. Howd *et al.* (1991) used an energy partitioning method between edge waves and shear waves by assuming that all infragravity energy lies in the region bordered by the dispersion curves for the 0-mode edge waves traveling in the positive and negative directions. Energy outside of this region is then attributed to shear waves. Here, a simpler approach is taken. First,

an estimate of the shear wave propagation speed c_{est} is made by inspection. An upper cutoff line with a slope of $2c_{est}$ intercepting at the origin is defined so that on this line $f = 2c_{est}k$. The lower cutoff line is defined with slope c_{est} intercepting the wavenumber axis at 0.01 (rad/m) so that on this line $f = c_{est}(k-0.01)$. These lines are also depicted in the frequency-wavenumber plots shown in Figures 6.2 through 6.5. All energy lying between these lines is attributed to shear waves. This method assures that all gravity wave energy is excluded from the estimates of shear wave motion (but not the opposite).

In order to obtain an estimate for the propagation speed of the shear waves, a frequency $\overline{f}$ is defined for every wavenumber k such that

$$\overline{f}(k) = \frac{\int_{f_{low}}^{f_{up}} fS(f,k)df}{\int_{f_{low}}^{f_{up}} S(f,k)df}, \tag{6.2}$$

where the lower and upper limits of integration are chosen such that only shear wave energy is included in the estimates.

$$\begin{aligned} f_{low} &= \begin{cases} 0 & \text{for } k < 0.01 \text{ (1/m)} \\ c_{est}(k-0.01) & \text{for } k \geq 0.01 \text{ (1/m)} \end{cases} \\ f_{up} &= 2c_{est}k. \end{aligned} \tag{6.3}$$

Assuming that the motions are nondispersive, a straight line can then be fitted through the points $(\overline{f}, k)$ by performing a weighted first order polynomial fit. The weight of each data point $(\overline{f}, k)$ is determined by the total energy in that wavenumber bin $S_f(k)$ given by

$$S_f(k) = \int_{f_{low}}^{f_{up}} S(f,k)df, \tag{6.4}$$

where the integration limits f_{low} and f_{up} were given in (6.3).

The slope and intercept values of the obtained linear fit then define the propagation speed. The best fit dispersion lines are also shown in Figures 6.2

through 6.5. The equation for the dispersion line is stated in the title of each figure. The dispersion lines obtained in this manner consistently show a higher intercept value for the cross-shore velocities suggesting that the motions are dispersive. The slope of the resulting curve is also higher than the curve associated with the longshore velocities. Dodd *et al.* (1992) also make this observation and state that the non-zero intercept values in the cross-shore velocity spectra are likely to be an artifact of the data analysis. They explain the phenomenon by stating that the cross-shore velocity spectrum has a peak at some frequency value greater than zero, it thus preferentially weights motions with larger wavenumbers in frequency bins below the peak frequency. The implication is that the apparent dispersion line is pulled to an intercept value with the abscissa at wavenumbers noticeably different from zero. However, frequency-wavenumber spectra obtained using longshore velocities intercept consistently near the origin which agrees with the linear instability theory.

An alternate approach to estimate the propagation speeds is to define a wavenumber $\overline{k}$ for each frequency f as

$$\overline{k}(f) = \frac{\int_{k_{low}}^{k_{up}} kS(f,k)dk}{\int_{k_{low}}^{k_{up}} S(f,k)dk}, \tag{6.5}$$

where the lower and upper limits of integration are chosen such that only shear wave energy is included in the estimates such that

$$k_{low} = \frac{f}{c_{est}}, \qquad k_{up} = \frac{f}{c_{est}} + 0.01. \tag{6.6}$$

A linear fit through the points $(f, \overline{k})$ weighted by the energy $S_k(f)$ in each frequency bin given by

$$S_k(f) = \int_{k_{low}}^{k_{up}} S(f,k)dk, \tag{6.7}$$

then results in an estimate of the dispersion line. This dispersion line for October 15 is shown in Figure 6.6. It is seen that this method results in the prediction

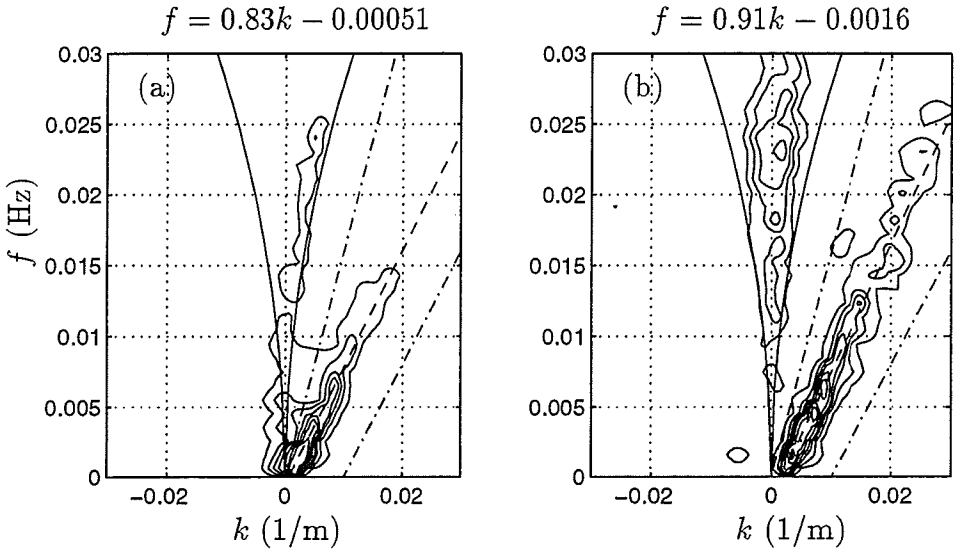

Figure 6.2: Frequency-cyclic longshore wavenumber spectra $S(f,k)$ (m^3/s) for (a) longshore and (b) cross-shore velocities from measurements on October 15. Contour levels plotted are (10, 30, 60, 100, 200, 400, 800). A value of 0.8 m/s is used for c_{est} in Equation (6.3) to construct the upper and lower cut-off lines (– · –) of the shear wave energy. The equation for the best fit dispersion line (— —) is noted above each plot. The 0-mode edge wave dispersion lines for a plane beach slope of 0.05 are also shown (thick ——).

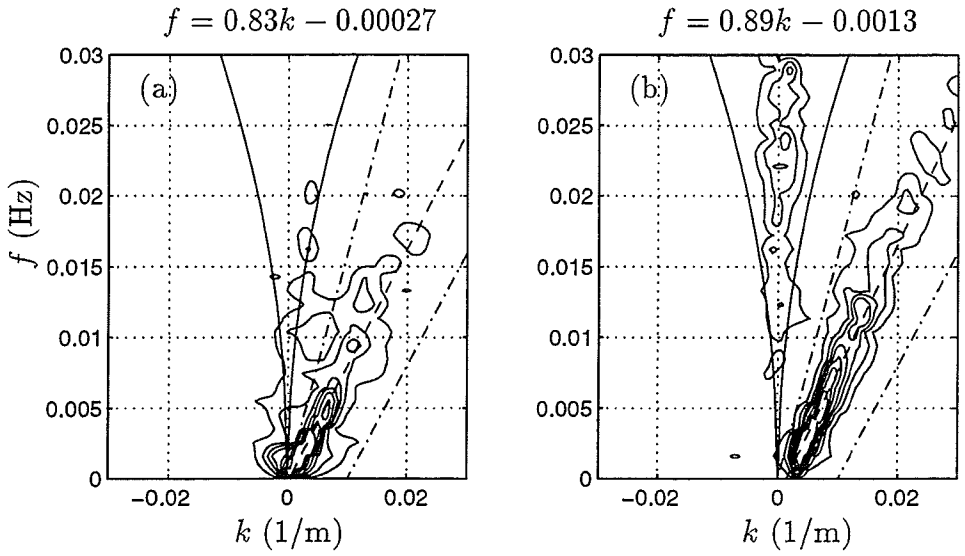

Figure 6.3: Frequency-cyclic longshore wavenumber spectra $S(f,k)$ (m^3/s) for (a) longshore and (b) cross-shore velocities from measurements on October 16. Contour levels plotted are (10, 30, 60, 100, 200, 400, 800). A value of 0.8 m/s is used for c_{est} in Equation (6.3) to construct the upper and lower cut-off lines (– · –) of the shear wave energy. The equation for the best fit dispersion line (– –) is noted above each plot. The 0-mode edge wave dispersion lines for a plane beach slope of 0.05 are also shown (thick ——).

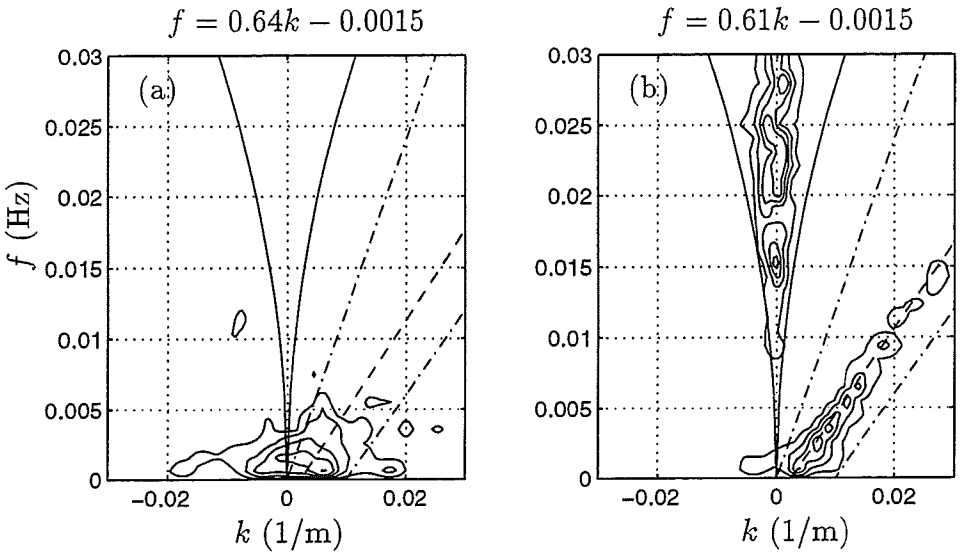

Figure 6.4: Frequency-cyclic longshore wavenumber spectra $S(f,k)$ (m^3/s) for (a) longshore and (b) cross-shore velocities from measurements on October 17. Contour levels plotted are (10, 30, 60, 100, 200, 400, 800). A value of 0.6 m/s is used for c_{est} in Equation (6.3) to construct the upper and lower cut-off lines (– · –) of the shear wave energy. The equation for the best fit dispersion line (— —) is noted above each plot. The 0-mode edge wave dispersion lines for a plane beach slope of 0.05 are also shown (thick ——).

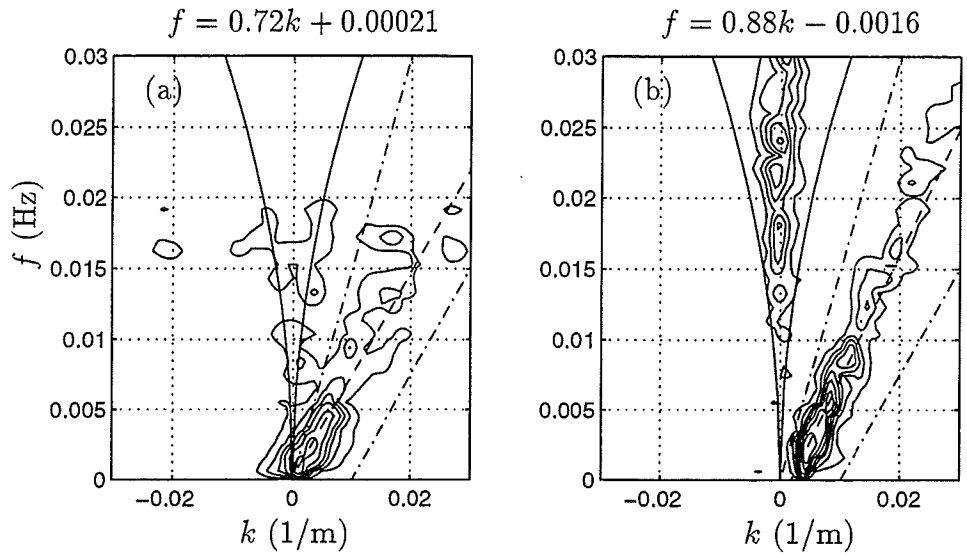

Figure 6.5: Frequency-cyclic longshore wavenumber spectra $S(f,k)$ (m^3/s) for (a) longshore and (b) cross-shore velocities from measurements on October 18. Contour levels plotted are (10, 30, 60, 100, 200, 400, 800). A value of 0.75 m/s is used for c_{est} in Equation (6.3) to construct the upper and lower cut-off lines (– · –) of the shear wave energy. The equation for the best fit dispersion line (– –) is noted above each plot. The 0-mode edge wave dispersion lines for a plane beach slope of 0.05 are also shown (thick ——).

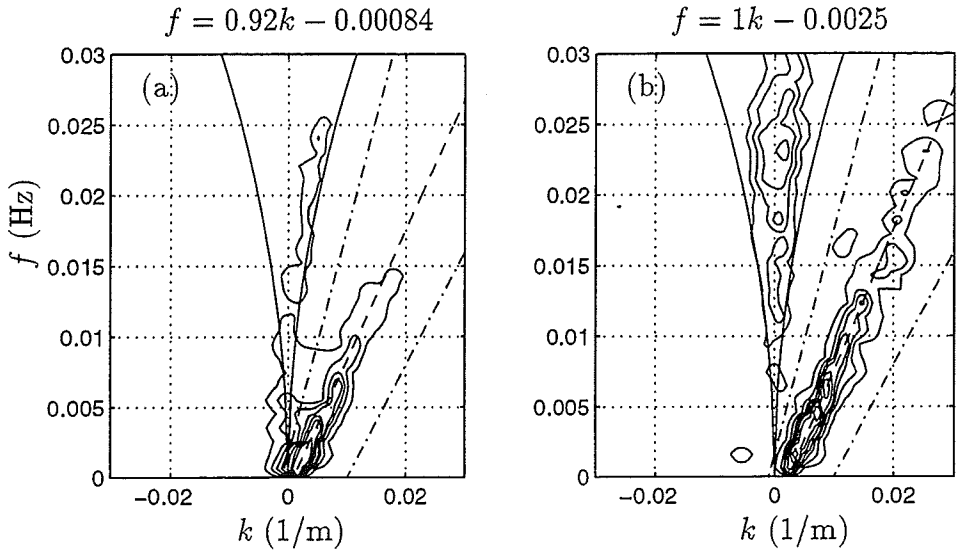

Figure 6.6: Frequency-cyclic longshore wavenumber spectra $S(f,k)$ (m^3/s) for (a) longshore and (b) cross-shore velocities from measurements for October 15. The equation for the best fit dispersion line (– –) is estimated using the alternate method and is noted above each plot.

of higher propagation speeds by about 10%. The intercept of the dispersion lines with the wavenumber axis also occurs at higher values for both the cross-shore and longshore velocity spectra.

The first method will be used in the remainder of the chapter. However, the 10% variation in the prediction of the speeds should be kept in mind when interpreting the results. The method outlined here is also used in order to estimate the propagation speeds of oscillations arising in the computations. Since model computations are carried out with high resolution in both space and time, a direct Fourier transform in both space and time is used to obtain the two-dimensional spectra from the computed time series.

6.3 Model Formulation

The nonlinear shallow water equations with short wave forcing, lateral momentum mixing and bottom friction terms added provide a good basis for modeling the long-time evolution of shear instabilities of the longshore current. They were derived in Chapter 2 and are given by

$$\frac{\partial \eta}{\partial t} + \frac{\partial}{\partial x}[ud] + \frac{\partial}{\partial y}[vd] = 0 \tag{6.8}$$

$$\begin{aligned} \frac{\partial u}{\partial t} + u\frac{\partial u}{\partial x} + v\frac{\partial u}{\partial y} &= -g\frac{\partial \eta}{\partial x} - \frac{1}{\rho d}\left(\frac{\partial S_{xx}}{\partial x} + \frac{\partial S_{xy}}{\partial y}\right) - \frac{\mu}{d}u \\ &\quad + \frac{2}{d}\frac{\partial}{\partial x}\left(\nu d\frac{\partial u}{\partial x}\right) + \frac{1}{d}\frac{\partial}{\partial y}\left(\nu d\frac{\partial v}{\partial x}\right), \end{aligned} \tag{6.9}$$

$$\begin{aligned} \frac{\partial v}{\partial t} + u\frac{\partial v}{\partial x} + v\frac{\partial v}{\partial y} &= -g\frac{\partial \eta}{\partial y} - \frac{1}{\rho d}\left(\frac{\partial S_{xy}}{\partial x} + \frac{\partial S_{yy}}{\partial y}\right) - \frac{\mu}{d}v \\ &\quad + \frac{1}{d}\frac{\partial}{\partial x}\left(\nu d\frac{\partial v}{\partial x}\right). \end{aligned} \tag{6.10}$$

Here, η is the short wave-averaged water surface elevation above the still water level, h is the depth with respect to the still water level, $d = (h + \eta)$ is the total water depth, u and v are the depth-averaged current velocities in the x and y directions, respectively, where x points offshore and y points in the longshore direction.

The effects of bottom friction are modeled using a linear damping term. The coefficient μ is defined as

$$\mu = \frac{2}{\pi}c_f u_0. \tag{6.11}$$

Here, c_f is a friction coefficient, u_0 is the horizontal orbital velocity of the short waves and can be expressed in terms of the wave height at a cross-shore location.

Lateral momentum mixing due to turbulence and the Taylor dispersion

process outlined by Svendsen and Putrevu (1994) are considered in a rudimentary fashion. Svendsen and Putrevu (1994) found that the vertical nonuniformity of the nearshore currents introduces additional terms into the depth-averaged momentum equations. They identified the dominant effect of the additional terms to be lateral momentum mixing. Other effects such as modifications to the radiation stress terms and the convective acceleration terms exist, but are expected to be less important (Putrevu and Svendsen, 1997). Therefore, as a first approximation, only the additional lateral mixing terms are retained. Further assuming small angle of incidence of the short waves, the leading order mixing terms reduce to two additional terms in the x-momentum equation and one additional term in the y-momentum equation.

Svendsen and Putrevu (1994) further found that the mixing induced by the Taylor dispersion process is larger than turbulent momentum mixing. Therefore, in this study turbulent mixing is neglected unless it is reinforced by the Taylor dispersion process. The eddy viscosity ν in (6.9) and (6.10) represents a combined viscosity $\nu = \nu_t + D_{xx}$, where ν_t is the turbulent eddy viscosity and D_{xx} is the mixing coefficient identified by Svendsen and Putrevu (1994). The coefficient D_{xx} is a function of the depth profiles of the undertow and the longshore current. Its specification requires the computation of the depth profiles using a profile model. In this study, we choose to include an order of magnitude estimate of the effect of D_{xx} by parameterizing the combined eddy viscosity ν following Battjes (1975) as

$$\nu = Md\left(\frac{\epsilon_b}{\rho}\right)^{1/3}, \tag{6.12}$$

where ϵ_b is the ensemble averaged energy dissipation due to wave breaking and M is a mixing coefficient. The order of magnitude of M for field applications is estimated to be

$$0.06 < M < 0.48. \tag{6.13}$$

A more detailed discussion of the treatment of the mixing terms as well as the estimation of the order of magnitude of M can be found in Chapter 2.

Results from simulations for shear instabilities on a plane beach showed that the presence of a steady setup has relatively minor effects. As a first approximation, the steady setup is neglected by subtracting the mean momentum balance in the absence of fluctuating motion in the x direction

$$g\frac{\partial \overline{\eta}}{\partial x} = -\frac{1}{\rho d}\left(\frac{\partial S_{xx}}{\partial x} + \frac{\partial S_{xy}}{\partial y}\right) \tag{6.14}$$

from the x-momentum equation. The governing equations are then given by the continuity equation

$$\frac{\partial \eta}{\partial t} + \frac{\partial}{\partial x}[ud] + \frac{\partial}{\partial y}[vd] = 0, \tag{6.15}$$

and the momentum equations

$$\begin{aligned}\frac{\partial u}{\partial t} + u\frac{\partial u}{\partial x} + v\frac{\partial u}{\partial y} = &- g\frac{\partial \eta}{\partial x} - \frac{\mu}{d}u \\ &- \frac{2}{d}\frac{\partial}{\partial x}\left(\nu d\frac{\partial u}{\partial x}\right) - \frac{1}{d}\frac{\partial}{\partial y}\left(\nu d\frac{\partial v}{\partial x}\right),\end{aligned} \tag{6.16}$$

$$\begin{aligned}\frac{\partial v}{\partial t} + u\frac{\partial v}{\partial x} + v\frac{\partial v}{\partial y} = &- g\frac{\partial \eta}{\partial y} - \frac{1}{\rho d}\left(\frac{\partial S_{xy}}{\partial x} + \frac{\partial S_{yy}}{\partial y}\right) - \frac{\mu}{d}v \\ &- \frac{1}{d}\frac{\partial}{\partial x}\left(\nu d\frac{\partial v}{\partial x}\right),\end{aligned} \tag{6.17}$$

where η should now be interpreted as the water surface elevation above the mean water level.

6.3.1 Short Wave Forcing

Given the wave field at the 8 m wave array, the transformation of the random waves into shallow water is simulated using the wave height transformation model by Thornton and Guza (1983). In order to apply this model, we

assume random waves with a narrow banded spectrum and Rayleigh distributed wave heights. The bathymetry transect measured by the sled is used assuming straight-and-parallel bottom contours. The applicability of these assumptions to the SUPERDUCK experiment has been addressed by Whitford (1988).

The random wave transformation model by Thornton and Guza (1983) involves approximating the narrow banded sea by a single wave component with a frequency corresponding to the peak frequency $\tilde{f}_p$ of the spectrum, a wave height H_{rms} and direction $\overline{\theta}$. The transformation of this representative wave component is computed using the energy equation for the short wave motions. For a stationary short wave field over straight-and-parallel bottom contours and in the absence of any wave-current interactions, this equation is given by

$$\frac{\partial E c_g \cos\overline{\theta}}{\partial x} = \epsilon_b. \tag{6.18}$$

Here, c_g is the group velocity corresponding to the wavenumber associated with the the peak frequency $\tilde{f}_p$. This wavenumber is computed using the linear dispersion relationship.

For straight-and-parallel contours the mean angle of incidence $\overline{\theta}$ is governed by Snell's law

$$\frac{\sin\overline{\theta}}{\tilde{c}} = \text{const} = \frac{\sin\overline{\theta}_0}{\tilde{c}_0} \tag{6.19}$$

where $\tilde{c}$ is the short wave celerity associated with the peak frequency and the subscripts 0 denote offshore values.

The parameter ϵ_b in (6.18) is an ensemble-averaged energy dissipation due to wave breaking defined by Thornton and Guza (1983). The form for ϵ_b suggested

by Whitford (1988) for the SUPERDUCK experiment is used.

$$\epsilon_b = \frac{3\sqrt{\pi}}{16}\rho g \tilde{f}_p B^3 \frac{H_{rms}^3}{h} C_1 \left[1 - \frac{1}{\left(1 + \left(\frac{H_{rms}}{\gamma h}\right)^2\right)^{5/2}}\right] \tag{6.20}$$

where

$$C_1 = 1 + \tanh\left(8\left(\frac{H_{rms}}{\gamma h} - 0.99\right)\right). \tag{6.21}$$

The coefficients used for the wave height transformation model are $B = 0.8$ (indicating the intensity of wave breaking) and $\gamma = 0.42$.

Finally, an estimation of the amplitude of the horizontal orbital velocity of the short waves is necessary since it enters the definition of the linear friction coefficient μ in (6.11). For Rayleigh distributed wave heights, the amplitude of the horizontal orbital velocity of the short waves can be expressed in terms of H_{rms} (Thornton and Guza, 1983) as

$$u_0 = \frac{1}{4}\sqrt{\frac{g\pi}{h}} H_{rms} \tag{6.22}$$

and is a function of the cross-shore location.

Given the bathymetry, the rms wave height H_{rms}, the peak frequency $\tilde{f}_p$ and the mean angle of incidence $\overline{\theta}$ at the offshore boundary, the wave height transformation of the short waves can be computed using the energy equation (6.18) along with the linear dispersion relationship and Snell's law (6.19). The values of H_{rms}, $\tilde{f}_p$ and $\overline{\theta}$ at the 8 m array for October 15 through October 18 are given in Table 6.1. The computed wave height variation for October 15 through October 18 along with the bottom bathymetry is shown in Figures 6.7 through 6.10.

Once the wave height transformation is computed the short wave forcing term in the governing equation for the longshore current motion (6.17) can be

Table 6.1: Offshore wave conditions for SUPERDUCK at 8 m water depth

Date	H_{rms} (m)	$\tilde{f}_p$ (Hz)	$\bar{\theta}$ (°)
October 15, 09:45 am	0.93	0.16	14
October 16, 10:20 am	0.98	0.19	21
October 17, 11:00 am	0.72	0.17	9
October 18, 11:40 am	0.93	0.19	16

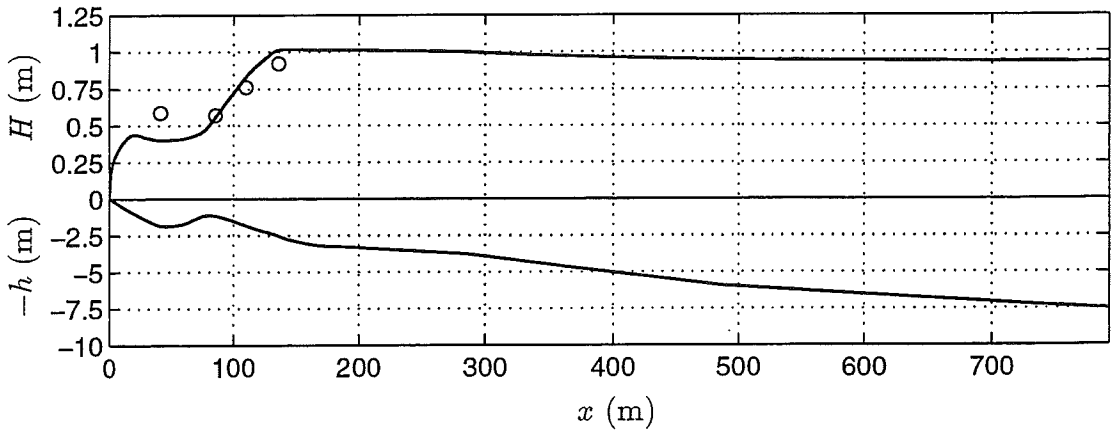

Figure 6.7: Computed wave height decay along with wave height measurements from the sled (o) and measured bathymetry for October 15.

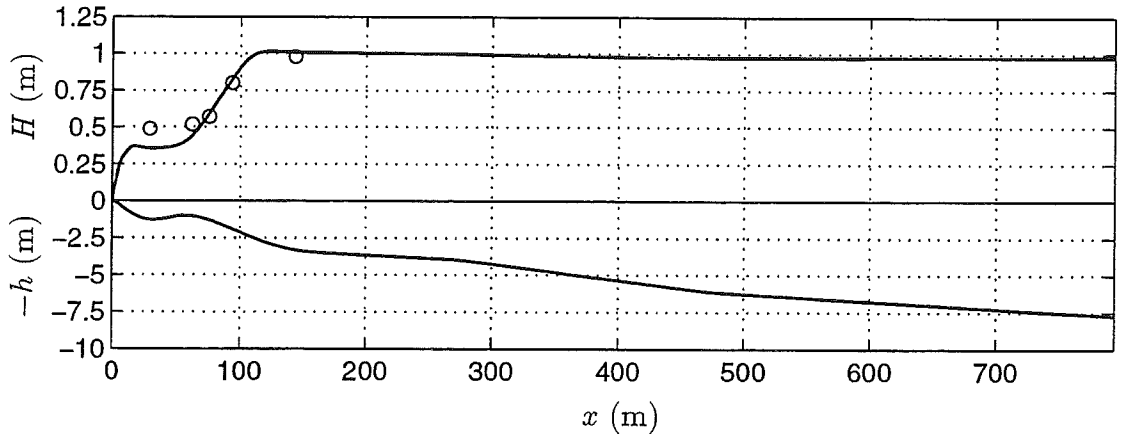

Figure 6.8: Computed wave height decay along with wave height measurements from the sled (o) and measured bathymetry for October 16.

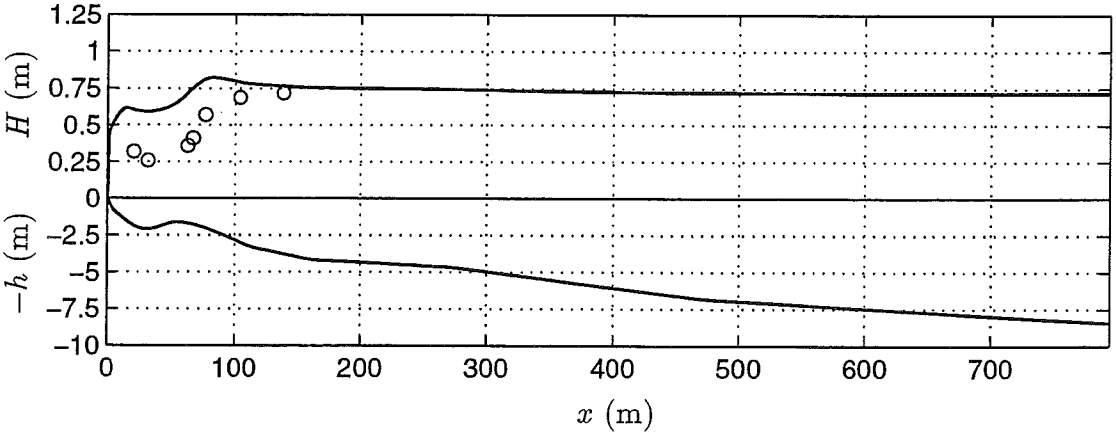

Figure 6.9: Computed wave height decay along with wave height measurements from the sled (o) and measured bathymetry for October 17.

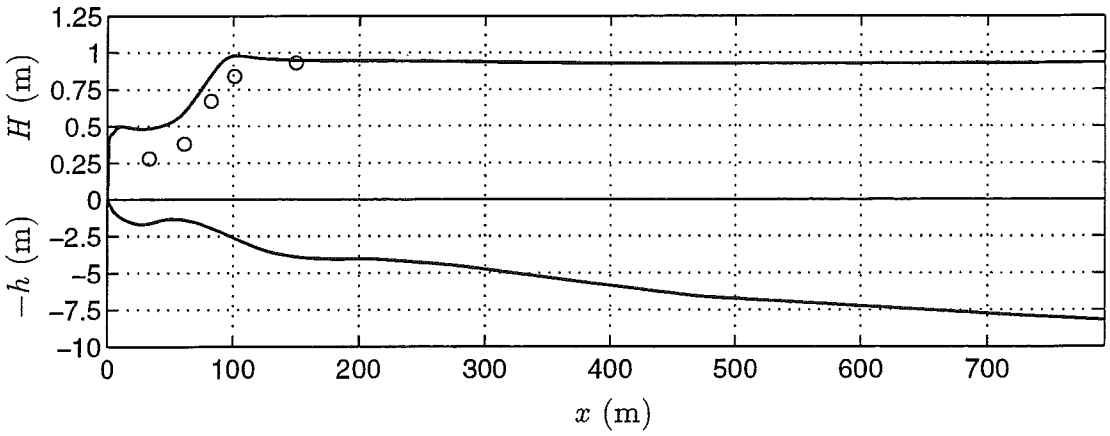

Figure 6.10: Computed wave height decay along with wave height measurements from the sled (o) and measured bathymetry for October 18.

specified. The short wave forcing term in (6.17) contains gradients of the wave-induced momentum fluxes in the y direction. It is modeled using a radiation stress formulation (Longuet-Higgins and Stewart, 1964) such that the forcing term $\tilde{\tau}_y$ is given by

$$\tilde{\tau}_y = -\frac{1}{\rho d}\left(\frac{\partial S_{xy}}{\partial x} + \frac{\partial S_{yy}}{\partial y}\right) \tag{6.23}$$

where the radiation stresses herein are modeled using linear theory as

$$S_{xy} = E\frac{c_g}{\tilde{c}}\sin\overline{\theta}\cos\overline{\theta}, \tag{6.24}$$

$$S_{yy} = E\left[\frac{c_g}{\tilde{c}}\left(\sin^2\overline{\theta}+1\right) - \frac{1}{2}\right]. \tag{6.25}$$

Due to the assumed longshore uniform nature of the wave field and Snell's law (6.19) the forcing term $\tilde{\tau}_y$ can be written as

$$\tilde{\tau}_y = -\frac{1}{\rho d}\frac{\sin\overline{\theta}_0}{\tilde{c}_0}\epsilon_b \tag{6.26}$$

where the dissipation due to wave breaking ϵ_b is defined by (6.20). It should be noted that the forcing is time-invariant; therefore, wave-current interactions are neglected.

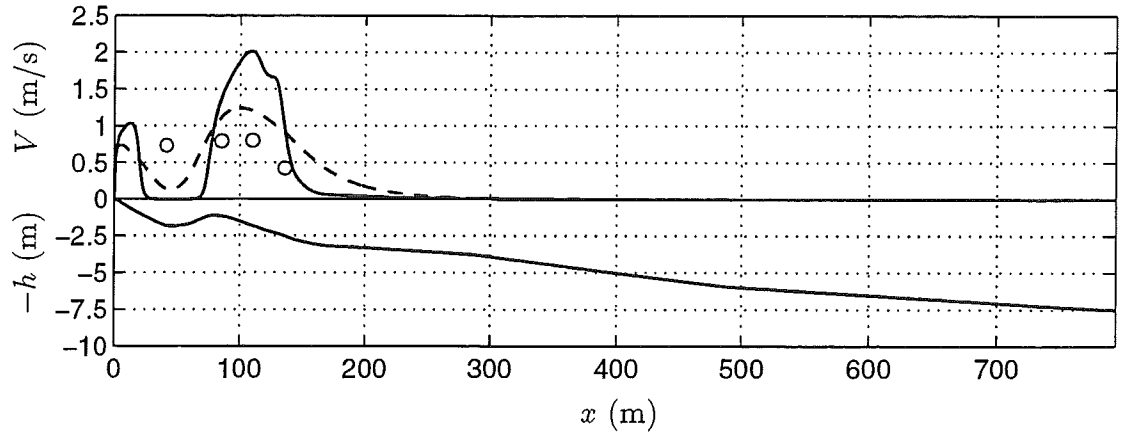

Figure 6.11: Computed longshore current for $c_f = 0.003$ along with measurements from the sled (o) and measured bathymetry for October 15 with $M = 0$ (——) and $M = 1$ (– –).

6.3.2 Mean Momentum Balance

In the absence of any fluctuating motions, the steady mean longshore current V results from the balance

$$-\frac{\partial}{\partial x}\left(\nu d\left(\frac{\partial V}{\partial x}\right)\right) + \mu V = -\frac{1}{\rho}\frac{\sin\overline{\theta}_0}{\tilde{c}_0}\epsilon_b. \tag{6.27}$$

The resulting current profile V in the absence of any fluctuations is shown in Figures 6.11 through 6.14 for M-values of zero (no lateral mixing) and unity for October 15 through October 18, respectively. Friction coefficients suggested by Dodd *et al.* (1992) for the four days were used. They are given by 0.003 for October 15 and 0.004 for October 16 through October 18.

In the presence of the fluctuating motions, the mean momentum balance in the longshore direction that leads to the generation of a longshore current can be obtained by longshore-averaging the y-momentum equation (6.17). The resulting

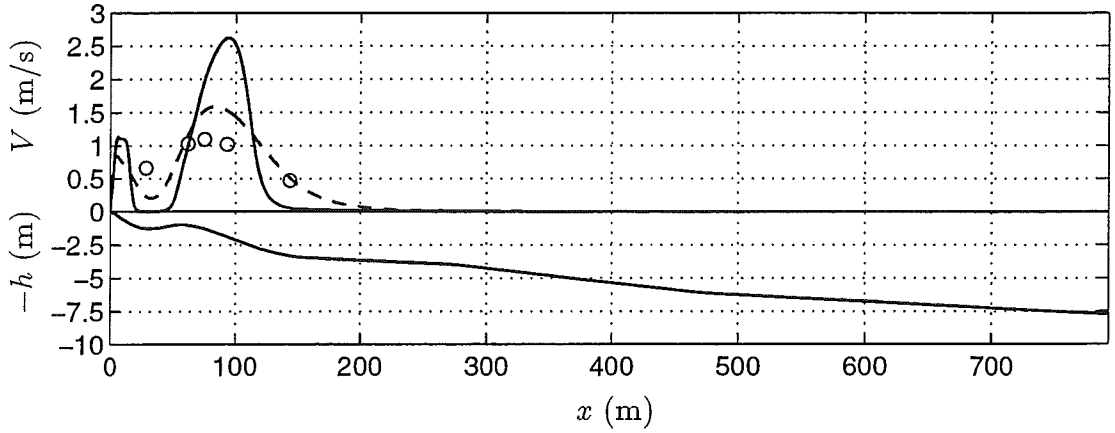

Figure 6.12: Computed longshore current for $c_f = 0.004$ along with wave height measurements from the sled (o) and measured bathymetry for October 16 with $M = 0$ (——) and $M = 1$ (– –).

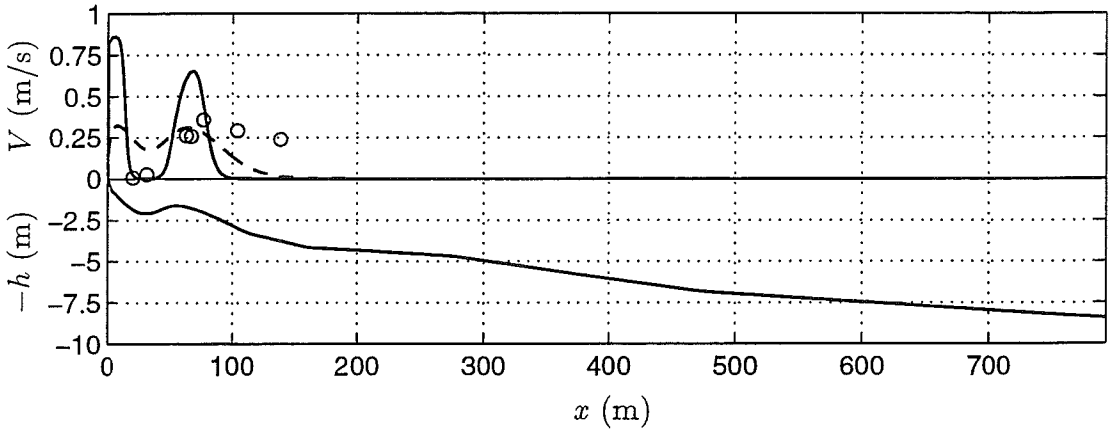

Figure 6.13: Computed longshore current for $c_f = 0.004$ along with wave height measurements from the sled (o) and measured bathymetry for October 17 with $M = 0$ (——) and $M = 1$ (– –).

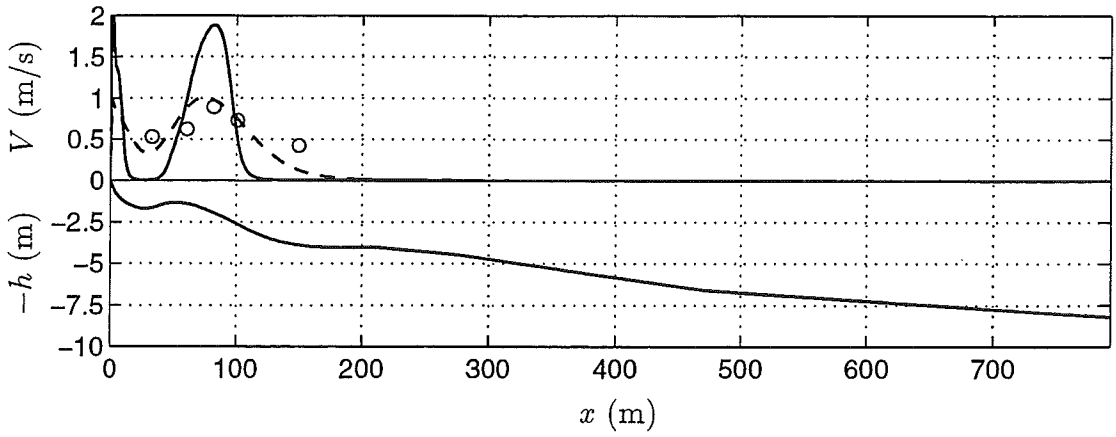

Figure 6.14: Computed longshore current for $c_f = 0.004$ along with wave height measurements from the sled (o) and measured bathymetry for October 18 with $M = 0$ (——) and $M = 1$ (– –).

equation is given by

$$\frac{\partial \langle v \rangle}{\partial t} + \langle u \frac{\partial v}{\partial x} \rangle = \langle \tilde{\tau}_y \rangle - \langle \frac{\mu}{d} v \rangle + \langle \tau_y' \rangle, \tag{6.28}$$

In the above equation, the longshore average of a variable $Q(x, y, t)$ is defined by

$$\langle Q \rangle (x, t) = \frac{1}{L_y} \int_0^{L_y} Q(x, y, t) dy. \tag{6.29}$$

The terms in the y-momentum equation involving y derivatives drop out of the mean balance. The short wave forcing $\tilde{\tau}_y$ is given by (6.26) and the lateral mixing term in the y direction τ_y' is given by

$$\tau_y' = \frac{1}{d} \frac{\partial}{\partial x} \left(\nu d \frac{\partial v}{\partial x} \right). \tag{6.30}$$

The effect of slow time variations in the mean longshore current $\langle v \rangle$ can be excluded by further time-averaging (6.28) over time scales much longer than the variations in $\langle v \rangle$. The time average of a variable $Q(x, y, t)$ is defined as

$$\overline{Q}(x, y) = \frac{1}{(t_f - t_i)} \int_{t_i}^{t_f} Q(x, y, t) dt. \tag{6.31}$$

Performing the time average of (6.28) the balance

$$\langle \overline{u\frac{\partial v}{\partial x}} \rangle + \langle \overline{\frac{\mu}{d} v} \rangle - \langle \overline{\tau_y'} \rangle = \langle \overline{\tilde{\tau}_y} \rangle \tag{6.32}$$

can be identified. Note that periodicity and longshore uniformity of the bathymetry imply that $\langle u \rangle = 0$. Defining the time and longshore-averaged velocities and the fluctuating components as

$$\begin{aligned} u &= \langle \overline{u} \rangle + u' \\ v &= \langle \overline{v} \rangle + v', \end{aligned} \tag{6.33}$$

the effect of the first term in (6.32) can be identified as lateral momentum mixing due to the fluctuating components since

$$\langle \overline{u\frac{\partial v}{\partial x}} \rangle = \langle \overline{u'\frac{\partial v'}{\partial x}} \rangle. \tag{6.34}$$

The resulting mean balance given by (6.32) states that the short wave forcing $\langle \overline{\tilde{\tau}_y} \rangle$ is balanced by bottom friction $\langle \overline{\frac{\mu}{d} v} \rangle$ and lateral mixing caused by the shear instabilities $\langle \overline{u\frac{\partial v}{\partial x}} \rangle$ as well as lateral mixing caused by other processes discussed earlier ($\langle \overline{\tau_y'} \rangle$). In Chapter 5 we already established that shear instabilities cause lateral momentum mixing in the surf zone. In this chapter we will analyze the importance of mixing due to the instabilities compared to mixing caused by processes such as turbulence and the Taylor dispersion process.

The mean kinetic energy density in the fluctuating velocity components can be defined as

$$E'(x) = \frac{1}{2} \langle \overline{u'^2} + \overline{v'^2} \rangle \tag{6.35}$$

and is referred to as the mean perturbation kinetic energy. It provides a good measure of the cross-shore distribution and extent of the fluctuations due to the shear instabilities.

6.4 Modeling domain and solution method

The modeling domain extends from the still water shoreline to a certain distance offshore. A moving shoreline boundary condition is incorporated at the onshore end of the modeling domain. However, for the simulations shown in this chapter, a wall boundary is incorporated at the shoreline instead to decrease the necessary computational time since the modeled water surface elevations are observed to be at the order of 1 cm and the runup associated with these values is of minor importance. The moving shoreline will become important when the wave-induced setup is included in the model.

An absorbing boundary condition originally developed by Van Dongeren and Svendsen (1997) is incorporated at the offshore boundary to allow transient gravity motions to leave the domain of interest. The boundary condition has been shown to perform favorably for gravity wave motions exiting the domain of interest (see Chapter 4). However, in the simulations shown in this chapter, vortices are often advected towards the offshore boundary. It is observed that the offshore boundary is not transparent to these vortices. If the vortices are weakened by bottom friction by the time they reach the boundary, they continue to dissipate at the location they encountered the offshore boundary. However, if the vortices are strong when they reach the offshore boundary, they are advected along the boundary but remain close to the boundary until they dissipate. Care has to be taken to place the offshore boundary far away from the surf zone so that offshore advection velocities are small when the vortices reach the offshore boundary. The offshore boundary is placed approximately six surf zone widths away from the shoreline at 550 m.

6.4.1 Longshore Domain Width

Periodicity is imposed in the longshore direction; therefore, the longshore width of the modeling domain needs to be long enough for sufficiently many waves to be present in the domain so that reliable statistical estimates can be obtained. The width of the domain is chosen using the following argument.

We will employ a linear instability analysis to identify a representative longshore length scale of the instabilities. A parameter that supplies such an estimate is the most unstable wavenumber $\lambda_{max} = 2\pi k_{max}$. In a linear instability analysis, the problems governing the mean longshore current and the perturbation velocities are decoupled through linearization. Linear instability studies such as Dodd (1994) and Falqués and Iranzo (1994) consider a given basic state (created using a fixed friction or mixing coefficient) and examine the effect of varying the coefficients in the perturbation equations. They find that the increase of the coefficients in the perturbation equations lowers the growth rates of the instability and changes the location of the most unstable wavenumber only slightly.

Dodd *et al.* (1992) previously applied the linear instability theory to October 15 through October 18 during the SUPERDUCK experiment using the bathymetry transect from sled measurements and assuming straight-and-parallel contours. They examined current profiles generated with a mixing coefficient M of unity and a friction factor chosen to obtain a best fit with measurements of the mean longshore current. They obtained good agreement of the unstable wavenumbers with the observed range of wavenumbers and stated that the most unstable wavenumber associated with $M = 1$ for each day defines a representative length scale for the observed motions. Therefore, in our modeling effort the domain length for each day is chosen to be 16 times the wavelength that corresponds to this wavenumber so that sufficiently many waves can exist in the modeling domain.

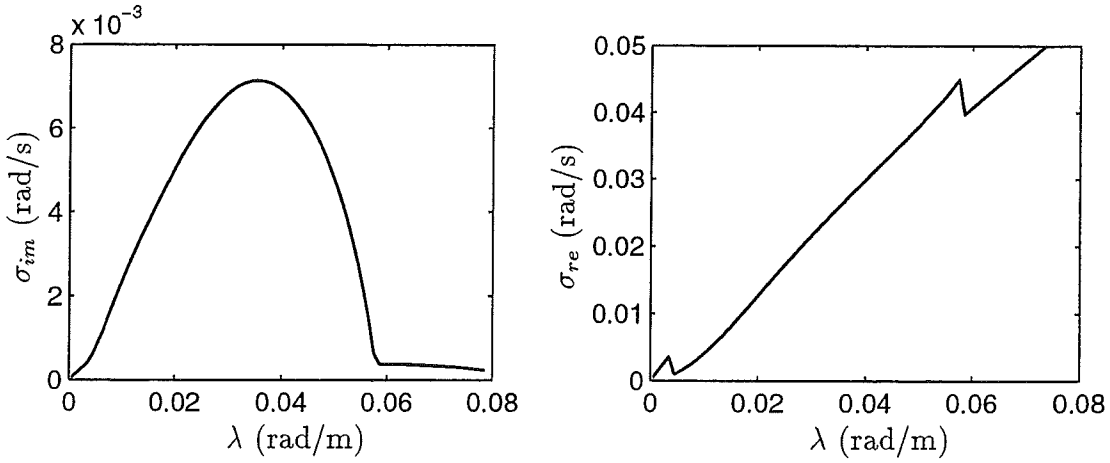

Figure 6.15: Linear instability results for October 15.

Table 6.2: Most unstable wavenumbers λ_{max} and corresponding longshore length scale L_max for October 15 through October 18.

Date	λ_{max} (rad/m)	L_max (m)
October 15, 09:45 am	0.0365	172.14
October 16, 10:20 am	0.0395	159.06
October 17, 11:00 am	0.0285	220.46
October 18, 11:40 am	0.0315	199.47

Since the prediction for λ_{max} is only altered slightly by the inclusion of the dissipational terms in the perturbation equations, the inviscid equations of Bowen and Holman (1989) are used. The current profiles for the four days with $M = 1$ were shown in Figures 6.11 through 6.14. The linear instability curves for these current profiles are shown in Figures 6.15 through 6.18. The speed of the motions predicted by the linear instability theory is given by $(\sigma_{re}/\lambda) = (f/k)$. The most unstable wavenumber λ_{max} along with the corresponding longshore length scale L_{max} are given in Table 6.2 for the four days of the SUPERDUCK experiment.

The longshore length scales defined above for each day are used for all

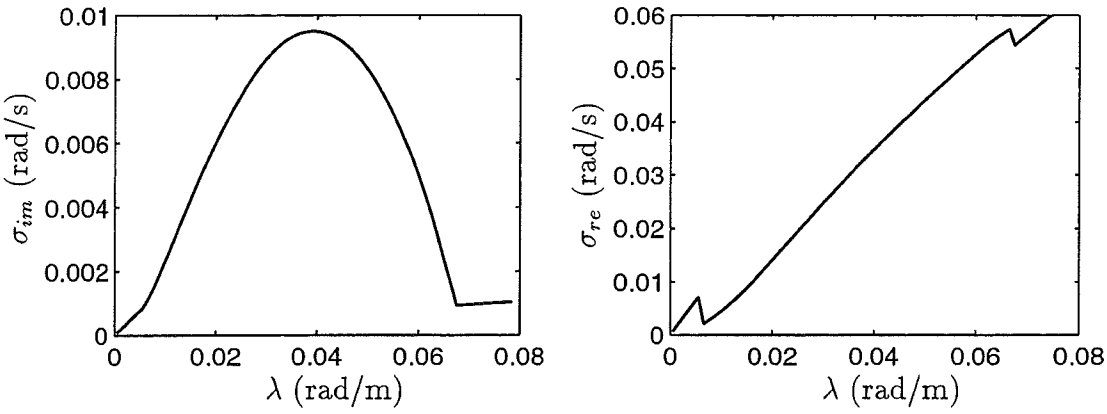

Figure 6.16: Linear instability results for October 16.

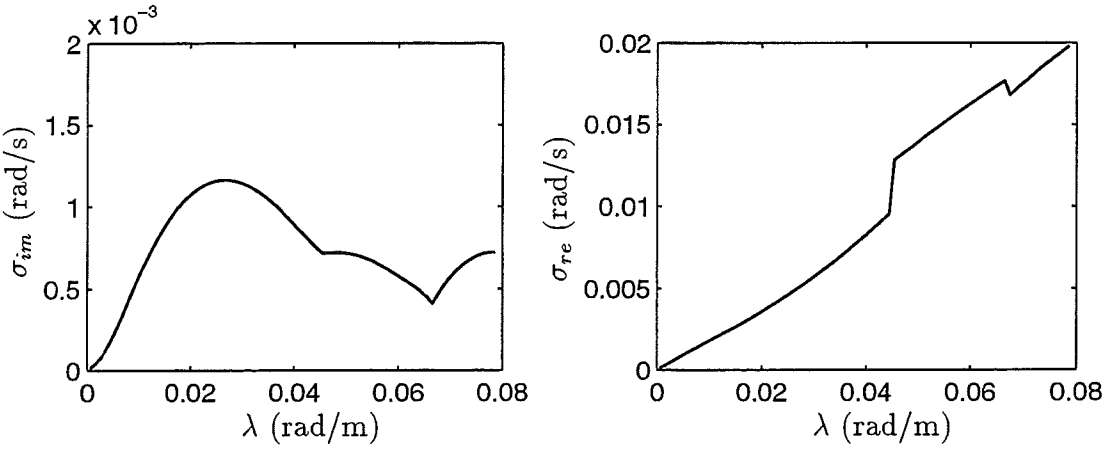

Figure 6.17: Linear instability results for October 17.

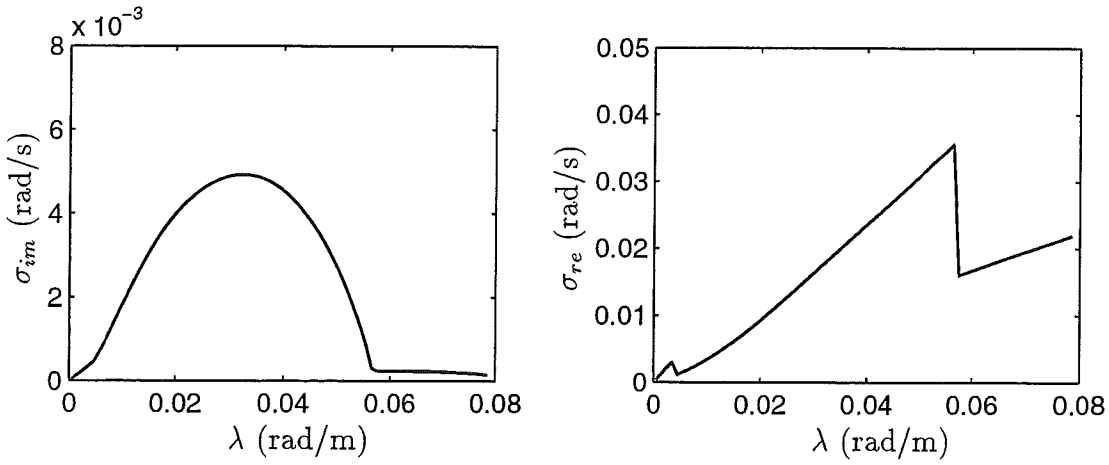

Figure 6.18: Linear instability results for October 18.

the simulations for that day even though the values of the friction factor and mixing coefficient are varied from one simulation to the next. For the purposes of identifying the most unstable wavenumber, the use of the inviscid perturbation equations of Bowen and Holman (1989) is justified. However, changing the damping coefficients alters the basic state that should be considered in the instability analysis. Examples of the resulting basic states for two different friction coefficients (c_f =0.003, 0.004) for October 16 are shown in Figure 6.19. Linear instability analysis (see Figure 6.20) predicts a higher growth rate for the current profile resulting from the lower choice of c_f but the most unstable wavenumber is not altered much. Note that the shear structure of the current profiles are not altered significantly so that the current profile for the lower c_f value has the same basic shape but a higher peak value. This result was also obtained by Dodd (1994).

Two basic states resulting from choosing a mixing coefficient M of zero and unity for October 16 were shown in Figure 6.12. Decreasing the mixing coefficient results in much higher gradients in the current profile along with a higher peak

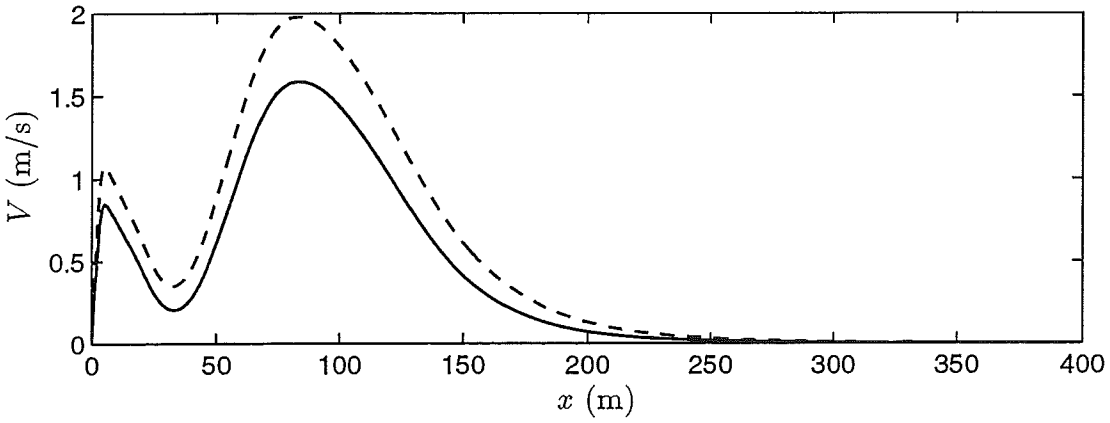

Figure 6.19: Longshore current for October 16 using $M = 1$. Friction coefficient $c_f = 0.004$ (——) and $c_f = 0.003$ (– –).

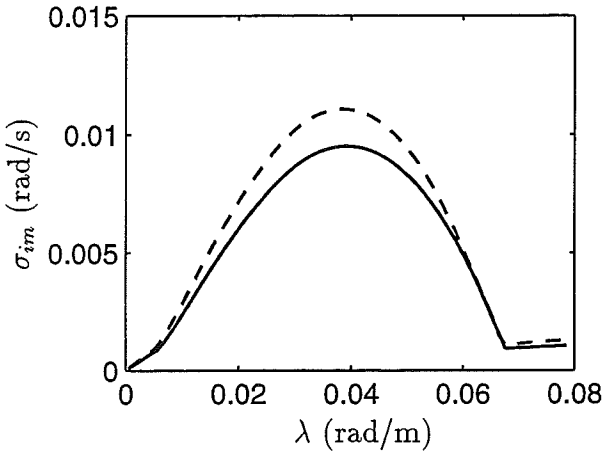

Figure 6.20: Growth rates for current profiles depicted in Figure 6.19. Friction coefficient $c_f = 0.004$ (——) and $c_f = 0.003$ (– –), $M = 1$.

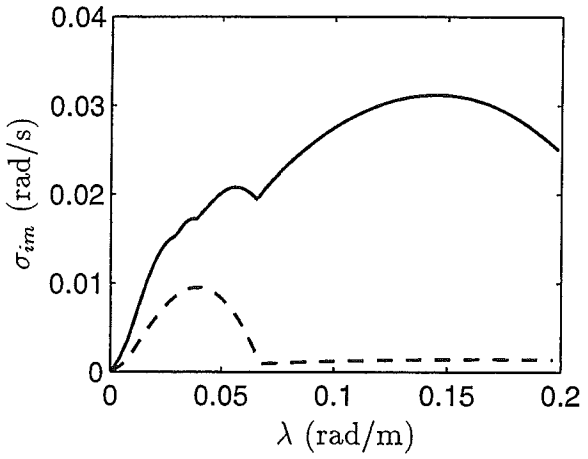

Figure 6.21: Growth rates for current profiles depicted in Figure 6.12. Mixing coefficient $M = 0$ (——) and $M = 1$ (– –) with $c_f = 0.004$.

value. Linear instability calculations for these two currents (see Figure 6.21) show that the current profile corresponding to $M = 0$ displays maximum growth rate at a higher wavenumber than the current profile with $M = 0$ resulting in shorter length scales for the instability. As a result, we can conclude that choosing λ_{max} associated with $M = 1$ is a conservative choice since the length scale associated with this profile is larger than for lower M-values. Therefore, the domain width for each day is defined by

$$L_y = 16 \times \left(\frac{2\pi}{\lambda_{max}} \right). \tag{6.36}$$

where the values for λ_{max} are given in Table 6.2.

6.4.2 Initial Conditions

Given an initial condition in the water surface elevation η and the velocities u and v, the governing equations are integrated in time. In contrast to the simulations in Chapter 5, the calculations are initiated with the fluid at rest except

for small perturbations in the longshore velocities given by

$$v(x, y, t = 0) = \frac{\epsilon}{\max\{f(y)\}} f(y) \tag{6.37}$$

where $\epsilon = 1 \times 10^{-4}$ and the function $f(y)$ is given by

$$f(y) = \sum_{j=1}^{\mathrm{ND}} \cos\left(\frac{2\pi j y}{L_y} + 2\pi\phi_j\right). \tag{6.38}$$

Here, ND is the number of times the most unstable wavelength fits into the modeling domain and is equal to 16, and ϕ_j represents a random phase function between -1 and 1. This initial condition ensures that the resulting longshore current is perturbed at the most unstable wavelength as well as all longer wavelengths that can exist in the modeling domain. Nonlinear interaction mechanisms present in the model equations will further cause the generation of any superharmonics.

The time integration of the governing equations is carried out using an explicit third order Adams-Bashforth scheme. A time step of 0.2 sec is used. Fourier and Chebyshev collocation schemes are used to compute spatial derivatives in the longshore and cross-shore directions, respectively. In the cross-shore direction 65 collocation points are used, whereas 512 collocation points are used in the longshore direction. The resolution in the y direction corresponds to the inclusion of 32 harmonics per most unstable wave. A Shapiro (1970) filter of order 16 is used in both horizontal directions. For more information about the solution method, the reader is referred to Chapters 3 and 4, or to Özkan-Haller and Kirby (1997).

Five hour simulations were carried out for each chosen combination of the coefficients c_f and M. Effects of varying one of the coefficients while keeping the second constant are analyzed.

6.5 Effects of Bottom Friction

We first analyze the effect of varying the friction coefficient from one simulation to the next. The value of the mixing coefficient M is kept constant at $M = 0.25$ which is an intermediate value in the range of realistic M-values given by (6.13). The resulting shear instabilities for each case propagate faster for lower values of c_f. The optimum choice of c_f is defined such that the propagation speed observed in the data is predicted to within 5%. In the next subsections we show simulations for October 15 through 18 for friction coefficients bracketing the optimum value with which the propagation speed of the disturbances in the data is reproduced.

6.5.1 Simulations of October 15

Simulations for October 15 were carried out for friction coefficients of $c_f = 0.0015, 0.002, 0.003$. On this day, the measurement array was located approximately 45 m offshore of the shoreline in the bar trough region. Time series for the simulations at this cross-shore location are shown in Figure 6.22. Also shown are velocity time series from the current meter located closest to the cross-shore transect where the utilized depth profile was measured as well as sled data were collected. The current measurements displayed in the lowermost panel of Figure 6.22 have been low-pass filtered with a cutoff frequency of 0.01 Hz.

We observe that the spin-up time of the instabilities is short compared to the simulations for the plane beach case documented in Chapter 5. The instabilities reach finite amplitude within an hour of the start of the simulations. As the friction coefficient is increased the spin-up time increases slightly. In all three time series short scale disturbances are observed to grow initially. The time scales

associated with these initial fluctuations are shorter for lower friction factor. Further into the simulations large amplitude long time oscillations develop and are especially pronounced in the longshore velocities. The time scales associated with these oscillations are in excess of 30 min. These long time oscillations are less evident in simulations with a high friction coefficient. In general, more energetic oscillations are observed for lower friction coefficients. The cross-shore velocities display periods of small energy fluctuations (indicating a primarily longshore directed flow) followed by periods of high amplitude fluctuations. This type of intermittent behavior is more evident for lower friction factor. The time scales associated with the intermittent high amplitude fluctuations in u are shorter for lower friction factor. Especially evident in the time series for $c_f = 0.002$ are situations where a near-zero longshore velocity occurs at the same time as a high cross-shore velocity (up to 0.3 m/s) indicating purely offshore directed flow. The data, shown in the lowermost panel of Figure 6.22, does not display an intermittent character and also shows no evidence of oscillations with time scales of 30 minutes or longer.

The longshore-averaged longshore velocity is observed to stay small until the instabilities grow to finite amplitude. A mean current is abruptly generated as the instabilities grow. The value of the mean current is higher for lower friction. Some time variability exists in the longshore-averaged current, especially in the case involving a lower friction factor.

Frequency-longshore wavenumber spectra for the three cases are constructed utilizing a Fourier transform in both longshore direction and time. The last 2.7 hours of the simulations are used. The spectra are calculated using a cosine taper on the first and last 10% of the time series. The resulting spectra are smoothed by averaging over 8 frequencies and 2 wavenumbers. The spectra obtained using

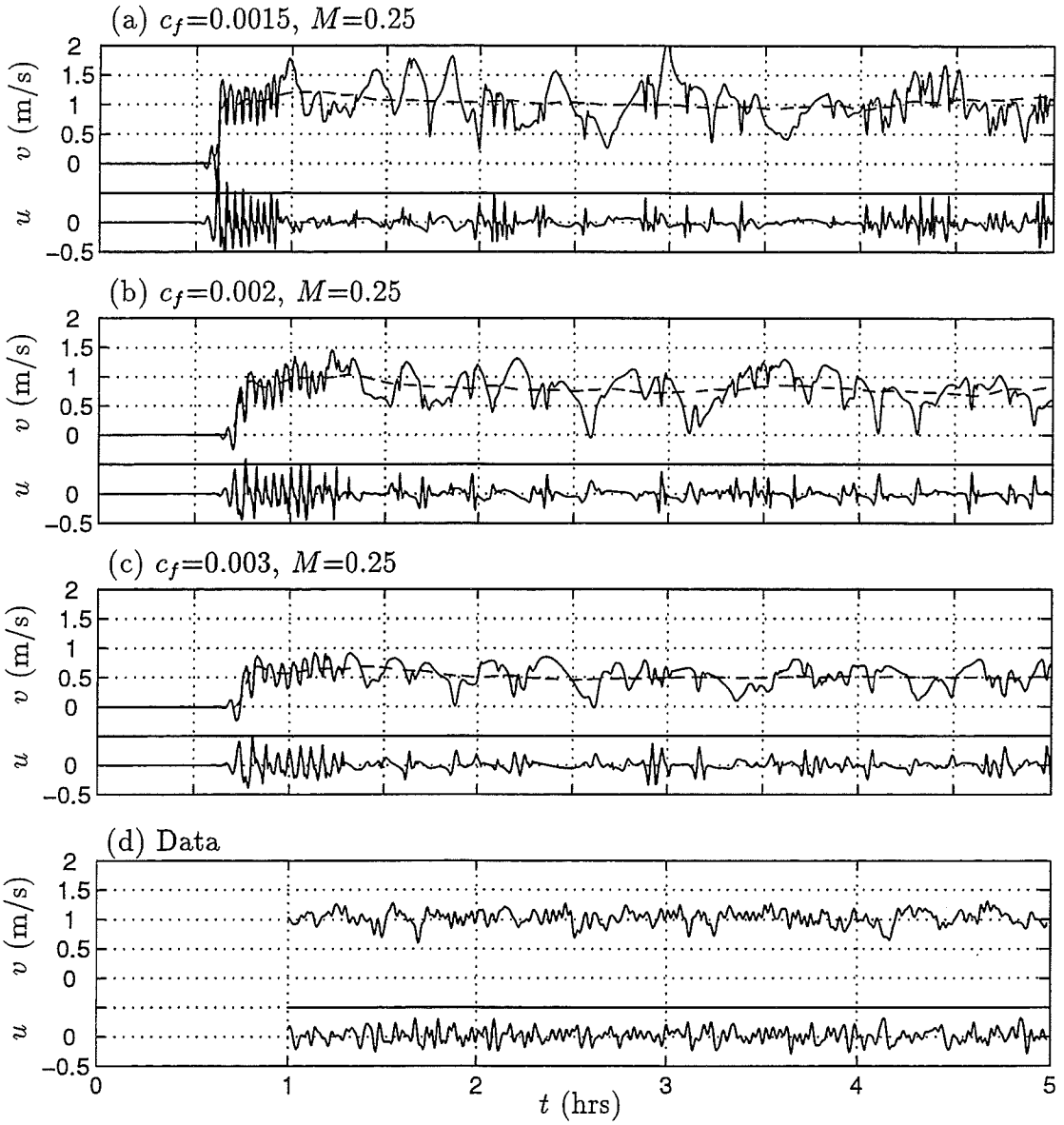

Figure 6.22: October 15: Time series of velocities u, v and $\langle v \rangle$ (– –) at (x, y)=(45 m, $L_y/2$) and time series of velocities u and v of data.

time series of longshore velocities are shown in Figure 6.23, whereas the spectra for the cross-shore velocities are shown in Figure 6.24. The frequency-wavenumber spectra of the measured velocities are also included for comparison.

Examining the frequency-wavenumber spectra of the longshore velocities, it is seen that the disturbances travel faster for a lower value of the friction coefficient. A 25% reduction in the friction factor from $c_f = 0.002$ to $c_f = 0.0015$ results in a 30% increase of the propagation speed. On the other hand, a 50% increase in the friction coefficient (from $c_f = 0.002$ to $c_f = 0.003$) results in a 20% decrease in propagation speed. The range of frequencies at which oscillations exists also increases with decreasing friction coefficient. The slopes and intercept values of the dispersion line predicted for $c_f = 0.002$ reproduce the data well. The spectra of the cross-shore velocities display similar trends.

The time and longshore-averaged mean longshore current velocities for the three cases are shown in Figure 6.25. The longshore averages are performed over the entire width of the domain while the time averages are computed using the last 2.7 hours of the computed time series. The three current profiles display similar gradients, but, as expected, a stronger current profile results from the choice of a low friction factor. A 25% reduction in the friction factor from $c_f = 0.002$ to $c_f = 0.0015$ results in a 20% increase of the peak current velocity. A 50% increase in the friction coefficient (from $c_f = 0.002$ to $c_f = 0.003$) results in a 20% decrease in the peak current velocity. The current profiles display a broad peak located about 100 m offshore and a localized peak close to the shore. Significant currents are observed in the trough region. The current resulting from the choice $c_f = 0.002$ reproduces the measured value of the current in the trough region whereas the case with $c_f = 0.003$ reproduces the peak current. Caution should be used in interpreting the sled data to model agreement since the measurements

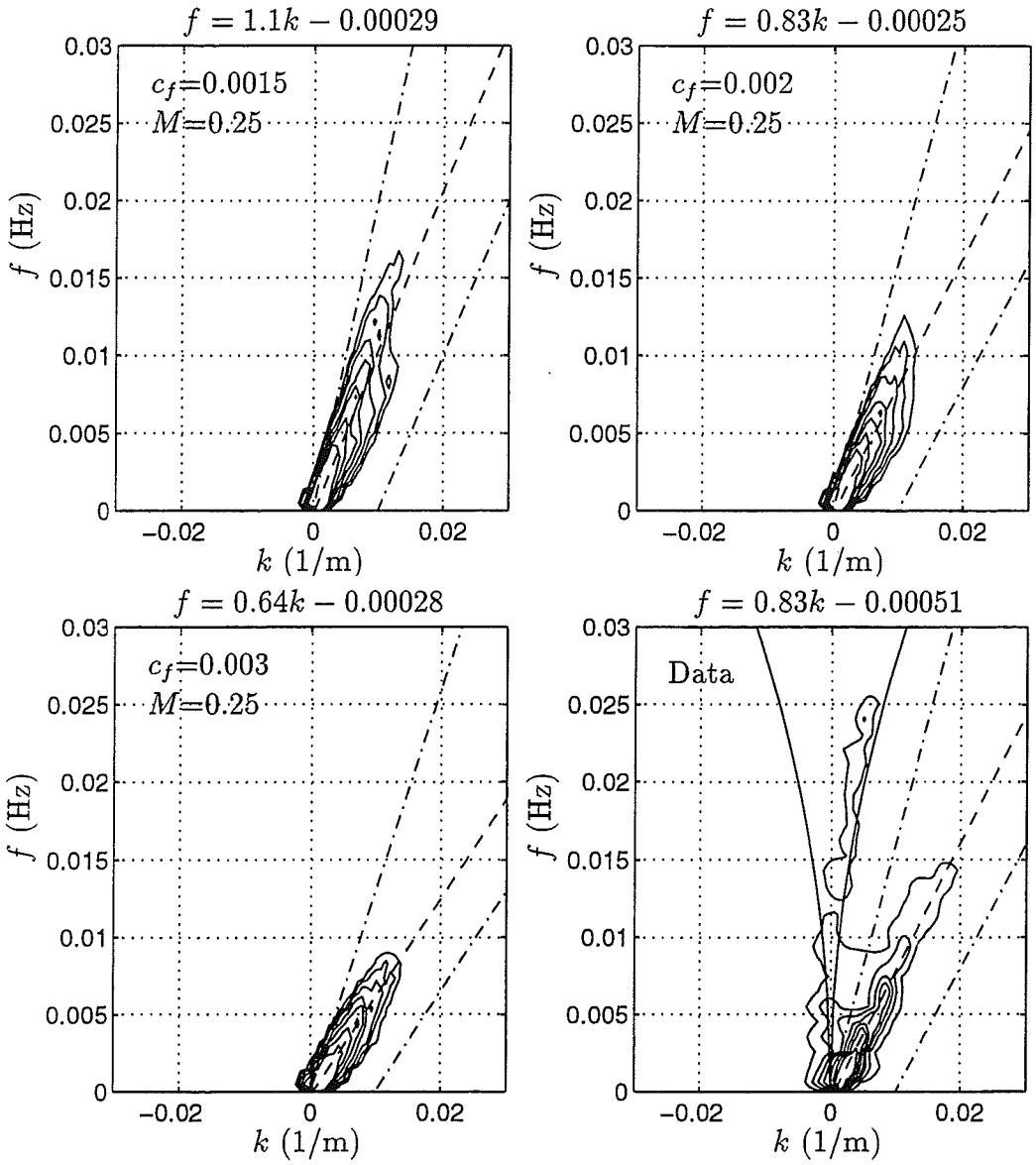

Figure 6.23: October 15: Frequency-cyclic wavenumber spectra $S(f,k)$ (m^3/s) for computed and measured longshore velocity at x =45 m. The values for c_{est} are 1 m/s for c_f = 0.0015, 0.8 m/s for c_f = 0.002, 0.75 m/s for c_f = 0.0015, and 0.8 m/s for data, and are used in Equation (6.3) to construct the upper and lower cut-off lines (– · –) of the shear wave energy. Contour levels plotted are (10, 30, 60, 100, 200, 400, 800). The equation for the best fit dispersion line (– –) is noted above each plot.

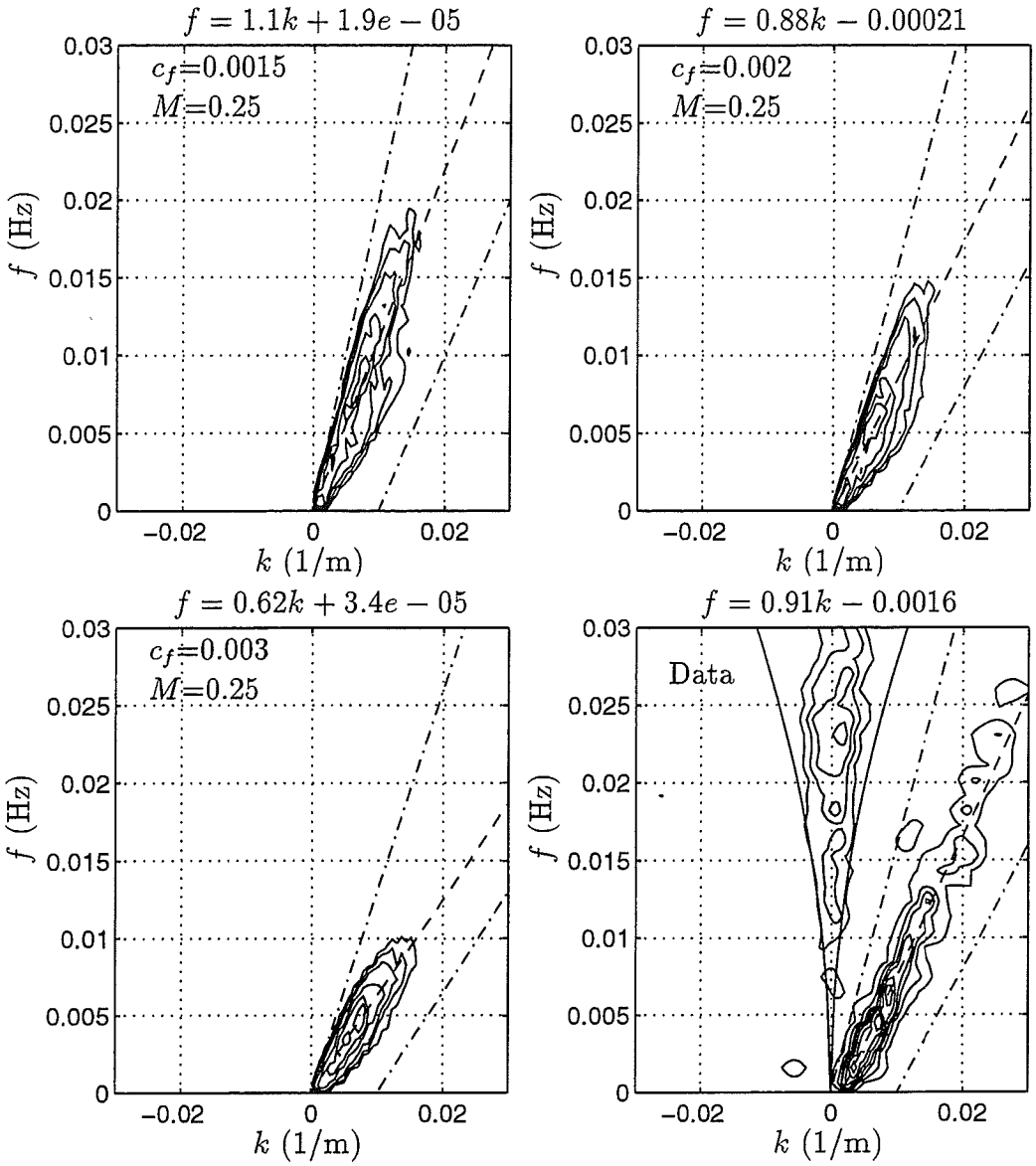

Figure 6.24: October 15: Frequency-cyclic wavenumber spectra $S(f,k)$ (m^3/s) for computed and measured cross-shore velocity at x =45 m. The values for c_{est} are 1 m/s for $c_f = 0.0015$, 0.8 m/s for $c_f = 0.002$, 0.75 m/s for $c_f = 0.0015$, and 0.8 m/s for data, and are used in Equation (6.3) to construct the upper and lower cut-off lines (– · –) of the shear wave energy. Contour levels plotted are (10 30 60 100 200 400 800). The equation for the best fit dispersion line (— —) is noted above each plot.

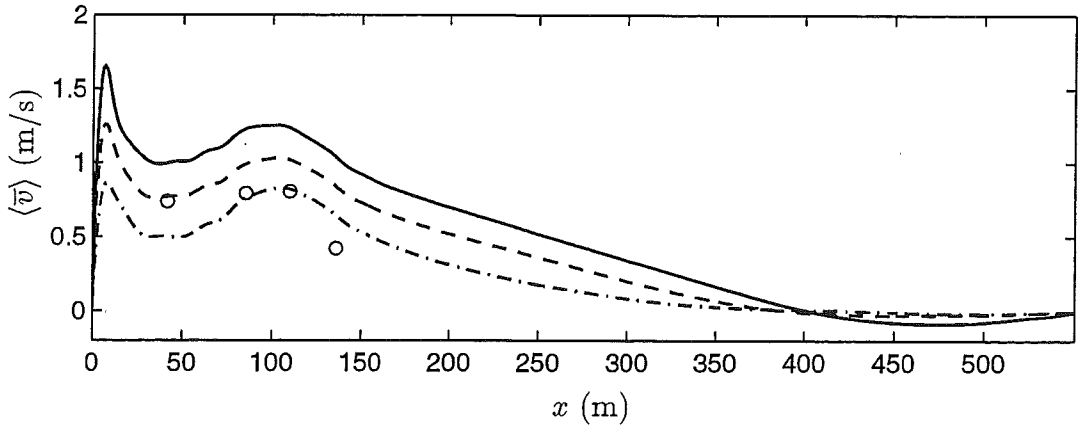

Figure 6.25: October 15: Time and longshore-averaged longshore currents $\langle\overline{v}\rangle$ for $c_f = 0.0015$ (——), $c_f = 0.002$ (– –), $c_f = 0.003$ (– · –) and sled data (o).

were carried out sequentially and sled data and model data are based on very different averaging periods.

The cross-shore variation of the perturbation kinetic energy is shown in Figure 6.26. We can observe that the motions resulting from the lower choice of the friction factor are more energetic. In the case with $c_f = 0.0015$, the motions are energetic at the offshore boundary and are possibly affected by it, since the shape of the curve for $c_f = 0.0015$ leaves the impression that energy is "piled up" against the offshore boundary. Except for the region close to the offshore boundary, the curves display similar shapes with two local maxima shoreward and seaward of the location of the mean current maximum. Although the mean current $\langle\overline{v}\rangle$ displays a local maxima close to the shoreline, the perturbation energy decreases monotonically inside the surf zone.

Contour plots of the vorticity

$$q = \frac{\partial v}{\partial x} - \frac{\partial u}{\partial y} \tag{6.39}$$

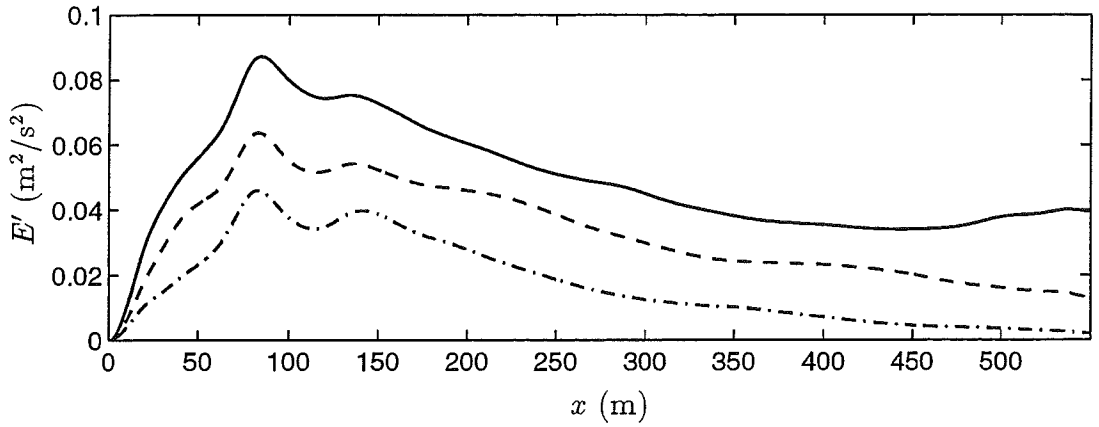

Figure 6.26: October 15: Time and longshore-averaged longshore perturbation kinetic energy $\frac{1}{2}\langle\overline{u'^2} + \overline{v'^2}\rangle$ for $c_f = 0.0015$ (——), $c_f = 0.002$ (– –), $c_f = 0.003$ (– · –).

at an instant in time are shown for the three cases in Figures 6.27 through 6.29. In the simulations of shear instabilities over a plane beach the potential vorticity associated with a longshore uniform longshore current was observed to display two regions with positive and negative vorticity inshore and offshore of the peak current position, respectively. Since the mean current profiles in the present simulations display two local maxima, the vorticity field in the absence of any fluctuating motions will display four regions of alternating positive and negative vorticity. Since the current peak located near the shoreline is very narrow, the first two layers of positive and negative vorticity are expected to be confined to a small region close to the shoreline.

Figure 6.27 shows snapshots of the vorticity field at two time levels for the simulation with $c_f = 0.0015$. The first two layers of positive and negative vorticity are observed to be closely confined to the shoreline. The outer two layers of vorticity display complicated behavior. As in the simulations for the plane beach, regions of concentrated positive and negative vorticity are observed. They are,

however, irregularly spaced in the longshore direction and display the character of vortex pairs. The vorticity in the regions of longshore directed flow between the vortex pairs is weak compared to the strength of the vortex pairs. This observation suggests that the longshore current profile does not display high gradients in the regions between vortex pairs. Vortices appear to be shed offshore, propagating as far out as the offshore boundary. The offshore vortices appear in the form of pairs (see $t = 5$ hrs, $(x, y) \approx (400, 2600)$ m) or single vortices surrounded by a region with opposite vorticity (see $t = 5$ hrs, $(x, y) \approx (400, 2000)$ m). Activity in the inner layer of vorticity is especially evident around $x \approx 500$ m at $t = 5$ hrs.

The vorticity field for $c_f = 0.002$ shown in Figure 6.28 displays a similar character; however, the vortices appear to be slightly weaker. Vortices are shed offshore but the build-up of vortices at the offshore boundary is less severe. For $c_f = 0.003$ (see Figure 6.29) the vorticity field is much less energetic. Especially the negative vortices appear to be weaker than for the cases involving lower friction factors. Vortices are still shed offshore, but judging from the number of offshore vortices, the process occurs less often. For the cases involving lower friction, vortices in the nearshore region are observed to appear grouped together, explaining the intermittent character of the time series.

In order to visualize the time dependent character of the flow, simulations were carried out for another hour for the case involving $c_f = 0.002$ and $M = 0.25$. Simulations are initiated with the vorticity field depicted in Figure 6.29 at $t = 5$ hrs. Snapshots of the vorticity field are recorded every 5 minutes and are displayed in Figures 6.30 through 6.33. Disturbances seen in the snapshots propagate in the $+y$-direction at the rate of approximately 250 m every 5 min.

Many interesting events can be observed in the series of snapshots. We will focus on four sequences. In Figure 6.30 we observe that at $t = 0$ min, positive and

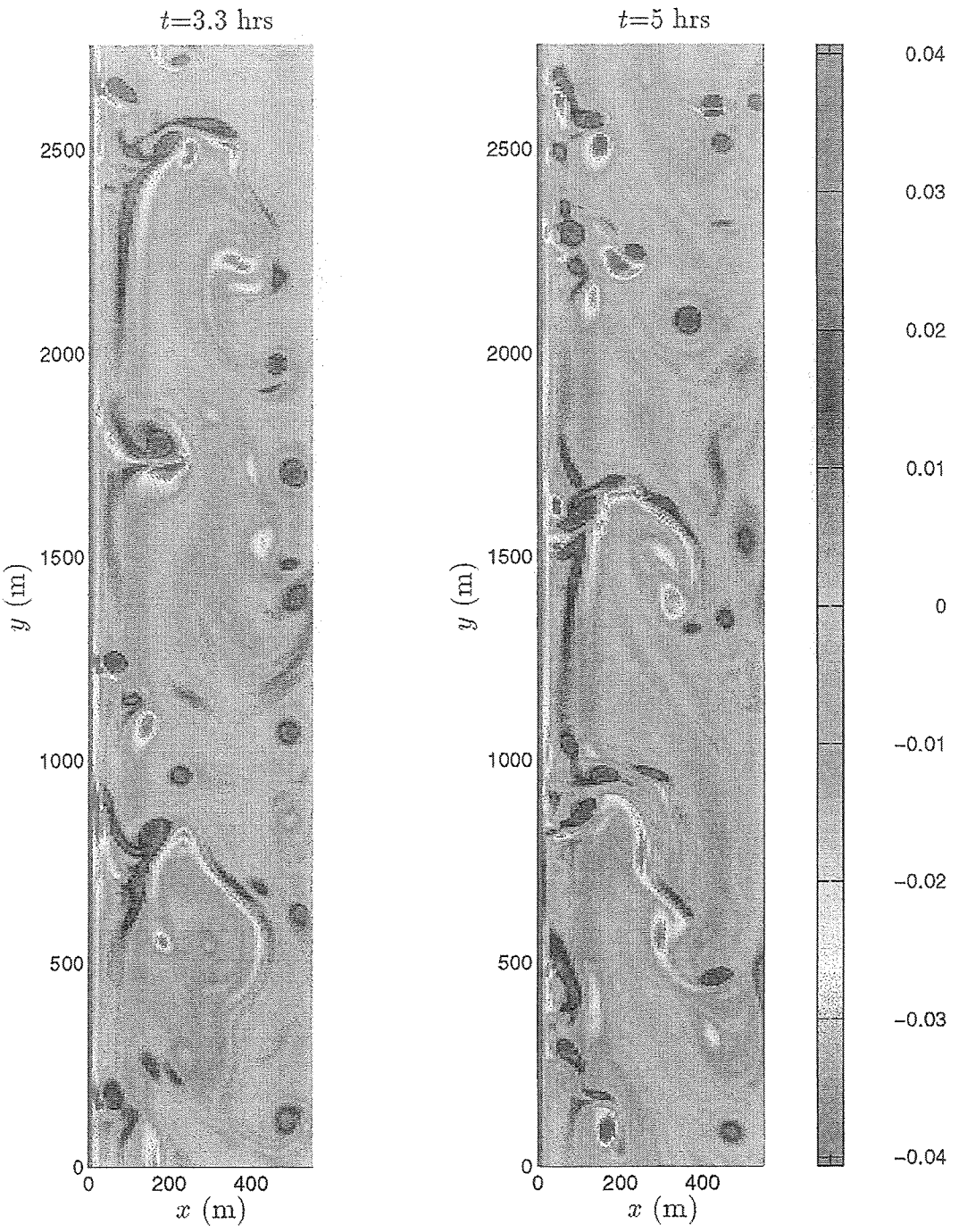

Figure 6.27: October 15: Contour plots of vorticity q (1/s) for $c_f = 0.0015$ and $M = 0.25$.

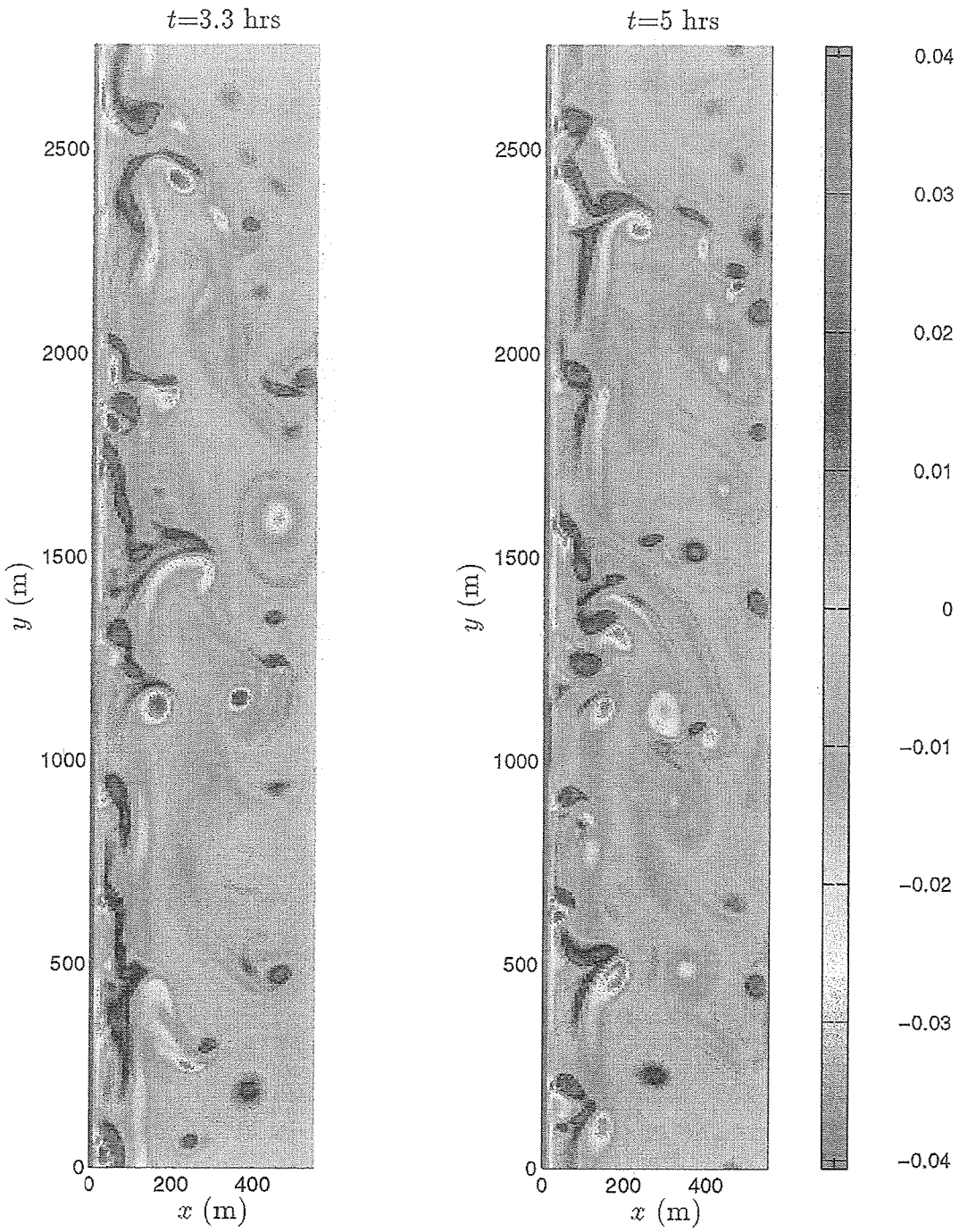

Figure 6.28: October 15: Contour plots of vorticity q (1/s) for $c_f = 0.002$ and $M = 0.25$.

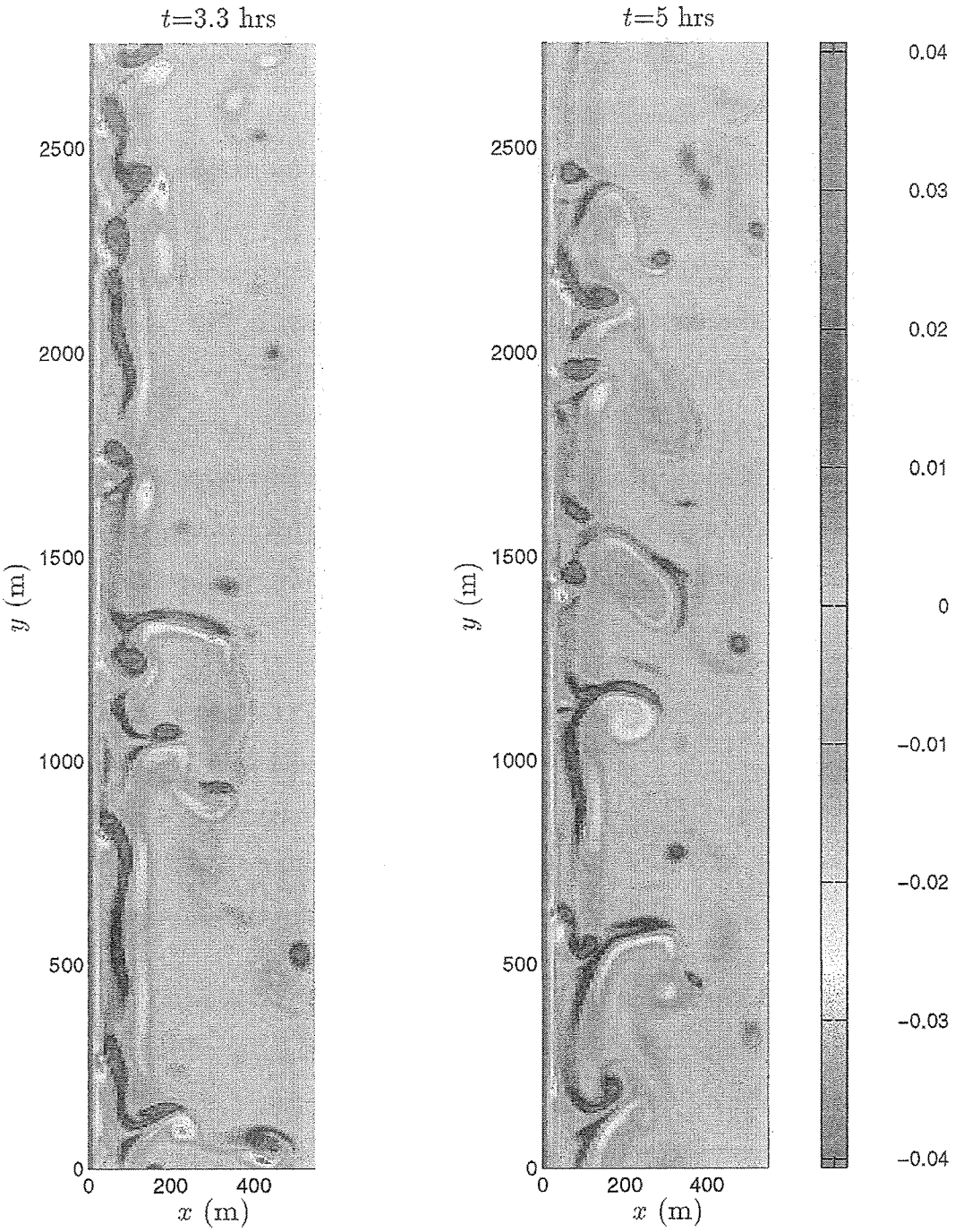

Figure 6.29: October 15: Contour plots of vorticity q (1/s) for $c_f = 0.003$ and $M = 0.25$.

negative vortices occur in a cluster in the nearshore region around $y = 1250$ m. At $t = 10$ min, the cluster has propagated to y =1750 m and has produced two vortex pairs that revolve around each other. Moving to Figure 6.31, we find that at $t = 15$ min one of the vortex pairs has intensified and is propelled offshore in a direction opposing the mean longshore flow. At $t = 20$ min, the vortex pair is located at $(x, y) = (450, 1600)$ m. The vortices of opposite sign appear to be rotating around each other. At $t = 25$ min, their location has not changed significantly; however, the two vortices appear to have separated slightly. In Figure 6.32, we notice that the positive vortex is located at $(x, y) = (400, 1500)$ m at $t = 30$ min whereas the negative vortex is located about 200 m downdrift. They are advected slightly in the 10 minutes that follow and can be observed to weaken. In Figure 6.33, their location does not change significantly. The negative vortex weakens and joins a region of negative vorticity whereas the positive vortex survives until $t = 55$ min.

A second relevant observation is related to the vortices that reach the offshore boundary. At $t = 0$ min, a strong positive vortex exists at the offshore boundary around y =500 m. Throughout the snapshots, this vortex is observed to remain at this location and weaken. Other vortices at the offshore boundary around $y = 2000$ m at $t = 0$ min are observed to interact with each other as time progresses; however, they remain close to their original position.

The third event details the evolution of a vortex pair that develops on the inner layers of negative vorticity. At $t = 0$ min, the pair is located very close to the shoreline at $y = 700$ m. At $t = 5$ min the vortex pair is observed to have detached from the inner layer but is still located close to the shoreline at $y = 1000$ m. The vortices appear to have drifted apart slightly at $t = 10$ min and are located around $y = 1300$ m. At $t = 15$ min the positive vortex appears to be stronger and is located around $y = 1700$ m. It is leaving the negative vortex behind which is

observed to weaken. At the same instance the vortex cluster we analyzed before is shedding two vortex pairs. The two vortices that we have been following in this paragraph propagate faster than the cluster. At $t = 20$ min, the positive vortex is joining the cluster at about $y = 2000$ m while the negative vortex is located just behind it in the inner surf zone and is weakened significantly. At $t = 25$ min, it is very difficult to pick out the negative vortex, but a strong vortex pair has evolved from the cluster and is located at $y = 2250$ m. At $t = 30$ min the vortex pair sheds vortices offshore which form a new vortex pair at $t = 40$ min around $(x, y) = (400, 2500)$ m. In the next 15 minutes the vortices forming this new pair separate and dissipate in a region around $(x, y) = (300, 2500)$ m.

Finally, we follow a disturbance located at $y = 200$ m at $t = 0$ min. It appears to be made up of two vortex pairs. One pair is associated with the outer layers of positive and negative vorticity, whereas the other is associated with the inner layers. At $t = 5$ min, the vortices have propagated to $y = 400$ m. At $t = 10$ min, the two pairs have separated slightly and are located around $y = 600$ m. At $t = 15$ min, the vortex pair associated with the outer layer has strengthened and is located at $y = 750$ m. The other vortex pair is in front of it at $y = 900$ m. At $t = 20$ min, the outer vortex pair is in the process of shedding a new vortex pair. At $t = 25$ min, the outer vortex pair is located around $y = 1100$ m and has shed a vortex pair offshore. It appears to be weakened significantly. It is also observed to retreat towards the shoreline. The new vortex pair is active at $x = 250$ m and $y = 1000$ m. The set of event outlined here carries the characteristics of a migrating transient rip current.

From our observations of the time-dependent behavior of the instability field, we can conclude that the offshore boundary is not transparent to vortex motions, but that vortices reaching the boundary tend to remain there. The motions

at the offshore boundary do not affect the bar trough region, which is located about 30–40 m away from the shoreline. Comparisons with field measurements will be carried out at this cross-shore location. The vortex structures are highly time dependent and, at times, are reminiscent of transient rip currents (see for example $t = 45$ min, $y = 750$ m).

6.5.2 Simulations of October 16

Simulations for October 16 were carried out for friction coefficients of $c_f = 0.003, 0.0035, 0.004$. The transect at which the sled measurements and depth profile were collected for October 16 was located further north than for October 15. At this location the measurement array was located approximately 35 m offshore of the shoreline. Time series for the simulations at this offshore location are shown in Figure 6.34. Also shown are low-pass filtered velocity time series from the current meter located closest to the cross-shore transect. The time series show that the instabilities reach finite amplitude about 30 minutes into the simulation. For $c_f = 0.003$ the instabilities reach finite amplitude slightly sooner than for the other cases. The mean current in each case is generated at the same time as the spin-up of the instabilities and displays some time variability. For all three cases, short time scale oscillations are observed during the first 30 minutes of the simulation after the instabilities are initiated. Further into the simulations, oscillations with longer time scales are observed. However, oscillations with time scales of 30 minutes, that were seen in time series for October 15, are not observed in this case. The longshore current oscillations are very energetic and are negative at times. This behavior is not observed in the time series of the data where longshore velocities are always observed to be larger than 0.25 m/s. The intermittent character of the motions is not as pronounced as for the October 15 simulations. The differences between the time series for the three friction coefficient are also

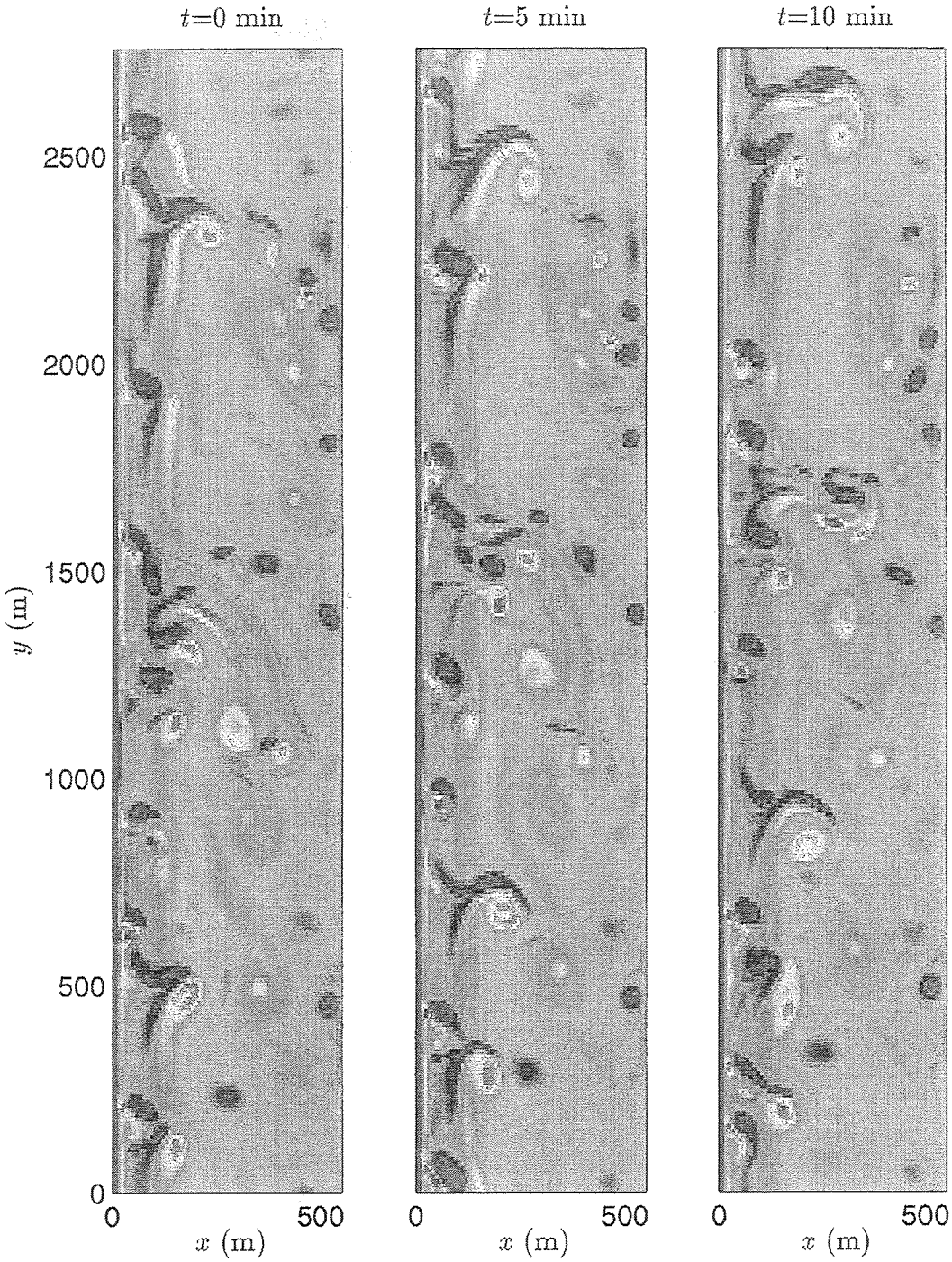

Figure 6.30: October 15: Time evolution of vorticity q (1/s) for $c_f = 0.002$ and $M = 0.25$.

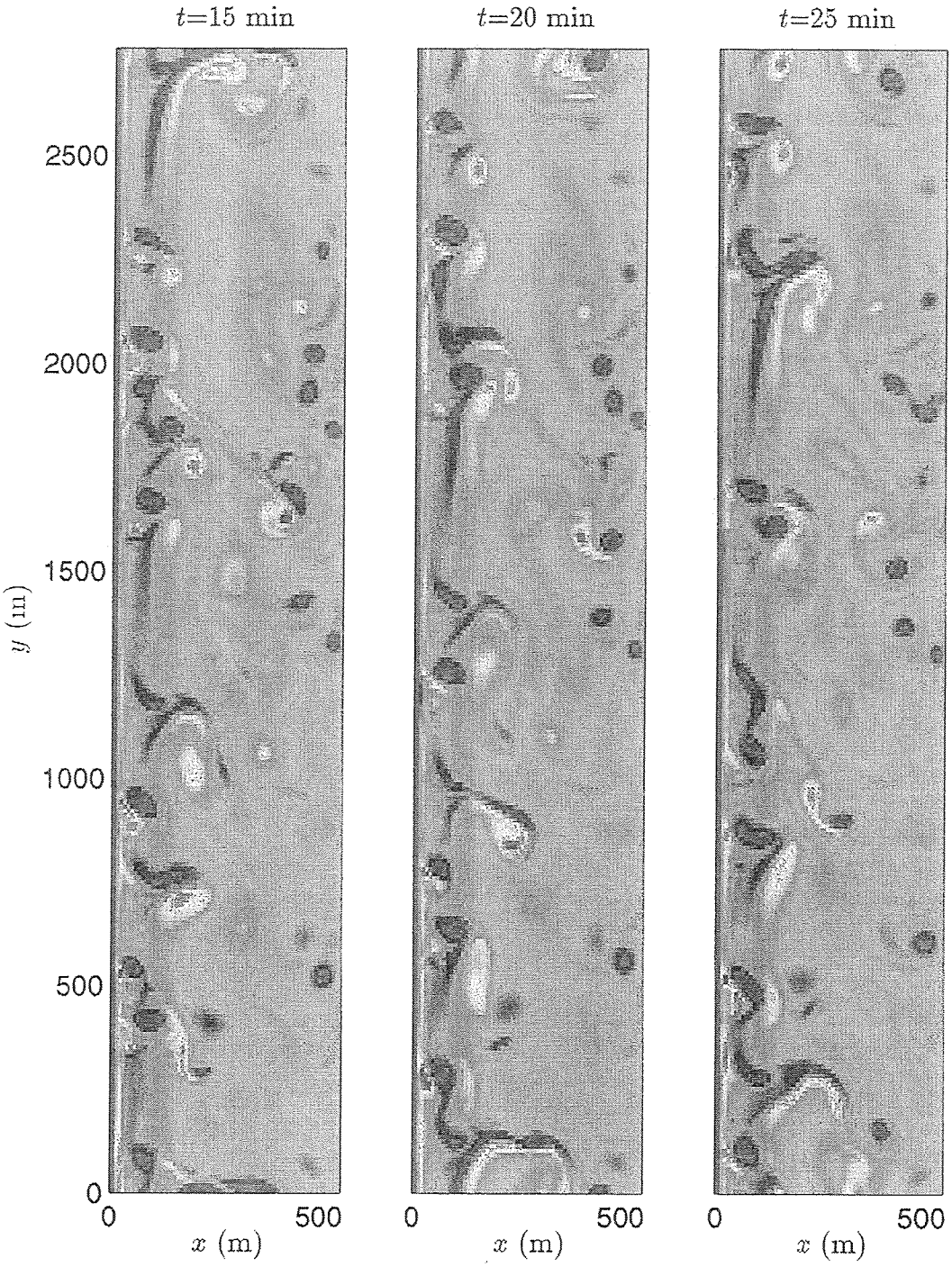

Figure 6.31: October 15: Time evolution of vorticity q (1/s) for $c_f = 0.002$ and $M = 0.25$ (continued).

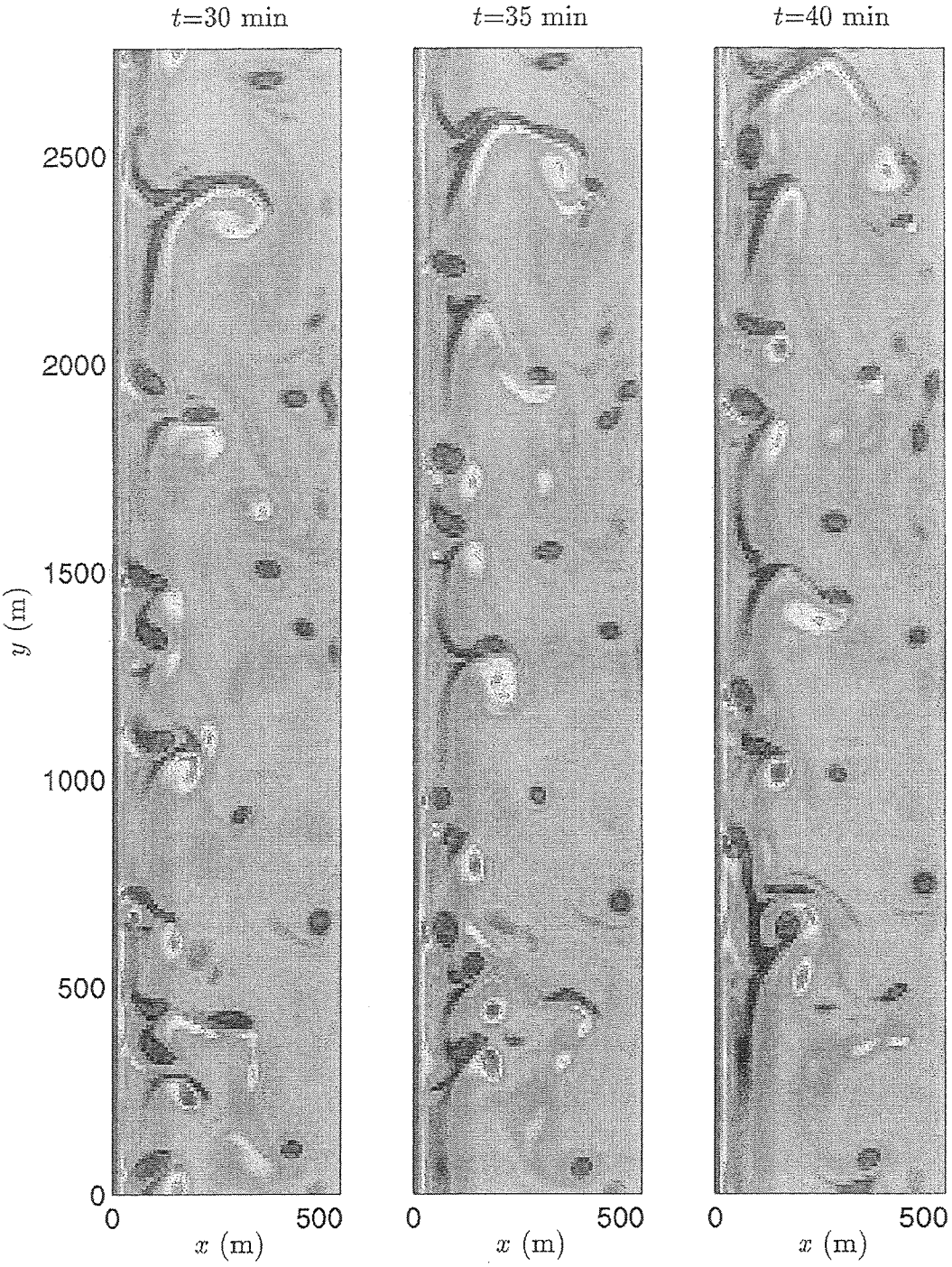

Figure 6.32: October 15: Time evolution of vorticity q (1/s) for $c_f = 0.002$ and $M = 0.25$ (continued).

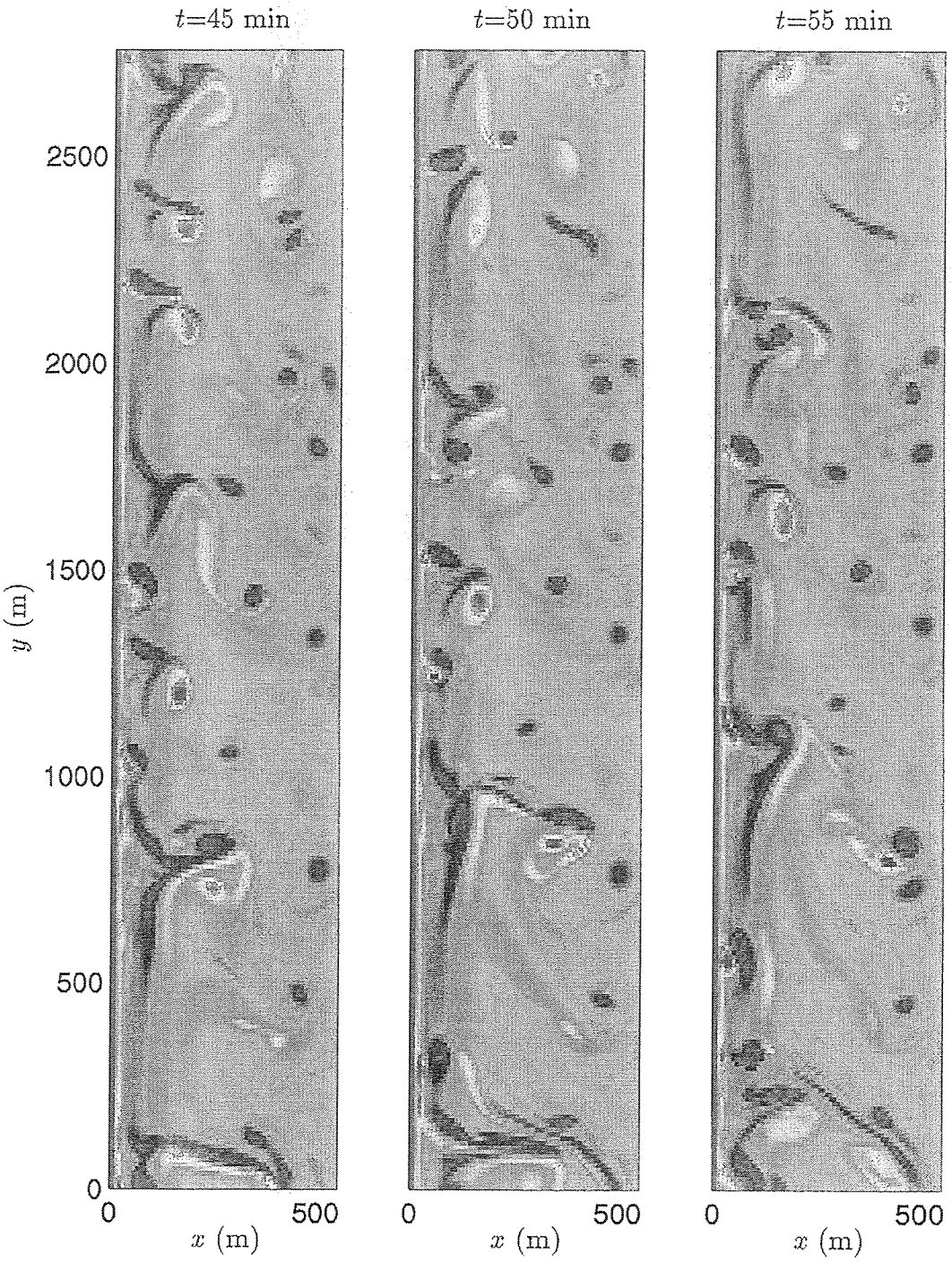

Figure 6.33: October 15: Time evolution of vorticity q (1/s) for $c_f = 0.002$ and $M = 0.25$ (continued).

not as pronounced. However, it should be noted that the variation in the friction coefficient from the mid value of 0.0035 to the high and low values is only 15%.

The frequency-longshore wavenumber spectra for the longshore velocities are shown in Figure 6.35 along with data. The range of frequencies affected by the instabilities is larger for lower friction factor. The intercept values of the best fit dispersion lines for the simulations and data are small. The slope of the dispersion lines decreases for increasing friction factor. An increase in the friction factor of 0.0005 from $c_f = 0.003$ to $c_f = 0.0035$ causes a decrease in the propagation speed of 0.15 m/s. Further increase in the friction factor by 0.0005 only decreases the propagation speed by 0.7 m/s suggesting that changes in the friction factor have a more pronounced effect for low friction. The slope of the dispersion line for the data is best reproduced by simulations for $c_f = 0.0035$. The frequency-longshore wavenumber spectra of the cross-shore velocities shown in Figure 6.36 display similar trends.

The differences between the three cases are most readily observed when analyzing the time and longshore-averaged quantities. The mean longshore currents associated with the three simulations are shown in Figure 6.37. It can be observed that the mean current associated with the lowest value of the friction factor is most energetic. The three current profiles display similar gradients. The longshore current velocity from sled measurements in the trough region (at about 35 m) is best reproduced by the profile with $c_f = 0.0035$. The current profiles exhibit two peaks. A narrow peak is located close to the shoreline while a broader peak is centered around 90 m.

Cross-shore distributions of the mean perturbation kinetic energy are shown in Figure 6.38. The cross-shore distributions are similar for all three cases but the kinetic energy associated with $c_f = 0.003$ is observed to be largest. Its offshore

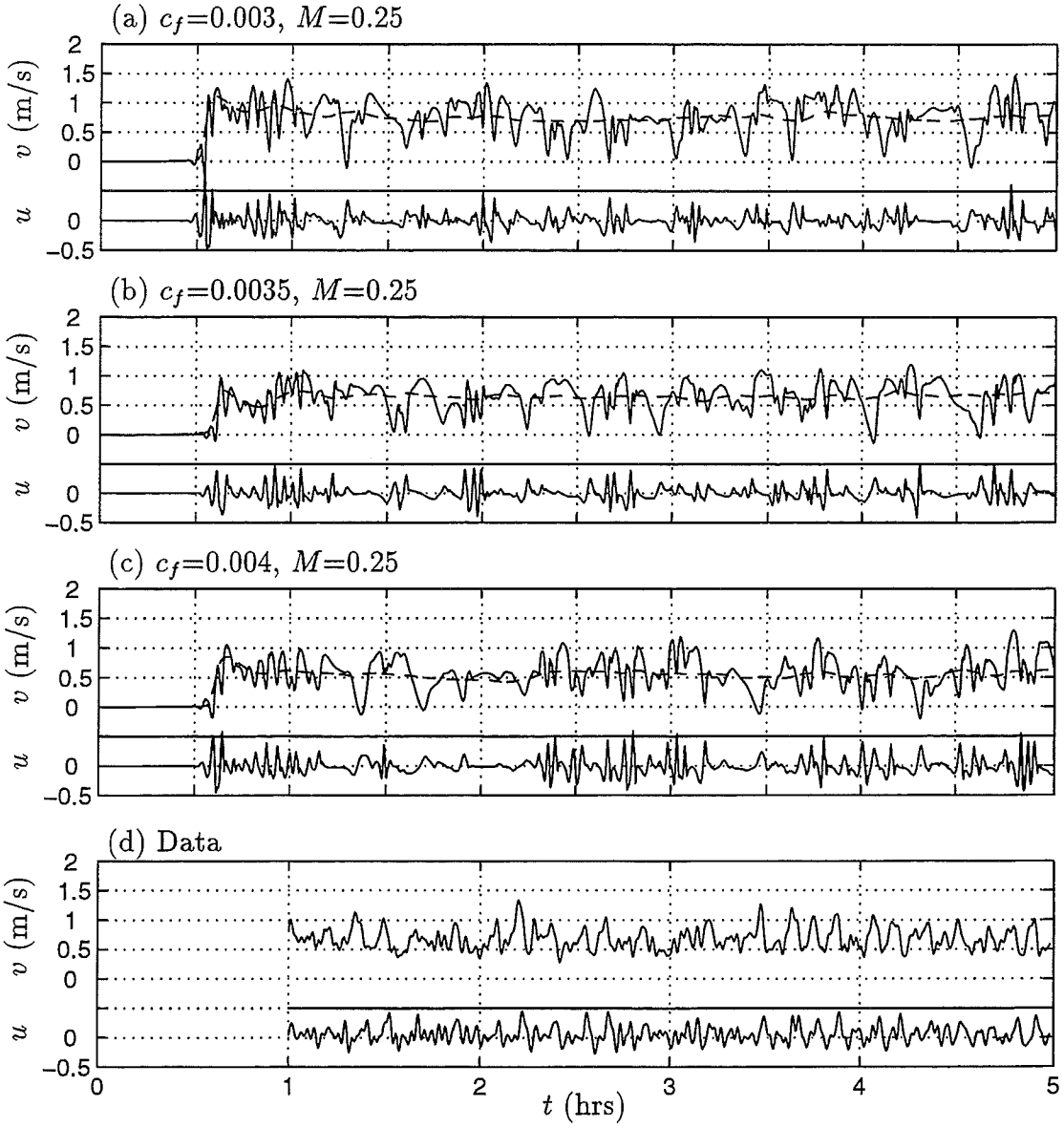

Figure 6.34: October 16: Time series of velocities u, v and $\langle v \rangle$ (– –) at (x, y)=(35 m, $L_y/2$) and time series of velocities u and v of data.

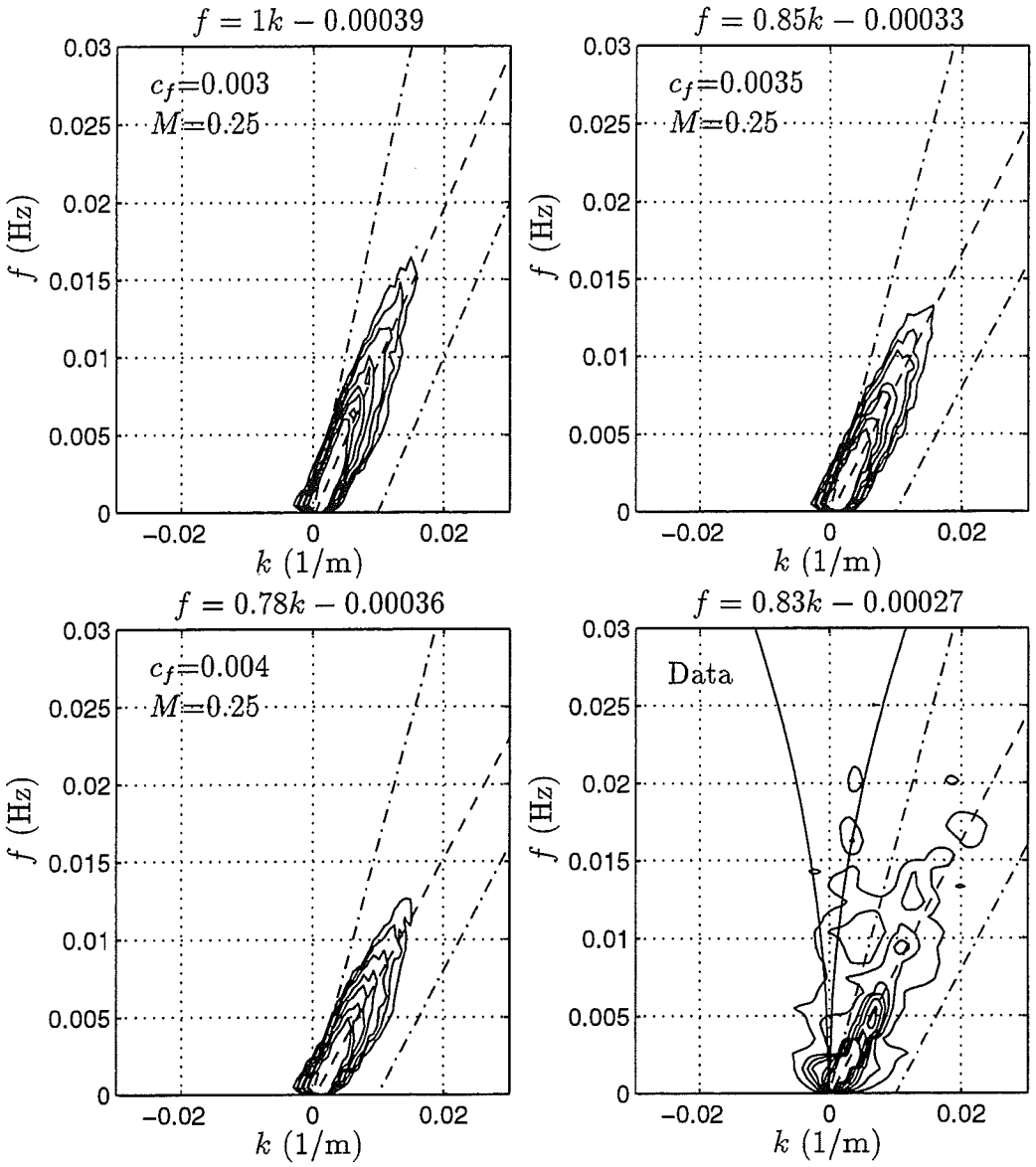

Figure 6.35: October 16: Frequency-cyclic wavenumber spectra $S(f,k)$ (m^3/s) for computed and measured longshore velocity at x =35 m. The values for c_{est} are 1 m/s for c_f = 0.003, 0.8 m/s for c_f = 0.0035 and c_f = 0.004, and 0.8 m/s for data, and are used in Equation (6.3) to construct the upper and lower cut-off lines (– · –) of the shear wave energy. Contour levels plotted are (10, 30, 60, 100, 200, 400, 800). The equation for the best fit dispersion line (— —) is noted above each plot.

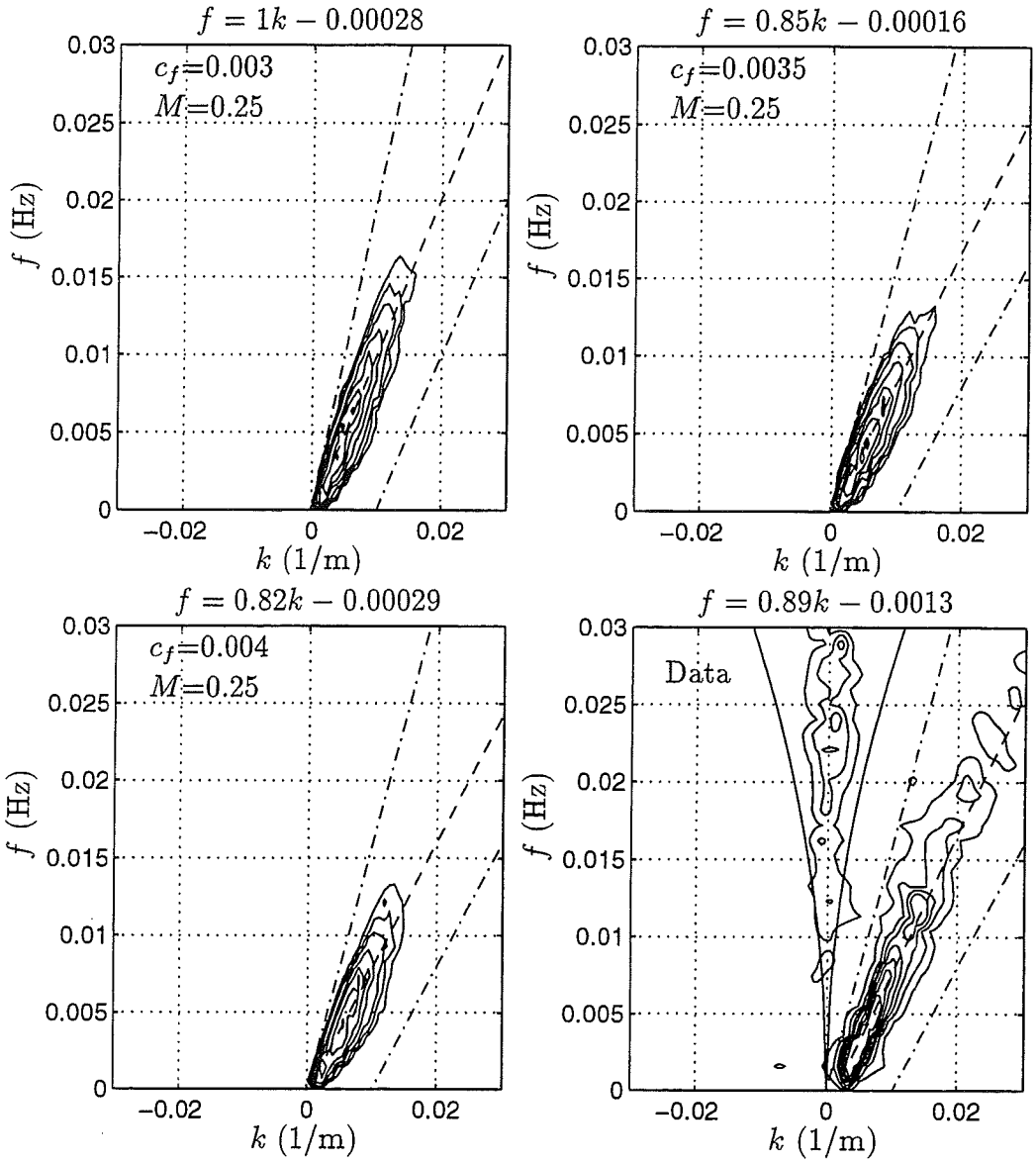

Figure 6.36: October 16: Frequency-cyclic wavenumber spectra $S(f,k)$ (m^3/s) for computed and measured cross-shore velocity at x =35 m. The values for c_{est} are 1 m/s for $c_f = 0.003$, 0.8 m/s for $c_f = 0.0035$ and $c_f = 0.004$, and 0.8 for data, and are used in Equation (6.3) to construct the upper and lower cut-off lines (– · –) of the shear wave energy. Contour levels plotted are (10 30 60 100 200 400 800). The equation for the best fit dispersion line (– –) is noted above each plot.

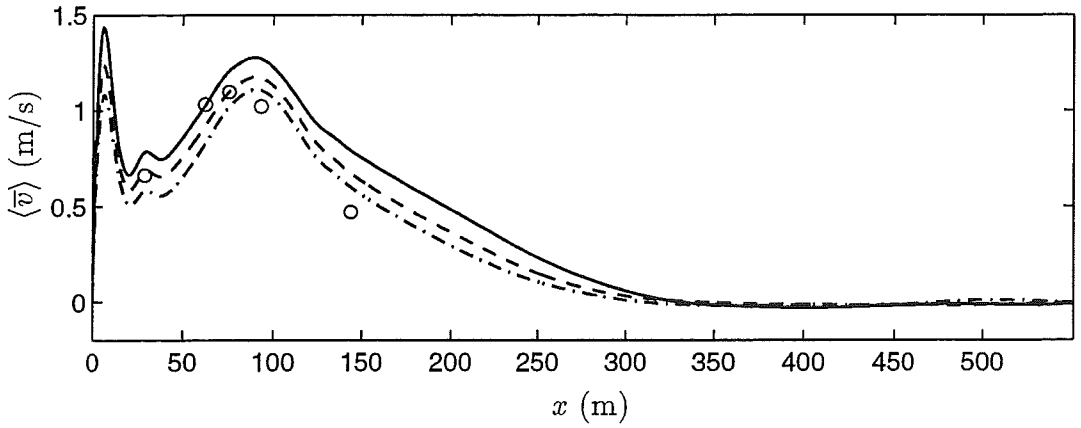

Figure 6.37: October 16: Time and longshore-averaged longshore currents $\langle\overline{v}\rangle$ for $c_f = 0.003$ (——), $c_f = 0.0035$ (– –), $c_f = 0.004$ (– · –) and sled data (o).

extent is not as pronounced as for the low friction case of October 15. The cross-shore variations are characterized by two peaks just inshore and offshore of the mean longshore current maximum. Comparing the two cases that reproduced the propagation speeds of the data for October 15 (see Figure 6.26) and 16, it can be observed that the maximum kinetic energy for October 16 is larger.

The plots of potential vorticity shown in Figure 6.39 for $c_f = 0.003$ and $c_f = 0.004$ display similar characters. The layers of positive and negative vorticity are being mixed. Features with positive and negative potential vorticity are seen to pair up to form vortex pairs. Some vortex pairs have previously been released offshore and are seen about 400 m offshore. An important difference between the two cases is that the vortices are more energetic for $c_f = 0.003$. This result is supported by the analysis of perturbation kinetic energy shown in Figure 6.38 and is especially evident offshore since the vortices associated with $c_f = 0.004$ are seen to be weaker.

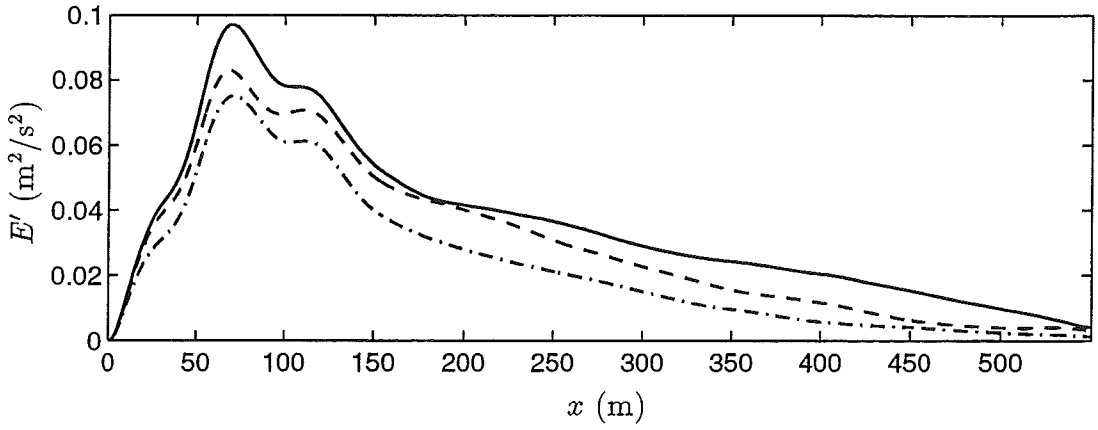

Figure 6.38: October 16: Time and longshore-averaged longshore perturbation kinetic energy $\frac{1}{2}\langle\overline{u'^2} + \overline{v'^2}\rangle$ for $c_f = 0.003$ (——), $c_f = 0.0035$ (– –), $c_f = 0.004$ (– · –).

6.5.3 Simulations of October 17

Simulations for October 17 were carried out for $M = 0.25$ and two friction coefficients given by $c_f = 0.001$ and $c_f = 0.002$. Time series were recorded at $x = 35$ m and are shown in Figure 6.40 along with time series of data from the closest current meter. The time series show that no instabilities are observed during the first 1.5 hours of the simulation. Instead, the generation of a longshore current in the absence of fluctuations is observed. The instabilities reach finite amplitude around 1.6 hours. The initial finite amplitude instabilities display a time scale similar to data. They quickly evolve into longer time scale disturbances. The generated mean current is positive and fairly steady. The mean current assessed from the measured time series is small and negative. The computed cross-shore velocities are much less energetic than the observed velocities. In addition, the value of the mean current is not altered much after the initiation of the instabilities. Therefore, the resulting shear instabilities display the character of weakly nonlinear equilibrated disturbances. Agreement with data is very poor,

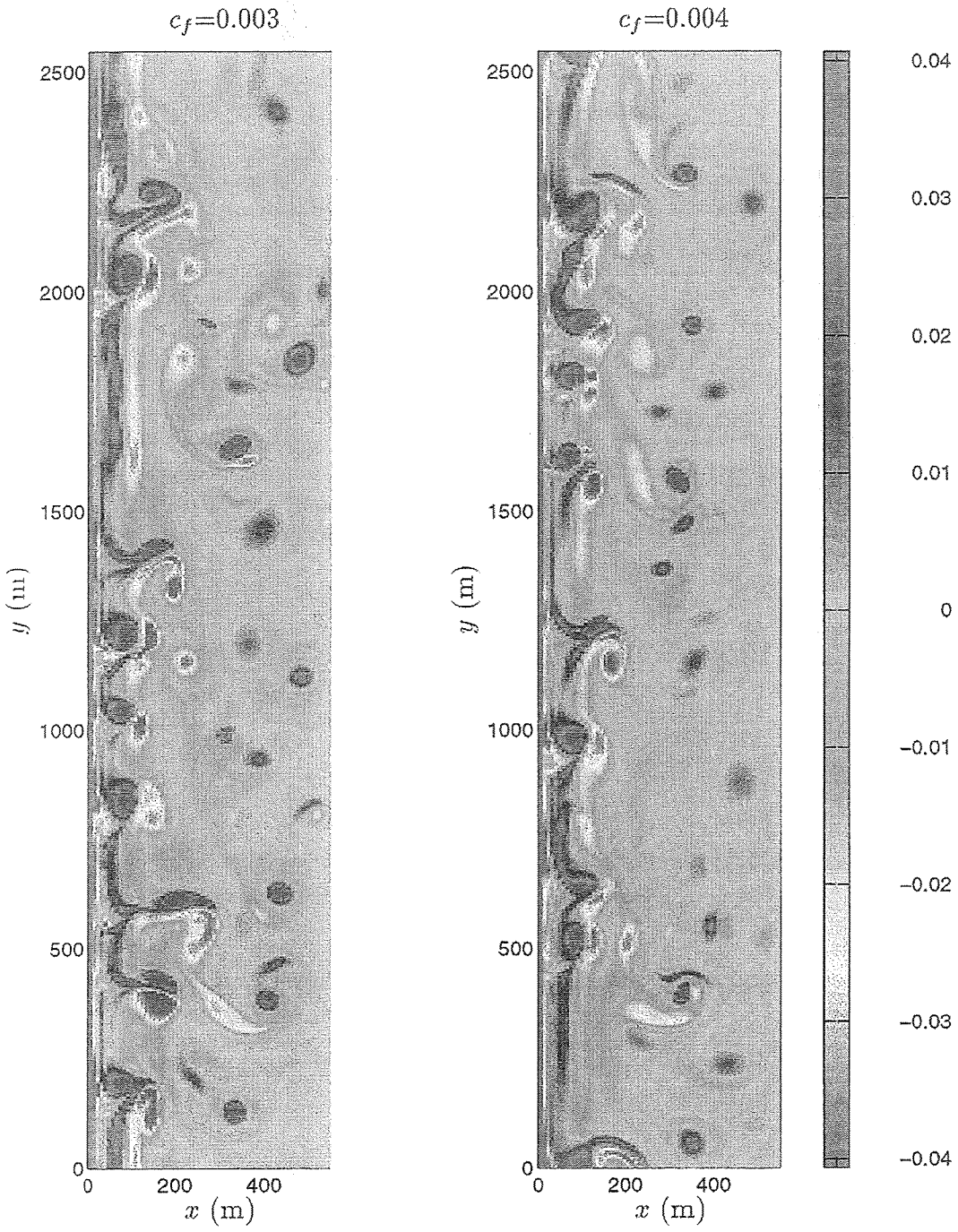

Figure 6.39: October 16: Contour plots of vorticity q (1/s) at $t = 5$ hrs for $c_f = 0.003$ and $c_f = 0.004$; $M = 0.25$

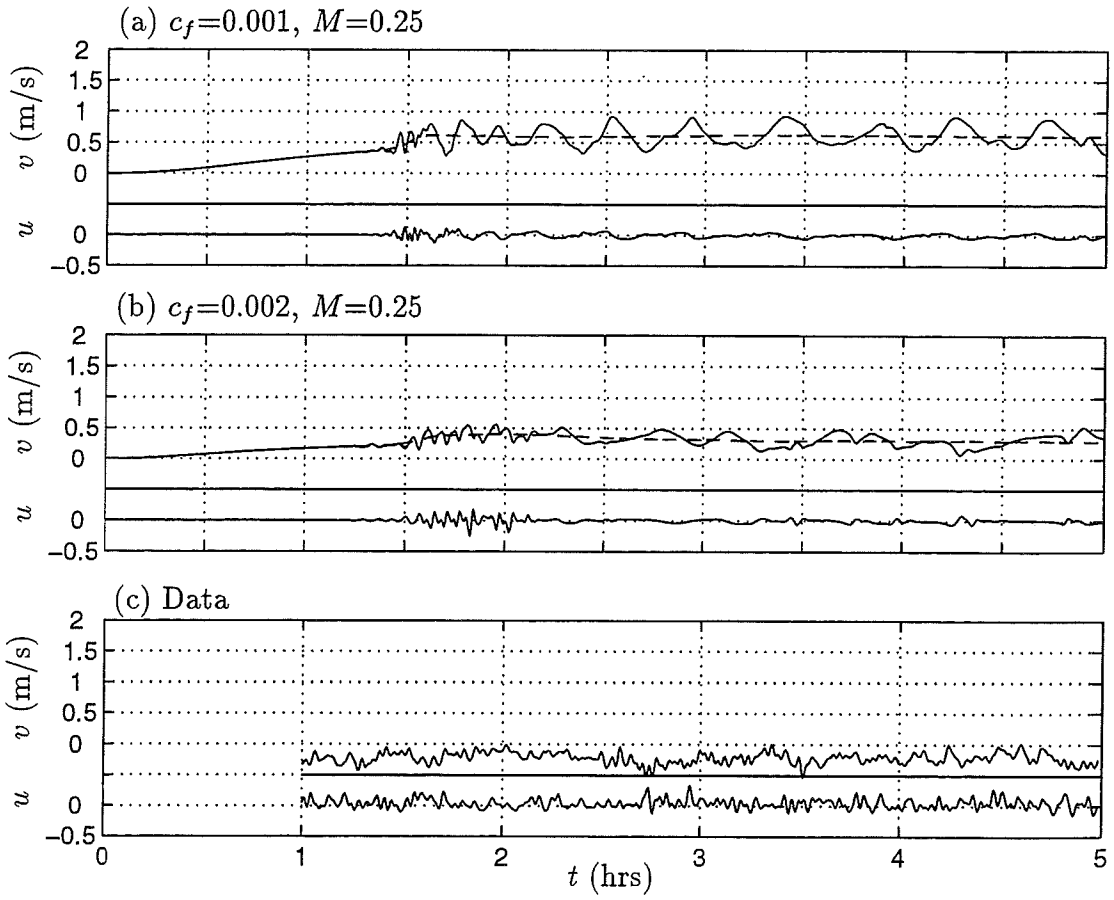

Figure 6.40: October 17: Time series of velocities u, v and $\langle v \rangle$ (– –) at (x, y)=(35 m, $L_y/2$) and time series of velocities u and v of data.

especially since the direction of the longshore flow is not predicted correctly.

Contour plots of the computed frequency-wavenumber spectra for the longshore and cross-shore velocities are shown in Figures 6.41 and 6.42, respectively. Comparison of the spectra for the longshore velocities with data is not possible since the motions are poorly defined in the data. Therefore, we turn to the spectra of the cross-shore velocities. The data to model comparison is difficult due to the large intercept value of the best fit dispersion line for the data. The

cross-shore data suggests that the motions are dispersive whereas the modeled motions are not. As discussed earlier, the large intercept value is likely to be a side effect of the data analysis techniques employed to create the estimate for the frequency-wavenumber spectrum of the data. Therefore, we proceed by comparing the slope values for the observations and simulations and find that the slope is underpredicted for both values of c_f.

Moving on to the mean longshore current displayed in Figure 6.43, we find that the predicted mean current profile overpredicts the measured values in the region shoreward of the bar. Near-zero velocities were observed during sled measurements in the trough region. The fact that the time series from a fixed current meter shown in Figure 6.40 also displays near-zero mean velocities lends confidence to the observation that no current existed in the trough region on October 17. This suggests that a fundamentally different longshore current generation mechanism is at work that the present modeling effort can not reproduce.

A possible explanation was provided by Whitford (1988) who observed that the wave regime on this day consisted of wind waves and less energetic swell approaching the beach from different directions. Whitford (1988) found evidence of intersecting wave trains in data for October 17 and postulated that the wind waves approaching the shore from the north quadrant, breaking on the nearshore bar and again on the shoreface could indeed be forcing a southward (positive) longshore current. However, the swell approaching the shore from the southern quadrant can propagate over the bar and break in the nearshore causing a northward swell-induced current that is confined to a narrow region close to the shoreline. Opposing longshore currents in the bar trough region could then explain the observed near-zero current velocities. It should be taken into account that if the events on October 17 are governed by the presence of intersecting wave trains, the

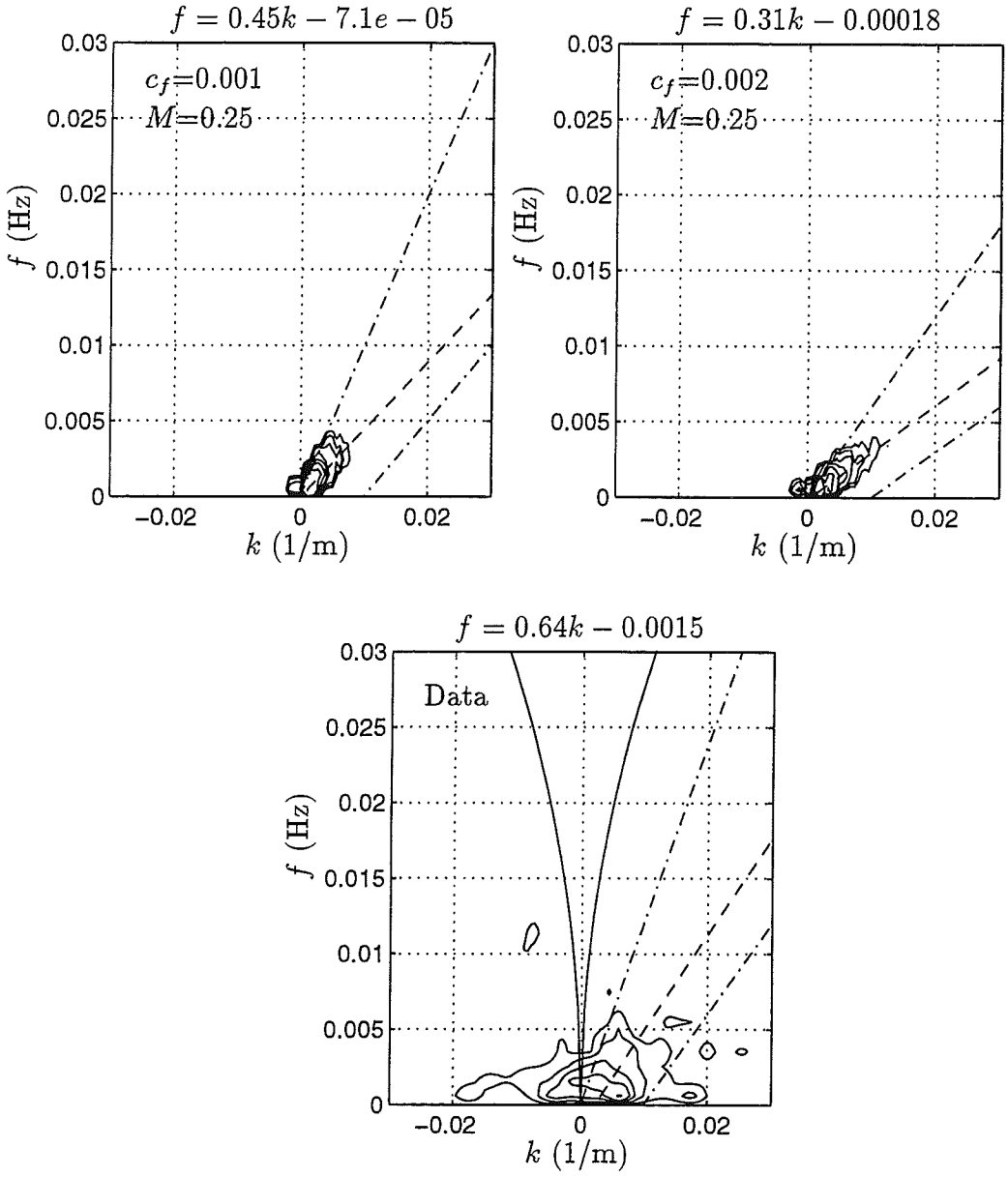

Figure 6.41: October 17: Frequency-cyclic wavenumber spectra $S(f,k)$ (m^3/s) for computed and measured longshore velocity at x =35 m. The values for c_{est} are 0.5 m/s for $c_f = 0.001$, 0.3 m/s for $c_f = 0.002$, and 0.6 m/s for data, and are used in Equation (6.3) to construct the upper and lower cut-off lines (– · –) of the shear wave energy. Contour levels plotted are (10, 30, 60, 100, 200, 400, 800). The equation for the best fit dispersion line (— —) is noted above each plot.

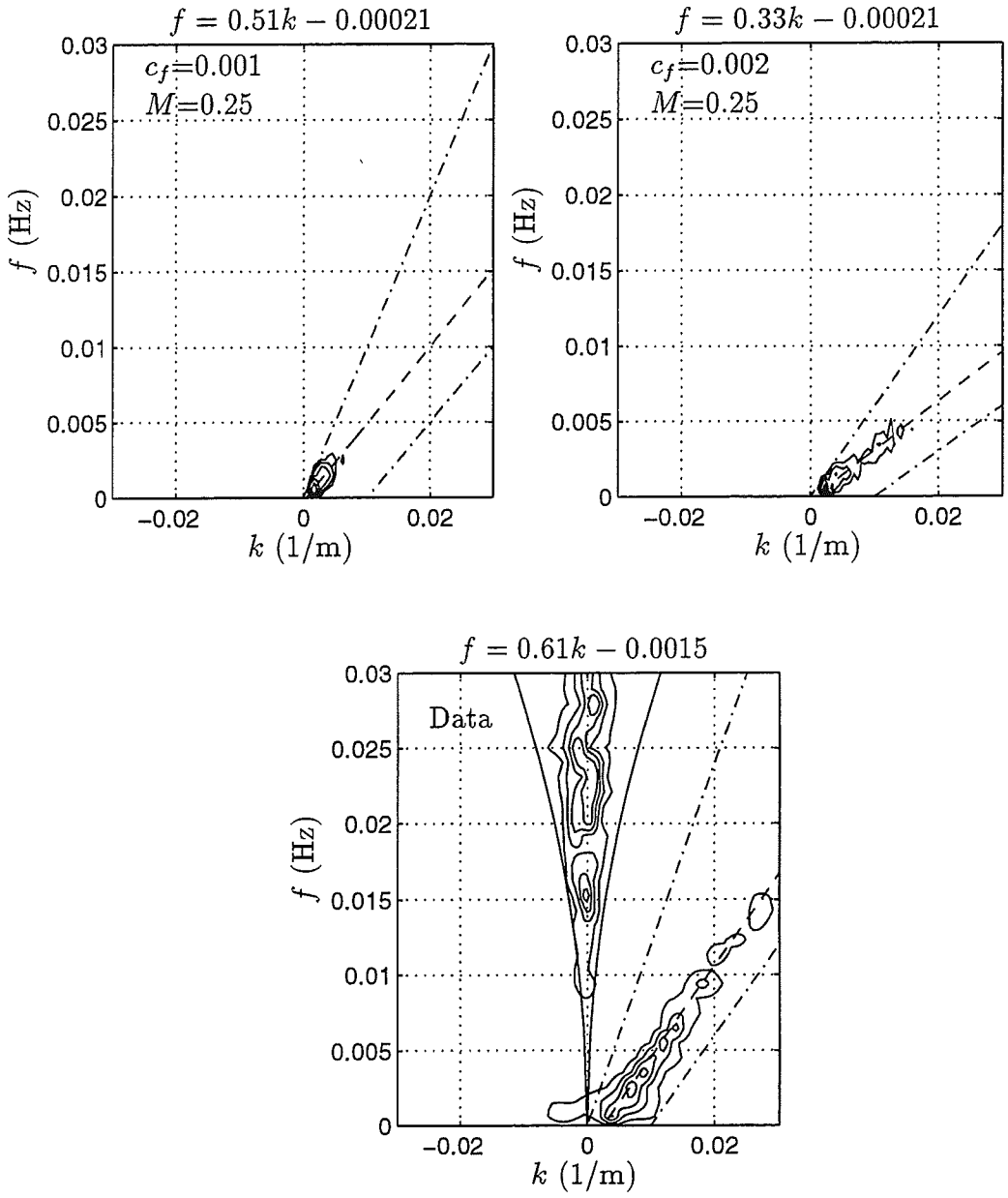

Figure 6.42: October 17: Frequency-cyclic wavenumber spectra $S(f,k)$ (m^3/s) for computed and measured cross-shore velocity at x =35 m. The values for c_{est} are 0.5 m/s for $c_f = 0.001$, 0.3 m/s for $c_f = 0.002$, and 0.6 for data, and are used in Equation (6.3) to construct the upper and lower cut-off lines (– · –) of the shear wave energy. Contour levels plotted are (10 30 60 100 200 400 800). The equation for the best fit dispersion line (– –) is noted above each plot.

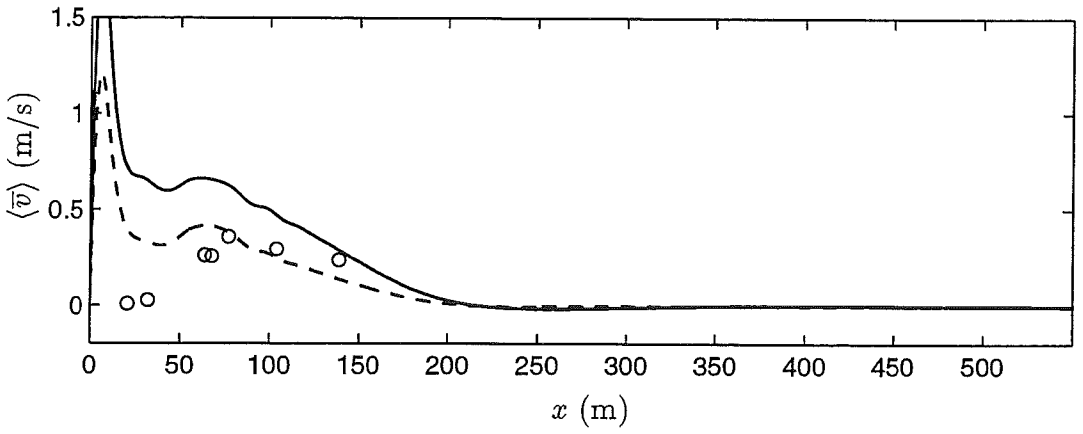

Figure 6.43: October 17: Time and longshore-averaged longshore currents $\langle\overline{v}\rangle$ for $c_f = 0.001$ (——), $c_f = 0.002$ (– –) and sled data (o).

resulting radiation stress forcing terms are possibly longshore and time-varying. The simple treatment of the forcing terms employed in this chapter prevents us from being able to study this case further. The extension to the model discussed in the next chapter will give us the opportunity to study this case in more detail in the future.

Although the behavior on October 17 is not reproduced well by the simulations, the results of the computations are nonetheless of interest since they detail the behavior of shear instabilities in a weakly nonlinear regime. The mean perturbation kinetic energy displayed in Figure 6.44 shows that the energy associated with the motions is much less than for October 15 and 16. The two peaks in the kinetic energy distribution observed in previous cases are still evident but less pronounced.

Contour plots of the potential vorticity for the two cases are shown in Figure 6.45. The vorticity patterns are much weaker than in the previous simulations. The layers of positive and negative vorticity do not form distinct vortex pairs in

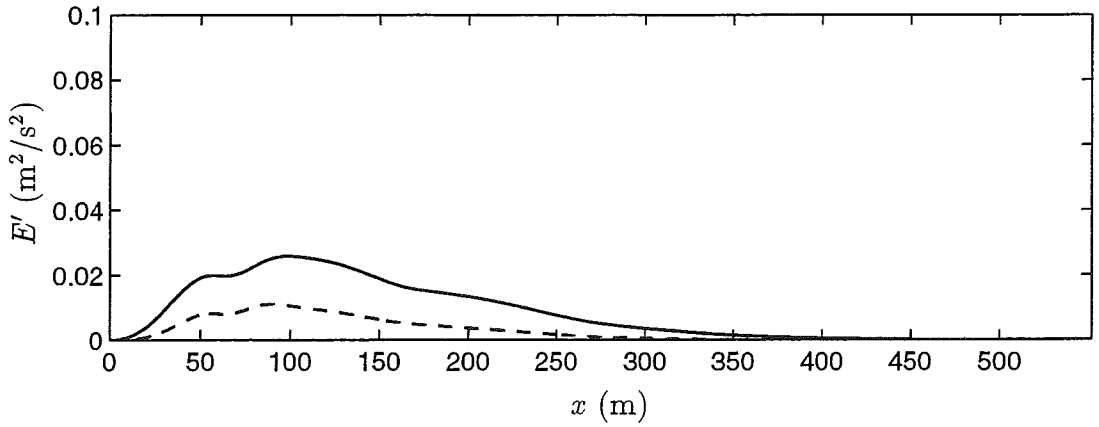

Figure 6.44: October 17: Time and longshore-averaged longshore perturbation kinetic energy $\frac{1}{2}\langle\overline{u'^2} + \overline{v'^2}\rangle$ for $c_f = 0.001$ (——) and $c_f = 0.002$ (– –).

the nearshore region. Some vortex shedding occurs, but the offshore vortices do not propagate out past 350 m. The patterns are closer in character to the results for the plane beach simulations than to results for October 15 or 16.

6.5.4 Simulations of October 18

Linear instability computations for October 18 documented in Section 6.4.1 showed that the instability on October 18 is weaker than the instability on October 16 for the same friction factor. The linear growth rates associated with October 18 are almost 50% less than the linear growth rates for October 16. Therefore, the instabilities are expected to be initiated less rapidly. Time series of simulations for three values for the frictional coefficients (see Figure 6.46) show that the instabilities reach finite amplitude about 45 minutes after the initiation of the simulations. During the time that passes while the instabilities are small, a longshore current is generated at this cross-shore location (x=35 m) indicating that the mixing terms associated with turbulence and dispersive mixing are

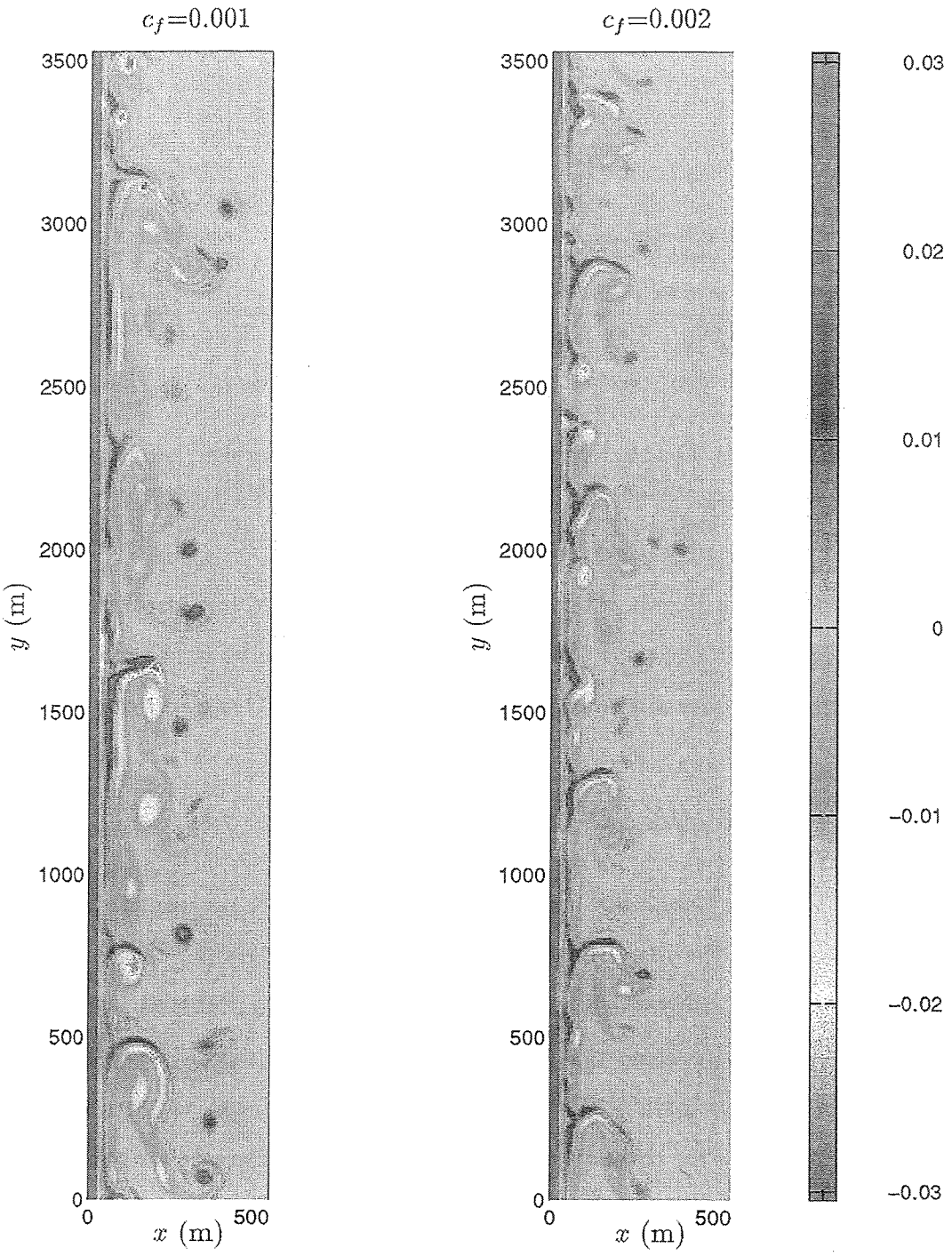

Figure 6.45: October 17: Contour plots of vorticity q (1/s) at $t = 5$ hrs for $c_f = 0.001$ and $c_f = 0.002$, $M = 0.25$. Note the change in the color axis compared to previous vorticity plots.

important. The development of a current velocity in the bar trough during the spin-up time was not observed for October 15 or 16. The reader is reminded that the instabilities fully developed in 30 minutes on October 16 for a similar friction factor.

As for October 16, the range of friction coefficients associated with the simulations documented in Figure 6.46 is narrow. Therefore, the time series display similar characters. The instabilities are generated slightly earlier for lower friction coefficient. The initial development is similar in all three cases. The initial disturbances display short time scales, subsequently longer time scale motions are generated. In contrast to October 17, the time scale of the original instabilities is preserved throughout the time series.

The frequency-longshore wavenumber spectra of the longshore velocities shown in Figure 6.47 document similar trends as seen in previous simulations. The differences in the propagation speeds for two cases are more pronounced for lower friction factor. In fact, spectra for $c_f = 0.003$ and $c_f = 0.0035$ only show minor differences in propagation speed. The case involving $c_f = 0.003$ reproduces the propagation speed of the data slightly better. Two-dimensional spectra of the cross-shore velocities (see Figure 6.48) show similar trends.

The time and longshore-averaged longshore current profiles for the three cases are shown in Figure 6.49. The current profile associated with $c_f = 0.003$ is seen to reproduce the sled measurements well. However, it is once again noted that this agreement has to be interpreted with caution due to the sequential nature of the measurements and differences in averaging periods. The presence of a strong shoreline jet is evident.

The average perturbation kinetic energy (see Figure 6.50) shows that the

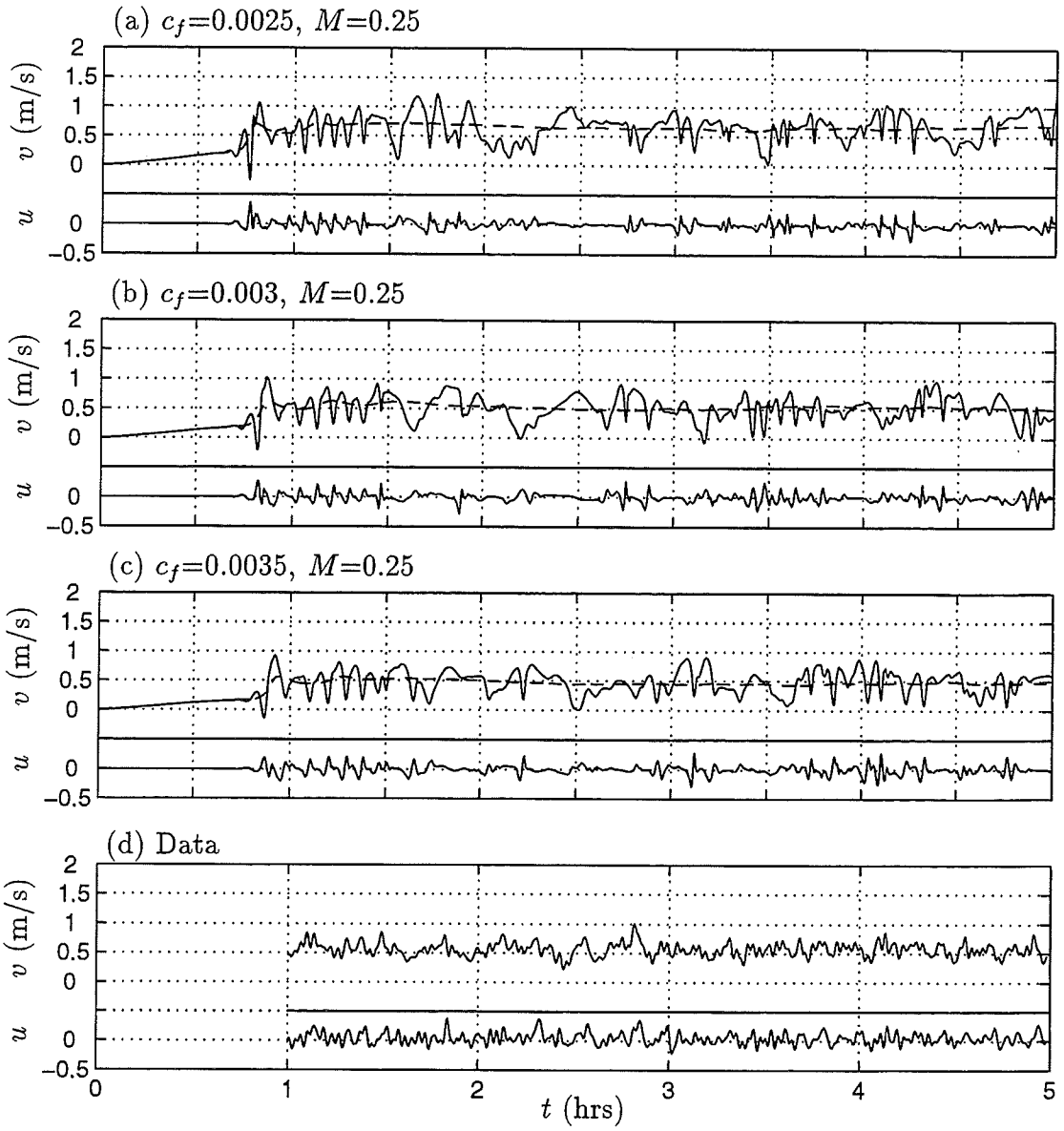

Figure 6.46: October 18: Time series of velocities u, v and $\langle v \rangle$ (– –) at (x, y)=(35 m, $L_y/2$) and time series of velocities u and v of data.

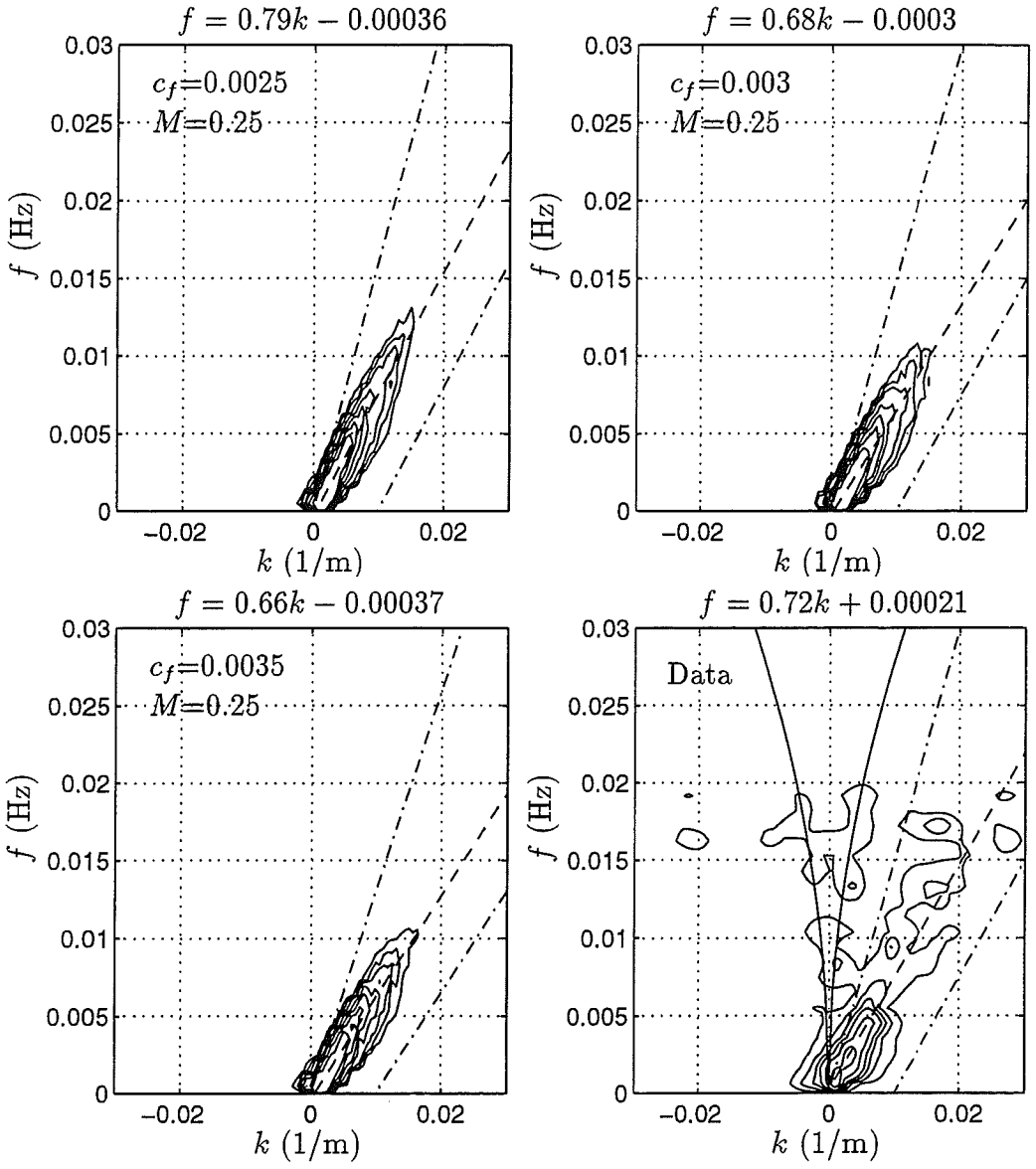

Figure 6.47: October 18: Frequency-cyclic wavenumber spectra $S(f,k)$ (m^3/s) for computed and measured longshore velocity at x =35 m. The values for c_{est} are 0.8 m/s for c_f = 0.0025, 0.75 for c_f = 0.003, 0.65 m/s for c_f = 0.0035, and 0.75 m/s for data, and are used in Equation (6.3) to construct the upper and lower cut-off lines (– · –) of the shear wave energy. Contour levels plotted are (10, 30, 60, 100, 200, 400, 800). The equation for the best fit dispersion line (– –) is noted above each plot.

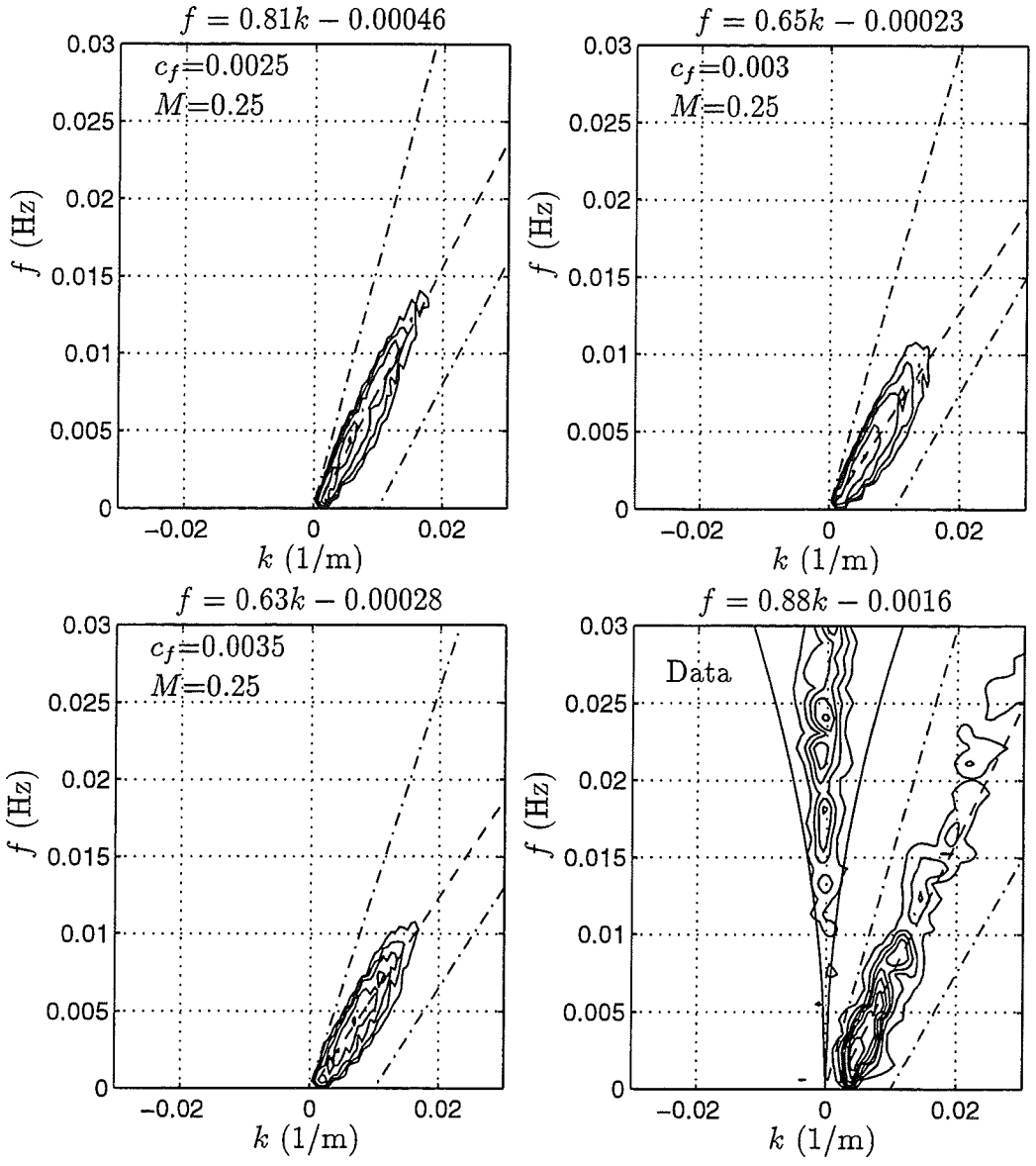

Figure 6.48: October 18: Frequency-cyclic wavenumber spectra $S(f,k)$ (m^3/s) for computed and measured cross-shore velocity at x =35 m. The values for c_{est} are 0.8 m/s for c_f = 0.0025, 0.75 for c_f = 0.003, 0.65 m/s for c_f = 0.0035, and 0.75 m/s for data, and are used in Equation (6.3) to construct the upper and lower cut-off lines (– · –) of the shear wave energy. Contour levels plotted are (10 30 60 100 200 400 800). The equation for the best fit dispersion line (— —) is noted above each plot.

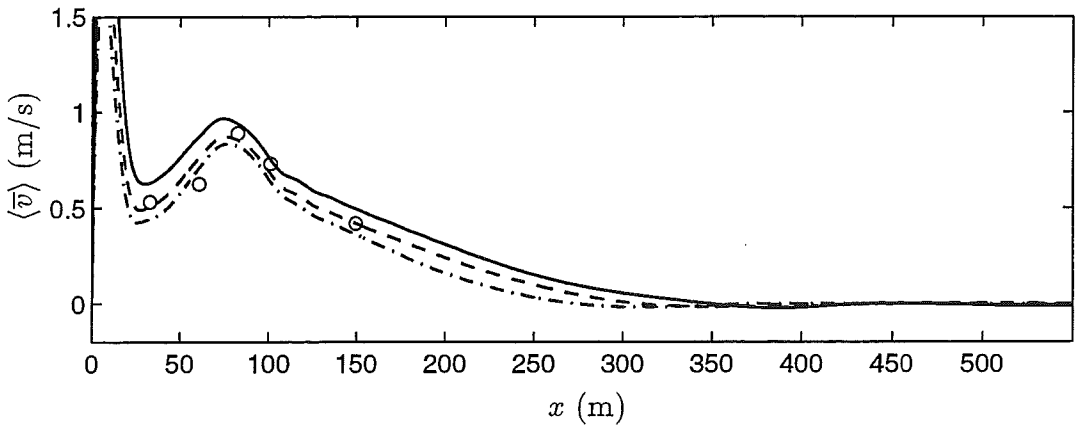

Figure 6.49: October 18: Time and longshore-averaged longshore currents $\langle\overline{v}\rangle$ for $c_f = 0.0025$ (——), $c_f = 0.003$ (– –), $c_f = 0.0035$ (– · –) and sled data (○).

motions associated with the lowest friction factor are strongest, differences are especially evident offshore. In the bar trough region ($x \approx 35$ m), the differences in perturbation kinetic energy are minimal. The reader is reminded that the time series displayed in Figure 6.46 were collected in the bar trough region.

Contour plots of vorticity depicted in Figure 6.51 for the lowest and highest friction coefficients of $c_f = 0.0025$ and $c_f = 0.0035$ show energetic vortex structures similar to those seen for October 15 and 16. Vortices are seen to pair up in the nearshore. The longshore length scales of the motions associated with the two cases are similar. Vortex pairs are advected offshore. The case associated with $c_f = 0.0025$ displays more energy offshore whereas for $c_f = 0.0035$ the vortex pairs do not propagate offshore past $x = 400$ m.

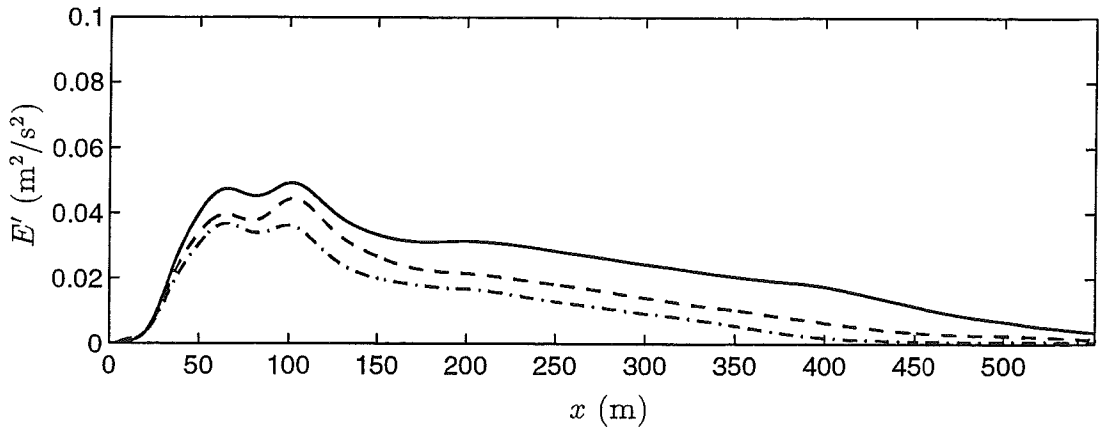

Figure 6.50: October 18: Time and longshore-averaged longshore perturbation kinetic energy $\frac{1}{2}\langle\overline{u'^2} + \overline{v'^2}\rangle$ for $c_f = 0.0025$ (——) and $c_f = 0.003$ (– –) and $c_f = 0.0035$ (– · –).

6.5.5 Summary

In this section we simulated the shear instability climate on October 15 through 18 at SUPERDUCK for a range of friction coefficients. The mixing coefficient is kept constant for all simulations at $M = 0.25$. The instabilities are seen to grow to finite amplitude rapidly. The resulting motions are in the form of unsteady longshore-propagating vortex structures that occasionally pair up, strengthen and shed vortices offshore. The evolution is at times reminiscent of transient rip currents. The offshore velocities associated with the motions can reach up to 0.3 m/s. These offshore velocities can sometimes occur at instances where near-zero longshore velocities are present indicating primarily offshore directed flow.

The range of friction coefficients is chosen to be narrow about a value which is observed to reproduce the propagation speeds of the data. When analyzing cases with different values of the friction coefficient we notice that lowering the friction factor results in a more energetic mean longshore current profile as well as

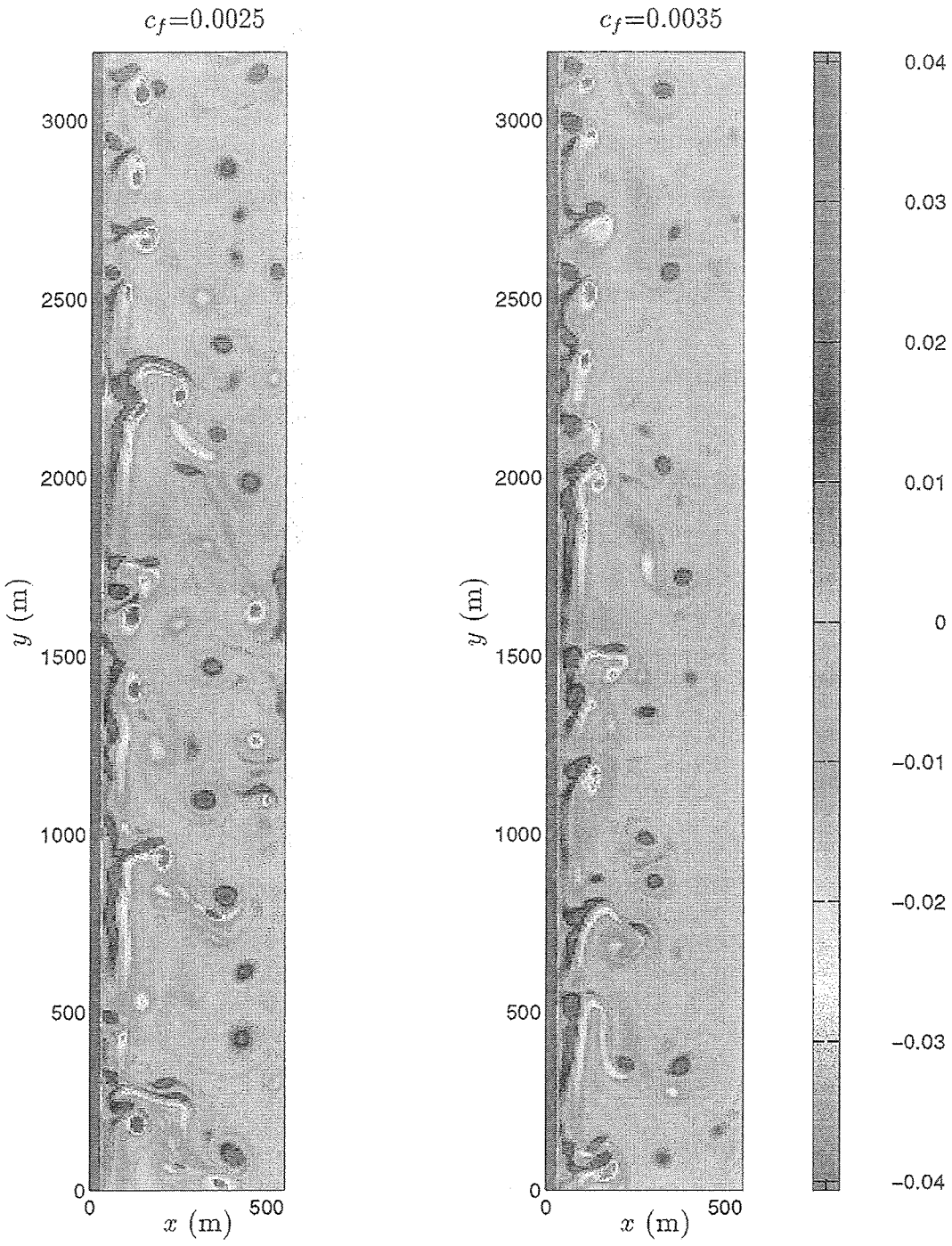

Figure 6.51: October 18: Contour plots of vorticity q (1/s) at $t = 5$ hrs for $c_f = 0.0025$ and $c_f = 0.0035$, $M = 0.25$.

more energetic fluctuations. The propagation speed inferred from the frequency-longshore wavenumber spectrum of the computations is also observed to increase with decreasing friction factor. For the narrow range of friction coefficients considered here, the general character of the flow patterns is not altered since the plots of potential vorticity display similar longshore length scales. However, the offshore extent of the motions, the amount of vortex shedding as well as the strength of the vortices in the nearshore region is decreased for increasing friction coefficient.

The friction coefficients that reproduce the propagation speed of the data are identified as $c_f = 0.002$ for October 15, $c_f = 0.0035$ for October 16 and $c_f = 0.003$ for October 18. The data comparison of computations for October 17 is poor. It is suspected that the underlying short wave forcing is not modeled properly for this day. As Dodd *et al.* (1992), who considered the linear instability problem for the same days at SUPERDUCK, we find that a lower friction coefficient is required to reproduce behavior on October 15 than for October 16 or 18 and that the friction factors for October 16 and October 18 are similar although motions on October 18 propagate slower. However, in contrast to Dodd *et al.*'s (1992) suggestion that the motions seen in the data are weakly nonlinear disturbances, we find that the motions associated with the chosen frictional values are large amplitude disturbances which affect a large region of the nearshore.

6.6 Effects of Lateral Mixing

Next, the friction factor c_f is fixed at the value that reproduces the propagation speed inferred from data. The mixing coefficient M is varied to identify the effect of lateral mixing in the surf zone due to processes other than the shear instabilities. The range of realistic mixing coefficients in the field was identified earlier as $0.06 < M < 0.48$. Simulations are carried out for October 15, 16 and 18 for three values of the mixing coefficient given by 0, 0.25 and 0.5. In addition, simulations with $M = 1$ are carried out for October 15. The simulations with $M = 0$ show the evolution of motions in the absence of any momentum mixing process other than the shear instabilities themselves. The M-values of 0.25 and 0.5 correspond to the range of realistic estimates for mixing including turbulence and dispersive mixing. The value of unity is unrealistically high, but simulations with this value will aid in the clarification of the trends as M increases. Since agreement with observation was poor for October 17, no further simulations for that day are carried out.

We identify the effects of varying the mixing coefficient by analyzing time series, two-dimensional spectra as well as cross-shore distributions of the mean quantities. We also examine the mean longshore momentum balance in order to asses the importance of mixing induced by the instabilities in relation to the amount of mixing present in the surf zone due to other processes.

6.6.1 Simulations of October 15

We carry out simulations for October 15 with four values for the mixing coefficient M of 0, 0.25, 0.5 and 1. The friction coefficient c_f is kept constant at 0.002. We first discuss time series of simulations for different values for M.

The time series of the velocities and data are shown in Figure 6.52. We find that the instabilities reach finite amplitude sooner for lower mixing coefficient, showing that the response of the motions to lateral mixing during the spin-up period is similar to their response to increased friction. Once the instabilities have equilibrated ($t > 1.5$ hrs), the time series for $M = 0$ display motions at shorter time scales than time series for larger M. Long time oscillations are present in all time series but are more pronounced as M increases since the higher frequency oscillations are not present in time series for high M-values. In the time series for $M = 1$, the generation of a mean current in the absence of fluctuations can be observed during the spin-up period. Once the instabilities are initiated the mean longshore current is altered rapidly. The generated mean longshore current is of similar magnitude for all M. It is noted that as M increases, the nature of the oscillations corresponds to data progressively less.

Frequency-longshore wavenumber plots in Figure 6.53 show that an additional effect of the mixing is to decrease the propagation speed of the motions. Varying M through its full range from 0 to 0.5 results in a reduction of the propagation speed of 10%. The size of this variation is equivalent to the uncertainty in the estimates of the propagation speed from the two-dimensional spectra (see Section 6.2.1). The plots corresponding to $M = 0$ and $M = 0.25$ do not show a significant change in the propagation speed. However, the spectra corresponding to $M = 0$ displays a broader peak. The spectra for the cross-shore velocities are shown in Figure 6.54. The tendency of the motions to extend to higher frequencies is seen to be suppressed as M increases.

Quantitative comparisons to data are made by constructing a frequency spectrum that only contains energy due to shear waves. For this purpose, the energy in the region bounded by the upper and lower cutoff lines shown on the

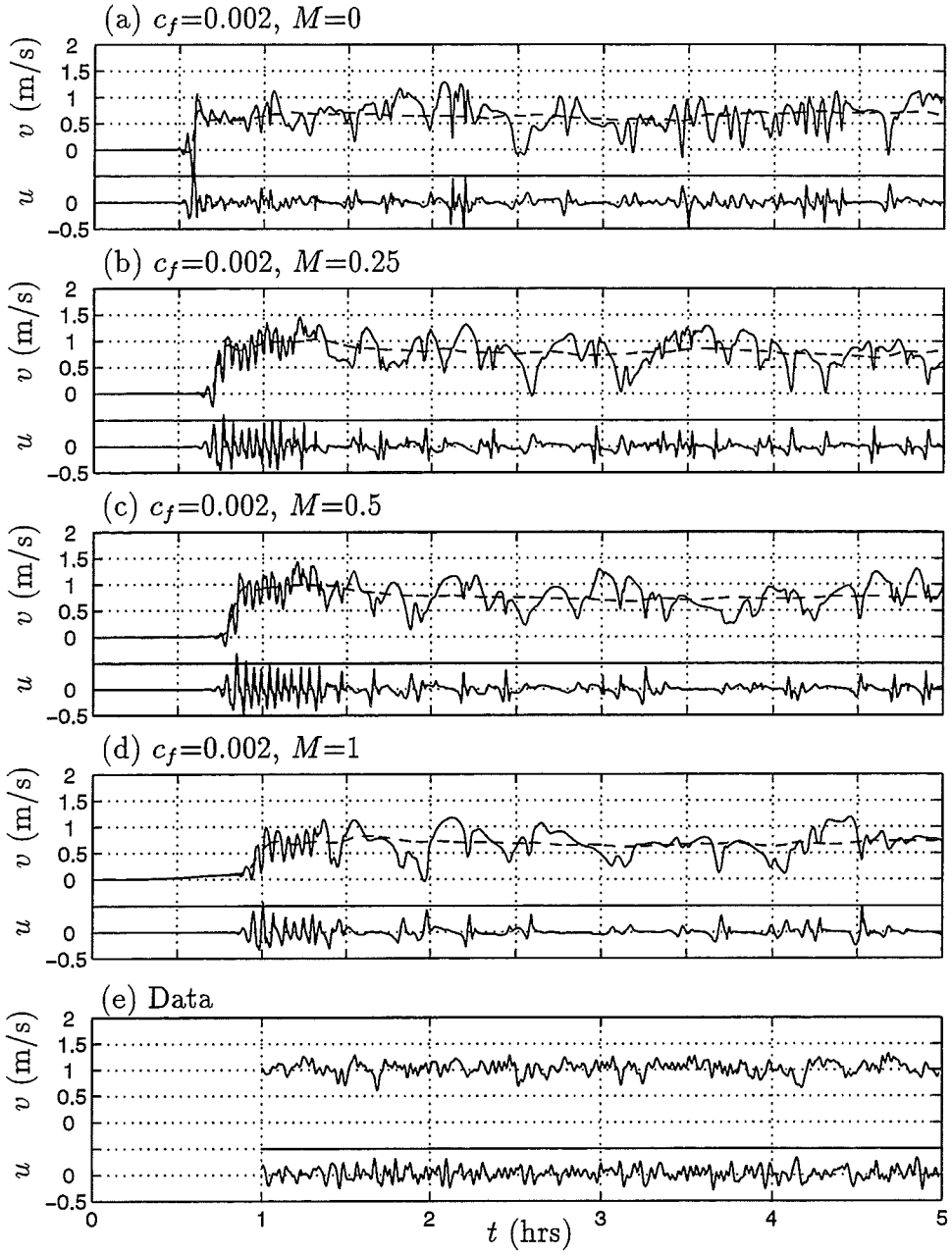

Figure 6.52: October 15: Time series of velocities u, v and $\langle v \rangle$ (– –) at (x, y)=(45 m, $L_y/2$) and time series of velocities u and v of data.

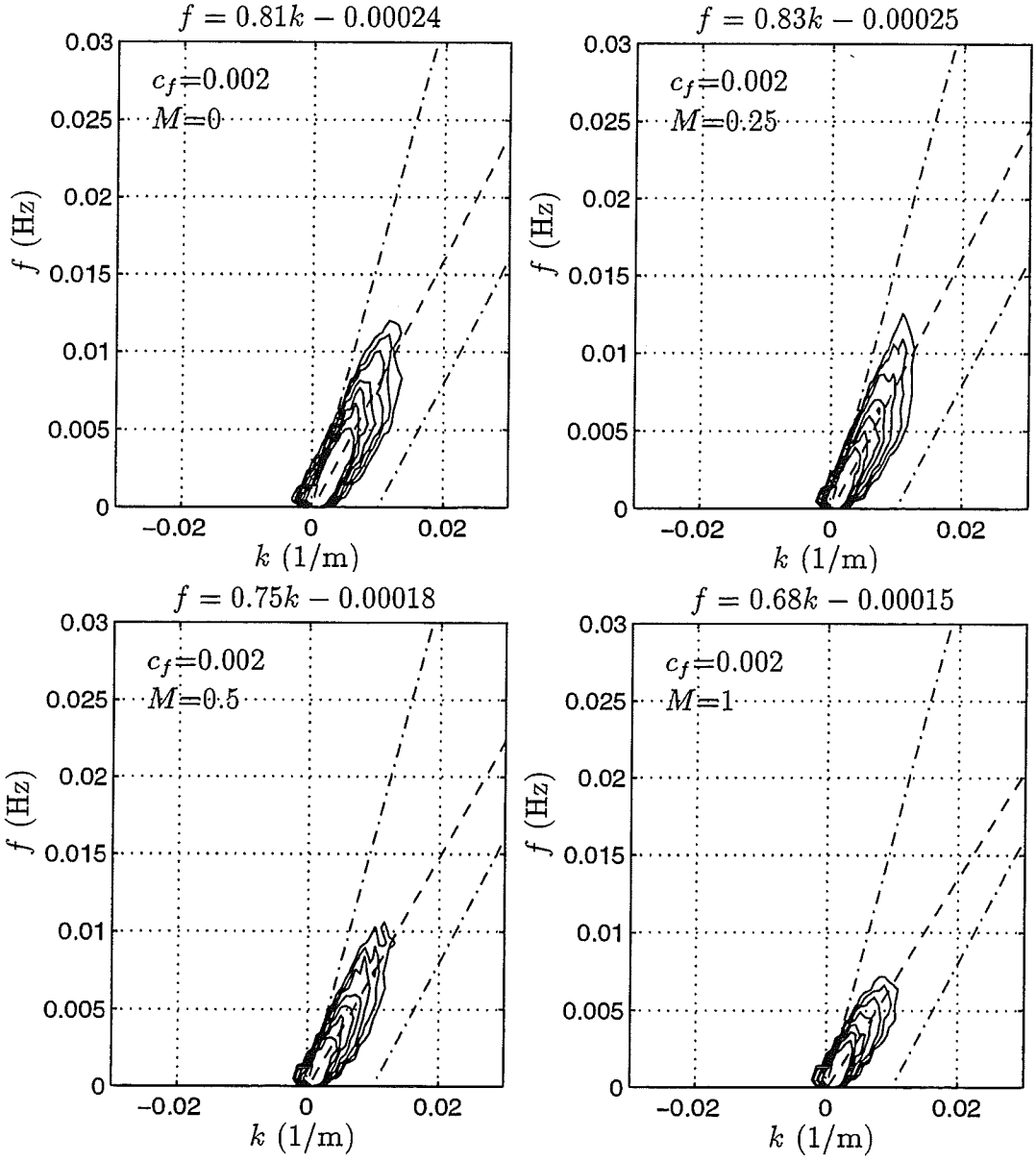

Figure 6.53: October 15: Frequency-cyclic wavenumber spectra $S(f,k)$ (m^3/s) for computed longshore velocity at x =45 m. The value for c_{est} is 0.8 m/s, and is used in Equation (6.3) to construct the upper and lower cut-off lines (– · –) of the shear wave energy. Contour levels plotted are (10, 30, 60, 100, 200, 400, 800). The equation for the best fit dispersion line (– –) is noted above each plot.

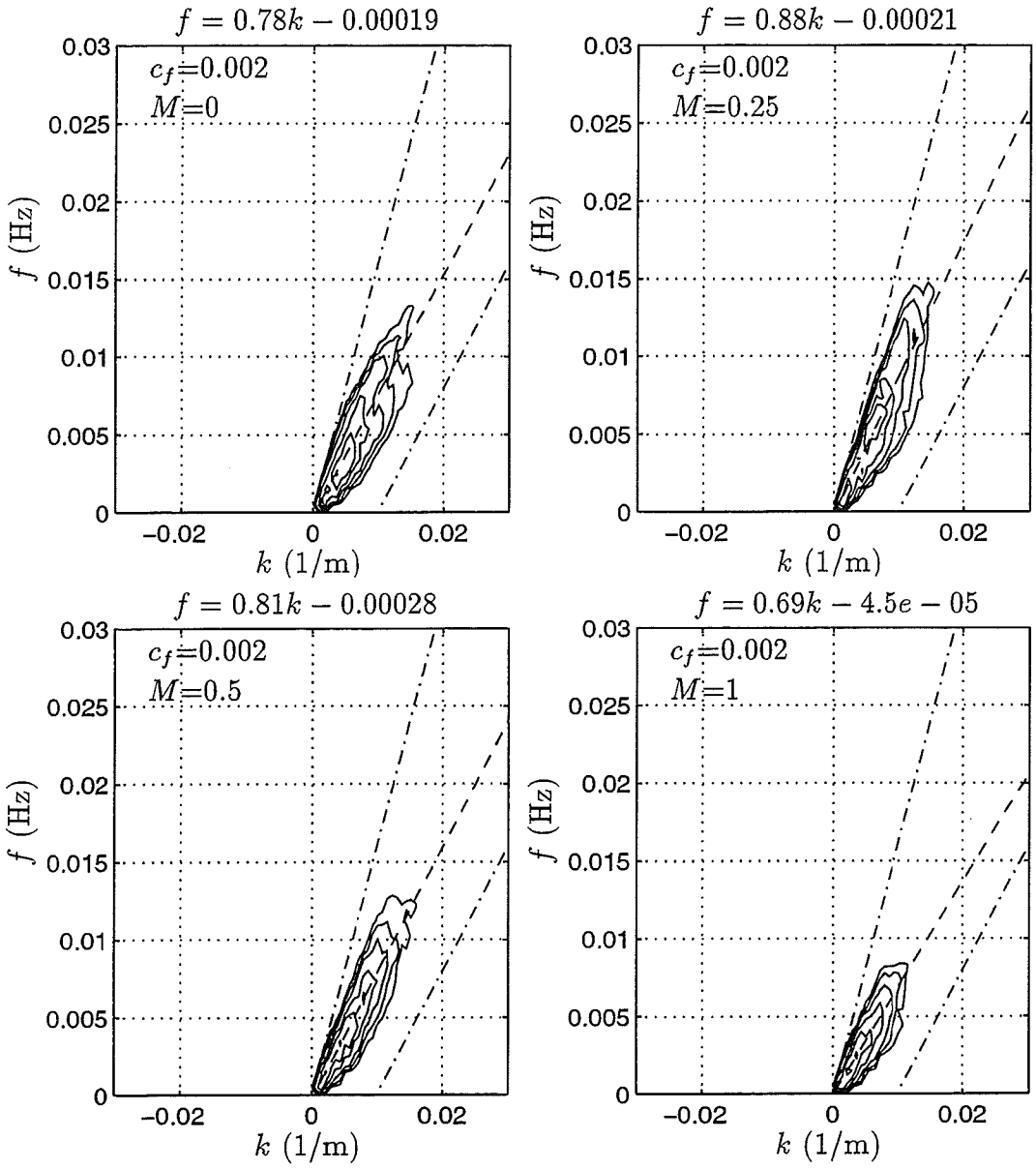

Figure 6.54: October 15: Frequency-cyclic wavenumber spectra $S(f,k)$ (m^3/s) for computed cross-shore velocity at x =45 m. The value for c_{est} is 0.8 m/s, and is used in Equation (6.3) to construct the upper and lower cut-off lines (– · –) of the shear wave energy. Contour levels plotted are (10, 30, 60, 100, 200, 400, 800). The equation for the best fit dispersion line (— —) is noted above each plot.

two-dimensional spectra plots is summed for each frequency bin. The frequency spectra is then given by

$$S_k(f) = \int_{k_{low}}^{k_{up}} S(f,k)dk, \tag{6.40}$$

where

$$k_{low} = \frac{f}{c_{est}}, \qquad k_{up} = \frac{f}{c_{est}} + 0.01. \tag{6.41}$$

The comparison of the frequency spectra for the data and the four cases involving different M-values is documented in Figure 6.55. The data is represented by the heavy line whereas results from computations are shown as thin lines of various types. The frequency spectrum of the longshore velocities shows that motions at low frequencies are overpredicted whereas motions with frequencies larger than 0.01 Hz are underpredicted. The tail of the spectra for the computed velocities displays a faster decay rate for larger M. This result is consistent with the observations made during the analysis of the time series, since we saw less high frequency oscillations as M increased. Returning to Figure 6.2 for the two-dimensional spectrum of the data, we find that shear wave motions are seen to be dominant over other low frequency motions in the range of frequencies $f < 0.007$ Hz. Focusing on the range $0.002 < f < 0.007$ Hz, we see that the frequency spectrum of the observed longshore velocities is overpredicted by $M = 0$ and underpredicted by $M = 1$. Simulations for $M = 0.25$ and $M = 0.5$ show reasonable agreement with the data.

Turning to the spectrum of cross-shore velocities we find that the general character of the spectrum is reproduced for the range $0 < f < 0.007$ by the simulations involving $M = 0, 0.25, 0.5$. The behavior at these values is similar. Once again, $M = 0.25$ and $M = 0.5$ display reasonable agreement although the peak is underpredicted by all cases.

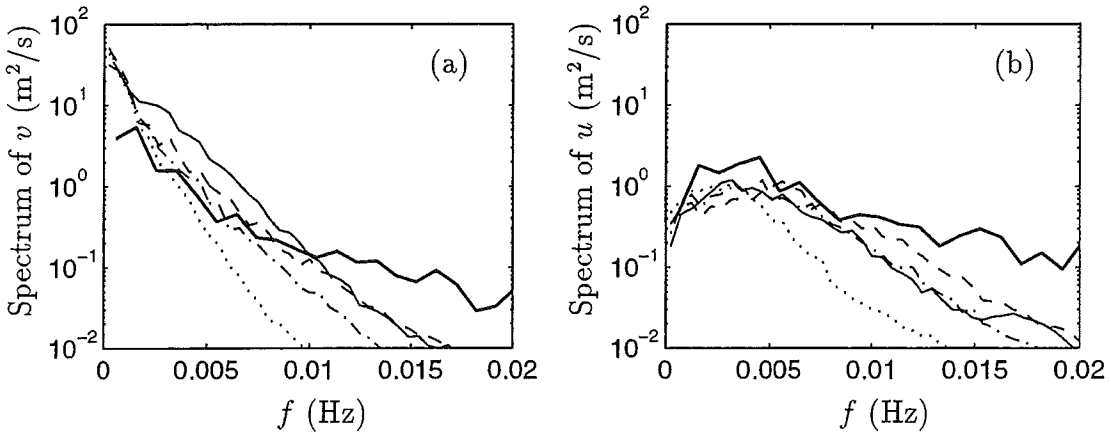

Figure 6.55: October 15: Frequency spectra of (a) longshore and (b) cross-shore velocities for data (thick ——), $c_f = 0.002$ and $M = 0$ (thin ——), $M = 0.25$ (– –), $M = 0.5$ (– · –), $M = 1$ (· · ·)

The cross-shore distribution of the mean longshore current is shown in Figure 6.56. For all four cases, a peak is predicted about 100 m offshore. The strength of the peak as well as the offshore shear of the current profiles for different M-values are remarkably similar although the instability climates that generated them are different. There are differences in the prediction of the size of the shoreline jet. The mean longshore current associated with $M = 0$ exhibits some oscillations. The appearance of these oscillations is suspected to be linked to the unrealistically high gradients associated with the shoreline jet. This effect is especially pronounced for $M = 0$ since no eddy viscosity mixing mechanism exists to smooth the shoreline jet.

The cross-shore distribution of the turbulent kinetic energy for the four cases is shown in Figure 6.57. We can observe that the total perturbation energy associated with $M = 0$ is highest, whereas the energy associated with $M = 1$ is lowest. Throughout most of the domain the mean perturbation kinetic energy for $M = 0$ is higher than for lower M-values. However, in a narrow region near

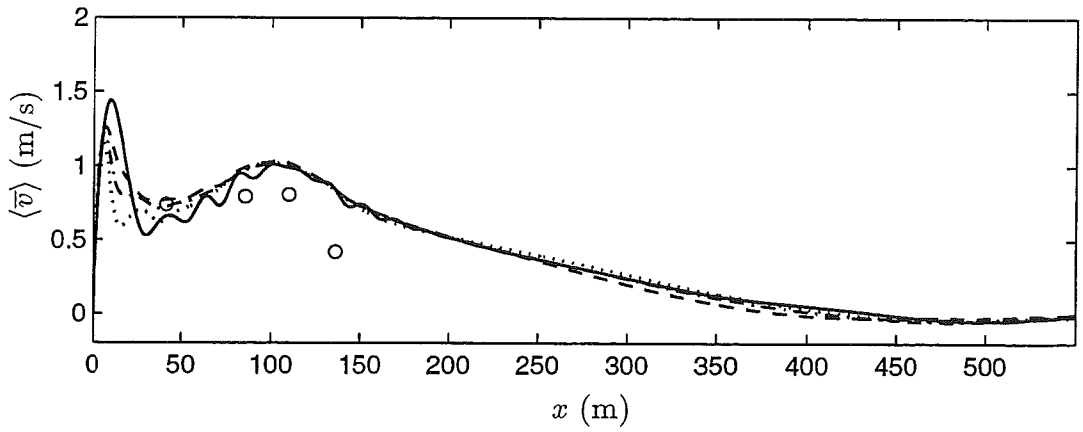

Figure 6.56: October 15: Time and longshore-averaged longshore currents $\langle\overline{v}\rangle$ for $c_f = 0.002$ and $M = 0$ (——), $M = 0.25$ (– –), $M = 0.5$ (– · –), $M = 1$ (· · ·) and sled data (o).

the shoreline ($x < 40$ m) the case associated with $M = 1$ exhibits the highest perturbation kinetic energy. This region corresponds to the part of the surf zone affected by the shoreline jet.

It is instructive to analyze the mean momentum balance that leads to the generation of the mean longshore current profiles shown in Figure 6.56 in order to asses the roles of momentum mixing due to the instabilities as well as the eddy viscosity term. The time and longshore-averaged momentum balance in the longshore direction was derived in Section 6.3.2 and is given by

$$\langle\overline{u\frac{\partial v}{\partial x}}\rangle + \langle\overline{\frac{\mu}{D}v}\rangle - \langle\overline{\tau_y'}\rangle = \langle\overline{\tilde{\tau}_y}\rangle. \tag{6.42}$$

In this equation, the first term represents lateral momentum mixing induced by the instabilities, the second term represents bottom friction and the third term represents the effects of lateral momentum mixing due to processes other than the instabilities, herein referred to as the mixing due to the eddy viscosity term. These three terms balance the effect of the short wave forcing term on the right

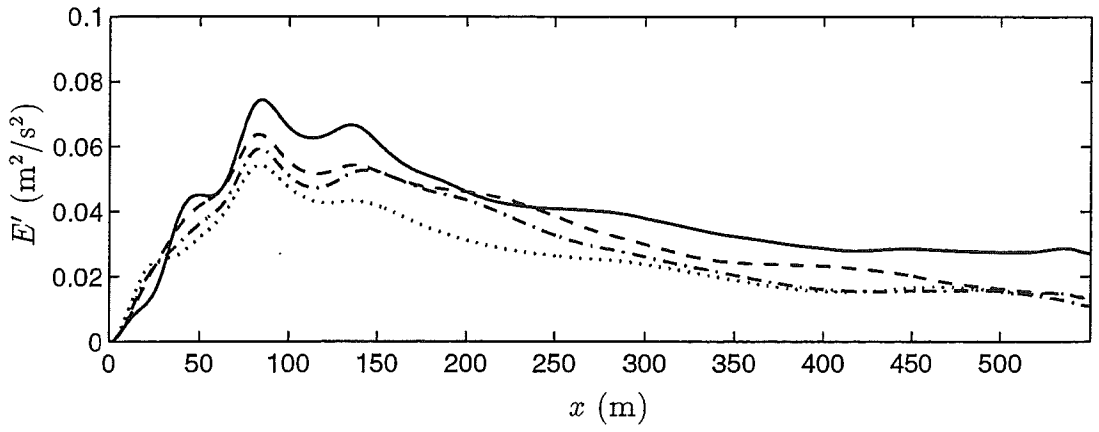

Figure 6.57: October 15: Time and longshore-averaged longshore perturbation kinetic energy $\frac{1}{2}\langle\overline{u'^2} + \overline{v'^2}\rangle$ for $c_f = 0.002$ and $M = 0$ (——), $M = 0.25$ (– –), $M = 0.5$ (– · –), $M = 1$ (· · ·).

hand side. The cross-shore variations of the terms for the four cases involving different M-values are shown in Figures 6.58 through 6.61. The longshore averages are performed over the entire width of the domain while the time averages are computed using the last 2.7 hours of the computed time series.

For $M = 0$ (Figure 6.58), the short wave forcing is seen to be balanced by bottom friction and mixing induced by the instabilities since other mixing mechanisms are neglected. The residual is observed to be small indicating that the estimates are statistically steady. The short wave forcing function is seen to be localized in two regions causing a shoreline jet and a longshore current peak around the bar crest. Mixing due to the instabilities around the shoreline jet is small, so the strength of the shoreline jet is not affected by the instabilities. It should be noted that the magnitude of the mixing term due to the instabilities is of the same order as the contribution due to bottom friction.

For $M = 0.25$ (Figure 6.59), we note that the mixing due to the eddy

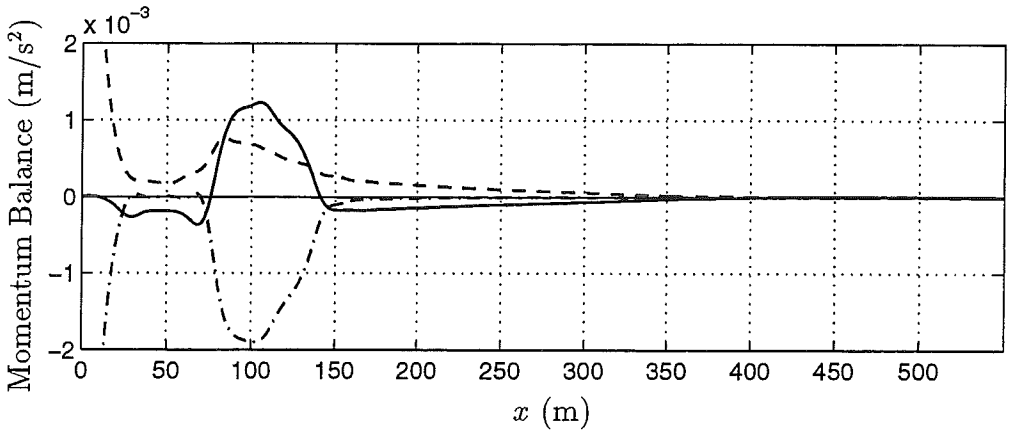

Figure 6.58: October 15: Mean longshore momentum balance for $c_f = 0.002$, $M = 0$. $\langle\overline{u(\partial v/\partial x)}\rangle$ (thick ——), -$\langle\overline{\tilde{\tau}_y}\rangle$ (– · –), -$\langle\overline{\tau'_y}\rangle$ (thin ——), $\langle\overline{\frac{\mu}{D}v}\rangle$ (thick – –), residual (thin – –).

viscosity term now contributes to the mean balance, especially in the area of the shoreline jet where the instabilities are not very active. The magnitude of the mixing due to the $\langle\overline{\tau'_y}\rangle$ term is small. Since the contribution of bottom friction is the same, the mixing caused by the instabilities at the current peak is slightly less; however, it is the dominant mixing process.

For $M = 0.5$ (Figure 6.59), the contribution of the $\langle\overline{\tau'_y}\rangle$ term is seen to be more pronounced. The shoreline jet is affected by this term. The contribution from the instabilities is decreased slightly while the effect of the bottom friction has not been altered.

Finally, for $M = 1$ (Figure 6.60), the contribution of the $\langle\overline{\tau'_y}\rangle$ term is seen to be significant. However, the instabilities are still providing the dominant mixing effect around the longshore current peak. The bottom friction contribution is the same as for the previous cases. This observation indicates that the generated longshore current displays the same structure for all cases regardless of the mixing

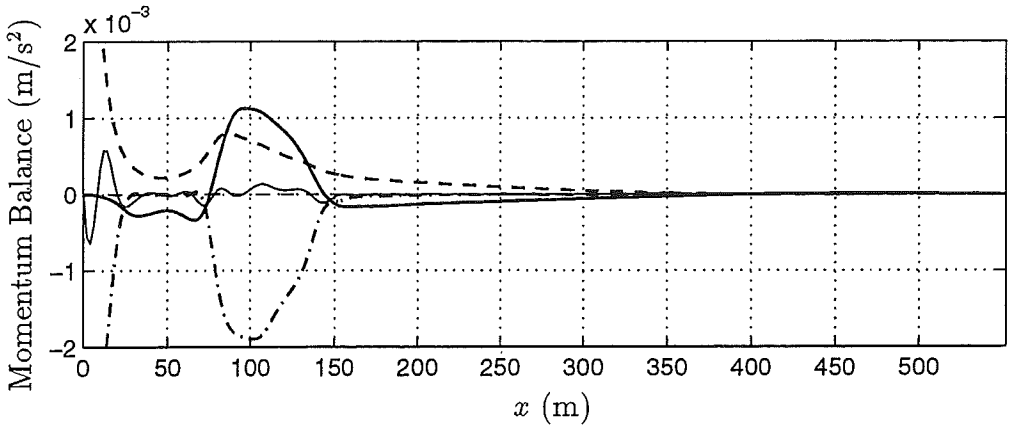

Figure 6.59: October 15: Mean longshore momentum balance for $c_f = 0.002$, $M = 0.25$. $\langle\overline{u(\partial v/\partial x)}\rangle$ (thick ——), -$\langle\overline{\tilde{\tau}_y}\rangle$ (– · –), -$\langle\overline{\tau'_y}\rangle$ (thin ——), $\langle\overline{\frac{\mu}{D}v}\rangle$ (thick – –), residual (thin – –).

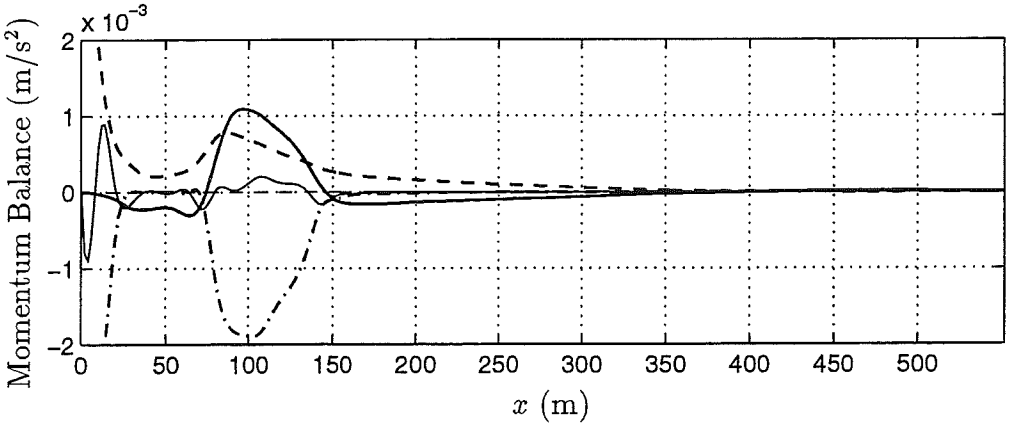

Figure 6.60: October 15: Mean longshore momentum balance for $c_f = 0.002$, $M = 0.5$. $\langle\overline{u(\partial v/\partial x)}\rangle$ (thick ——), -$\langle\overline{\tilde{\tau}_y}\rangle$ (– · –), -$\langle\overline{\tau'_y}\rangle$ (thin ——), $\langle\overline{\frac{\mu}{D}v}\rangle$ (thick – –), residual (thin – –).

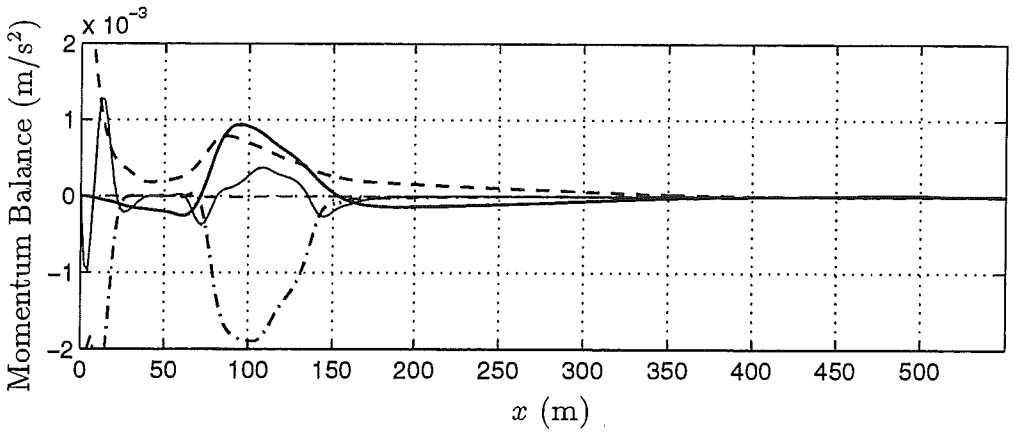

Figure 6.61: October 15: Mean longshore momentum balance for $c_f = 0.002$, $M = 1$. $\langle\overline{u(\partial v/\partial x)}\rangle$ (thick ——), -$\langle\overline{\tilde{\tau}_y}\rangle$ (– · –), -$\langle\overline{\tau_y'}\rangle$ (thin ——), $\langle\overline{\frac{\mu}{D}v}\rangle$ (thick – –), residual (thin – –).

coefficient M. This was also observed when analyzing the cross-shore distribution of the mean longshore current in Figure 6.56. Especially for $M = 0.25, 0.5$ and 1, the longshore current profile in the region offshore of the bar trough displays a remarkably similar strength and shape. The momentum mixing required to generate this profile is in all three cases provided in different proportions by the two lateral mixing terms $\langle\overline{\tau_y'}\rangle$ and $\langle\overline{u(\partial v/\partial x)}\rangle$.

The contribution of the mixing term $\langle\overline{\tau_y'}\rangle$ due to turbulence or the Taylor dispersion process to the momentum balance is seen to be small for realistic mixing coefficients of $M = 0.25$ and $M = 0.5$. Mixing caused by the instabilities is observed to be stronger. The contribution of the eddy viscosity term $\langle\overline{\tau_y'}\rangle$ in the absence of shear instabilities can be assessed by confining the longshore length scale of the domain to prevent the growth of the instabilities, effectively simulating the one-dimensional problem.

The mean momentum balance resulting from such a simulation for $M =$

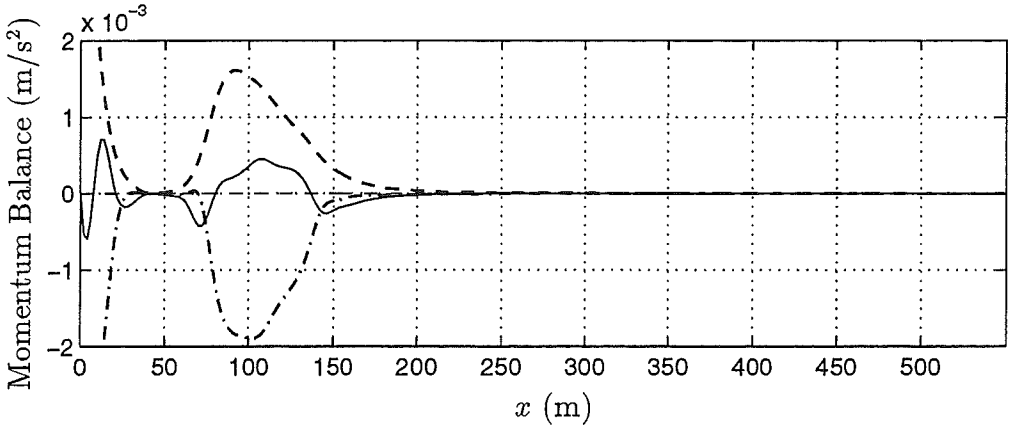

Figure 6.62: October 15: Mean longshore momentum balance in the absence of shear instabilities for $c_f = 0.002$ and $M = 0.25$. $-\langle\overline{\tilde{\tau}_y}\rangle$ (– · –), $-\langle\overline{\tau_y'}\rangle$ (thin ——), $\langle\overline{\frac{\mu}{D}v}\rangle$ (thick – –), residual (thin – –).

0.25 is shown in Figure 6.62 and reveals that in the absence of instabilities the only mixing process is due to the $\langle\overline{\tau_y'}\rangle$ term. The magnitude of the mixing effect around the location of the current peak is 0.5 $\times 10^{-3}$ m/s^2. The mean longshore current profiles resulting from the simulations including and neglecting shear instabilities are shown in Figure 6.63 and are seen to be very different, confirming that mixing due to the instabilities is significant. These two current profiles can be considered to be the profiles before and after the onset of the instabilities.

Our expectation is that mixing due to the $\langle\overline{\tau_y'}\rangle$ term, which is present in the absence of instabilities, will continue to act in the presence of them while the mixing due to the instabilities is added to the system and alters the mean current profile further. However, we find that the mixing term $\langle\overline{\tau_y'}\rangle$ becomes less important when the mixing due to the instabilities is considered. A comparison of the mixing terms $\langle\overline{\tau_y'}\rangle$ in the absence and presence of the instabilities is shown in Figure 6.64 and shows that the contribution of these terms to the momentum balance is reduced significantly when shear instabilities are present.

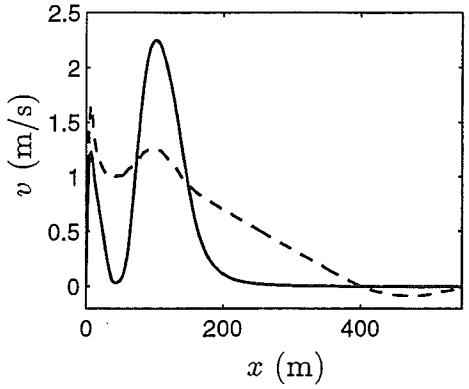

Figure 6.63: October 15: Time and longshore-averaged longshore currents $\langle \overline{v} \rangle$ for $c_f = 0.002$ and $M = 0.25$ suppressing (——) and including (– –) shear instabilities.

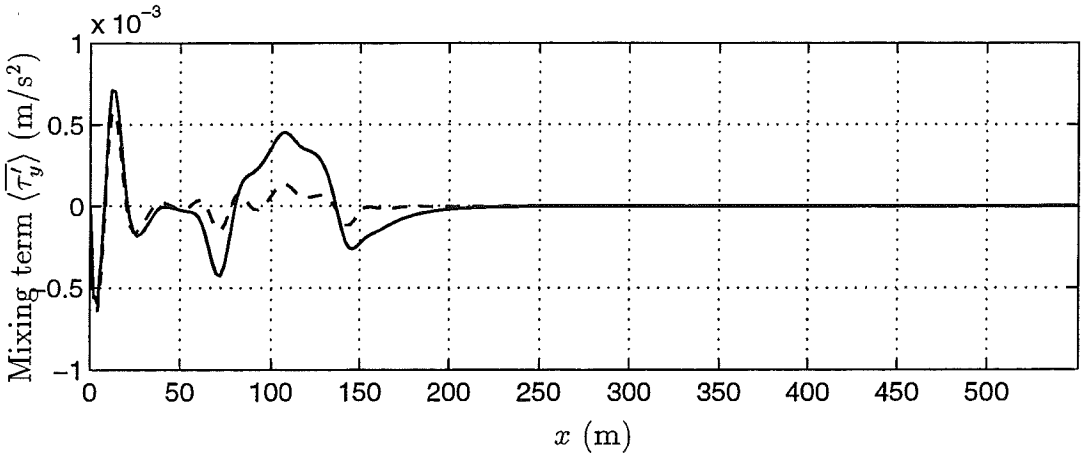

Figure 6.64: October 15: Contribution to the mean momentum balance of the mixing term $\langle \overline{\tau_y'} \rangle$ for $c_f = 0.002$ and $M = 0.25$ in the absence (——) and presence (– –) of shear instabilities.

Although the contribution of the momentum mixing due to turbulence or Taylor dispersion is smaller than the mixing caused by the instabilities themselves, the effect of the eddy viscosity mixing on the shear instabilities is significant. Mixing due to the instabilities acts on the mean current profile; however, mixing due to the eddy viscosity terms in the momentum equations acts on both the mean current as well as the shear instabilities. We had already observed that large values of M cause the propagation speed of the instabilities to decrease. Examining snapshots of the vorticity fields for different M-values we can further analyze the dissipative effects of the mixing terms.

For $M = 0$, snapshots of the vorticity displayed in Figure 6.65 show the presence of strong vortices both in the nearshore as well as offshore whereas vorticity fields for $M = 0.5$ (Figure 6.66) and $M = 1$ (Figure 6.67) show that the length scales associated with the disturbances increase since the fast oscillations are damped out by the diffusional effect of the eddy viscosity mixing term. The vortices associated with the higher M-values can also be observed to be weaker.

6.6.2 Simulations of October 16

Simulations for October 16 were carried out for three values of the mixing coefficient M given by 0, 0.25 and 0.5. The friction coefficient is kept constant at $c_f = 0.0035$. This value for the friction coefficient reproduced the propagation speed observed in the data. Time series of the resulting motions are shown in Figure 6.68. The time series were obtained in the trough region of the bar where measurements from current meters are available.

The time series depicted in Figure 6.68 show that instabilities reach finite amplitude quicker for lower M. In the time series for $M = 0.5$ the generation of

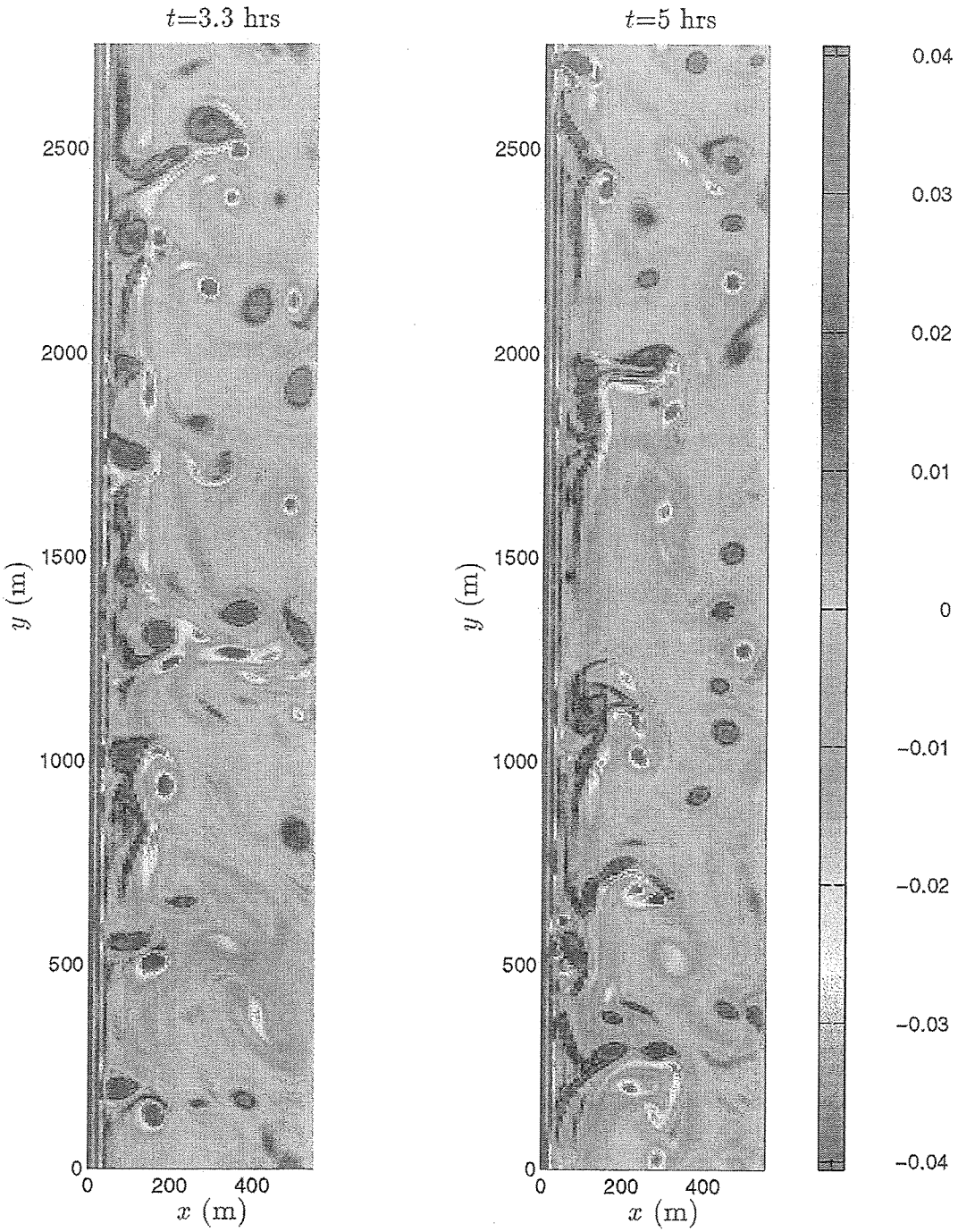

Figure 6.65: October 15: Contour plots of vorticity q (1/s) for $c_f = 0.002, M = 0$

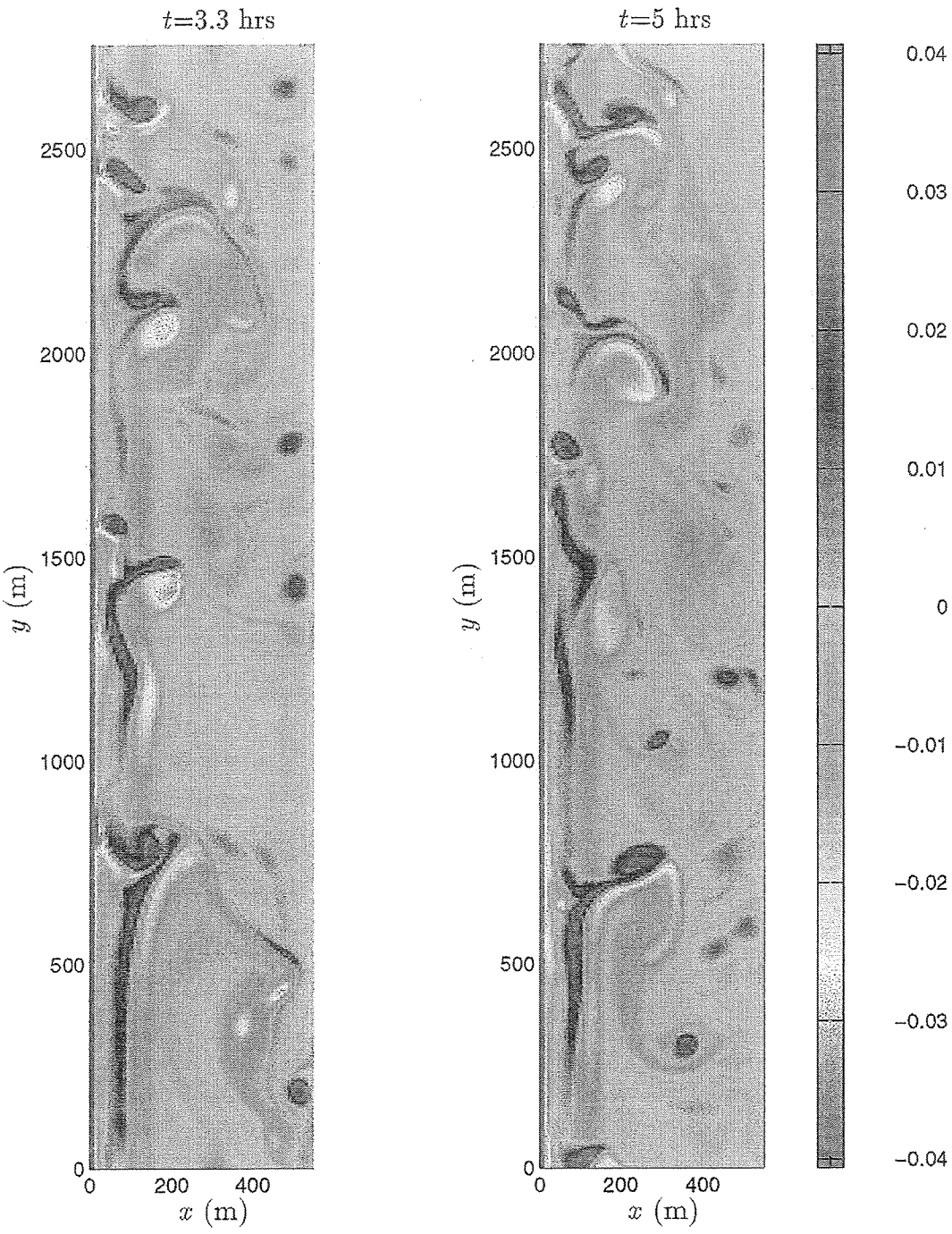

Figure 6.66: October 15: Contour plots of vorticity q (1/s) for $c_f = 0.002, M = 0.5$

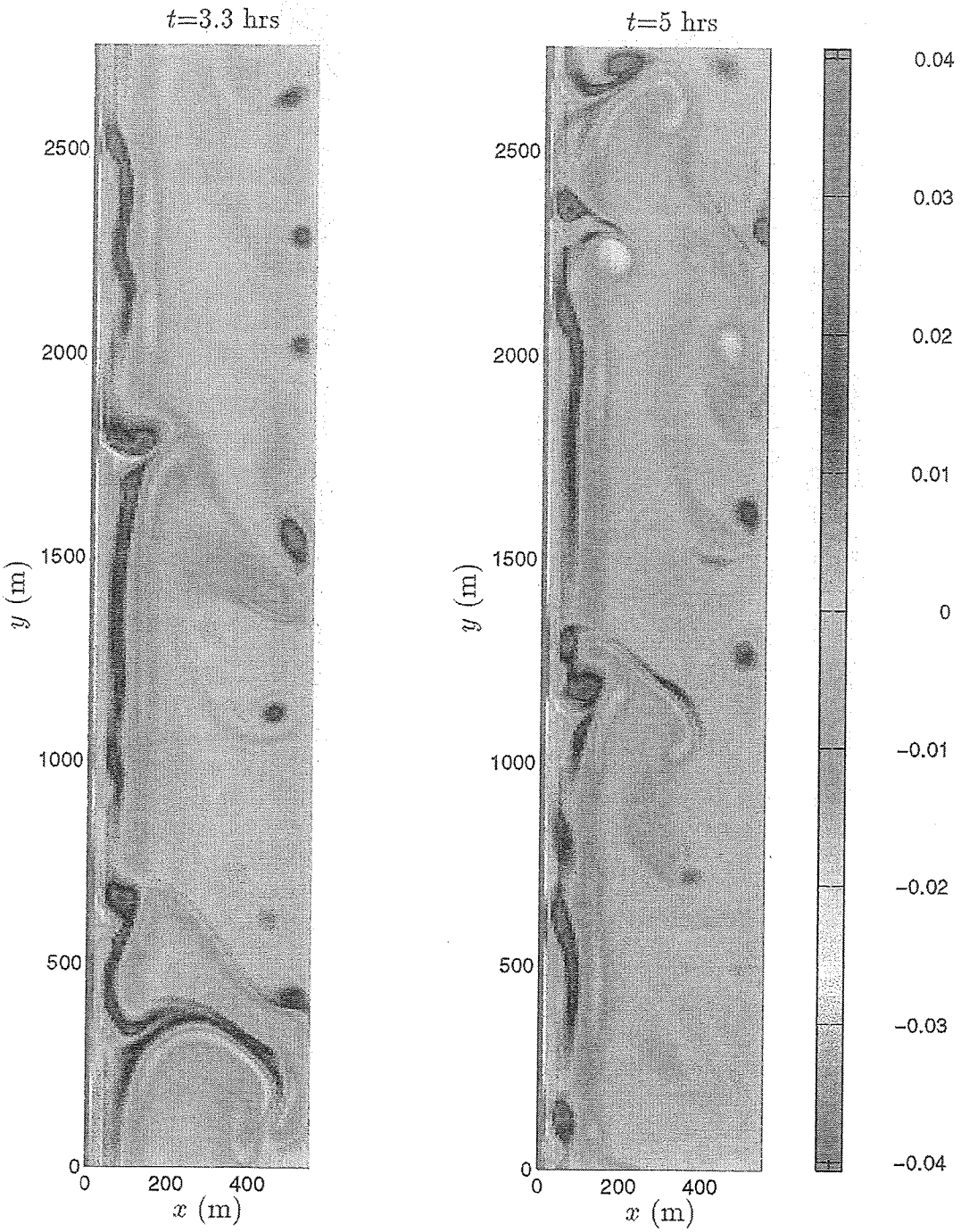

Figure 6.67: October 15: Contour plots of vorticity q (1/s) for $c_f = 0.002, M = 1$

a longshore current before the onset of instabilities is evident. As the instabilities reach finite amplitude, the mean current is also altered rapidly. The time series for $M = 0$ display the initial growth of disturbances with time scales of 200 sec. Although lower frequency oscillations are evident later in the simulation, oscillations at 200 sec persist. As M is increased longer time oscillations become more prominent.

Frequency-longshore wavenumber spectra of the longshore velocities are shown for the three cases as well as data in Figure 6.69. It is observed that the propagation speeds decrease by less than 10% for higher values of M. The propagation speed inferred from the data is well reproduced. Spectra of the cross-shore velocities shown in Figure 6.70 also reproduce the propagation speed of the data. It is noted that the spectra for the longshore as well as the cross-shore velocities do not exhibit significant differences for the different M values.

Quantitative comparison of the frequency spectra of the computations and data are shown in Figure 6.71. As for October 15, we see that the spectrum of the longshore velocities is overpredicted for $f < 0.01$ Hz and underpredicted for $f > 0.01$ Hz. The cases involving different M-values do not exhibit significant differences. The energy contained in the shear wave band is similar for all three cases. The same statement can be made for the spectra of the cross-shore velocities. The case involving $M = 0$ is seen to be less energetic for $f < 0.01$ Hz. The general trends of the spectra of the observed cross-shore velocities is reproduced for $f < 0.01$ Hz; however, the spectra of the computations has a high decay rate for high frequencies.

The time and longshore-averaged longshore currents for the three cases involving $M = 0, 0.25, 0.5$ are shown in Figure 6.72. Once again we notice that the mean current velocities are very similar. Especially the peak current and

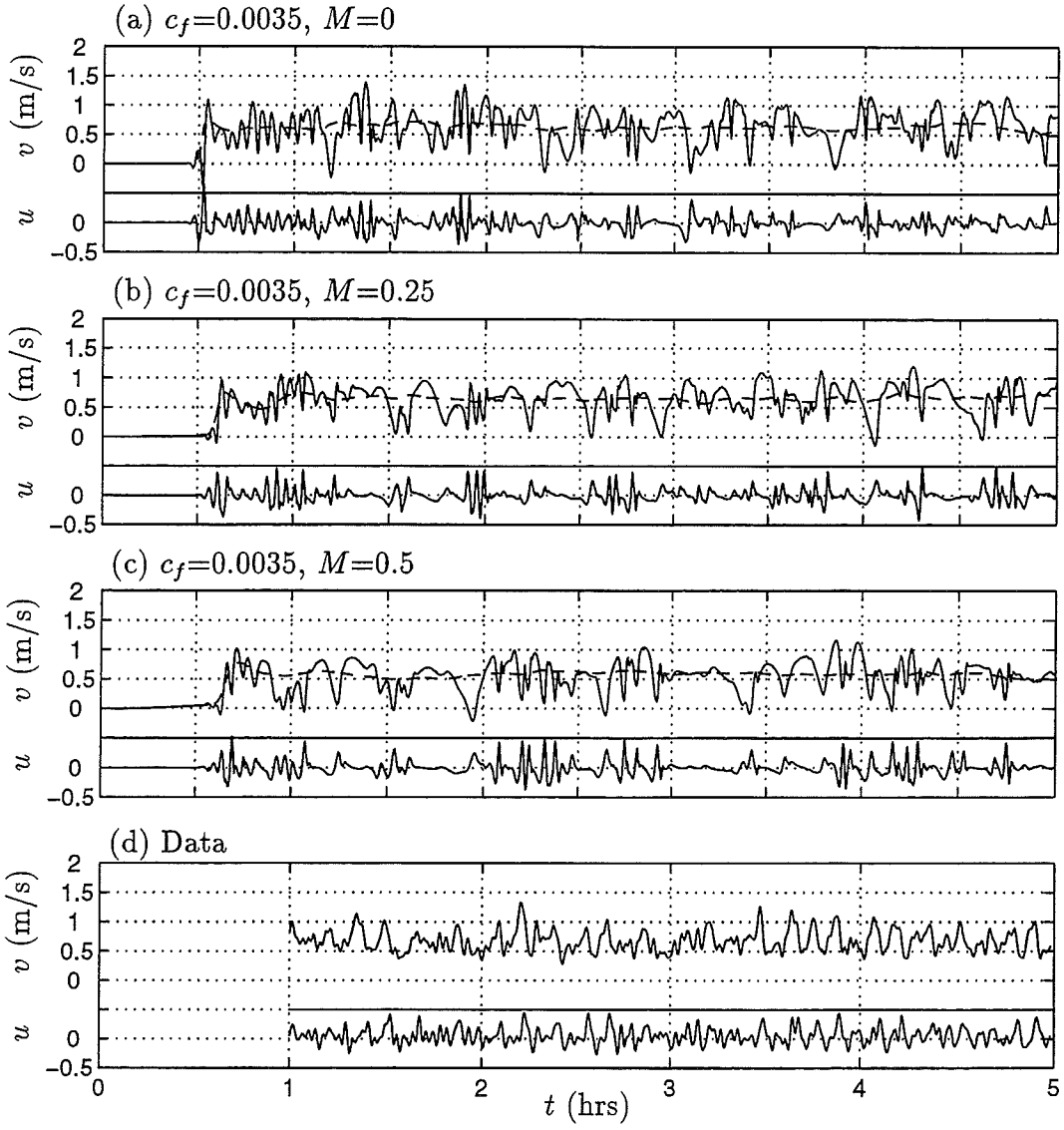

Figure 6.68: October 16: Time series of velocities u, v and $\langle v \rangle$ (– –) at (x, y)=(35 m, $L_y/2$) and time series of velocities u and v of data.

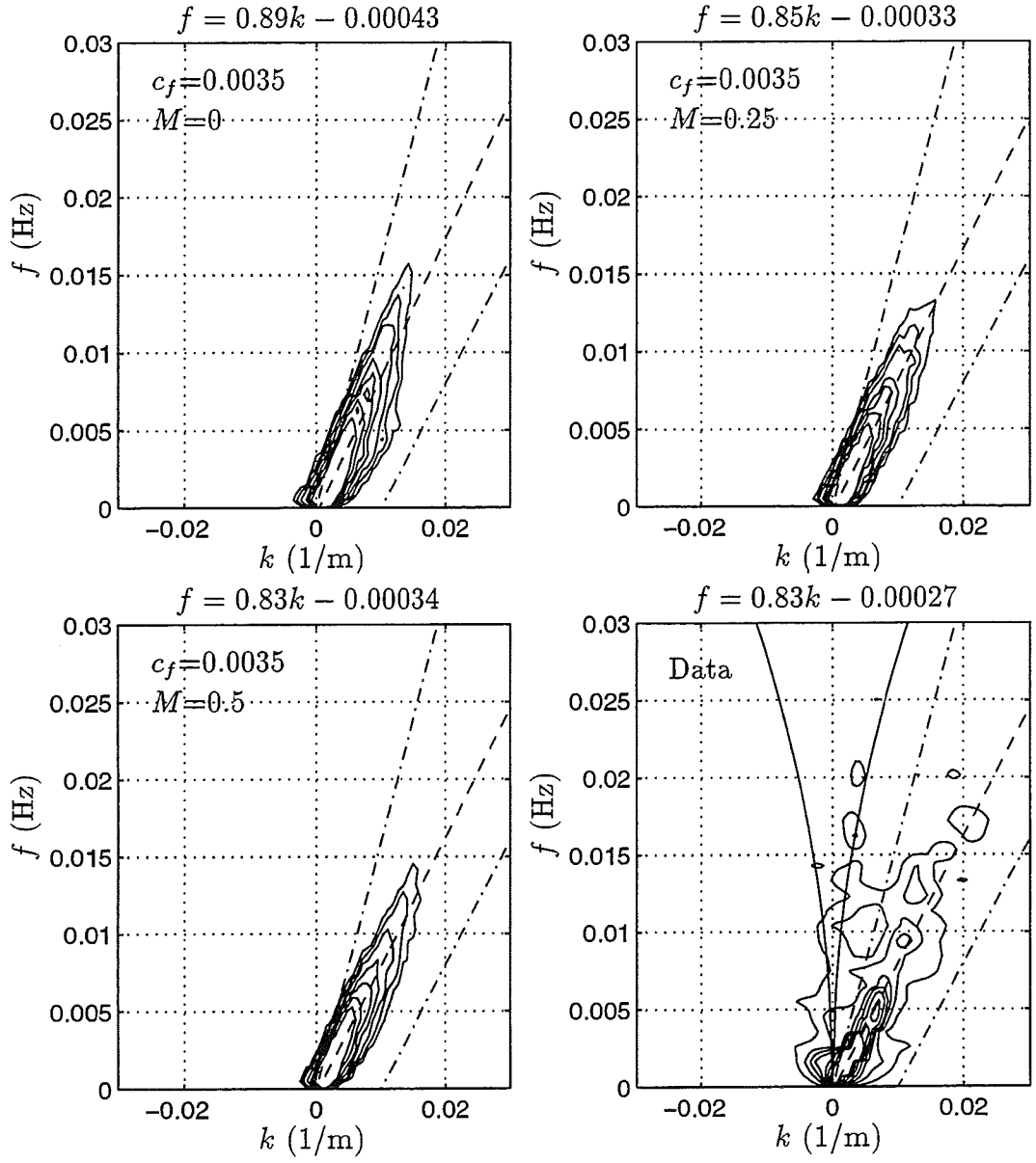

Figure 6.69: October 16: Frequency-cyclic wavenumber spectra $S(f,k)$ (m^3/s) for computed and measured longshore velocity at x =35 m. The value for c_{est} is 0.8 m/s, and is used in Equation (6.3) to construct the upper and lower cut-off lines (– · –) of the shear wave energy. Contour levels plotted are (10, 30, 60, 100, 200, 400, 800). The equation for the best fit dispersion line (— —) is noted above each plot.

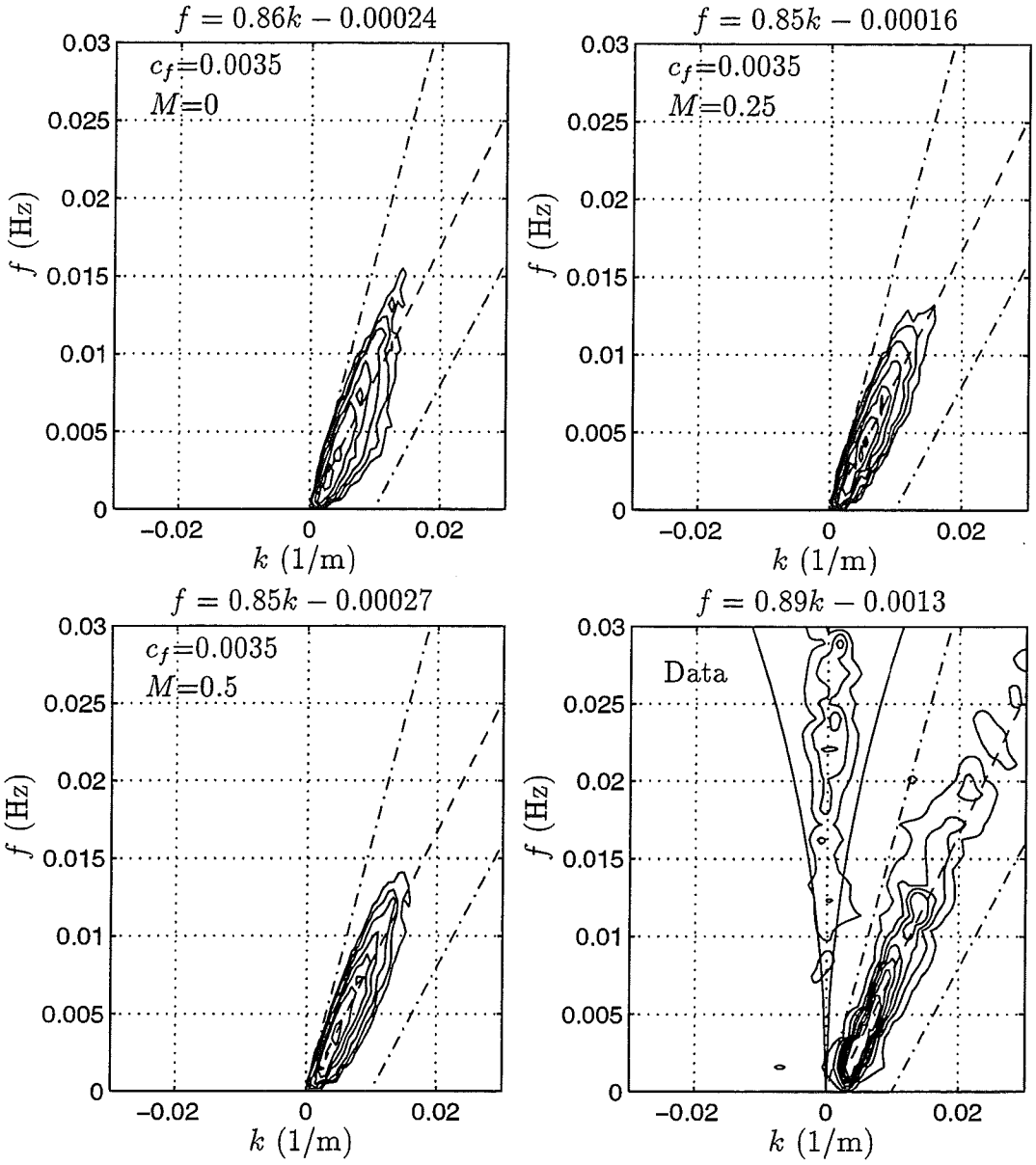

Figure 6.70: October 16: Frequency-cyclic wavenumber spectra $S(f,k)$ (m^3/s) for computed and measured cross-shore velocity at x =35 m. The value for c_{est} is 0.8 m/s, and is used in Equation (6.3) to construct the upper and lower cut-off lines (– · –) of the shear wave energy. Contour levels plotted are (10, 30, 60, 100, 200, 400, 800). The equation for the best fit dispersion line (– –) is noted above each plot.

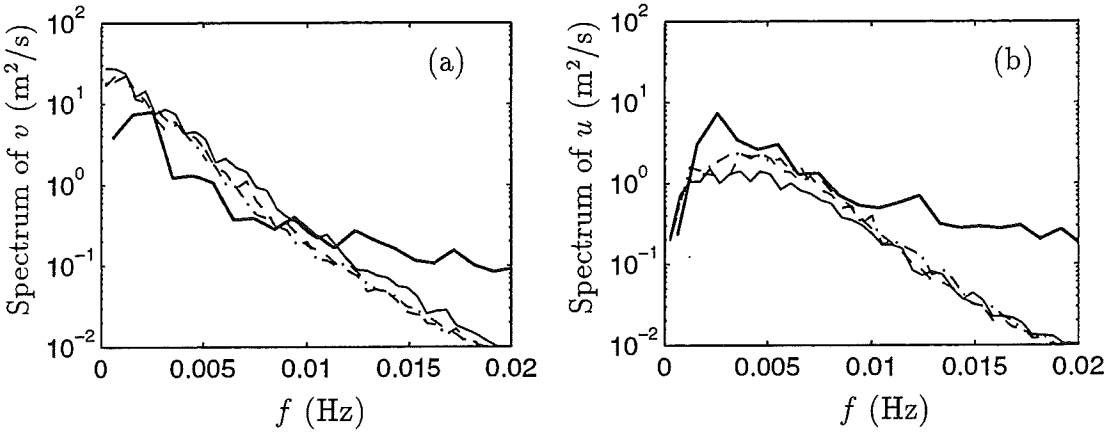

Figure 6.71: October 16: Frequency spectra of (a) longshore and (b) cross-shore velocities for data (thick ——), $c_f = 0.0035$ and $M = 0$ (thin ——), $M = 0.25$ (– –), $M = 0.5$ (– · –)

the seaward shear of the current profiles are very similar. Some differences exist around the area of the shoreline jet. Current measurements from the sled in the bar and trough regions are reproduced. The predicted maximum current is also of the measured size.

The mean perturbation kinetic energy for the three cases is shown in Figure 6.73. We observe the two peaks in the cross-shore distribution of the perturbation kinetic energy. The peaks are located around the peak of the mean longshore current depicted in Figure 6.72. It is suspected that the two peaks are associated with the layers of positive and negative vorticity just shoreward and seaward of the longshore current peak. The cross-shore distributions for the different M-values display similar trends as for October 15. We notice that in the region shoreward of the longshore current peak and especially around $x = 30$ m, the perturbation kinetic energy for the cases involving different M-values is very similar. This explains the minor differences in the frequency spectra for the different cases since time series used to generate the spectra were collected at $x = 35$ m. However,

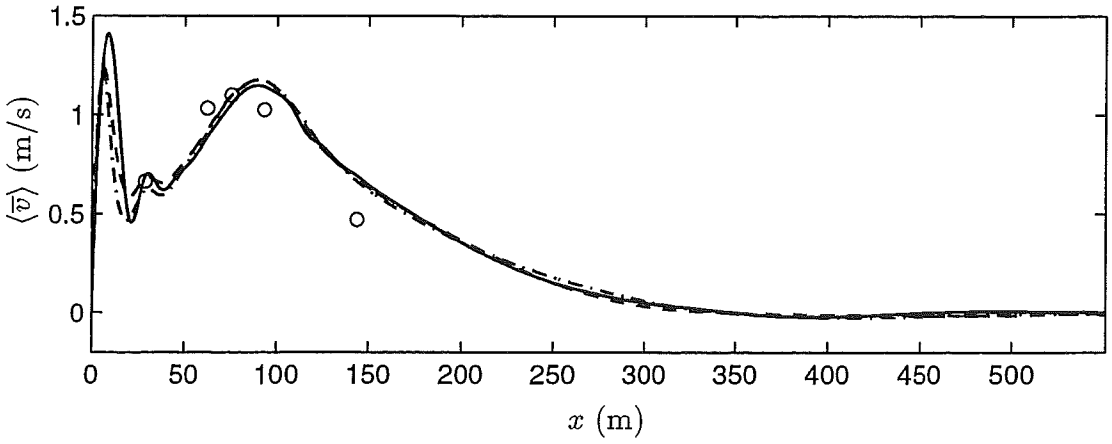

Figure 6.72: October 16: Time and longshore-averaged longshore currents $\langle\overline{v}\rangle$ for $c_f = 0.0035$ and $M = 0$ (——), $M = 0.25$ (– –), $M = 0.5$ (– · –) and sled data (o).

seaward of the location of the longshore current peak, the energy associated with $M = 0$ is much higher than for lower values of M. Unfortunately, time series of current measurements are only available in the trough region of the bar. Therefore, we have no means of determining which M-value is more appropriate in this case.

We will examine the mean momentum balance in the longshore direction for the three cases utilizing Figure 6.74. The contribution of the bottom friction is very similar for all three cases confirming that the resulting mean longshore current profile for all the cases should also be similar. The mixing caused by the instabilities in the trough region is almost identical in all three cases, confirming that differences between the cases should be minor in the bar trough region. The short wave forcing term is the same for all three cases. The eddy viscosity mixing term $\langle\overline{\tau_y'}\rangle$ makes no contribution for $M = 0$. Its contribution increases as M increases. The term is especially active around the shoreline jet, where the shear instabilities do not induce mixing, and around the longshore current peak. We note that the mixing caused by the instabilities is much larger than

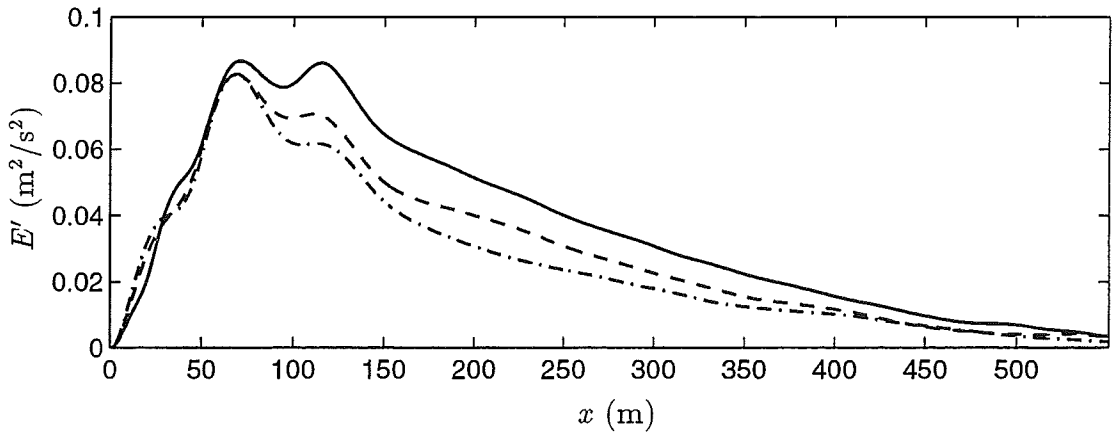

Figure 6.73: October 16: Time and longshore-averaged longshore perturbation kinetic energy $\frac{1}{2}\langle\overline{u'^2} + \overline{v'^2}\rangle$ for $c_f = 0.0035$ and $M = 0$ (——), $M = 0.25$ (– –), $M = 0.5$ (– · –).

mixing induced due to the $\langle\overline{\tau'_y}\rangle$ term. However, the contribution due to the shear instabilities decreases as the contribution of the $\langle\overline{\tau'_y}\rangle$ term increases.

During the simulations for October 15, we found that the contribution of the mixing caused by the $\langle\overline{\tau'_y}\rangle$ term is more pronounced in the absence of the instabilities. We test this hypothesis once more for October 16. Simulations are carried out with a narrow longshore width so that the generation of the instabilities is suppressed. The values for the coefficients are chosen as $c_f = 0.0035$ and $M = 0.5$. The resulting steady longshore current is depicted in Figure 6.76 and represents a balance between the short wave forcing, the bottom friction and lateral mixing due to turbulence or Taylor dispersion (Figure 6.75). We note that the size of the mixing term $\langle\overline{\tau'_y}\rangle$ is 0.001 m/s^2. When the shear instabilities are included, the resulting momentum balance shown in Figure 6.74 (c) suggests that the maximum contribution to the mean balance due to the shear instabilities is 0.0015 m/s^2 whereas the contribution of the $\langle\overline{\tau'_y}\rangle$ term is reduced to 0.0005 m/s^2. The resulting mean longshore current is shown in Figure 6.76.

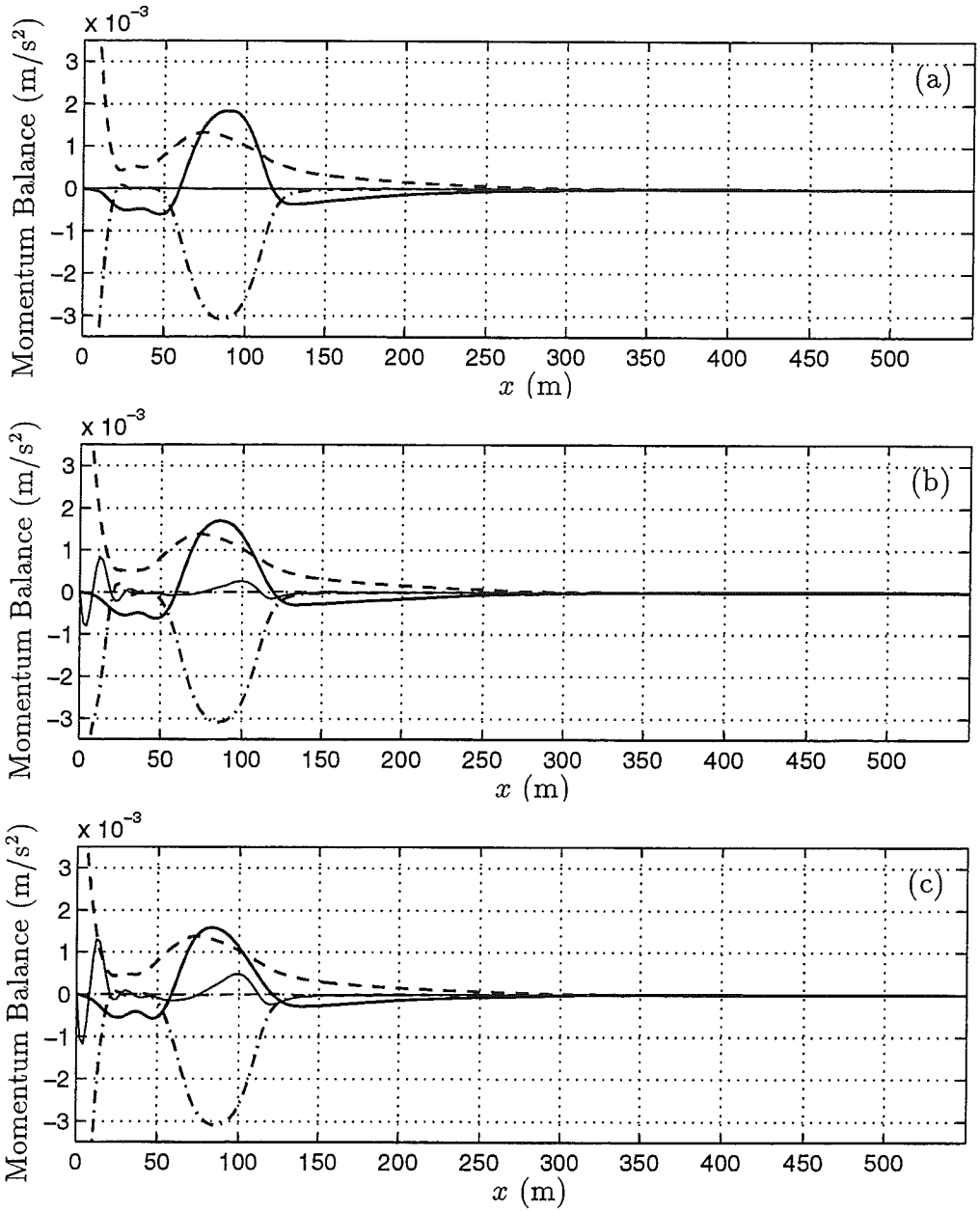

Figure 6.74: October 16: Mean longshore momentum balance for $c_f = 0.0035$ and (a) $M = 0$, (b) $M = 0.25$ and (c) $M = 0.5$. $\langle\overline{u(\partial v/\partial x)}\rangle$ (thick ——), $-\langle\overline{\tilde{\tau}_y}\rangle$ (– · –), $-\langle\overline{\tau_y'}\rangle$ (thin ——), $\langle\overline{\frac{\mu}{D}v}\rangle$ (thick – –), residual (thin – –).

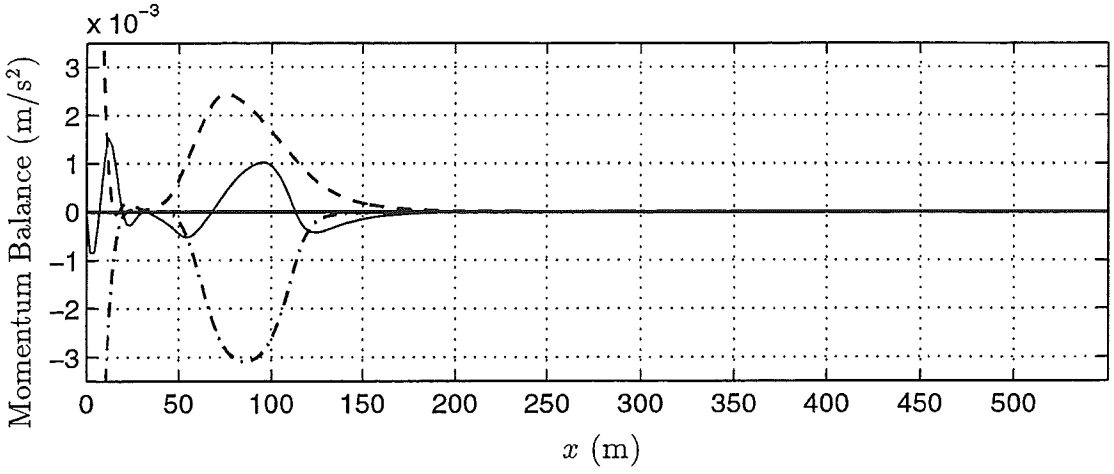

Figure 6.75: October 16: Mean longshore momentum balance in the absence of shear instabilities for $c_f = 0.0035$ and $M = 0.5$. $-\langle\overline{\tilde{\tau}_y}\rangle$ (– · –), $-\langle\overline{\tau'_y}\rangle$ (thin ——), $\langle\overline{\frac{\mu}{D}v}\rangle$ (thick – –), residual (thin – –).

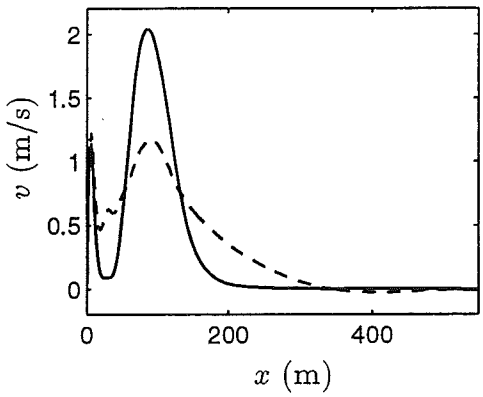

Figure 6.76: October 16: Time and longshore-averaged longshore currents $\langle\overline{v}\rangle$ for $c_f = 0.0035$ and $M = 0.5$ suppressing (——) and including (– –) shear instabilities.

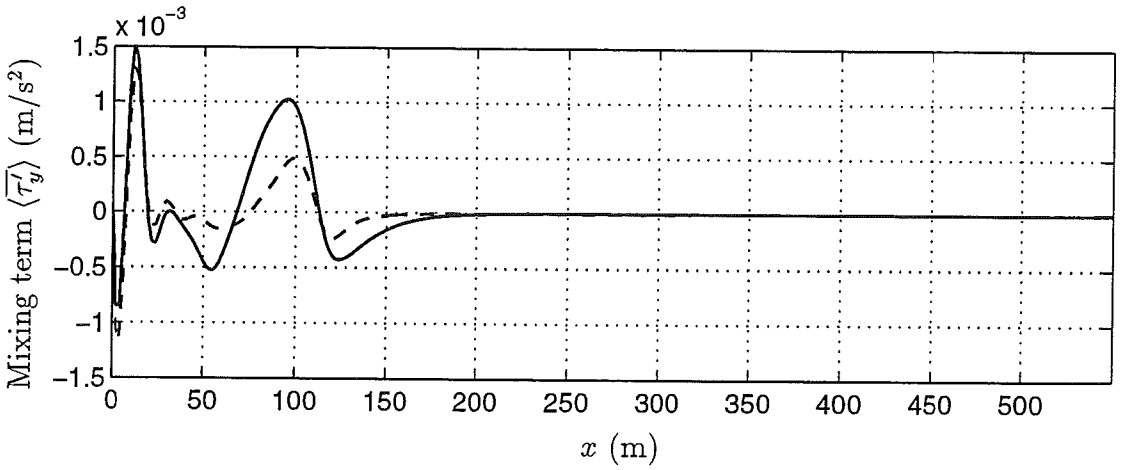

Figure 6.77: October 16: Contribution to the mean momentum balance of the mixing term -$\langle\overline{\tau_y'}\rangle$ for $c_f = 0.0035$ and $M = 0.5$ in the absence (——) and presence (– –) of shear instabilities.

The contribution of the $\langle\overline{\tau_y'}\rangle$ term in the absence and presence of shear instabilities are plotted together in Figure 6.77. The contributions are similar in the area of the shoreline jet where the instabilities are not active. However, the contribution is decreased by 50% if the instabilities are included.

Snapshots of the vorticity field are depicted in Figure 6.78 for M =0, 0.25 and 0.5. We notice that the length scales associated with the motions are larger as M increases. The layer of positive vorticity in the nearshore region appears to be of similar strength for the three cases. This observation is consistent with the finding that the perturbation kinetic energy for the cases does not differ significantly in the region shoreward of the longshore current peak. However, the layer of negative vorticity appears to be weaker for higher M, consistent with the observation that the perturbation kinetic energies for the three cases differ significantly offshore of the current peak. The amount of energy close to the offshore boundary also decreases for larger M.

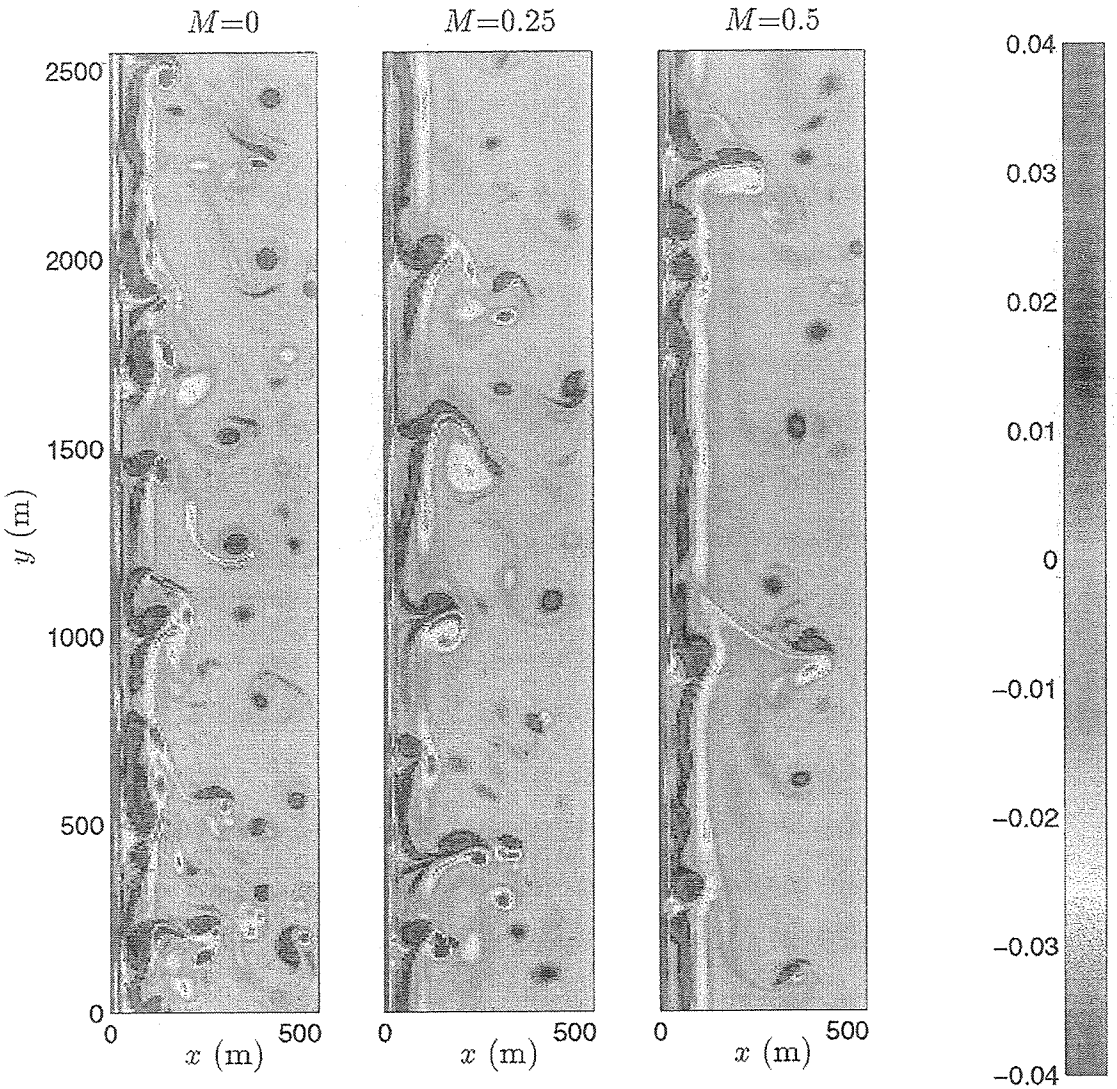

Figure 6.78: October 16: Contour plots of vorticity q (1/s) at $t = 5$ hrs for $c_f = 0.0035$ and $M = 0, 0.25, 0.5$.

6.6.3 Simulations of October 18

Simulations are carried out for October 18 using a fixed friction coefficient c_f of 0.003. The value of the mixing coefficient M is chosen as 0, 0.25 and 0.5. The reader is reminded that the instabilities were slightly weaker for October 18 than they were for October 15 and 16 and also displayed lower propagation speeds.

Time series of the computed velocities as well as data are shown in Figure 6.79. The time series clearly show that the spin-up time is longer for larger M confirming the dissipational nature of the mixing terms. The time series show less high frequency oscillations as M is increased. Especially the cross-shore velocities show that the instabilities have less energy for higher M. The generated mean longshore current has similar magnitude in all three cases. However, the longshore current generation for $M = 0.5$ is due in a large measure to the eddy viscosity mixing effects since the longshore current is generated prior to the onset of the instabilities. Oscillations at the time scale of 300 sec are evident in the time series for $M = 0$ and $M = 0.25$. Underlying longer oscillation can also be observed. Only oscillations with longer time scales are seen for $M = 0.5$ suggesting that the high frequency oscillations are damped out by the eddy viscosity mixing effects. We once again observe that near-zero longshore velocities occur for low values of M. Simultaneously, high cross-shore velocities are observed suggesting that the flow in the bar trough region becomes offshore directed.

Frequency-longshore wavenumber plots are depicted in Figures 6.80 and 6.81 for the longshore and cross-shore velocities, respectively. The spectra of the longshore velocities for $M = 0$ and $M = 0.25$ do not show significant differences. The spectrum for $M = 0.5$ displays noticeably less energy. The differences in energy content for the three cases are especially evident in the spectra of the cross-shore velocities. The energy content is seen to decrease significantly as M

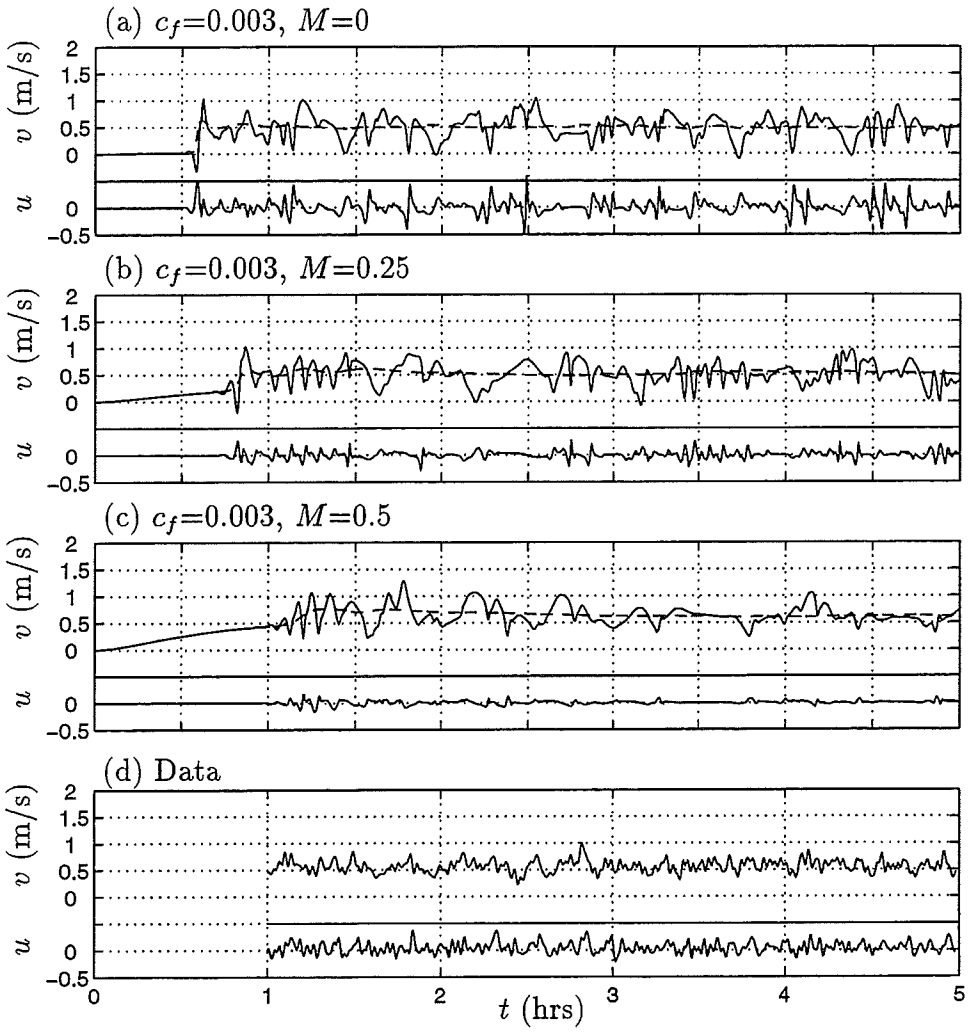

Figure 6.79: October 18: Time series of velocities u, v and $\langle v \rangle$ (– –) at (x, y)=(35 m, $L_y/2$) and time series of velocities u and v of data.

increases. However, variations in the predicted propagation speeds are small.

Comparison of the computed and measured frequency spectra (Figure 6.82) show that the amount of energy in the range $0.002 < f < 0.007$ Hz is predicted reasonably well for the longshore velocities with $M = 0$ and $M = 0.25$. Energy at frequencies below this range are again overpredicted whereas energy above this range is underpredicted. Turning to the spectra of the cross-shore velocities we note that the case involving $M = 0$ produces results closest to the observations in the range $0.002 < f < 0.007$ Hz. The cases involving higher values for M cause underprediction.

The time and longshore-averaged mean longshore current shown in Figure 6.83 confirms that the similarity of the current profiles for different M-values is a robust feature. Some variability in the current maximum is observed but the overall shapes of the current profiles are seen to agree offshore of the bar trough. As seen in the previous days, the predictions for the magnitude of the shoreline jet vary.

Examining Figure 6.84, we note that higher perturbation kinetic energies are observed throughout the modeling domain for lower M. The inflection point in the curves around the bar trough observed for October 15 and 16 is not observed on this day. This is consistent with the fact that significantly different levels of energy were observed in the frequency spectra for different M-values.

The mean longshore momentum balance for the three cases (Figure 6.85) shows that the $\langle\overline{\tau_y'}\rangle$ term is more active in the bar trough region. For $M = 0.5$, the contributions of mixing due to the instabilities and due to the $\langle\overline{\tau_y'}\rangle$ term are closer in magnitude than for the previous days. However, the mixing due to the instabilities still dominates in the region of the longshore current peak. In turn,

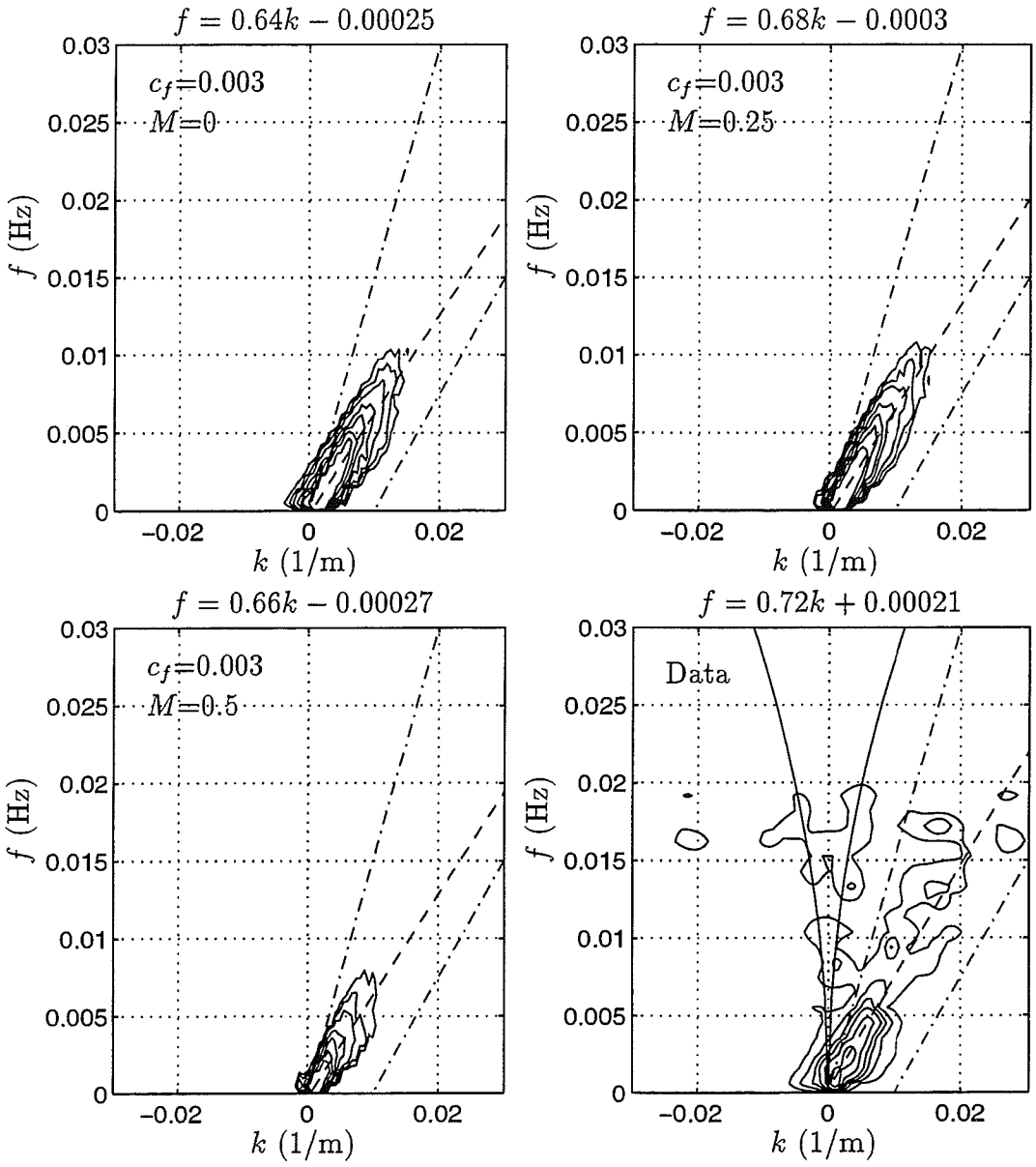

Figure 6.80: October 18: Frequency-cyclic wavenumber spectra $S(f,k)$ (m^3/s) for computed and measured longshore velocity at x =35 m. The value for c_{est} is 0.75 m/s, and is used in Equation (6.3) to construct the upper and lower cut-off lines (– · –) of the shear wave energy. Contour levels plotted are (10, 30, 60, 100, 200, 400, 800). The equation for the best fit dispersion line (– –) is noted above each plot.

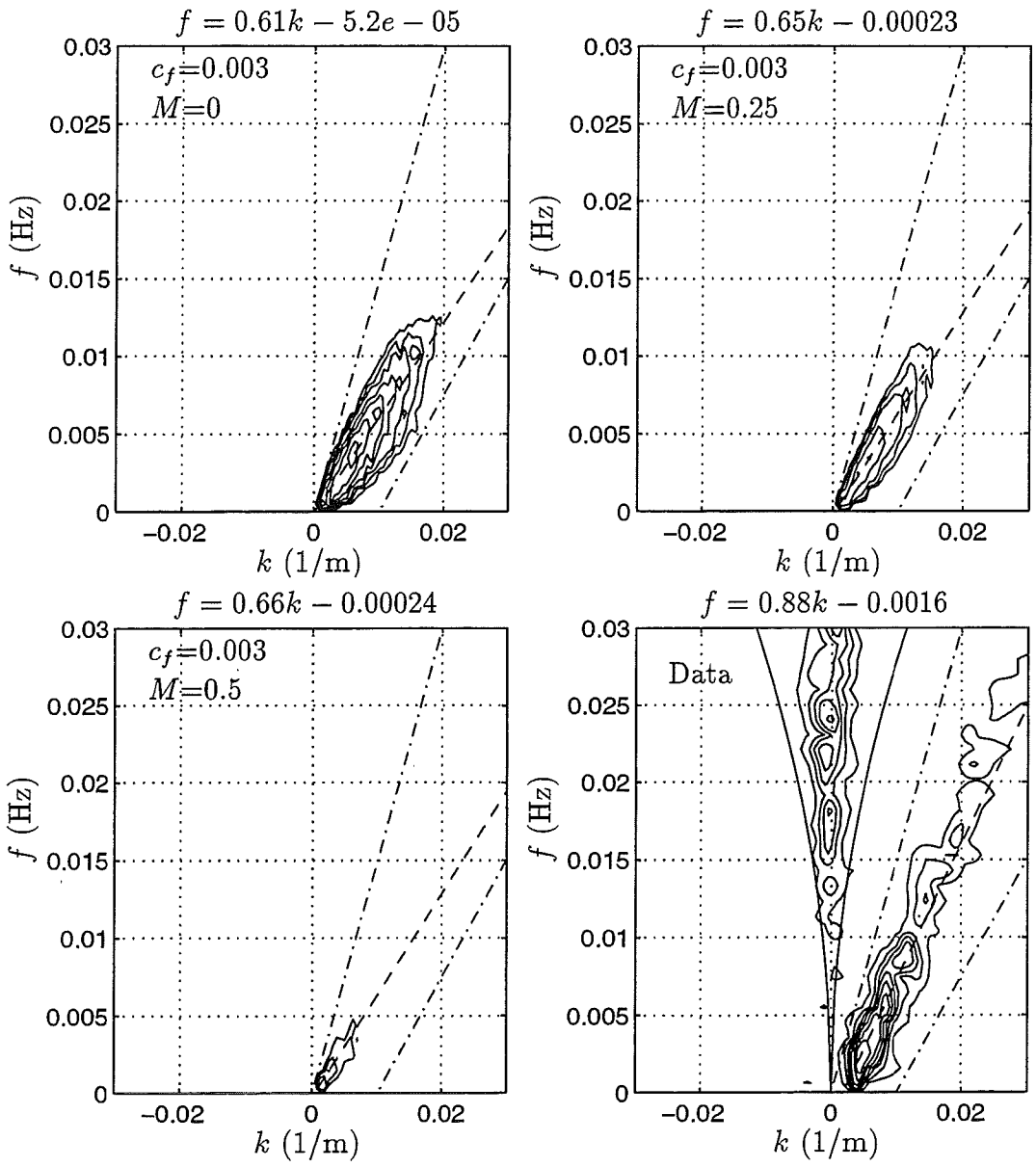

Figure 6.81: October 18: Frequency-cyclic wavenumber spectra $S(f,k)$ (m^3/s) for computed and measured cross-shore velocity at x =35 m. The value for c_{est} is 0.75 m/s, and is used in Equation (6.3) to construct the upper and lower cut-off lines (– · –) of the shear wave energy. Contour levels plotted are (10, 30, 60, 100, 200, 400, 800). The equation for the best fit dispersion line (– –) is noted above each plot.

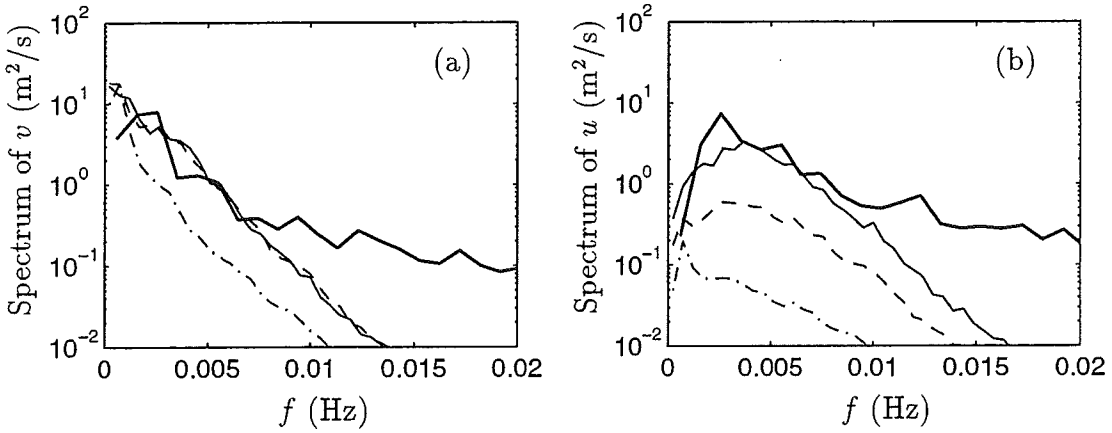

Figure 6.82: October 18: Frequency spectra of (a) longshore and (b) cross-shore velocities for data (thick ——), $c_f = 0.003$ and $M = 0$ (thin ——), $M = 0.25$ (– –), $M = 0.5$ (– · –)

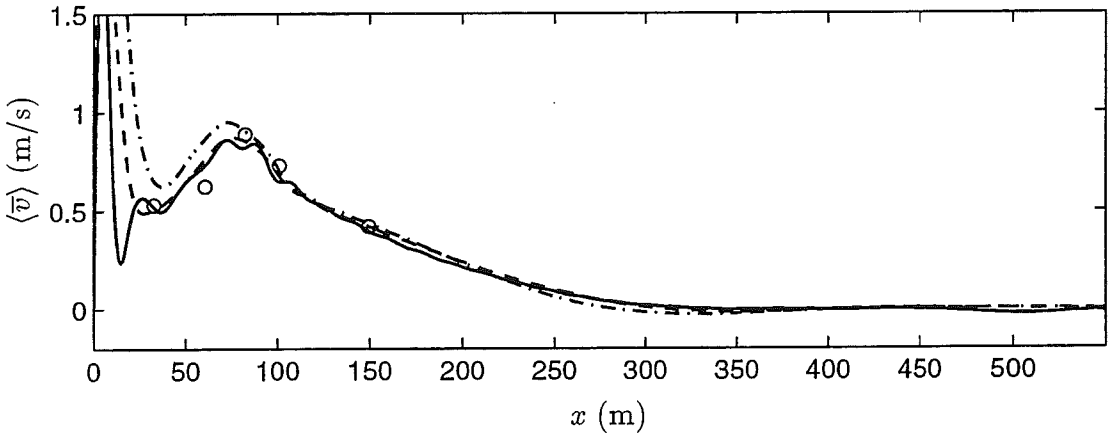

Figure 6.83: October 18: Time and longshore-averaged longshore currents $\langle\overline{v}\rangle$ for $c_f = 0.003$ and $M = 0$ (——), $M = 0.25$ (– –), $M = 0.5$ (– · –) and sled data (○).

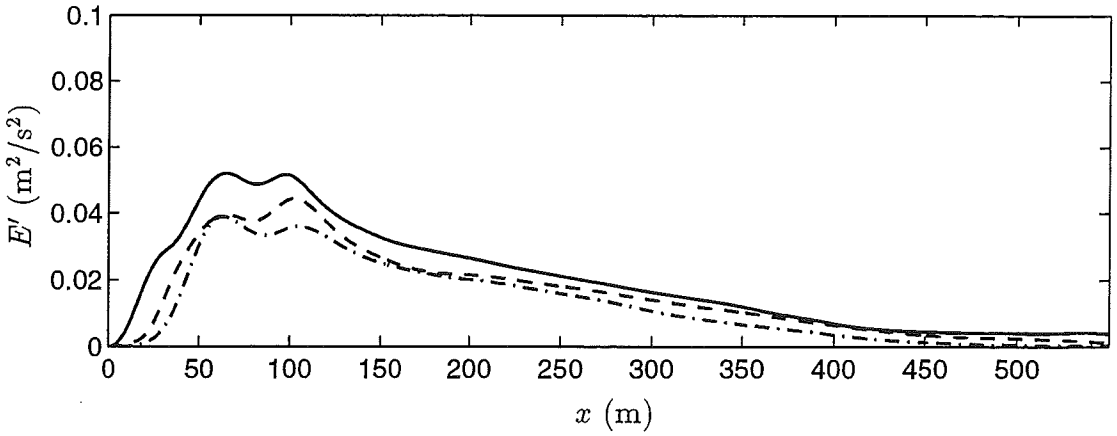

Figure 6.84: October 18: Time and longshore-averaged longshore perturbation kinetic energy $\frac{1}{2}\langle\overline{u'^2} + \overline{v'^2}\rangle$ for $c_f = 0.003$ and $M = 0$ (——), $M = 0.25$ (– –), $M = 0.5$ (– · –).

the $\langle\overline{\tau'_y}\rangle$ term is seen to dominate in the region $x < 25$ m.

Snapshots of the vorticity fields are depicted in Figure 6.86. For $M = 0$, we see that a relatively short longshore length scale is evident in the nearshore region. The features are energetic and shed vortex pairs offshore. For $M = 0.25$, especially the layer of negative vorticity is weaker. In addition, the length scales of the motions are longer. For $M = 0.5$, the vorticity field is reminiscent of the flow features observed during the plane beach simulations. The features have long length scales and are primarily confined to the surf zone. Occasional vortex shedding occurs. The increase in the amount of eddy viscosity mixing causes the amount of high wavenumber oscillations to decrease. The result is a decrease in the number of features in the modeling domain, consequently the apparent longshore length scales of the motions increases. The motions are also weakened due to the dissipational effect of the mixing.

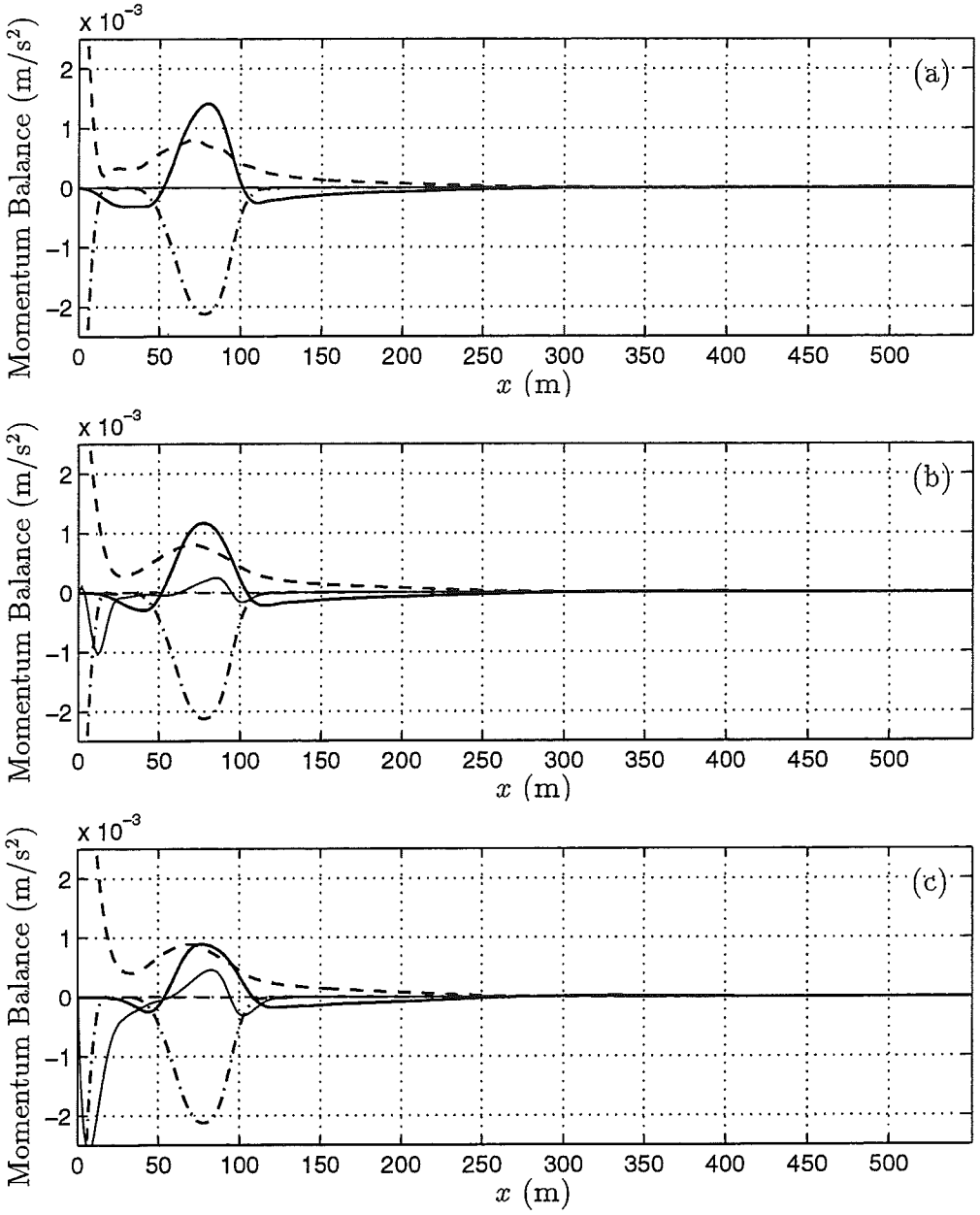

Figure 6.85: October 18: Mean longshore momentum balance for $c_f = 0.003$ and (a) $M = 0$, (b) $M = 0.25$ and (c) $M = 0.5$. $\langle\overline{u(\partial v/\partial x)}\rangle$ (thick ——), -$\langle\overline{\tilde{\tau}_y}\rangle$ (– · –), -$\langle\overline{\tau_y'}\rangle$ (thin ——), $\langle\overline{\frac{\mu}{D}v}\rangle$ (thick – –), residual (thin – –).

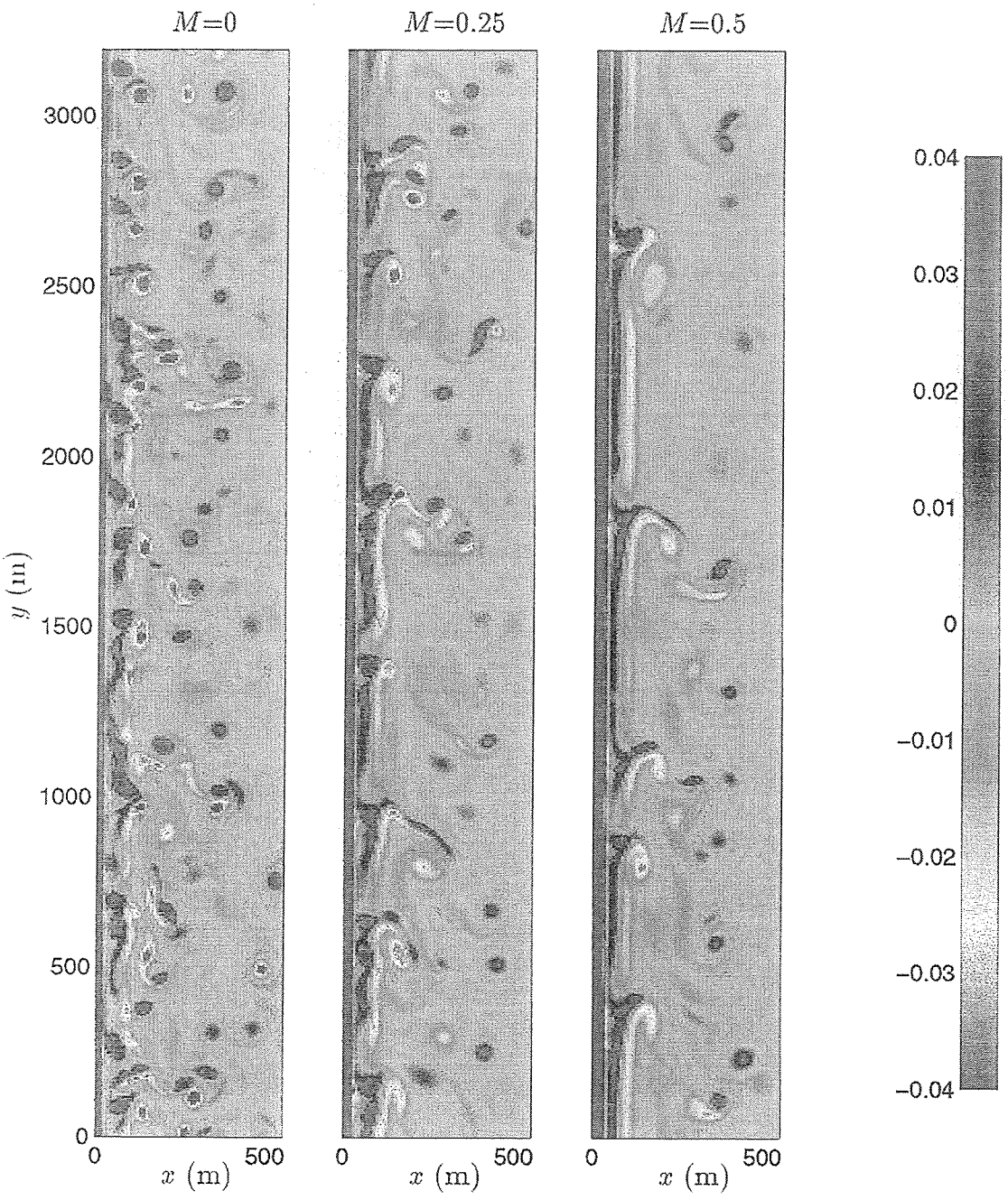

Figure 6.86: October 18: Contour plots of vorticity q (1/s) at $t = 5$ hrs for $c_f = 0.003$ and $M = 0, 0.25, 0.5$.

6.6.4 Summary

In this section, we simulated the shear instability climate for October 15, 16 and 18 at SUPERDUCK for a fixed friction coefficient and a range of mixing coefficients. The choice of the friction coefficient was determined in the previous section by comparing the predicted and observed propagation speeds of the resulting motions.

In the previous section, simulations were carried out for $M = 0.25$. The friction coefficient that best reproduced the observed propagation speed was determined. Variations in the predicted propagation speeds were seen to be significant when the friction factor was varied. In this section, we find that the predictions of the propagation speed for fixed c_f show relatively minor variations for $0 < M < 0.5$. The variations in the predictions are less than 10%. This value is of the same order as the amount of uncertainty in the assessment of the propagation speed for a given frequency-wavenumber spectrum.

As M is varied, the character of the instability climate is observed to change. As M is increased, the spin-up time of the instabilities increases. In addition, the motions are weakened due to the diffusive character of the mixing terms, their longshore length scales also increase.

One significant observation is that the longshore current peak and offshore shear do not vary for different values of M. Therefore, the total amount of mixing due to the instabilities and other processes is constant. Examination of the mean longshore momentum balance showed that mixing due to instabilities was the dominant effect. However, since the total amount of mixing is constant, the mixing due to the instabilities decreases as M is increased. Also noteworthy is the finding that the eddy viscosity mixing effects are less active in the presence

of the instabilities than they are in the absence of the instabilities. This finding indicates that the shear instabilities tend to dominate the longshore momentum balance. If information about the mean current profile is needed, the inclusion of the mixing due to the instabilities is crucial. However, if the nature of the instabilities themselves is analyzed, the inclusion of the effects of the eddy viscosity terms is important. In other words, the effects of the eddy viscosity terms are more pronounced in the shear instability climate and less pronounced in the mean longshore current.

For October 15 and 16, the instability climate offshore of the bar trough was clearly affected by the choice of M. However, the energy levels in the trough region of the bar were similar, making it difficult to distinguish between the cases when comparing to data. For October 18 more energy due to the instabilities was observed in the entire modeling domain. The simulations for October 18 show that the energy content in the data is best reproduced for $M = 0$. However, the case involving $M = 0.5$ is also of interest since the resulting motions are reminiscent of the motions obtained for a plane beach in Chapter 5.

Frequency spectra comparisons showed that the shear instabilities appear to be energetic enough to account for the amount of energy observed in the measurements. But the distribution of the energy in frequency is weighted towards lower frequencies. Data to model correspondence can be observed for the range of frequencies given by $0.002 < f < 0.007$ Hz. Energy at frequencies below this range is consistently overpredicted, whereas energy at frequencies above this range is underpredicted. The modeled frequency spectra have a well defined drop-off with increasing frequency. In contrast, the data displays a broader spectral shape.

6.7 Discussion of Flow Properties

In Chapter 5, we found that the details of vortex interactions were best understood when examining the time evolution of the vorticity q as a function of longshore distance. Such figures illustrate the propagation speeds as well as energetics of the disturbances. In the plane beach simulations that were documented in Chapter 5, we found periodic disturbances with modulated amplitudes that occasionally collided and merged with each other. The details of the collision processes were examined. In this section we investigate if similar interactions between vortices occur in the case of a barred beach.

We choose four representative cases from the simulations documented in the previous sections. For October 15, we choose a representative case defined by the parameter choices $c_f = 0.002$ and $M = 0.25$. A sequence of snapshots of the vorticity field for this case was discussed in Section 6.5.1. In Figure 6.87 we show a contour plot of the vorticity $q(x_0, y, t)$ where $x_0 = 100$ m. This cross-shore location corresponds to the position of the peak of the mean longshore current. The left panel of Figure 6.87 displays a time series of the vorticity $q(x_0, y_0, t)$ where $y_0 = 860$ m. This longshore location is also marked on the contour plot with a thick black line. The blue and purple regions represent positive vorticity whereas the yellow and orange regions represent negative vorticity.

In comparison to similar plots obtained for the plane beach simulations, Figure 6.87 appears to display an unorganized character. However, the vortex interactions can still be picked out. We can see several energetic features with positive vorticity that propagate through the domain, the milder the slope of the resulting blue line the faster the propagation speed dy/dt. Smaller positive vorticity features are frequently observed to catch up with the large vortices. As an example, the positive vortex structure that is located at $y = 1500$ m at $t = 2.7$

hrs experiences about 4 vortex collision events as it propagates to $y = 2750$ m. The first collision event occurs at $y = 2200$ m around $t = 3.2$ hrs. Many of the features identified for the plane beach simulations apply. The faster positive vortex is observed to catch up to the slower vortex in front of it. As the two vortices attempt to merge, the trailing vortex is observed to gain energy and slow down. It takes the place of the vortex in front, which loses almost all of its energy and speeds up to the original speed of the trailing wave. A phase shift is introduced at the time of the collision since the lines representing the lower and higher speeds do not intersect. The weakened disturbance in front propagates into a region of negative vorticity and continues to lose energy. Due to frequent collisions in the form described above, the pattern in Figure 6.87 displays strong propagating positive vortex features with long "streaks" on their left sides, representing the faster vortices as they catch up, and small "streaks" on their right sides, representing the vortices in front that lose energy but gain speed as a result of the interaction.

The faster vortices appear to originate from regions of negative vorticity. As an example, we can observe that a vortex originates in an area of negative vorticity at $y = 860$ m (where the thick black line is located) and $t = 3.25$ hrs. It propagates through the domain and interacts with the slower positive vorticity front at $y = 2000$ m and $t = 3.6$ hrs. A closer examination of the origin of the vortex reveals that it is actually related to a weakened vortex that has propagated into the region of negative vorticity after a collision event that took place at $y = 0$ m and $t = 3.1$ hrs. The vortex propagating away from this earlier collision can be observed to weaken further as it propagates. It almost disappears around $y = 600$ m but then begins to gain energy and forms the vortex at $y = 860$ m and $t = 3.25$ hrs.

The interactions described herein also occur in larger scales. A cluster of vortices that can be seen at $y = 0$ m and $t = 4$ hrs is observed to interact in much the same way with the cluster of vortices behind it. The collision process occurs at $y = 860$ m (where the thick black line is located) and $t = 4.5$ hrs. The phase shift introduced due to the interaction is large.

For October 16, we choose a representative case defined by $c_f = 0.0035$ and $M = 0.25$. The time and longshore variation of the vorticity q at $x = 100$ m is shown in Figure 6.88. The time series on the left panel is recorded at $y = 696$ m. We notice that the qualitative nature of the pattern is similar to October 15. The main difference between the patterns for the two days is due to the fact that vortices for October 16 do not display the tendency to form clusters. The vortices are well defined and very localized as can also be deduced from the time series on the left panel of the figure. Collisions of the form observed for October 15 exist. Some vortices undergo multiple collisions. The positive vortex located at $y = 696$ m and $t = 4$ hrs undergoes a collision at about $y = 1250$ m, consequently speeds up and loses energy. It encounters another vortex in front of it, interacts again, this time gaining energy and slowing down. In simulations for a plane beach we had noticed that the collision processes reduced the number of disturbances in the domain. Here we see that the weakened vortices sometimes dissipate and the number of disturbances in the domain is reduced. At other times, however, they do not disappear and gain energy again. Larger scale collision events also occur. One such event can be observed around $y = 1000$ m and $t = 3.8$ hrs.

The number of positive vortices in the domain at any instant can be deduced from Figure 6.88 by drawing a horizontal transect at a desired time and analyzing the blue or purple lines crossing that transect. In this manner, we can observe that the flow field has a transient nature since a horizontal transect drawn

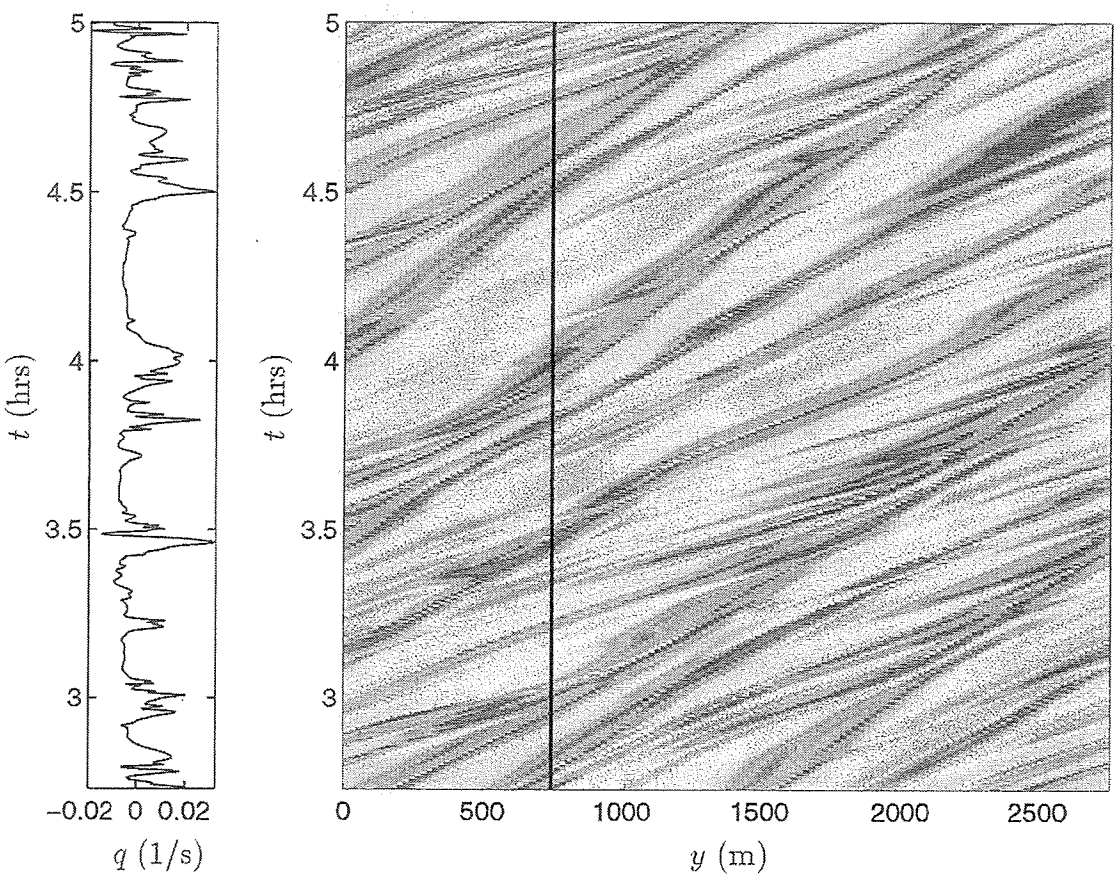

Figure 6.87: October 15: Contour plot of vorticity q as a function of y and t at $x = 100$ m. $c_f = 0.002$ and $M = 0.25$.

at $t = 2.8$ hrs, for example, shows the existence of 7 disturbances in the domain whereas a transect at $t = 3.25$ hrs indicates 9 vortices. A snapshot at $t = 4.1$ hrs, on the other hand, indicates 6 disturbances. The time dependent behavior, therefore, involves the strengthening, weakening and interaction of the vortices leading to changes in the number of waves in the domain.

The vorticity structure for October 18 is analyzed for $c_f = 0.003$ and two values of the mixing coefficient given by 0 and 0.5. Figure 6.89 shows the vorticity pattern for $M = 0$ as a function of y and t at $x_0 = 100$ m. On October 18, the peak of the longshore current occurs about 75 m offshore (see Figure 6.83). Therefore, the cross-shore location $x_0 = 100$ m corresponds to the layer of negative vorticity seaward of the longshore current peak. The time series shown on the left panel is recorded at $y = 870$ m. In contrast to the previous figures, we observe that more disturbances exist in the domain. Broad regions of negative vorticity do not exist. Instead, localized positive (purple) and negative (orange) vortices are observed to propagate together as pairs. Interactions between vortices occur but are not as pronounced as for the previous cases. The interactions do not cause a reduction in the number of vortices in the domain. All the disturbances appear to propagate at similar speeds. It can be confirmed that this speed is less than the propagation speed for October 15 or 16.

A final case involves a value for the mixing coefficient of $M = 0.5$. While a analyzing snapshot of vorticity for this case (see Figure 6.86), we had observed that the behavior in this case is reminiscent of the simulations for a plane beach. Contour plots of $q(x_0, y, t)$ with $x_0 = 100$ m are shown in Figure 6.90 along with a time series of the vorticity at $y = 870$ m. Positive vortices are localized and propagate in the longshore direction. The pattern is indeed similar to the pattern observed during the plane beach simulations shown in Figure 5.22. The

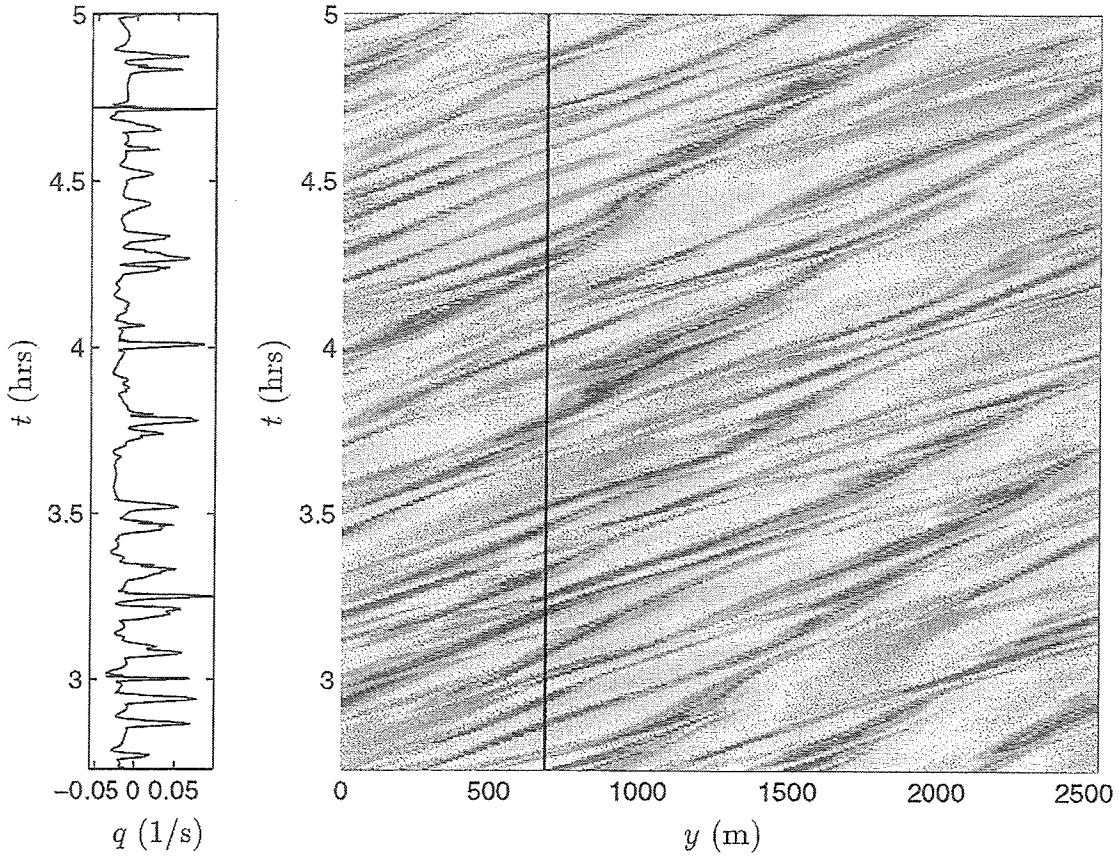

Figure 6.88: October 16: Contour plot of vorticity q as a function of y and t at $x = 100$ m. $c_f = 0.0035$ and $M = 0.25$.

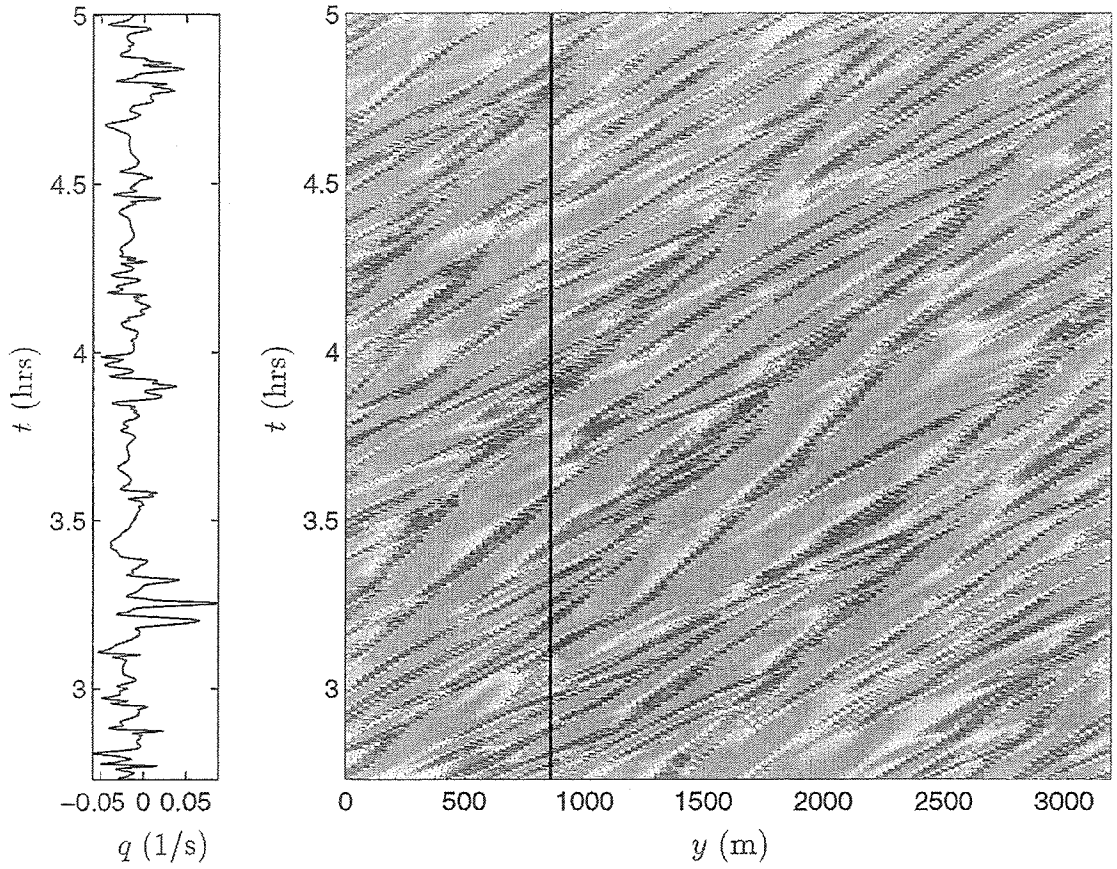

Figure 6.89: October 18: Contour plot of vorticity q as a function of y and t at $x = 100$ m. $c_f = 0.003$ and $M = 0$.

interactions between the vortices are clearly visible. In contrast to the plane beach simulations, the vortices that are weakened as a result of the collisions do not dissipate in the regions of negative vorticity. Instead, they propagate through the regions of negative vorticity and interact with the next region of positive vorticity that they encounter. This type of behavior was also observed for October 15 and 16, but was not as clearly visible.

6.8 Summary

In this chapter, numerical simulations have been carried out to model the shear instability climate during four days of the SUPERDUCK field experiment. The bottom bathymetries for the four simulated days are characterized by a steep foreshore slope and a shore-parallel bar formation. Bathymetry measurements at a cross-shore transect are used, straight-and-parallel bottom contours are assumed.

The short wave forcing terms in the governing equations are specified by utilizing the wave height transformation model by Thornton and Guza (1983). Following Whitford (1988), we assume that the incoming wave spectrum can be characterized as narrow banded and that the wave heights are Rayleigh distributed. The short wave field is considered to be stationary and the time-invariant short wave forcing terms in the governing equations are specified using formulations for the radiation stress terms given by linear water wave theory.

Bottom friction effects are included utilizing linear damping terms in the momentum equations. The size of the friction coefficient was deduced from measurements by Whitford and Thornton (1996) for the four modeled days . Dominant effects of the Taylor dispersion process outlined by Svendsen and Putrevu (1994) are included in a rudimentary fashion. Turbulent momentum mixing is neglected

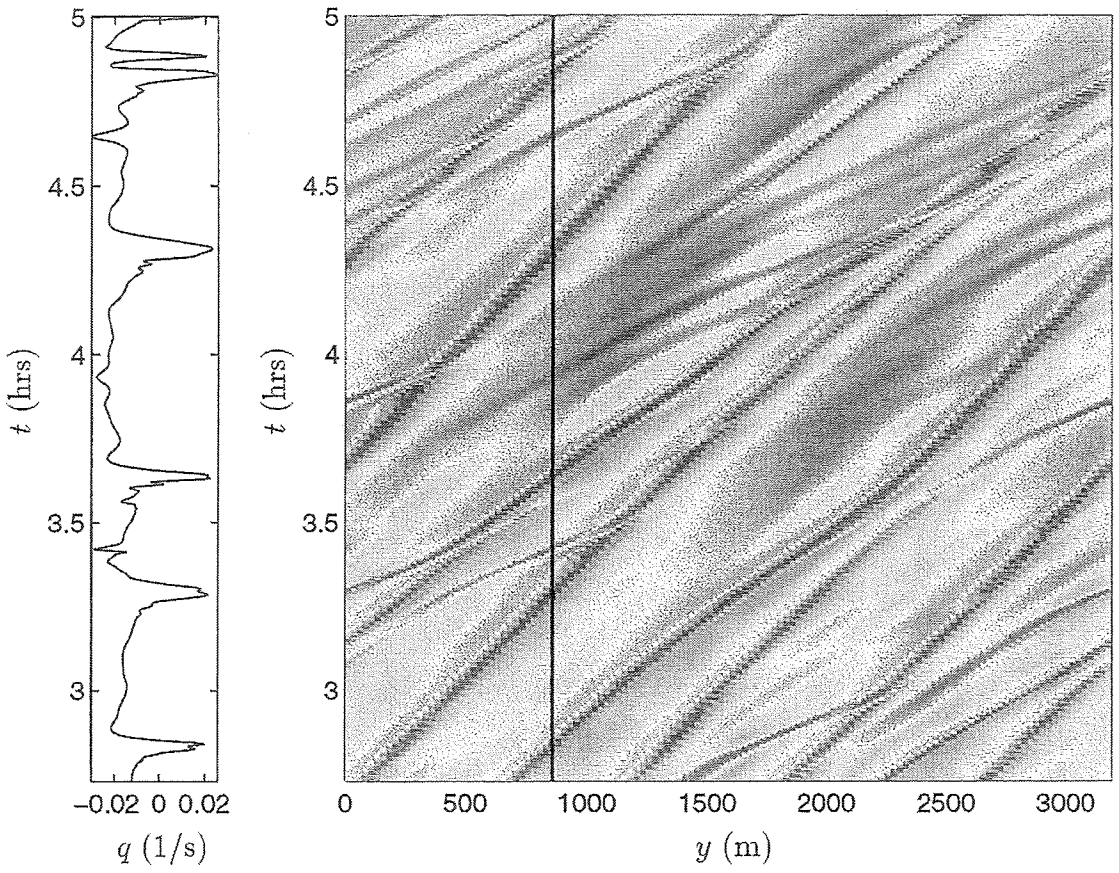

Figure 6.90: October 18: Contour plot of vorticity q as a function of y and t at $x = 100$ m. $c_f = 0.003$ and $M = 0.5$.

unless it is reinforced by the Taylor dispersion process. The order of magnitude of the mixing terms is assessed so that a realistic range for the mixing coefficient can be specified. Simulations are carried out for each day for a range of bottom friction and mixing coefficients.

In summary, we find that a stronger mean current, more energetic fluctuations in the velocities, faster propagation speeds and more energetic vortex structures result as the friction coefficient is decreased. On the other hand, increasing the mixing coefficient results in less energetic motions with longer longshore length scales since the high wavenumber components are preferentially damped by the mixing terms. Even for high values of the mixing coefficient, the lateral momentum mixing caused by the instabilities is found to make an important contribution to the mean momentum balance and, therefore, is an important factor in the generation of a mean longshore current. Remarkably similar mean longshore current profiles are obtained for all values of the mixing coefficient. This observation suggests that the total amount of lateral mixing, which is a combination of mixing due to the instabilities and other mechanisms in the surf zone, is constant.

The propagation speed of the shear instabilities agrees well with observations for a realistic value for the friction coefficient. Frequency spectra comparisons of computations to observations show that the energy content in the frequency range $0.002 < f < 0.007$ Hz can be reproduced. However, energy at lower frequencies is substantially overpredicted whereas energy at higher frequencies is underpredicted. The predictions of the peak longshore current values agree with current measurements from the sled.

Although the propagation speeds of the instabilities as well as the maximum longshore current are predicted with satisfactory agreement, the observed frequency spectra are not modeled very well. The computed shear instabilities

appear to have enough energy to account for the energy present in the shear wave band in data; however, the distribution of the energy in the frequency spectrum is not reproduced.

The details of the time-dependent behavior of the flow structures is analyzed in the last section. We find that vortex collisions of the type observed for plane beach simulations occur. The time-dependent nature of the flow involves the strengthening, weakening and interaction of the vortices. Vortices are frequently shed offshore. During this process the flow structures exhibit properties of transient rip currents.

Chapter 7

INTERACTIONS WITH THE SHORT WAVE CLIMATE

In this chapter we document the extensions to the modeling effort that were performed in order to address some of its shortcomings. Example calculations are not presented since they are the subject of future investigations.

7.1 Introduction

The nonlinear shallow water equations with short wave forcing, momentum mixing and bottom friction terms added provide a good basis for modeling the long-time evolution of shear instabilities of the longshore current. They were derived in Chapter 2 and are given by

$$\begin{aligned}
&\frac{\partial \eta}{\partial t} + \frac{\partial}{\partial x}[ud] + \frac{\partial}{\partial y}[vd] = 0 \\
&\frac{\partial u}{\partial t} + u\frac{\partial u}{\partial x} + v\frac{\partial u}{\partial y} = -g\frac{\partial \eta}{\partial x} + \tilde{\tau}_x + \tau'_x - \tau_{bx} \\
&\frac{\partial v}{\partial t} + u\frac{\partial v}{\partial x} + v\frac{\partial v}{\partial y} = -g\frac{\partial \eta}{\partial y} + \tilde{\tau}_y + \tau'_y - \tau_{by}.
\end{aligned} \tag{7.1}$$

Here, η is the mean water surface elevation above the still water level, h is the water depth with respect to the still water level, $d = (h + \eta)$ is the total water depth, u and v are the depth-averaged current velocities in the x and y directions, respectively, where x points offshore and y points in the longshore direction.

The parameters $\tilde{\tau}_x$ and $\tilde{\tau}_y$ represent short wave forcing effects, τ'_x and τ'_y represent the effects of lateral mixing due to turbulence or other mechanisms. Bottom friction effects are included through the terms τ_{bx} and τ_{by}. The subscripts denote the direction in which the stresses act.

In the previous chapters, the behavior of shear instabilities of the longshore current has been analyzed in mathematically simple settings. The longshore current has been assumed to be forced by time-invariant forcing terms $\tilde{\tau}_x$ and $\tilde{\tau}_y$. Temporally and spatially coherent features in the short wave field as well as slow changes in the wave climate, such as wave groups, have therefore been excluded. Furthermore, the effects of the time-varying currents on the wave field have also been neglected. Even in the absence of offshore wave groups, this interaction will cause time variability of the short wave field. Therefore, in order to model a more realistic short wave forcing field, the assumption of a stationary wave field has to be lifted. This can be achieved by computing the time-dependent short wave field utilizing the energy equation for the short wave motions.

The primary effect of the current field on the short wave motions on an open coast is in the form of wave refraction around opposing currents. If the opposing currents are strong, current limited breaking can also occur. The results of the computations for shear instabilities on plane and barred beaches display offshore directed motions that are potentially strong enough to cause wave refraction. The refraction of the short waves around offshore directed currents will, in turn, introduce longshore variability of the short wave forcing into the problem. This type of feedback is likely to intensify the offshore directed features associated with shear instabilities much like rip currents are intensified by wave refraction. The inclusion of this effect is likely to improve the spatial distributions of the current velocities.

Another shortcoming of the modeling effort presented in the previous chapters involves the simplistic treatment of the bottom friction terms τ_{bx} and τ_{bx}. The mathematically simplest formulation for bottom friction was utilized, resulting in linear damping terms in the momentum equations. We show in the previous chapters that the bottom friction coefficient is an important factor controlling the behavior of the resulting motions. The inclusion of the nonlinear formulation for the bottom friction can, therefore, lead to more realistic simulations.

In the next sections we discuss the incorporation of the short wave energy equation, the short wave refraction equation as well as the incorporation of nonlinear bottom friction into the modeling effort. The effect of the currents will be included while modeling the short wave transformation. However, we retain the assumption that the wave field is well described by linear water wave theory. The treatment of the effects summarized in this section is carried out parallel to Ebersole and Dalrymple (1979).

7.2 Short Wave Transformation in the Presence of Currents

The shoaling of the short waves is affected by the interaction of waves and currents. The effect on the waves can be determined by solving the energy equation for the short waves and can be captured even if linear water wave theory is used. The linearized form of the energy equation for the short waves including the effects of currents has been derived by Phillips (1977) and can be expressed as

$$\begin{aligned} \frac{\partial E}{\partial t} &+ \frac{\partial}{\partial x}\left[E\left(u + c_g \cos\theta\right)\right] + \frac{\partial}{\partial y}\left[E\left(u + c_g \sin\theta\right)\right] \\ &+ S_{xx}\frac{\partial u}{\partial x} + S_{xy}\left(\frac{\partial v}{\partial x} + \frac{\partial u}{\partial y}\right) + S_{yy}\frac{\partial v}{\partial y} = \epsilon_b. \end{aligned} \tag{7.2}$$

In this equation, E is the short wave energy density, c_g is the group velocity of the short waves, θ is the angle of incidence of the short waves, ϵ_b is the dissipation due to wave breaking, and S_{xx}, S_{xy} and S_{yy} are the components of the radiation stress tensor. The cross-shore variations in the wave celerity $\tilde{c}$, the group velocity c_g and the angle of incidence θ have to be computed accounting for the presence of the current velocities.

The energy equation (7.2) is integrated in time along with the continuity and momentum equations (7.1) using an explicit Adams-Bashforth scheme. The spatial derivatives contained in (7.2) are computed using a Fourier-Chebyshev collocation method as described in Chapter 3. For a smooth start-up of the model, the initial conditions are specified such that there is no initial motion in the modeling domain. The short waves of wave height H are introduced at the offshore boundary utilizing a ramping function in time.

The refraction of short waves is governed by the irrotationality of the wavenumber given by

$$\frac{\partial}{\partial x}(\tilde{k}\sin\theta) - \frac{\partial}{\partial y}(\tilde{k}\cos\theta) = 0. \tag{7.3}$$

For straight-and-parallel bottom contours this equation reduces to Snell's law, which has been utilized in the computation of the wave field in Chapter 6.

Furthermore, the dispersion relationship for the short waves in the presence of currents is given by

$$(\omega - \tilde{k}u\cos\theta - \tilde{k}v\sin\theta)^2 = g\tilde{k}\tanh\tilde{k}h, \tag{7.4}$$

where ω is the absolute frequency $(2\pi/T)$ and T is the short wave period. After the current velocities are computed from the governing equations, the value of $\tilde{k}$ can be determined at each time step utilizing a Newton-Raphson iteration method.

The refraction equation (7.3) can be rewritten as

$$\frac{\partial A}{\partial x} = \frac{\partial B}{\partial y} \tag{7.5}$$

where $A = \tilde{k}\sin\theta$ and $B = \tilde{k}\cos\theta$. Given the values for $\tilde{k}$ and θ at the offshore boundary, the above equation is integrated towards the shoreline with a explicit forward stepping scheme. The longshore derivatives in the equation are computed using Fourier collocation. The wave direction θ is then given by $\theta = \arcsin(A/\tilde{k})$.

7.3 Bottom Friction Formulation

The short wave-averaged bottom friction term $\tau_{b\alpha}$ in the governing equations (7.1) can be expressed in empirical form as

$$\tau_{b\alpha} = \frac{1}{d} c_f \overline{|\vec{u} + \vec{\tilde{u}}_b|(u_\alpha + \tilde{u}_{b\alpha})}, \tag{7.6}$$

where the index α represents the x and y directions, $\vec{u}$ is the current vector, $\vec{\tilde{u}}_b$ is the near-bottom short wave orbital velocity vector and the overbar denotes time-averaging over the short wave period. The short wave orbital velocity can be expressed as

$$\tilde{u}_{b\alpha} = u_{0\alpha}\cos\phi \tag{7.7}$$

where ϕ is the phase function of the short waves. Putrevu and Svendsen (1991) derived the form of the bottom friction term for arbitrary wave and current situations following the derivation by Liu and Dalrymple (1978) by performing the time-averaging in (7.6). The resulting expression for the bottom friction term can be written as

$$\tau_{b\alpha} = \frac{1}{d} c_f u_0 \left[\overline{\beta_1(\phi)} u_\alpha + \overline{\beta_2(\phi)} u_{0\alpha}\right], \tag{7.8}$$

where u_0 is the magnitude of the wave orbital velocity and

$$\begin{aligned} \beta_1(\phi) &= \left(\delta^2 + 2\delta\cos\theta_c\cos\phi + \cos^2\phi\right)^{1/2} \\ \beta_2(\phi) &= \beta_1(\phi)\cos\phi. \end{aligned} \tag{7.9}$$

In the above, θ_c is the angle between the current vector and the wave orbital velocity vector and can be computed from

$$\theta_c = \arctan\left(\frac{v}{u}\right) - \theta, \tag{7.10}$$

and δ is defined as the ratio of the magnitude of the current vector to the magnitude of the wave velocity vector

$$\delta = \frac{\sqrt{u^2+v^2}}{u_0}. \tag{7.11}$$

Investigators such as Longuet-Higgins (1970) and Liu and Dalrymple (1978) derived approximations for this expression for several special cases involving only longshore directed currents. Weak current-small angle of incidence, weak current-large angle of incidence or strong current approximations exist.

Using the above definitions, the nonlinear bottom friction terms in the x and y directions will be given by

$$\begin{aligned} \tau_{bx} &= \frac{1}{d}c_f u_0^2 \left[\frac{1}{2\pi}\int_0^{2\pi}\left(\frac{u}{u_0}+\cos\theta\cos\phi\right)\beta_1(\phi)d\phi\right], \\ \tau_{by} &= \frac{1}{d}c_f u_0^2 \left[\frac{1}{2\pi}\int_0^{2\pi}\left(\frac{v}{u_0}+\sin\theta\cos\phi\right)\beta_1(\phi)d\phi\right]. \end{aligned} \tag{7.12}$$

The orbital velocity u_0 is defined utilizing linear theory as discussed in Chapter 2. The integrals over phase on the right-hand-sides of these expressions have to be evaluated at each time step. Following Ostendorf and Madsen (1979), the integrations in (7.12) are carried out using a five point Gaussian quadrature formula given by

$$\begin{aligned} \frac{1}{2\pi}\int_0^{2\pi} f(\phi)d\phi = 0.284 f(\pi) &+ 0.239\left[f(1.538\pi)+f(0.462\pi)\right] \\ &+ 0.118\left[f(1.906\pi)+f(0.094\pi)\right]. \end{aligned} \tag{7.13}$$

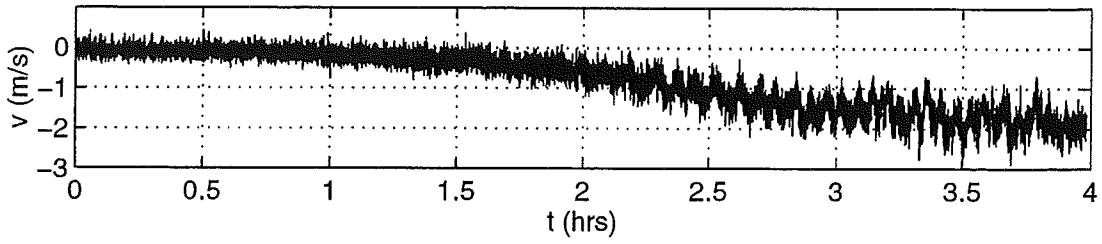

Figure 7.1: October 10: Time series of measured longshore current.

7.4 Suggestions for Applications

The extended model described above can be used to simulate vorticity as well as gravity-dominated low frequency motions. Three possible applications of the extended model are stated in this section and define our short term goals.

In Chapter 6, we simulated the shear instability climate for realistic barred profiles as well as realistic short wave conditions that were derived from observations made on October 15 through 18 during the SUPERDUCK experiment. On these days, the short wave climate was relatively stationary. On other days during the experiment, the short wave field exhibited time variations. One such day was October 10. Observations reported by Oltman-Shay *et al.* (1989) show that within the course of 4 hours, the offshore significant wind wave height increased from 0.4 m to 2.1 m. The southward flowing longshore current in the surf zone increased from 0.1 m/s to 2 m/s. Time series of the longshore velocities recorded on October 10 (see Figure 7.1) show the generation of the longshore current due to the increase in offshore wave heights. The time series also show that the magnitudes of the velocity oscillations at the shear wave frequencies dramatically change. The generation of the longshore current and the spin-up of low frequency motions is observed to occur simultaneously.

The observations on October 10 raise questions about the time scales required for the generation of a longshore current and associated shear instabilities. The extensions of the modeling effort outlined in this chapter provide the means to study the time-dependent generation of longshore currents and associated shear instabilities. The situation on October 10 can be simulated by modeling the time-dependent short wave forcing terms. The energy dissipation model of Thornton and Guza (1983) can again be applied. However, the evolution of a strong shoreline jet is inevitable. Therefore, it is instructive to study a longshore current and shear wave spin-up in a simpler setting first. A realistic plane beach geometry, such as the one for the NSTS experiment at Leadbetter beach provides a good starting point. Information about the spin-up time scales of a longshore current in the absence of shear instabilities should be obtained first. Subsequently, the spin-up period in the presence of the instabilities can be simulated to observe if the instabilities alter the spin-up time of the longshore current and if simultaneous growth of the longshore current and instabilities occurs.

The extended model can also be used to investigate the effects of wave-current interaction on the offshore directed features associated with fully developed shear instabilities. In order to asses the importance of this effect, the shear instability climate in a simple setting can be simulated in the absence as well as in the presence of wave-current interaction terms. Simulations for a plane beach situation documented in Chapter 5 showed that cross-shore velocities of 0.2 m/s can be obtained when the shear instability climate is considered. The plane beach geometry for the NSTS experiment at Leadbetter beach can be utilized to study the interactions in a realistic setting.

During the simulations of the SUPERDUCK experiment, model to data

agreement for October 17 was observed to be poor. Observations show near-zero velocities shoreward of the nearshore bar, whereas model predictions suggest that high mean velocities exist in that region. A possible explanation for the discrepancy was proposed by Whitford (1988) who stated that the dynamics are dictated by intersecting wave trains formed by the wind waves and less energetic swell approaching the shore from different directions, causing opposing currents in the bar trough. Haller *et al.* (1997) suggested that in the presence of such intersecting wave trains, the radiation stress forcing terms will also exhibit longshore variations and could directly force motions at the shear wave time scales. This possibility can be investigated by neglecting wave-current interaction and imposing the variable radiation stress forcing.

Chapter 8

SUMMARY AND CONCLUSIONS

The focus of this work has been the numerical simulation of nonlinear shear instabilities of the surf zone longshore current. For the purposes of analyzing the long-time behavior of shear instabilities, equations governing the depth-averaged currents in the surf zone were solved numerically. The short wave and depth-averaged continuity and momentum equations form a two-dimensional model for the time-varying behavior of surf zone currents. They are in the form of the shallow water equations with additional terms to account for the forcing, damping and diffusion of the currents.

Since the momentum equations are time-averaged over the time scale of the short waves, the effects of motions at the short wave time scales are reduced to a short wave forcing term, whereas effects at the turbulence time scales are reduced to momentum mixing terms. Depth-averaging the resulting equations causes the effects of the depth variations in the surf zone currents to be reduced to several new terms in the depth-averaged momentum equations. These terms have been identified by Svendsen and Putrevu (1994) and Putrevu and Svendsen (1997). The dominant effect due to these terms is additional lateral momentum mixing.

In the scope of this study, the effects of short wave forcing, bottom friction, turbulent momentum mixing as well as the effects of nonuniformities in the current velocities were included in a rudimentary fashion. We incorporated simplifying assumptions that reduced the effects of these processes to the mathematically simplest formulations. The bottom friction effects were modeled using linear damping terms in the momentum equations with an empirical friction coefficient. The mixing processes were parameterized using an eddy viscosity formulation. A mixing coefficient was introduced. The short wave forcing effects were modeled utilizing linear water wave theory. Although linear wave theory has many limitations in the surf zone, the ease of application for a range of conditions has made it the tool of choice. These simple formulations were purposefully incorporated to study the evolution of shear instabilities in a mathematically simple setting.

Spectral collocation methods were used to compute the spatial derivatives in the governing equations. Given initial and boundary conditions, the time evolution of the current field was computed using an explicit time integration method. Since our primary interest is in the simulation of temporal instabilities that are longshore progressive, periodic boundaries were utilized in the longshore direction. A curvilinear moving boundary condition was constructed at the shoreline using an Eulerian model in conjunction with a moving grid. The movement of the grid was damped with distance from the shoreline. An absorbing-generating boundary condition developed by Van Dongeren and Svendsen (1997) was applied at the offshore boundary. The boundary condition has been shown to perform well for gravity wave motions exiting the domain of interest. However, the boundary was not transparent to vorticity motions.

The question of whether the method is capable of reproducing unstable behavior in a well understood case was addressed by modeling the growth of

subharmonic standing edge waves. These waves evolve on a beach as a result of an instability of a normally incident (and reflected) long-crested wave. This instability has been studied extensively, and predictions for equilibrium edge wave amplitudes as a function of incident wave conditions and frictional damping rates are available. The present method was observed to be capable of reproducing the neutral stability boundaries and equilibrium amplitude predictions for this particular class of motions.

The solution method was applied to the simulation of shear instabilities of the longshore current on plane and barred beaches. The simulations for a plane beach were carried out using an analytic longshore current profile. We found that the instabilities grow to finite amplitude. The amplitude of the fluctuation velocity in the longshore direction was observed to reach values of 50% of the peak longshore current. The cross-shore velocity amplitudes reached values of 20% of the peak longshore current. We also found that the propagation speed associated with larger disturbances was lower. This finding suggests that nonlinearity acts to reduce the propagation speed of the motions indicating negative amplitude dispersion.

We examined the effect of including the wave-induced steady setup and the shoreline fluctuations due to the instabilities. The surface elevations, and hence the shoreline runup due to the instabilities was found to be small for this case. The presence of the steady setup did not alter the character of the resulting motions. A more conclusive statement about the effect of the setup on the instability mechanism can, however, not be made. Dalrymple and Lozano (1978) previously showed that, in addition to the solution consisting of a steady setup, a neutrally stable solution in the form of steady rip current circulation cells exist for normally incident waves over straight-and-parallel contours. An instability mechanism that

can lead to these neutrally stable solutions has not been identified to date. If such a mechanism is present, the existence of a longshore current will alter the neutral solution and advect features in the longshore direction. This possibility has to be investigated.

Results for the plane beach showed that the initial development of the flow is dominated by vortex collision and pairing events. The resulting flow structures exhibit offshore directed velocity vectors and are observed to propagate in the longshore direction at a fraction of the longshore current peak. These results are intriguing and possibly suggestive of a generation mechanism for migrating rip currents. A data set that involved observations of rip currents on a plane beach was obtained during the NSTS experiment at Torrey Pines Beach in 1978. Tang and Dalrymple (1989) reported that "migrating and pulsating" rip currents were observed during this experiment. The migration velocities were such that oscillations with time scales of 1000 sec or longer were observed. Simulations for the plane beach case documented in this study showed the presence of migrating rip-like features. "Pulsating" motions were not observed since the features in the plane beach simulations display a highly periodic character.

"Pulsating" features were, however, observed during the simulations of the SUPERDUCK field experiment, where the bathymetry is characterized by a shore-parallel bar formation. Meandering longshore currents were first observed by Oltman-Shay *et al.* (1989) during this experiment. The shear wave climate at SUPERDUCK is very distinct since the shear wave motions dominate the frequencies less than 0.01 Hz. Computations have been carried out for four days from the field experiment for a realistic range of friction and mixing coefficients in an attempt to find the values for the coefficients that best reproduce the observed propagation speed and energy content. Measured time series collected in the trough region

of the bar formation were utilized for data to model comparisons. A total of 18 model runs were documented in Chapter 6.

The results of the simulations showed that vortex collisions of the type observed for plane beach simulations occur. The time-dependent nature of the flow involves the strengthening, weakening and interaction of the vortices. Vortices are frequently shed offshore. During this process the flow structures exhibit properties of transient rip currents.

We found that a stronger mean longshore current, more energetic fluctuation velocities and faster propagation speeds result if the friction factor is decreased. For the narrow range of friction coefficients utilized, the longshore length scales of the motions were not affected, but the vortex fields were more energetic at all cross-shore locations for smaller friction factor. For three days from the SUPERDUCK data set, observed propagation speeds were reproduced. The general shape of the frequency-longshore wavenumber spectra of the velocities was reproduced for frequencies less than 0.01 Hz.

The effects of mixing were analyzed by fixing the friction coefficient at the value that reproduced the observed propagation speed. We found that an increase in the mixing coefficient causes relatively small variations in the propagation speeds. The resulting motions had longer longshore length scales. The total energy in the fluctuations decreased for higher mixing coefficient. However, differences in fluctuation energy are less pronounced in the nearshore region, especially in the bar trough. Since velocity observations during SUPERDUCK were carried out in the bar trough region, it can at times be difficult to deduce the "correct" value of the mixing coefficient by comparing measurements to computations. Time series for a range of mixing coefficients can represent the data in the bar trough region with the same degree of accuracy, making it difficult to discriminate

between the cases. Although similar in the bar trough region, the cases associated with the different mixing coefficients are very different since an increase in the mixing coefficient results in longer, less energetic motions with weaker vortices throughout most of the modeling domain. The existence of current measurements on the bar crest or offshore of the bar crest would be beneficial in order to assess with a higher degree of confidence which mixing coefficient reproduces data best. Such measurements were collected during the DELILAH experiment, where an alongshore array of current meters was deployed offshore of the bar crest. An alongshore array of current meters in the bar trough region as well as a cross-shore current meter array were also deployed during DELILAH. The existence of the cross-shore array makes it possible to compare cross-shore profiles of the predicted mean longshore velocity with data. Such comparisons could only be made with sled measurements at SUPERDUCK, but it was already pointed out that those comparisons must be interpreted with care due to the sequential nature of the sled data and the different averaging periods associated with sled measurements and model results.

Observations at DELILAH showed that the shear instability climate was not dominant at low frequencies. Instead, infragravity and far-infragravity motions coexisted at low frequencies. The model developed in this study is especially well suited for studies where gravity wave motions and vorticity motions are considered in tandem. Therefore, simulations of the DELILAH experiment are of interest.

A shortcoming of the current modeling effort is related to the predictions of wave height decay. The wave height transformation model by Whitford (1988), which is based on Thornton and Guza (1983), is utilized. Since this model assumes that all wave energy is dissipated in the surf zone, a strong jet of longshore velocities is predicted close to the shoreline. Given the fact that the foreshore

slope at SUPERDUCK has a relatively large value of 0.1, the assumption of total dissipation might not be entirely justified. In addition, the longshore current velocity is assumed to be zero at the shoreline boundary. This condition might also not be realistic, as discussed by Brochini and Peregrine (1996). As a result, an unrealistically high peak and large gradients of the velocities are predicted close to the shoreline. Although there is no indication from the computations that the shoreline jet contributes to the computed shear instability climate, the modeling of the longshore current profile is nonetheless unreasonable.

As a result of the simulations for the SUPERDUCK experiment, we find that the shear instabilities provide a significant amount of lateral momentum mixing. The momentum mixing due to the instabilities is especially pronounced around the longshore current peak. Mixing is also induced in the bar trough region causing the generation of significant mean longshore current velocities even in the absence of other more traditional mixing mechanisms. In the presence of other mixing mechanisms, that we parameterize using an eddy viscosity formulation, the mixing due to the instabilities decreases. We find that the total amount of mixing in the surf zone is a constant for a fixed friction coefficient, so that virtually the same mean longshore current profile is generated regardless of the value of the mixing coefficient. If the mixing coefficient is increased, the amount of mixing due to the instabilities decreases proportionally.

Examining the mean longshore momentum balance, we found that the mixing induced by the instabilities was larger than mixing due to the eddy viscosity terms for reasonable mixing coefficients. In addition, we found that the contribution of the eddy viscosity terms is larger in the absence of instabilities than it is in the presence of instabilities. This suggests that in the presence of shear instabilities in a surf zone, the mixing associated with the instabilities dominates

the momentum mixing process in the surf zone. We note that the cross-shore distribution of the momentum mixing due to the instabilities is such that the location of the longshore current peak is not altered. For all simulations carried out for the SUPERDUCK experiment, the longshore current peak was located over the bar crest. Sled measurements during SUPERDUCK also indicate that the current maximum occurred on the bar crest. It is noted that a useful engineering tool would be obtained if an appropriate parameterization of the mixing induced by the shear instabilities can be constructed. The mean longshore current profile in the presence of the instabilities can then be computed without carrying out lengthy computations of the time-dependent nature of the flow.

The situations simulated for October 15, 16 and 18 correspond to storm events. Results from simulations showed the presence of energetic vortices in the surf zone. It was observed that the vortices frequently detach from the surf zone and are shed offshore. These vortices have the potential of transporting sediment offshore. In situations where weaker currents are present in the surf zone (such as model predictions for October 17) the resulting structures are weaker and only occasionally shed vortices offshore, resulting in less potential to transport sediment offshore.

Quantitative comparison of computations and data were carried out by examining the computed and measured frequency spectra for the value of the friction coefficient that reproduced the observed propagation speeds. We found that for all days (except October 17) energy in the frequency range $0.002 < f < 0.007$ Hz was predicted reasonably well, whereas energy at frequencies below this range was consistently overpredicted. Energy for $f > 0.01$ Hz was consistently underpredicted. For October 17, data comparison was poor. We suspect that the dynamics on this day are dictated by intersecting wave trains at the wind wave

and swell frequencies. Such an offshore wave field has the potential of directly forcing low frequency vorticity motions (Haller *et al.*, 1997). This possibility can be explored using the extensions to the model described in Chapter 7.

The computed shear instabilities appear to have enough energy to account for the energy present in the shear wave band in data; however, the distribution of the energy in the frequency spectrum is not reproduced. Other mechanisms are necessary to distribute the energy to higher frequencies. One such mechanism could be provided by interactions of the shear instabilities with the edge wave climate. Therefore, the low frequency gravity wave and vorticity wave climates need to be considered in tandem. The model developed in this study is comprehensive so that such interactions can be studied in the future.

REFERENCES

Abbott, M.B. (1979). *Computational Hydraulics. Elements of the Theory of Free Surface Flows.* Pitman Publishing.

Allen, J.S., P.A. Newberger and R.A. Holman (1996). "Nonlinear shear instabilities of alongshore currents on plane beaches." *J. Fluid Mech.*, **310**, 181–213.

Battjes, J. (1975). "Modeling of turbulence in the surf zone." *Proc. Symposium on Modeling Techniques*, San Francisco, 1050–1061.

Birkemeier W.A. and R.A. Dalrymple (1975). "Nearshore water circulation induced by wind and waves." *Proceedings Modelling '75*, 1062–1081.

Bowen, A.J. (1969). "The generation of longshore currents on a plane beach." *J. Marine Res.*, **73**, 2569–2577.

Bowen, A.J. and D.L. Inman (1971). "Edge waves and crescentic bars." *J. Geophys. Res.*, **76**, 8662–8671.

Bowen, A.J. and R.A. Holman (1989). "Shear instabilities of the mean longshore current. 1. Theory." *J. Geophys. Res.*, **94**, 18023–18030.

Boyd, J.P. (1988). *Chebyshev & Fourier Spectral Methods.* Springer-Verlag, New York, N.Y.

Brochini, M. and D.H. Peregrine (1996). "Integral flow properties of the swash zone and averaging." *J. Fluid Mech.*, **317**, 241–273.

Canuto, C. M.Y. Hussaini, A. Quarteroni and T.A. Zang (1987). *Spectral Methods in Fluid Dynamics.* Springer-Verlag, New York, N.Y.

Carrier, G.F. and H.P. Greenspan (1958). "Water waves of finite amplitude on a sloping beach." *J. Fluid Mech.*, **4**, 97–109.

Church J.C., E.B. Thornton and J. Oltman-Shay (1992). "Mixing by shear instabilities of the longshore current." *Proc. 23rd Intl. Conf. Coastal Eng.*, 2999–3011.

Crowson, R.A., W.A. Birkemeier, H.M. Klein and H.C. Miller (1988). "SUPERDUCK nearshore processes experiment: Summary and studies CERC field research facility." *Tech. Rep. CERC-88-12*, 81 pp., Coastal Eng. Res. Cent., Vicksburg, Miss.

Dalrymple, R.A. and C.J. Lozano (1978) "Wave-current interaction models for rip currents." *J. Geophys. Res.*, **83**, 6063–6071.

Dalrymple R.A., J.T. Kirby and P.A. Martin (1994). "Spectral methods for forward-propagating water waves in conformally-mapped channels." *Appl. Ocean Res.*, **16**, 249–266.

Deigaard, R., E.D. Christensen, J.S. Damgaard and J. Fredsøe (1994). "Numerical simulation of finite amplitude shear waves and sediment transport." *Proc. 24th Intl. Conf. Coastal Eng.*, 1919–1933.

De Vriend, H.J. and M.J.F. Stive (1987). "Quasi-3D modeling of nearshore currents." *Coastal Engineering*, **21**, 565–601.

Dodd, N. (1994). "On the destabilization of a longshore current on a plane beach: Bottom shear stress, critical conditions, and onset of stability." *J. Geophys. Res.*, **99**, 811–824.

Dodd, N.,and E.B. Thornton (1990). "Growth and energetics of shear waves in the nearshore." *J. Geophys. Res.*, **95**, 16075–16083.

Dodd, N. and E.B. Thornton (1992) "Longshore current instabilities: Growth to finite amplitude." *Proc. 23rd Intl. Conf. Coastal Eng.*, 2655–2668.

Dodd, N., Oltman-Shay, J. and Thornton, E. B. (1992) "Shear instabilities in the longshore current: A comparison of observation and theory." *J. Phys. Oceanography*, **22**, 62–82.

Dodd, N. and A. Falqués (1996). "A note on spatial modes in longshore current shear instabilities." *J. Geophys. Res.*, **101**, 22,715–22,726.

Drazin P.G. and L.N. Howard (1966). "Hydrodynamic stability of parallel flow of inviscid fluid." in *Advances in Applied Mechanics*, vol. 7, G. Kuerti, Ed., Academic Press, 1–89.

Drazin P.G. and W.H. Reid (1982). *Hydrodynamic Stability.* Cambridge University Press, Cambridge, UK.

Ebersole B.A. and R.A. Dalrymple (1979). "A numerical model for nearshore circulation including convective accelerations and lateral mixing." *Ocean Engineering Rep. No. 21*, University of Delaware, 87 pp.

Falqués, A. and V. Iranzo (1992). "Edge waves on a longshore shear flow." *Phys. Fluids A*, **4**, 2169–2190.

Falqués, A. and V. Iranzo (1994) "Numerical simulation of vorticity waves in the nearshore." *J. Geophys. Res.*, **99**, 825–841.

Falqués, A., V. Iranzo and M. Caballería (1994) "Shear instability of longshore currents: Effects of dissipation and nonlinearity." *Proc. 24th Intl. Conf. Coastal Eng.*, 1983–1997.

Faria, A.F.G., E. Thornton and T. Stanton (1995). "A quasi-3D model of longshore currents." *Proc. Coastal Dynamics 1995*, Gdansk, Poland, 389–400.

Feddersen F. (1996), "Weakly nonlinear finite amplitude shear waves." *Transactions of the American Geophysical Union Fall Meeting, EOS suppl.*, p. 400, San Francisco, California.

Fowler, R.E. and R.A. Dalrymple (1990). "Wave group forced nearshore circulation." *Proc. 22nd Intl. Conf. Coastal Eng.*, 729–742.

George R., R.E. Flick and R.T. Guza (1994). "Observations of turbulence in the surf zone." *J. Geophys. Res.*, **99**, 801–810.

Gopalakrishnan, T.C. and C.C. Tung (1983). "Numerical analysis of a moving boundary problem in coastal hydrodynamics." *Intl. J. Numer. Meth. Fluids*, **3**, 179-200.

Gottlieb, D., M. Gunzburger and E. Turkel (1982). "On numerical boundary treatments for hyperbolic systems." *SIAM J. Numer. Anal.*, **19**, 671–697.

Guza, R.T. and A.J. Bowen (1976). "Finite amplitude edge waves." *J. Marine Res.*, **34**, 269–293.

Guza, R.T. and R.E. Davis (1974). "Excitation of edge waves by waves incident on a beach." *J. Geophys. Res.*, **79**, 1285–1291.

Guza, R.T. and D.L. Inman (1975). "Edge waves and beach cusps." *J. Geophys. Res.*, **80**, 2997–3012.

Haller, M.C., U. Putrevu, R.A. Dalrymple and J. Oltman-Shay (1997). "Wave group forcing of low frequency surf zone motions." Manuscript.

Helmholtz, H. von (1868). "Über discontinuirliche Flüssigkeitsbewegungen." *Monats Königl. Preuss. Akad. Wiss. Berlin*, **23**, 215–228.

Higgins, A.L., R.J. Seymour and S.S. Pawka (1981). "A compact representation of ocean wave directionality." *Appl. Ocean Res.*, **3**, 105–111.

Howd, P.A., O. Oltman-Shay and R.A. Holman (1991). "Wave variance partitioning in the trough of a barred beach." *J. Geophys. Res.*, **96**, 12,781–12,795.

Keely J.R. and A.J. Bowen (1977). "Longshore variation in longshore currents." *Canadian Journal of Earth Science*, **14**, 1897–1905.

Larson M. and N.C. Krauss (1991). "Numerical model of longshore currents over bar and trough beaches." *Journal of Waterway, Port, Coastal and Ocean Engineering*, **117**, 326–347.

Liu, P.L.-F and R.A. Dalrymple (1978). "Bottom frictional stresses and longshore currents due to waves with large angles of incidence." *J. Marine Res.*, **36**, 357–375.

Liu, P.L.-F., Y.-S. Cho, M.J. Briggs, U. Kanoglu and C.E. Synolakis (1995). "Runup of solitary waves on circular island." *J. Fluid Mech.*, **302**, 259–285.

Longuet-Higgins, M.S. (1970). "Longshore currents generated by obliquely incident sea waves. Part 1 and 2." *J. Geophys. Res.*, **75**, 6778–6789 and 6790–6801.

Longuet-Higgins, M.S. and Stewart (1962). "Radiation stress and mass transport in gravity waves." *J. Fluid Mech.*, **13**, 481–504.

Longuet-Higgins, M.S. and Stewart (1963). "A note on wave set-up." *J. Marine Res.*, **21**, 4–10.

Longuet-Higgins, M.S. and Stewart (1964). "Radiation stress in water waves, a physical discussion with application." *Deep Sea Res.*, **11**, 529–563.

Lynch, D.R. and W.G. Gray (1980). "Finite element simulation of flow in deforming regions." *J. Comp. Phys.*, **36**, 135–153.

Noda, E.K. (1974). "Wave-induced nearshore circulation." *J. Geophys. Res.*, **79**, 4097–4106.

Oltman-Shay, J., P.A. Howd and W.A. Birkemeier (1989). "Shear instabilities of the mean longshore current. 2. Field observations." *J. Geophys. Res.*, **94**, 18031–18042.

Ostendorf, D.W. and O.S. Madsen (1979). "An analysis of longshore currents and associated sediment transport in the surf zone." Massachusetts Institute of Technology, Report MITSG 79-13.

Özkan, H.T. and Kirby, J.T. (1995). "Finite amplitude shear wave instabilities." *Proc. Coastal Dynamics 1995*, 465–476.

Özkan-Haller, H.T. and Kirby, J.T. (1996a). "Numerical study of low frequency surf zone motions." *Proc. 25th Intl. Conf. Coastal Eng.*, 1361–1374.

Özkan-Haller, H.T. and Kirby, J.T. (1996b). "Shear Instabilities of the Longshore Current During Superduck." *Transactions of the American Geophysical Union Fall Meeting, EOS suppl.*, p. 394, San Francisco, California.

Özkan-Haller, H.T. and J.T. Kirby (1997). "A Fourier-Chebyshev collocation method for the shallow water equations including shoreline runup." *Appl. Ocean Res.*, in press.

Panchang, V.G. and D.A. Kopriva (1989). "Solution of two-dimensional water-wave propagation problems by Chebyshev collocation." *Mathl. Comput. Modelling*, **12**, 625–640.

Pawka, S. (1983). "Island shadows in wave directional spectra." *J. Geophys. Res.*, **88**, 2579–2591.

Pedersen, G. and B. Gjevik (1983). "Run-up of solitary waves." *J. Fluid Mech.*, **135**, 283-299.

Phillips, O.M. (1977). *The dynamics of the upper ocean.* Cambridge University Press, 336 pp.

Putrevu, U. and I.A. Svendsen (1991). "Wave induced nearshore currents: A study of the forcing, mixing and stability characteristics." Dept. of Civil Eng., University of Delaware, Report CACR-91-11, 242 pp.

Putrevu, U. and I.A. Svendsen (1992) "Shear instability of longshore currents: A numerical study." *J. Geophys. Res.*, **97**, 7283–7303.

Putrevu, U. and I.A. Svendsen (1997). "Shear dispersion of momentum in the nearshore." *J. Fluid Mech.*, in review.

Rayleigh, Lord (1880). "On the stability, or instability, of certain fluid motions." *Proc. London Math. Soc.*, **11**, 57–70.

Reniers, A.J.H.M., J.A. Battjes (1996). "Cross-shore momentum flux due to shear instabilities." *Proc. 25th Intl. Conf. Coastal Engrng.*, 175–185.

Reniers, A.J.H.M., J.A. Battjes, A. Falqués, D.A. Huntley (1994). "Shear wave laboratory experiment." *Proc. Int. Symp. : Waves - Physical and Numerical Modeling*, Vancouver, Canada, 356–365.

Reniers, A.J.H.M., J.A. Battjes, A. Falqués, D.A. Huntley (1997). "A laboratory study on the shear instability of longshore currents." *J. Geophys. Res.*, **102**, 8597–8609.

Reynolds, O. (1883). "An experimental investigation of the circumstances which determine whether the motion of water shall be direct or sinuous, and of the law of resistance in parallel channels." *Phil. Trans. Roy. Soc.*, **174**, 935–982.

Rockliff, N. (1978). "Finite amplitude effects of free and forced edge waves." *Proc. Camb. Phil. Soc.*, **83**, 463–479.

Sanchez-Arcilla, A., F. Collado and A. Rodriguez (1992). "Vertically varying velocity field in q-3d nearshore circulation." *Proc. 23rd Intl. Conf. Coastal Eng.*, 2811–2824.

Schäffer, H.A. (1993). "Infragravity waves induced by short-wave groups." *J. Fluid Mech.*, **247**, 551–558.

Schäffer, H.A. (1994). "Edge waves forced by short-wave groups." *J. Fluid Mech.*, **259**, 125–148.

Shapiro, R. (1970). "Smoothing, filtering and boundary effects." *Reviews of Geophys. and Space Phys.*, **8**, 359–387.

Shemer, L., N. Dodd and E.B. Thornton (1991). "Slow-time modulation of finite-depth nonlinear water waves: Relation to longshore current oscillations." *J. Geophys. Res.*, **96**, 7105–7113.

Slinn, D.N., J.S. Allen, P.A. Newberger and R.A. Holman (1997). "Nonlinear shear instabilities of alongshore currents over barred beaches." *J. Geophys. Res.*, in review.

Svendsen, I.A. (1987). "Analysis of surf zone turbulence." *J. Geophys. Res.*, **92**, 5115–5124.

Svendsen, I.A. and R.S. Lorenz (1989). "Velocities in combined undertow and longshore currents." *Coastal Engineering*, **13**, 55–79.

Svendsen, I.A. and U. Putrevu (1990). "Nearshore circulation with 3-D profiles." *Proc. 22nd Intl. Conf. Coastal Eng.*, 241–254.

Svendsen, I.A. and U. Putrevu (1994). "Nearshore mixing and dispersion." *Proc. Roy. Soc. Lond. A*, **445**, 561–576.

Svendsen, I.A., H.A. Schäffer and J.B. Hansen (1987). "The interaction between undertow and boundary layer flow on a beach." *J. Geophys. Res.*, **92**, 11845–11856.

Tang E. C.-S. and R.A. Dalrymple (1989). "Rip currents and wave groups." in *Nearshore Sediment Transport*, R.J. Seymour, Ed., Plenum Press, 205–230.

Taylor, G.I. (1954). "The dispersion of matter in a turbulent flow through a pipe." *Proc. Roy. Soc. Lond. A*, **219**, 446–468.

Thornton, E.B. and R.T. Guza (1983). "Transformation of wave height distribution." *J. Geophys. Res.*, **88**, 5925–5938.

Thornton, E.B. and R.T. Guza (1986). "Surf zone longshore currents and random waves: Field data and models." *J. Phys. Oceanography*, **16**, 1165–1178.

Van Dongeren, A.R. and I.A. Svendsen (1997). "An absorbing-generating boundary condition for shallow water models." *Journal of Waterway, Port, Coastal and Ocean Engineering*, in press.

Van Dongeren, A.R., F.E. Sancho, I.A. Svendsen and U. Putrevu (1994). "SHORECIRC: A quasi 3-D nearshore model." *Proc. 24th Intl. Conf. Coastal Eng.*, 2741–2754.

Verboom, G.K. and A. Slob (1984). "Weakly-reflective boundary conditions for two-dimensional shallow water flow problems." *Adv. Water Resources*, **7**, 192–197.

Whitford, D.J. (1988). "Wind and wave forcing of longshore currents across a barred beach." Ph.D. Dissertation, Naval Postgraduate School, 202 pp.

Whitford, D.J. and E.B. Thornton (1996). "Bed shear stress coefficients for longshore currents over a barred profile." *Coastal Engineering*, **27**, 243–262.

Wind, H.G. and C.B. Vreugdenhill (1986). "Rip current generation near structures." *J. Fluid Mech.*, **171**, 459–476.

Wright, L.D., R.T. Guza and A.D. Short (1982). "Surf zone dynamics on a high energy dissipative beach." *Marine Geology*, **45**, 41–62.

Zelt, J.A. (1986). "Tsunamis: The response of harbours with sloping boundaries to long wave excitation." Report No. KH-R-47, California Institute of Technology, Pasadena, California.

Zelt, J.A. and F. Raichlen (1990). "A Lagrangian model for wave-induced harbour oscillations." *J. Fluid Mech.*, **213**, 203–225.